The University Of Sheffield.

Access To Thesis.

- A bound copy of every thesis which is accepted as worthy for a higher degree, must be deposited in the University of Sheffield Library, where it will be made available for borrowing or consultation in accordance with University Regulations.
- All students registering from 2008–09 onwards are also required to submit an electronic copy of their final, approved thesis. Students who registered prior to 2008–09 may also submit electronically, but this is not required.

Author: Patricia Bessiere Dept: Physics & Astronomy

Thesis Title: Characterising the host galaxies of type II quasars Registration No: 100242414

For completion by all students:

Submit in print form only (for deposit in the University Library): ☐

Submit in print form and also upload to the *White Rose eTheses Online* server: In full ☑

Edited eThesis ☐

Please indicate if there are any embargo restrictions on this thesis. Please note that if no boxes are ticked, you will have consented to your thesis being made available without any restrictions.

Embargo details: (complete only if requesting an embargo to either your print and/or eThesis)	Embargo required?		Length of embargo (in years)
Print Thesis	Yes ☐	No ☑	____
eThesis	Yes ☐	No ☑	____

Supervisor: I, the supervisor, agree to the named thesis being made available under the conditions specified above.

Name: Clive Tadhunter Dept: Physics & Astronomy

Signed: C.N. Tadhunter Date: 6/01/15

Student: I, the author, agree to the named thesis being made available under the conditions specified above.

I give permission to the University of Sheffield to reproduce the print thesis in whole or in part in order to supply single copies for the purpose of research or private study for a non-commercial purpose.

I confirm that this thesis is my own work, and where materials owned by a third party have been used copyright clearance has been obtained. I am aware of the University's *Guidance on the Use of Unfair Means* (www.sheffield.ac.uk/lets/design/unfair)

I confirm that all copies of the thesis submitted to the University (including electronic copies on CD/DVD) are identical in content.

Name: Patricia Bessiere Dept: Physics & Astronomy

Signed: P Bessiere Date: 06/01/15

For completion by students also submitting an electronic thesis (eThesis):

I, the author, agree that the University of Sheffield's eThesis repository (currently WREO) will make my eThesis available over the internet via an entirely non-exclusive agreement and that, without changing content, WREO may convert my thesis to any medium or format for the purpose of future preservation and accessibility.

I, the author, agree that the metadata relating to the eThesis will normally appear on both the University's eThesis server and the British Library's EThOS service, even if the thesis is subject to an embargo. I agree that a copy of the eThesis may be supplied to the British Library.

I confirm that the upload is identical to the final, examined and awarded version of the thesis as submitted in print to the University for deposit in the Library (unless edited as indicated above).

Name: Patricia Bessiere Dept: Physics & Astronomy

Signed: P Bessiere Date: 06/01/15

THIS SHEET MUST BE BOUND IN THE FRONT OF THE PRINTED THESIS BEFORE IT IS SUBMITTED

Characterising the host galaxies of type II quasars

Patricia S. Bessiere

Department of Physics & Astronomy
The University of Sheffield

A dissertation submitted in candidature for the degree of Doctor of Philosophy at the University of Sheffield

October 2014

Declaration

I declare that no part of this thesis has been accepted, or is currently being submitted, for any degree or diploma or certificate or any other qualification in this University or elsewhere.

This thesis is the result of my own work unless otherwise stated.
The following chapters have been based on publications:

- Chapter 3 – Bessiere et al. (2012).
- Chapter 4 – Bessiere et al. (2014).

Acknowledgements

There are a number of people to whom I owe my sincere thanks. First and foremost I would like to thank my supervisor, Clive Tadhunter, for his invaluable help, guidance, support and patience throughout my Ph.D. I would also like to thank Cristina Ramos Almeida for providing help, advice and insight without which this thesis would probably never have seen the light of day. I owe them both a debt of gratitude. Montserrat Villar Martín has also been a great help to me and I would like to thank her, amongst many other things, for taking me on my first observing trip. It was an education.

I would also like to thank my wonderful family and friends, especially my mother Aurelia and sister Caroline, for their unwavering support. Their belief and encouragement has helped me through the difficult times.

Thanks also to my fellow Ph.D students and post docs who have made the journey a significantly more enjoyable one. To Saida Caballero Nieves, Marvin Rose, Emile Doran, Dave Sahman, Chris Rosslowe, Liam Hardy, and all the rest, past and present, cheers!

Abstract

AGN are thought to play an essential role in the evolution of galaxies. Despite this, the means by which the nuclear activity is triggered remains a matter of much debate. In this thesis, the triggering issue is addressed by investigating the properties of a sample of 20 ($0.3 \leq z \leq 0.41$) type II quasar host galaxies, using high-quality optical imaging and spectroscopic data obtained using Gemini GMOS-S

Evidence for galaxy interactions in the form of tidal features (tails, fans, shells), double nuclei and close pairs is presented in Chapter 3. It is found the 75% of the sample show clear evidence of recent mergers, consistent with the rate found for a matched control sample of early-type galaxies. However, the surface brightnesses of the tidal features in the type II quasars are up to two magnitudes brighter than those of the control sample.

Major mergers also lead to intense bursts of star formation. Therefore, an analysis of the stellar populations of the type II quasar host galaxies is presented in Chapters 4 and 5. It is shown that, in 79% of the type II quasars, spectral synthesis models *require* the inclusion of a young stellar component with an age < 100 Myr.

The stellar masses derived from the spectral synthesis modelling are presented in Chapter 6. It is shown that type II quasars are exclusively hosted by galaxies with stellar mass $> 10^{10}$ $M_{\odot}$, and, in a minimum of 26% of cases, major gas-rich mergers are required to form the young stellar populations.

The results presented in the thesis clearly demonstrate that the host galaxies of type II quasars are dynamic, evolving systems, with compelling evidence that the luminous AGN activity has been triggered by recent mergers in the majority of cases. They also suggest that quasar activity is triggered at around the same time as the merger-induced starbursts.

Contents

List of Figures

List of Tables

Chapter 1

Introduction

Active galactic nuclei (AGN) represent some of the most luminous sources in the Universe. Distant, powerful quasars shine like beacons, illuminating the Universe over cosmic time, giving us an insight into the evolution of galaxies from very early epochs. Currently, the most distant known AGN is at a redshift of $z = 7.085$ (Mortlock et al., 2011), however, AGN are found at all intervening redshifts and with a wide range of luminosities.

1.1 The historical perspective

The first discovery of an AGN was made by E.A. Fath in 1908, when he took a spectrum of the nearby galaxy NGC 1068, and found it to have some unusual properties. However, the true study of AGN began with the discovery that a subset of 'extragalactic nebulae' showed unusual emission from their nuclear regions (Seyfert, 1943). This took the form of a much higher luminosity nucleus than would be expected for normal galaxies. Their spectra also showed Doppler broadened hydrogen emission lines (up to 8500 km s^{-1} full width at zero intensity) that appeared to be broader at higher luminosities, as well as strong high excitation lines such as [OIII]λ5007. Figure 1.1 shows a comparison of two galaxies, one of which hosts an AGN whilst the other does not. It is clear that the central region of the AGN NGC 5548 (panel (a)) is substantially brighter than the normal galaxy M101 (panel (b)), with the bright point source in NGC 5548 causing diffraction spikes in the image.

The discovery of quasars did not come about until the first large-scale radio surveys, such as the third Cambridge (3C) catalogue (Edge et al., 1959), which had sufficient resolution to to allow radio sources to be unambiguously associated with optical coun-

(a) NGC 5548 (b) Messier 101

Figure 1.1: A comparison of the properties of the central region of (a) the AGN NGC 5548 (taken from ESA/Hubble press release[1]) with (b) the normal galaxy M101 (credit: NASA/ESA/K Kuntz (JHU)/F Bresolin (University of Hawaii)/J Trauger (JPL)/J Mould (NOAO)/Y-H-Chue (university of Illinois)/STScI.)

terparts. This led to the discovery of powerful radio sources which were associated, in optical images, with what appeared to be normal galactic stars. However, their spectra showed that these objects could *not* have a stellar origin because their optical counterparts had strong, broadened emission lines that were found at wavelengths not identified with any known transitions. It was not until Schmidt (1963) realised that these lines were actually the hydrogen Balmer series with a cosmological redshift that the true significance of this class object became apparent.

Schmidt (1963) calculated a large (at the time) redshift of $z = 0.158$ for 3C 273, which implied that this source was extremely luminous. In fact, this interpretation would result in the nucleus being 100 times more luminous than all the stars in our own Galaxy. Unsurprisingly, this met with a certain amount of scepticism, with many alternative explanations being put forward. However, by the early 1980s, imaging observations of these mysterious objects, such as those of Malkan et al. (1984), had clearly demonstrated that these extremely luminous sources are indeed associated with galaxies at cosmological distances, and the matter was laid to rest.

With the interpretation that these unusual objects are, in fact, highly luminous came

[1] http://www.spacetelescope.org/news/heic1413/

a significant problem, namely how to generate such copious amounts of energy across the electromagnetic spectrum in such a small volume. It is now widely accepted that AGN are powered by accretion of material by super massive black holes (SMBH) (Zel'dovich & Novikov, 1965; Lynden-Bell, 1969) that are though to reside in the nuclei of massive galaxies (Magorrian et al., 1998). This is because accretion onto black holes is the most efficient means of converting mass to energy; from the observed luminosities we can infer mass accretion rates of 10^{-5} to 100 $M_{\odot}$ yr^{-1} in the most extreme cases.

1.2 The many flavours of AGN

Since these early discoveries, various surveys across the electromagnetic spectrum have discovered numerous examples of the AGN phenomenon, with bolometric luminosities ranging from 10^{39} erg s^{-1} for low-ionization nuclear emission-line region AGN (LINERs) to 10^{48} erg s^{-1} for the most powerful quasars (Jogee, 2006). Recent examples of such surveys include the Sloan Digital Sky Survey (SDSS; York et al. 2000) and the Great Observatories Origins Deep Survey[2] (GOODS; Dickinson et al. 2003). The variations in the characteristics of AGN have led to a complex classification scheme, based on factors such as bolometric luminosity, radio luminosity, and whether broad emission lines are detectable in the spectrum. The main groups are outlined below.

Seyfert Galaxies

Seyfert galaxies were the first type of AGN to be discovered (Seyfert, 1943), and are objects in which, typically, the AGN have optical luminosities that are comparable with those of the integrated starlight of the host galaxies. Schmidt & Green (1983) defined Seyfert galaxies to have moderate luminosities, where the AGN themselves have absolute magnitudes $M_B > -21.5 + 5\ \log h_0$. However, as it became increasingly clear that AGN are a diverse class of objects, with a wide range of properties, it became necessary to divide them into sub-classes, in order to better understand their characteristics.

The class is further divided into two sub-classes based on the characteristics of the spectra. Type I objects are those which have both narrow and broad permitted lines, as well as narrow forbidden lines. The typical full width half maximum (FWHM) for the narrow lines is 400 km s^{-1}, while for the broad lines, a typical FWHM is 5000 km s^{-1}. It is thought that the broad lines originate in higher density material close to the central engine, while both the permitted and forbidden narrow lines originate in lower density

[2] http://www.stsci.edu/science/goods/

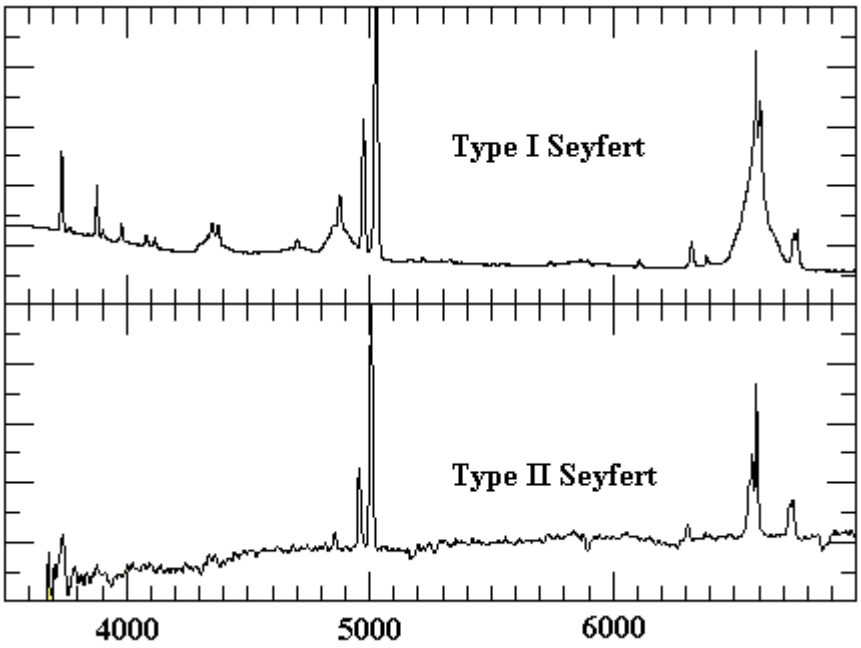

Figure 1.2: A comparison of the spectra of type I and type II AGN. The top panel shows a typical broad line spectrum in which the strong broadening of Hβ and Hα can clearly be seen. The bottom panel shows a typical narrow line spectrum in which these lines only have narrow components[3].

gas at a greater distance. In contrast type II Seyfert galaxies only have the narrow permitted and forbidden lines in their spectra, and the stellar component of the galaxy is much more prominent than in type I objects. Figure 1.2 shows a comparison between the spectra of typical type I and type II objects, and the difference in the widths of the Hβ (λ4861) and Hα(λ6563) can clearly be seen. Observational studies of the morphological type of Seyfert host galaxies have revealed that a substantial fraction ($\sim$ 70%) reside in disc dominated galaxies (e.g. Adams 1977).

Quasars

Quasar nuclei are essentially the same objects as type I Seyfert nuclei, in that their spectra share many of the same characteristics, but they form the high end of a continuous range of AGN luminosities. Where as a Seyfert nucleus will have a similar luminosity to the its host galaxy, a quasar can be up to 10^4 times more luminous than its host. Quasars tend to be found at higher redshifts than Seyfert galaxies simply because they are rarer. It is common for the host galaxies of quasars to be difficult to detect and study because the light from the quasar point source is so dominant. Quasars are also

[3]Image taken from http://www.uni.edu/morgans/astro/course/Notes/section3/new13.html

divided into type I and type II, however, large samples of type II quasars have only recently become available (e.g. Zakamska et al. 2003; Reyes et al. 2008), with the advent of large-scale surveys such as the SDSS and infrared (IR) facilities such as *Spitzer*. In contrast to Seyfert galaxies, quasars are more commonly found in bulge dominated host galaxies (e.g. Bahcall et al. 1997; Dunlop et al. 2003; Floyd et al. 2004).

LINERs

LINERs were first identified by Heckman (1980), and are at the opposite end of the luminosity scale to quasars, having the lowest level of nuclear activity of all AGN. They are potentially the most common type of AGN in the Universe, with $> 30\%$ of all galaxies showing evidence of LINER activity (Ho et al., 1997a). LINERs are distinctly different from both Seyferts and quasars because, in comparison to their more powerful cousins, low-ionisation lines such as [OI] and [NII] are relatively more prominent in their spectra.

Radio-loud AGN

AGN are not only prodigious in the optical, but a sub-set of them ($\sim 10\%$) are powerful radio emitters, or radio-loud AGN. In previous studies, different authors have used varying criteria in order to categorize an AGN as radio-loud. In this thesis, the definition of Xu et al. (1999) is adopted, which defines radio-loudness based on the relationship between radio power at 5 GHz and the luminosity of [OIII]. In this scheme, it is the magnitude of the radio power to the optical luminosity which defines whether an object is radio-loud, not the *absolute* radio power. Nevertheless, however radio-loudness is defined, the activity takes the form of jets issuing from the central source, which can extend up to the mega-parsec (Mpc) scale.

The radio morphologies of radio-loud AGN fall into two classes, defined by Fanaroff & Riley (1974), known as FRI and FRII. FRI radio sources have the lower radio power of the two groups, with a brighter core and lobes decreasing in surface brightness towards the edges. In contrast FRIIs are more powerful, with extended lobes that terminate in hotspots. FRIIs are also quasars, whereas FRIs tend to have lower luminosity AGN at their heart. Once again, these can be classed as type I or type II objects, depending on whether the broad permitted lines are directly detectable in their optical spectra. In the case of radio-loud AGN, these are known as broad line radio galaxies (BLRG) and narrow line radio galaxies (NLRG) respectively. However, not all radio-loud AGN are luminous in the optical, with only weak optical emission lines in their spectra. This class of object is therefore known as weak line radio galaxies (WLRG). Regardless of their

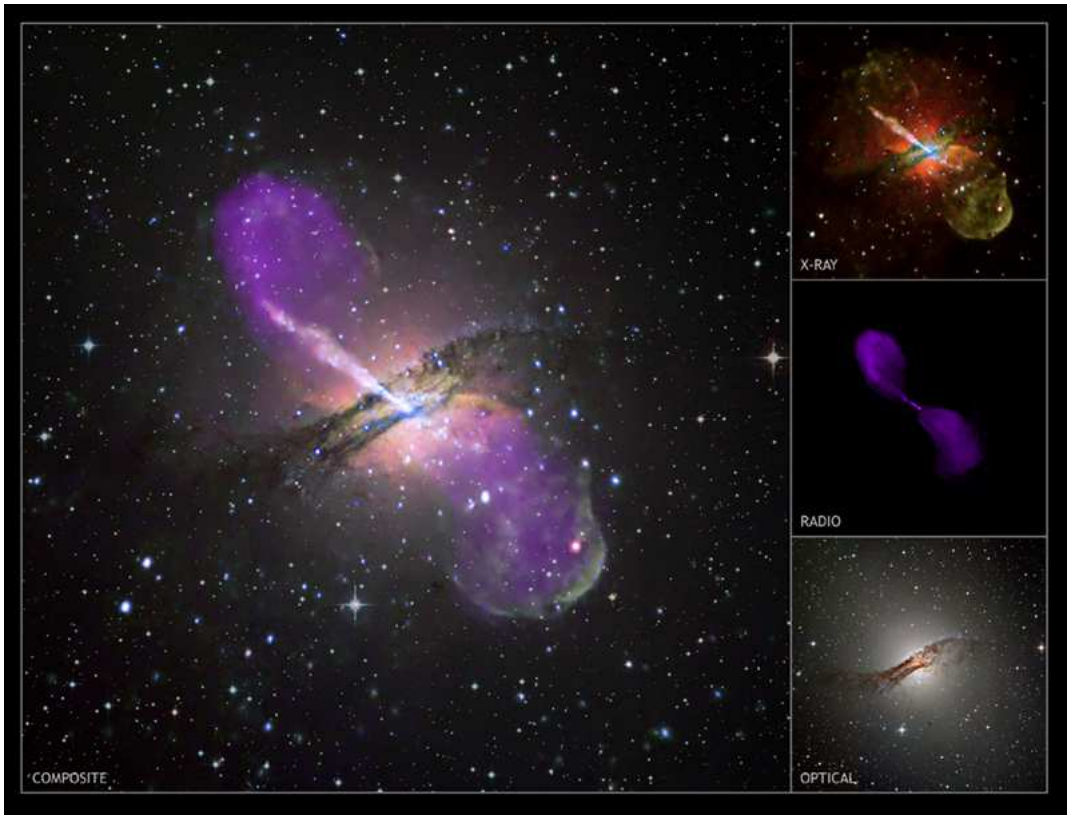

Figure 1.3: The archetypal FRI radio galaxy Centaurus A. The three panels on the left show imaging of Centaurus A in three different regions of the spectrum. The top left panel shows the X-ray emission, the middle shows the radio emission and the bottom panel shows the optical emission. The main image is a composite of the 3 and clearly illustrates the extended lobes powered by the jets emanating from the central source. This image is taken from the Chandra X-ray observatory website[4]and is credited to NASA/CXC/CfA/R.Kraft et al.

optical classification, radio-loud AGN are found to reside almost invariably in massive, early-type galaxies (e.g. McLure et al. 1999; Dunlop et al. 2003). The transition between FRIs and FRIIs was defined by Bridle & Perley (1984) as $L_\nu(1.4\ \mathrm{GHz}) = 10^{25}\ \mathrm{W\ Hz^{-1}}$. Figure 1.3 shows the archetypical FRI source Centaurus A.

1.3 Orientation-based unified models

In order to explain the diversity of AGN at optical wavelengths, in particular the relationship between type I and type II AGN, orientation-based unified schemes have been proposed (e.g. Barthel 1989; Antonucci 1993). They suggested that the apparent differ-

[4] www.http://chandra.harvard.edu

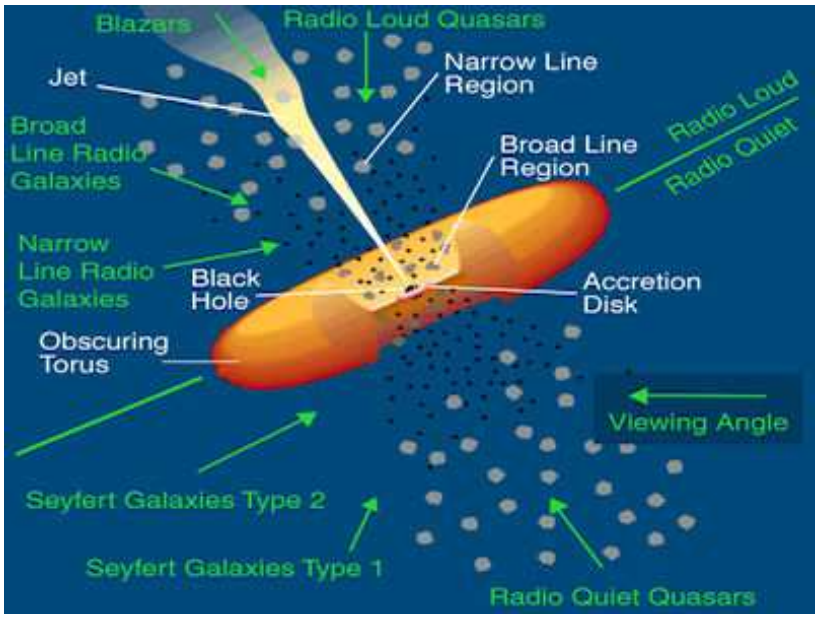

Figure 1.4: A schematic representation of the Unified Scheme for AGN, depicting the torus surrounding the central engine and how the viewing angle the determines the classification.

ences could be explained in terms of the distribution of material in the region around the central engine, in conjunction with the angle at which it is viewed. In this scenario, the ultimate power source of all AGN is fundamentally the same, consisting of a central SMBH, onto which material is accreting, thereby generating the prodigious luminosities that we observe. This region is then surrounded by a torus of dusty dense material. Originally, this material was considered to be smoothly distributed (e.g. Pier & Krolik 1992), although more recent work assumes that it is, in fact, much more clumpy in its structure (e.g. Nenkova et al. 2008).

Figure 1.4 shows a schematic view of the orientation-based unified scheme, with the different regions in which the various spectral characteristics, outlined in the previous section, are generated. The upper part of the diagram represents radio-loud AGN, while the bottom half is demonstrative of their radio-quiet counterparts. It is important to note that this model *does not* explain why 10% of AGN are radio-loud, while the remaining 90% are radio-quiet, but rather, it relates to the observed properties given that an AGN is either radio-loud or radio-quiet. The figure shows that the clouds from which the broad emission lines (broad line region, BLR) are emitted are close to the central SMBH. This means that there is a large spread in the velocities of the clouds, due to the strong gravitational field, which results in extreme Doppler broadening of the emitted lines. Reverberation mapping of the BLR for a number of AGN has shown that

its spatial scale varies with the luminosity of the AGN, but the BLR is less than a parsec (pc) in size (e.g. Wandel et al. 1999). In contrast the narrow permitted and forbidden lines are emitted from clouds at much larger distances from the central source, and thus have a much smaller spread in velocities. Once again, the exact size of the NLR has been found to be dependent of the luminosity of the AGN, but is on the order of a few $\times 10^4$ pc (e.g. Bennert et al. 2002).

Taking into consideration the different spatial scales on which the narrow and broad emission lines are emitted, in this particular model, whether an AGN is classified as a type I or a type II object is dependent on whether the torus is viewed close to face-on, so that the BLR and accretion disc are visible, or whether the system is viewed close to edge-on, so that these regions are obscured, and only the NLR can be observed.

Howerver, this picture does not explain the characteristics of LINERs and WLRGs, in which there is often little evidence for a BLR or extended NLR. These sources have very low accretion rates, and it is thought that they are powered by gas cooling directly from the intracluster medium and falling onto the SMBH (i.e. cooling flows). In this scenario, neither the geometrically thin, opticaly thick accretion disc or the surrounding torus of obscuring material exist.

1.4 Energy Generation

The luminosity of the AGN and therefore, whether it is classified as a Seyfert galaxy or a quasar, is determined by the rate at which material is being accreted by the SMBH, because

$$L_{bol} = \eta \dot{M} c^2 \tag{1.1}$$

where L_{bol} is the bolometric luminosity of the AGN, η is the efficiency, which in the case of compact accreting objects such as this is thought to be ~ 0.1 ($0.04 \leq \eta \leq 0.16$) (e.g. Marconi et al. 2004; Merloni 2004), and $\dot{M}$ is the mass accretion rate. This implies that, in order to power an AGN of quasar-like luminosity ($10^{45}\,\mathrm{erg\ s^{-1}}$), a mass accretion rate of

$$\frac{10^{45}\,\mathrm{erg\ s^{-1}}}{0.1c^2} \sim 0.2\,\mathrm{M_\odot\ yr^{-1}} \tag{1.2}$$

would be required.

However, there is a theoretical upper limit to the accretion rate, and thus luminosity of an AGN, known as the Eddington luminosity. This limit is reached when the radiation

pressure, driven by the accretion, exceeds the inward gravitational force, resulting in the material surrounding the SMBH being pushed away, thus starving the black hole of further fuel. This limit is given by

$$L_{EDD} = \frac{4\pi G m_p c}{\sigma_e} M_{BH} \tag{1.3}$$

where G is the gravitational constant, m_p is the mass of a proton, which is moving under the influence of the gravitational force, σ_e is the Thompson cross-section, and M_{BH} is the mass of the SMBH. This demonstrates that more massive black holes are capable of sustaining higher luminosity AGN, because all the other factors in the above equation are constants.

However, this upper limit is theoretical, and is also based on the accretion being spherically symmetric. This however, is not the true geometry of the accreting material, which is thought to fall into the SMBH from the inner edge of an optically thick, geometrically thin accretion disc. This difference between the actual and assumed accretion geometry may go some way to explaining why evidence of super-Eddington accretion has been found in some previous studies, such as that of Marconi et al. 2004, who find Eddington ratios in the range 0.1–1.7.

1.5 Detecting AGN

Given the fact that AGN have such diverse observational characteristics, several different techniques have used to select AGN from the general galaxy population. These include radio, X-ray, IR and optical techniques, which all probe different components of the AGN structure.

The most efficient method of identifying AGN is undoubtedly through X-ray emission, which has been used to detect large numbers of AGN in deep field surveys such as the Chandra Deep Field North (e.g. Alexander et al. 2003), Chandra Deep Field South (e.g. Giacconi et al. 2002) and the XMM-Newton Lockman Hole (Hasinger, 2004). The X-ray emission itself is produced via Compton up-scattering from the accretion disc corona. The reason that it is such an effective technique is that X-rays are thought to be produced by every AGN. In addition, studies have shown that at least 70–80% of X-ray sources found in the deepest surveys are AGN (Bauer et al., 2004). X-rays also have the advantage of penetrating all but the densest (Compton thick; $N_H > 1.5 \times 10^{24}$ cm^{-2}) obscuration, thus allowing identification regardless of viewing angle or dust obscuration from the interstellar medium (ISM) of the host galaxy.

Radio identification is also effective in selecting AGN out to high redshifts. However, not all AGN emit strongly in the radio, and at lower levels, the radio emission may in fact be associated with vigorous star formation rather than AGN activity (Padovani et al., 2009; Condon et al., 2013). Therefore, it is necessary to disentangle the two before secure identifications can be made.

Mid-IR techniques rely on detecting the dust-reprocessed photons originally emitted by the AGN. The shorter wavelength photons from the AGN will heat the dust in the region around the central engine (i.e. the torus), which then re-radiates the energy at longer wavelengths. Due to the strong IR emission this process produces, AGN can be selected based on their mid-IR colours, because they will appear redder than normal galaxies (Stern et al., 2005). However, it is likely that selection by IR colours is biased towards higher luminosity, more obscured AGN (Eckart et al., 2010), and thus, may miss a substantial number of objects.

There are two main optical techniques for selecting AGN. Firstly, AGN have been selected based on their optical, broad-band colours. The strong emission from the AGN makes the object appear bluer than would be expected for an object dominated by a stellar continuum. However, this method only allows the selection of type I objects, because the central source will otherwise be obscured. Most notably, this technique has been exploited by the SDSS (Richards et al., 2002) in order to target potential quasars for follow-up spectroscopy.

The second, more flexible optical technique, which was used to select the sample of powerful AGN on which this thesis is based, is through optical spectroscopy. In the case where broad permitted lines are detected, this allows for a secure identification because no other process produces such broad lines ($10^3\,\mathrm{km\ s^{-1}} \leq \Delta v \leq 10^4\,\mathrm{km\ s^{-1}}$). Where only narrow lines are detected (i.e. type II objects), the situation is not quite so clear cut. Strong emission lines associated with AGN activity, such as [OIII]λ5007, can be used to identify possible candidates, however, these lines may be contaminated by emission from star forming regions in the host galaxy. In order to overcome this problem, it is common practice to compare the ratios of the fluxes of AGN emission lines with different ionisation potentials in order to separate AGN from HII regions. However, it is not possible to discriminate between the two mechanisms on the basis of one set of line ratios alone. Therefore, it is common practice to compare two sets of line ratios, so that not only the hardness of the ionising source can be determined, but also the *range* of ionisations can be probed. This allows for the selection of AGN because, although young hot stars photoionise the gas clouds in which they are born, they do not produce

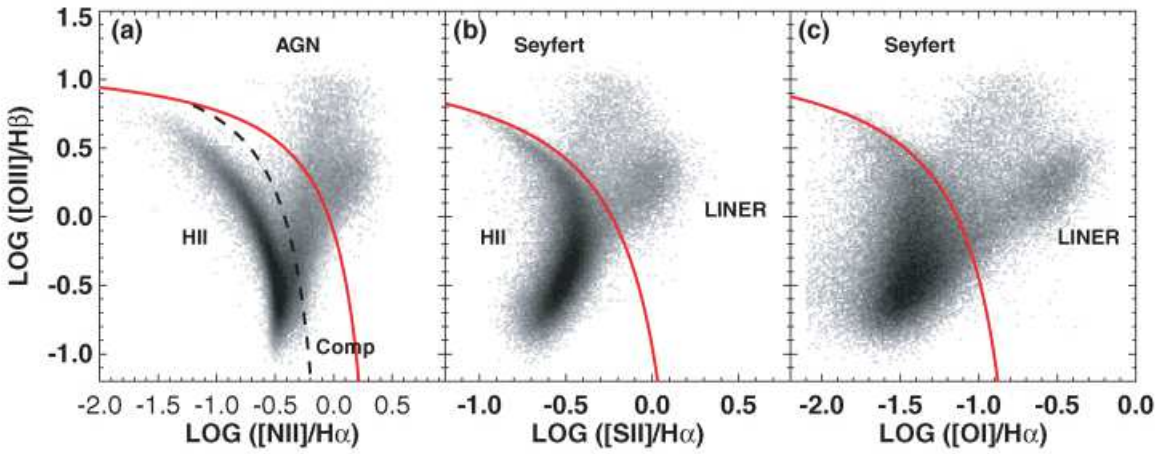

Figure 1.5: An example of a BPT diagram used to classify the dominant ionisation mechanism in a galaxy as either star formation or AGN activity. The solid red line shows the division between the two groups, with AGN on the right of the line and HII regions on the left. The region in between the dotted black line and solid red line in panel 1 is a composite region in which both mechanisms operate but neither are dominant.

as wide a range of ionisation states as an AGN. This is because an AGN will produce sufficient high energy photons to create an extended, partially ionised zone at the backs of the photoionised clouds, whereas, a star forming region will not.

The technique outlined above is particularly effective when coupled with wide-field spectroscopic surveys, such as the SDSS. Figure 1.5, taken from Kewley et al. (2006), demonstrates this selection technique using Baldwin-Phillips-Terlevich (BPT) diagrams (Baldwin et al., 1981), which compare the ratios of lines with different ionisation potentials. The solid red line in all three panels denotes the separation between the parts of the diagrams in which star formation and AGN are the dominant ionisation mechanisms. In the region between the dashed black line and solid red line in the first panel, the objects show composite characteristics.

1.6 AGN and galaxy evolution

For a long period after their discovery, AGN were considered to be rare and exotic objects. However, this perception has shifted dramatically in recent years, and AGN

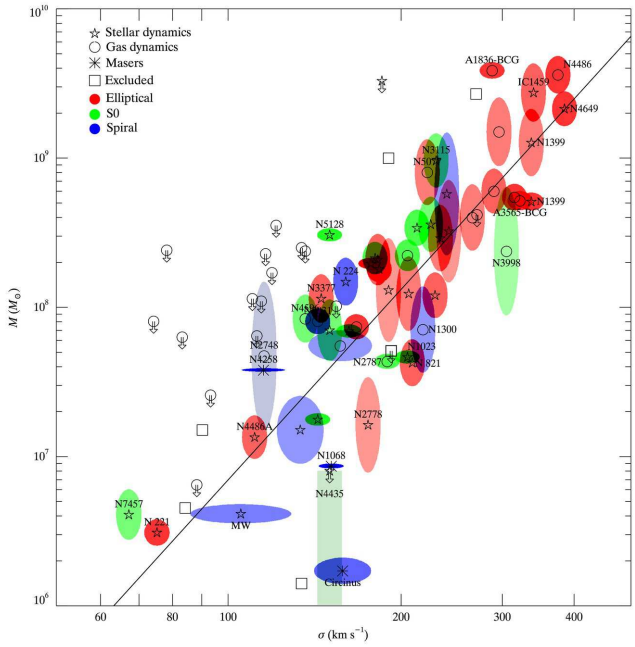

Figure 1.6: The $M_{BH} - \sigma_*$ relation for galaxies which have dynamical mass measurements. The figure is taken from Gültekin et al. (2009) and shows the mass of the SMBH plotted against the stellar velocity dispersion of its host galaxy. The colour of the ellipses identify the Hubble type associated with the galaxy, while their extent show the errors. The symbols indicate the method that was used to measure the SMBH mass, and line shows the best fit to the data. The key for all the symbols and colours used in the figure is show in the plot.

activity is now though to be a fundamental phase in the evolution of all galaxies that have a bulge/spheroid component. This change was brought about, in part, by the discovery of strong correlations between the mass of the SMBH and the properties of the bulge/spheroid components they inhabit.

Initially, it was discovered that a correlation exists between between M_{BH} and the luminosity of the galaxy bulge component (e.g. Dressler 1989; Kormendy 1993; Kormendy & Richstone 1995; Magorrian et al. 1998). It was also realized that there is a strong correlation between the stellar velocity dispersion (σ_*) and M_{BH} (e.g. Ferrarese & Merritt 2000; Gebhardt et al. 2000; Tremaine et al. 2002; Gültekin et al. 2009; Greene et al. 2010; McConnell & Ma 2013). The latter correlation is shown schematically in Figure 1.6, which is taken from Gültekin et al. (2009). The figure clearly demonstrates the increase in the velocity dispersion with M_{BH} for a sample of local galaxies (including our own) for which reliable black hole mass measurements have been made.

Ultimately, bulge luminosity and velocity dispersion both trace the mass of the spheroid component of the galaxy. Therefore, the fundamental correlation is that be-

tween the mass of the spheroid (M_{Sph}) and the mass of the SMBH, such that $0.001 \leq M_{BH}/M_{Sph} \leq 0.002$ (Merritt & Ferrarese, 2001; McLure & Dunlop, 2002; Marconi & Hunt, 2003; Häring & Rix, 2004). There is also limited evidence that this relationship may evolve with redshift (McLure et al., 2006; Bennert et al., 2011), with Bennert et al. (2011) finding the ratio of the SMBH mass to the bulge mass increases towards high redshifts as $M_{BH}/M_{Sph} \propto (1+z)^{(1.96\pm0.55)}$, suggesting that black hole growth preceded spheroid growth at higher redshift.

These relationships lead naturally to the idea that the galaxy spheroid component and its central black hole grow in step with one another. However, accumulating evidence suggests that these relations may not be as fundamental as originally thought. As more SMBH masses are measured, particularly at the lower end of the mass range, it is becoming increasingly evident that it may only be in cases where the host galaxy has a spheroid component that a correlation exists. M_{BH} does not appear to correlate with properties such as the mass of a galaxy disc, or that of a pseudo bulge, leading Kormendy & Ho (2013) (and references therein) to suggest that the $M_{BH} - M_{Sph}$ relation is the result of the build up of spheroidal mass through major mergers, not a fundamental property of *all* galaxies and their SMBH.

Another piece of evidence which supports this idea of co-evolution is the remarkable similarity between the SMBH accretion density history and star formation history of the Universe (Madau et al., 1996; Ueda et al., 2003). This is demonstrated in Figure 1.7, taken from Kormendy & Ho (2013), which shows the evolution with redshift of the SMBH accretion density $\times 5000$, compared with the variation is star formation rate with redshift. The figure clearly shows the rapid increase in both quantities up to a redshift $z \simeq 1.5-2$, after which both quantities begin to decline.

However, although the SMBH is indeed massive (as the name implies!), its sphere of gravitational influence ($r_{inf} = G\,M_{BH}\,/\sigma_*^2$) is at least three orders of magnitude less than the size of its host galaxy, and therefore, we must question how these correlations arise. It is in this context that AGN activity comes to the fore as a prime candidate for mediating the relationship between the SMBH mass and the galaxy spheroid mass. This could be accomplished by feedback generated by the process of accretion onto the SMBH (e.g. di Matteo et al. 2005; Hopkins et al. 2006; Johansson et al. 2009) which is though to occur in two different modes (Croton et al., 2006; Bower et al., 2006). The first of these is 'radio-mode', in which the mechanical energy of the radio jet heats gas on large scales, thus preventing the gas from cooling to form stars and from accreting onto the SMBH. This is thought to happen in low accretion rate, massive systems, and is considered to be

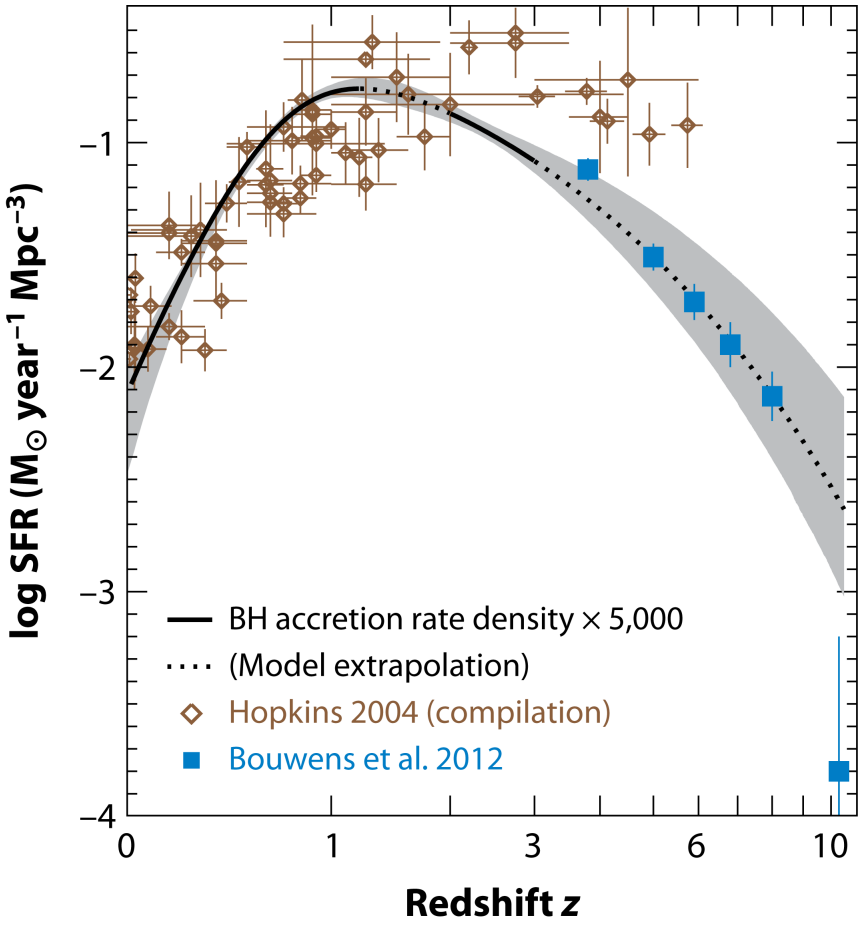

Figure 1.7: A comparison of the evolution of star formation rate density and SMBH accretion density with redshift. This figure is taken from Kormendy & Ho (2013) and shows the SMBH accretion rate density ×5000 and star formation rate density plotted against redshift. The colour of the points denotes which study they were taken from, while the black solid line shows the measured SMBH accretion density. The dotted line shows the model extrapolation and the grey shaded area are the errors.

the main mechanism preventing an over-abundance of massive galaxies, as compared to the shape of the observed galaxy luminosity function (Croton et al., 2006). The evidence for this mechanism is convincing, with clear detections of large X-ray cavities excavated by the radio-jets (e.g. Boehringer et al. 1993; McNamara et al. 2000; Fabian et al. 2000, and also see Figure 1.3).

The second mechanism is 'quasar-mode' feedback, which is though to occur in the high accretion, radiatively efficient systems on which this thesis is based. It is postulated that winds associated with energy generated by accretion blast out the gas and dust around the SMBH/galaxy-wide, thus shutting down further accretion onto the SMBH

and also halting star formation. Although observational evidence for this mode of feedback remains ambiguous, the number of claimed detections of outflows in various gas phases is increasing (Tremonti et al., 2007; Alexander et al., 2010; Sturm, 2011; Rupke & Veilleux, 2011; Farrah et al., 2012; Greene et al., 2012). One of the most spectacular detections to date is that by Maiolino et al. (2012), who claim a detection of a prodigious outflow of $\sim 3500\,\mathrm{M}_{\odot}\ \mathrm{yr}^{-1}$ at high redshift ($z = 6.4189$). Despite the growing observational evidence, it is still not entirely clear whether these outflows are quenching star formation, or on what scales they can affect their host galaxies. This particular field of enquiry is still in its early stages, and much more work needs to be done in order to determine the interplay between outflows and their host galaxies, before their significance in galaxy evolution can be truly understood.

Although not associated directly with the mass of the SMBH, large scale multi wavelength surveys such as the SDSS have uncovered a bimodal distribution of galaxies in terms of both their mass and colours. These are separated into the red sequence and the blue cloud, with the green valley occupying the sparsely inhabited territory between the two. Figure 1.8, taken from Schawinski et al. (2014), clearly demonstrates this distribution by plotting dust corrected $u - r$ colours for a large sample of galaxies selected from SDSS ($0.02 < z < 0.05$) against their stellar mass.

AGN feedback has been suggested as the mechanism by which these galaxies move from the low-mass, late-type dominated, star forming blue cloud, to the higher-mass, early-type red sequence, following mergers between gas-rich galaxies. In this process, the merger triggers both star formation and AGN activity, while at the same time transforming the galaxies from late- to early-type morphologies. It is thought that the rapid quenching of star formation, through AGN feedback, moves the galaxy from the blue cloud, via the green valley and onto the red sequence (e.g. Silk & Rees 1998; Springel et al. 2005; Croton et al. 2006; Hopkins et al. 2008).

Thus, through regulating both the growth of the SMBH and the growth of the stellar mass of the host galaxy, AGN activity takes on a pivotal role in our understanding of galaxy evolution, and allows us to understand how a SMBH, with its very limited gravitational influence on its host galaxy, can extend its reach to galaxy-wide scales. However, despite their likely importance in galaxy evolution, there are many gaps in our understanding of how the process of accretion onto the SMBH is triggered and the means by which the energy released during an accretion episode interacts with the host galaxy. Therefore, in order to fully incorporate AGN into our models of galaxy evolution, robust solutions to these outstanding issues are imperative.

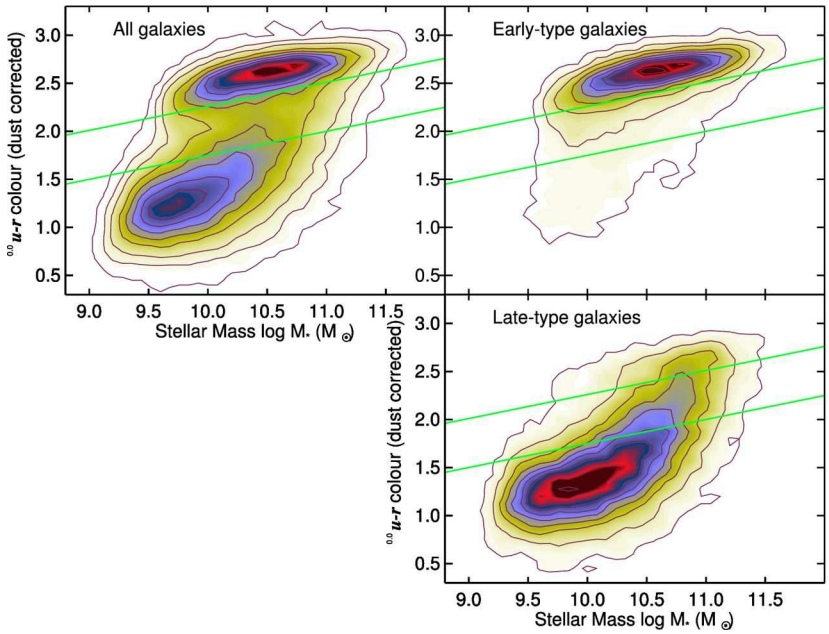

Figure 1.8: This figure, taken from Schawinski et al. (2014), shows the bimodal distribution of galaxy colours in relation to their mass. The top left panel shows their full sample of galaxies, with a clear bimodal distribution and the 'green valley' highlighted by the green lines. The top right hand panel shows the same, but considering only early-type galaxies, while the bottom right panel show only late type galaxies. This figure demonstrates that there is a tail to the red cloud which extend across the green valley. Schawinski et al. (2014) suggest that these may be the objects that are being quenched and are rapidly moving across the green valley to the red sequence. The contours are scaled to the highest value in each case.

1.7 Triggering AGN activity

Once a consensus on the source of energy generation, and to a large extent, the geometry of the source had been reached, the real problem became how to move sufficient mass into the central region ($<$ 1pc) of a galaxy to power the AGN through its lifetime of $\sim 10^6 - 10^8$years (Martini, 2004). This is known as the angular momentum problem because, to move gas from a position of a few kpc to the central region where it can be accreted by the SMBH, the material must shed around 99% of its angular momentum (Jogee, 2006). The mechanism by which this is achieved is a matter of debate, with some suggesting that mergers between galaxies are required to provide both the required fuel and the gravitational torques to move the gas to the centre, and others arguing that secular processes within the galaxies, such as bars, are sufficient to funnel enough gas to the centre to provide the necessary fuel.

1.7.1 Secular evolution

The case for triggering by secular processes is most plausible in the case of AGN with Seyfert-like luminosities, due to the moderate accretion rate required to power the activity. It has been suggested that galactic bars might be an important factor in triggering activity in Seyfert galaxies (Simkin et al., 1980; Friedli & Benz, 1993; Heller & Shlosman, 1994). Gravitational instabilities, caused by the bar, funnel the gas towards the centre of the galaxy until it reaches the inner Lindblad resonance. Gas then piles up because it is pushed outwards into the gas which is still being funnelled in, possibly triggering a starburst. At this point, nuclear bars take over as the predominant mechanism to transport material further inwards, where in can be accreted by the SMBH, triggering the activity (Jogee, 2006).

If this scenario is true, a higher fraction of barred spirals should host AGN in comparison to unbarred spirals, or conversely, AGN should preferentially be found in galaxies with a bar. Many observational studies have been carried out to determine whether this is the case, but they have produced mixed results. Some surveys have found that Seyferts are up to twice as likely to be barred as inactive galaxies (Knapen et al., 2000; Maia et al., 2003; Laurikainen et al., 2004; Coelho & Gadotti, 2011; Oh et al., 2012) while others have reported no difference in bar fraction and perturbations (Ho et al., 1997b; Mulchaey & Regan, 1997; Hunt & Malkan, 1999; Slavcheva-Mihova & Mihov, 2011; Cisternas et al., 2013). A possible reason for these contradictory results is that, although the bar may be necessary in order to drive the gas inwards, the transfer of angular momentum between the stellar component of the bar and the inward flowing gas could eventually generate instabilities, leading the bar to dissipate on timescales < 2 Gyr (Bournaud et al., 2005). Therefore, although the bar allows gas to be funnelled inwards, it will not necessarily exist concurrently with the AGN.

In this bar-driven scenario, it would also be expected that circumnuclear gas rings and enhanced star formation should be detected at scales ≤ 1 kpc in AGN host galaxies. This is because, as mentioned previously, the gas travelling along the bar stalls at the inner Lindblad resonance, causing a build up. This has indeed been borne out observationally (Knapen et al., 1995; Sakamoto et al., 1999; Böker et al., 2008; Comerón et al., 2010). For example, observational studies that trace the amount of gas through CO (Sakamoto et al., 1999) provide good evidence for higher concentrations of gas with $M(R < 500 \text{ pc}) \sim 10^8 - 10^9$ $M_\odot$, in barred galaxies with a derived gas inflow rate of 0.1 - 1 $M_\odot$ yr^{-1}. However, these observations only track gas down to the central kpc, which is still too far out to directly fuel the SMBH. Therefore further processes must be invoked in order

to move the gas into the central parsec.

It has been suggested that nested nuclear bars, that is, bars within bars (Shlosman et al., 1989) are necessary to remove the remainder of the angular momentum. Nuclear bars can in theory have a slower, faster or equal rotation speed to the primary bar. This will determine the magnitude of the gravitational torque that it is capable of exerting on the gas, with the most effective configuration being the nested bar rotating faster than the primary bar. However, observational studies (e.g. Laine et al. 2002) do not find an excess of nuclear bars in Seyferts.

One reason that there is little direct evidence that a non-axisymmetric potential (i.e. a bar) is required to trigger the AGN may be that, for the accretion rate required to power low-luminosity AGN ($10^{-5} < \dot{M}/\,\mathrm{M}_{\odot}\ \mathrm{yr}^{-1} < 10^{-2}$), it is not necessary to funnel gas in from galaxy-wide scales. It is possible that dynamical friction of the cloud against bulge stars is sufficient to remove the required angular momentum allowing the AGN to be triggered. Ho et al. (1997b) also argued that local processes such as mass loss from evolved stars and Bondi accretion of hot gas are capable of providing more than enough fuel to power low-luminosity AGN.

1.7.2 Mergers and interactions

It has long been thought that AGN are triggered in galaxy mergers or interactions, because theoretical work shows that the distorted gravitational potential generated in such encounters can be an efficient means of delivering fuel to the nucleus (Toomre & Toomre, 1972; Heckman et al., 1986; Hopkins et al., 2006). Major mergers or interactions cause instabilities in the galaxy discs, which then funnel material through the disc to the central few hundred parsecs. Once there, changes in the gravitational potential puts the gas on crossing orbits which leads to shocks, removing angular momentum, thus allowing gas to accrete onto the SMBH.

Over the last 25 - 30 years, numerous observational studies have been made in an effort to determine whether interaction events are significant. These studies use two main techniques. One is to focus on looking for evidence of morphological disturbance in the AGN host galaxies, such as tidal tails, fans, shells and dust lanes. The other approach is to attempt to quantify the local environments of AGN compared to those of normal inactive galaxies, in an effort to determine whether AGN have an excess of close companions compared to inactive galaxies with matching properties.

Although making comparisons of the optical morphologies is a relatively simple affair in the local Universe, it is much more difficult to gain images of sufficient resolution

and depth to carry out similar work at higher redshift. Many of the features that are indicative of a merger event are of relatively low surface brightness. At higher redshift, cosmological dimming becomes an important factor (surface brightness decreasing as $(1+z)^4$), and can make such evidence very difficult to detect. This presents a problem, because it makes it difficult to infer how important mergers may have been at the peak of AGN activity around $z \sim 2$.

This rapid decrease in surface brightness with increasing redshift is driven by the expansion of the Universe, which produces both geometric and time dilation effects. If the distance to an object is defined to be its co-moving distance D_C, then its angular diameter distance will be $D_A = (1+z)^{-1} D_C$, and its luminosity distance is given by $D_L = (1+z)^2 D_A$. The geometric effects can be accounted for by considering the solid angle subtended by an object on the sky, which is given by $\Omega = \frac{A}{D_A^2} = \frac{A}{(1+z)^{-2} D_C^2}$, where A is the projected area of the source on the sky. The time dilation effects can be understood by the fact that the rate at which photons are received in unit time will a factor of $(1+z)$ less than that a which they are emitted, while the energy of each photon will also be decreased by a further factor of $(1+z)$. Surface brightness is defined as

$$I = \frac{F}{\Omega} = \frac{L}{4\pi D_L^2} \frac{(1+z)^{-2} D_C^2}{A} \tag{1.4}$$

This gives

$$I = \frac{L}{4\pi A (1+z)^4} = \frac{I_E}{(1+z)^4} \tag{1.5}$$

where I_E is the emitted surface brightness. Thus, the observed surface brightness is a strong function of redshift.

Observational studies that attempt to quantify host galaxy morphologies tend to come in two types. Either, they rely on high resolution optical images which are visually inspected for tidal features associated with merger events, or they rely on model fitting to the surface brightness profiles in an attempt to find asymmetries in the host galaxy which would indicate disruption due to an interaction. Such studies have produced mixed results.

A study of radio galaxies, radio-loud and radio-quiet quasars, based on single orbit Hubble Space Telescope (*HST*) imaging by McLure et al. (1999) and Dunlop et al. (2003) found that the majority of host galaxies appear to be undisturbed elliptical galaxies. Bahcall et al. (1997) also used *HST* imaging to analyse a sample of type I quasars (both radio-loud and radio-quiet) and found that only 3/20 show signs of gravitational interactions. Other morphological studies which utilise shallow *HST* images, such as

those of Grogin et al. (2003) and Cisternas et al. (2011), based on 37 and 140 X-ray selected AGN respectively, produce similar results, showing little direct evidence for galaxy interactions being a significant factor in the triggering of the nuclear activity.

In contrast to this, ground based studies (e.g. Heckman et al. 1986; Smith & Heckman 1989; Ramos Almeida et al. 2011) and deeper *HST* imaging studies (e.g. Bennert et al. 2008) do suggest that large proportions of the host galaxies of powerful AGN show signs of morphological disturbance.

At least part of this apparent discrepancy may be due to the differences in the depth of the images used to make the classifications. Diffuse, low surface brightness features will remain undetected in shallow *HST* images, and only galaxies with bright and obvious features will be classified as being morphologically disturbed. This is clearly demonstrated by Bennert et al. (2008), who find that deeper *HST* images of five of the galaxies classified by Dunlop et al. (2003) as undisturbed show signs of morphological disturbance. Factors such as this, and differences in the way samples are selected, can make it difficult to compare the results of different studies.

Another important factor may be the luminosity of the AGN: it has been suggested on the basis of galaxy evolution simulations (Hopkins et al., 2008), and the details of the $M_{BH} - \sigma$ relationship (Kormendy, Bender & Cornell, 2011), that there may be a dichotomy in AGN triggering mechanisms, with low/moderate luminosity AGN ($L_{BOL} < 10^{45}$ erg s^{-1}) triggered by secular processes (e.g. Combes (2001)) and more luminous quasar-like AGN triggered in gas-rich mergers. In this context, it is notable that the studies of Cisternas et al. (2011) and Grogin et al. (2003) concern low/moderate luminosity AGN.

Attempting to detect morphological features in the host galaxies of luminous, quasars-like AGN ($L_{BOL} > 10^{38}\ W$) also comes with its own inherent problems, not least of which is that the extremely bright point source of the quasar can wash out fainter features associated with a merger, leading to misclassification. Therefore, it is important to undertake studies of luminous AGN in which the quasar nucleus is hidden from our direct view at optical wavelengths. Ramos Almeida et al. (2011), have taken this approach, using deep Gemini GMOS-S images of a complete sample of powerful radio galaxies (PRG; Tadhunter et al. 1993) where, in the majority of cases, the broad-line AGN is obscured or does not dominate the light of the galaxy. They find that 94% of the strong line radio galaxies (SLRG) in their sample show evidence of morphological peculiarities at relatively high levels of surface brightness ($\tilde{\mu}_V^{corr} = 23.6\ mag\ arcsec^{-2}$).

In the same vein, observational studies that attempt to quantify whether AGN have

excess companions or prefer richer environments have also produced mixed results, with some (e.g. Dahari 1984; Gehren et al. 1984; Serber et al. 2006; Ellison et al. 2011) claiming an increase in close companion counts, but others (e.g. Fuentes-Williams & Stocke 1988; Schmitt 2001; Grogin et al. 2003; Li et al. 2006) finding no such effect. It is difficult to reconcile the results of such studies because they all adopt their own selection criteria for both AGN and control samples, introducing different biases. It is also important to consider the redshift range of each sample, because it is possible that the results will differ with look-back time.

One approach is to divide these studies into the types of objects under consideration: are they Seyferts or quasars; are they radio-loud or radio-quiet? For example, as mentioned above, there is mounting evidence that low luminosity, Seyfert-like AGN may have a different triggering mechanism to high-luminosity quasars. In terms of separating samples based on their radio power, Ramos Almeida et al. (2013), performed a comparison between the environments of radio-loud and radio-quiet quasars (based on the sample presented in this thesis) and found that, while radio-loud quasars prefer denser environments, radio-quiet quasars are more likely to be found in field or group environments. Therefore, failure to account for such behaviour may also affect the results.

Early work in this area suffered from small sample sizes and lack of well-matched control samples. For example Dahari (1984) took no account of morphological types when constructing the control sample. Therefore, the earlier-type hosts of AGN, which are more likely to be found in groups or clusters, were compared to later-type spirals, which are more likely to be found in the field, thus leading to the conclusion that AGN have more close companions than inactive galaxies.

Later work (e.g. Schmitt 2001; Li et al. 2006) used more homogeneous criteria for the selection of both their AGN and control samples, taking into consideration factors such as morphology, luminosity and redshift. These studies of Seyferts in the local Universe suggest that Seyfert galaxies do not have an excess of companions. On the other hand, Ellison et al. (2011) take the opposite approach by selecting a sample of $\sim$ 11000 galaxy pairs from the SDSS, and then determining, as a function of projected separation, what fraction of those pairs contain an AGN. They find a marked increase in the incidence of AGN at the smallest separations they are able to probe, compared to their control sample of unpaired galaxies (a factor of 2.5). This is clearly demonstrated in Figure 1.9 (from Ellison et al. 2011), which shows the fraction of paired galaxies that host an AGN (top panel) as a function of projected separation (filled symbols) compared with their

matched, unpaired control galaxies (open symbols)[5]. The bottom panel shows the sharp increase in the excess of AGN in the paired galaxies over the unpaired control sample, as the projected septation decreases. It appears that this finding is not dependent on the luminosity of the AGN, with the effect being seen equally in objects classified as AGN using a BPT diagram (selected from the SDSS main galaxy sample), and those selected as quasars. However, it should be noted that, in this sample, the maximum fraction of pairs that host AGN is $\sim 20\%$, and the majority of AGN ($\sim 80\%$) are not actually found in pairs (Silverman et al., 2011).

When considering only high-luminosity quasars, it appears that they are more likely to be found group environments. Serber et al. (2006) define a sample of ~ 2000 quasars with $z < 0.4$ and a sample of $\sim 10^5$ control galaxies, both selected from the SDSS. They find an over-density in the environments of quasars on scales < 100 kpc, compared to normal L_* galaxies, and they also find that the magnitude of this increase in over-density is luminosity dependent, with the effect being more pronounced at the luminous end of their AGN sample. These findings are strong evidence in support of the theory that mergers play a more significant role in triggering luminous quasars than in triggering lower-luminosity Seyferts and LINERs. This is because, galaxy mergers are more likely to occur in group environments than in either lower density (field) or higher density (cluster) environments.

One point to consider in these surveys is that each author has their own definition of a close companion, based on distance from the AGN and limiting magnitude, when considering whether it is a physical companion or a chance projection. An example of this can be seen in Fuentes-Williams & Stocke (1988). From their original selection criteria for what constituted a close companion, they did not find a statistically significant increase around Seyferts than compared with their well matched control sample. However, when they considered fainter galaxies that appeared within their distance criteria, they did find a significant excess. Therefore, caution must be exercised when attempting to interpret the findings of such studies.

Finally, if mergers are indeed significant in triggering AGN activity, there are many possible configurations in which an interaction between galaxies could occur. Therefore the possible parameters and what effect they may have on the ability of interactions to fuel AGN must be considered. These parameters include: the sense of the interaction, that is, whether it is prograde; retrograde or polar, the inclination angle of the merging galaxies; and the mass ratio of the two galaxies. A major (1:1) or intermediate (3:1)

[5]For the unpaired galaxies, the projected separation refers to the separation of the pair galaxy to which the control galaxy has been matched. See Ellison et al. (2011) for a detailed explanation.

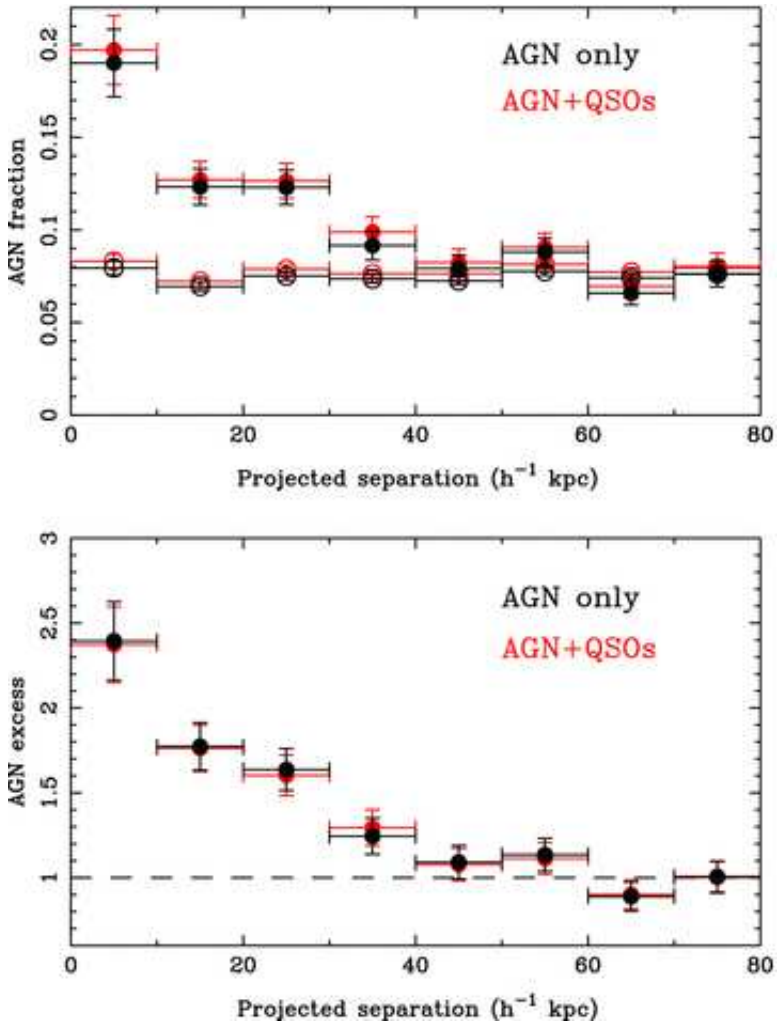

Figure 1.9: The top panel shows the fraction of paired galaxies that are found to contain AGN as a function of their separation compared to a matched sample of control galaxies. The bottom panel show the ratio of AGN fraction in pairs relative to the matched control sample, again dependent on separation. In both cases, the black symbols denote objects that were selected using BPT diagrams, while the red symbols also include objects selected by the SDSS for spectroscopy as part of the quasar survey. This figure is taken from Ellison et al. (2011).

merger will cause the disruption of the disc whereas a minor merger (10:1) may not do so, and may also be very hard to detect (Walker et al., 1996).

Keel (1996) carried out a survey of Seyfert galaxies that had already been found to be in pairs, in order to try to determine the significance of the geometry of the encounter, and see whether there was some common property between them that would be a necessary condition to trigger activity. Spectroscopic observations of a sub-set of his sample were used to interpret the sense of the encounter, and he concluded that

there is no preference with prograde, retrograde and polar encounters all represented. He further concluded that it was the presence of the perturbation that was the most important factor, rather than its exact form.

The evidence presented in this section suggests that the triggering mechanism for AGN may have some dependence on luminosity, with high-luminosity quasars triggered by galaxy mergers, and low-luminosity Seyferts triggered by secular processes. However, due to the different AGN sample selection, control sample selection (if any) and the widely varying depths of the data used to draw conclusions in different studies, the exact relationship between AGN activity and galaxy mergers remains unclear.

1.7.3 The starburst–AGN connection

If mergers do play a key role in triggering AGN, then the tidal disruption of the quasar host galaxies will not be the only observational signature. It is also expected that there will be an accompanying burst of prodigious star formation activity, also driven by the cold gas injected into the central regions during the merger events. This scenario has been investigated through a number of simulations of major, gas-rich mergers (di Matteo et al., 2005; Springel et al., 2005; Hopkins et al., 2006; Johansson et al., 2009). Figure 1.10, taken from Springel et al. (2005), illustrates this scenario, with the star formation rate and SMBH accretion rate both peaking at the point of coalescence of the two black holes. If, as these simulations suggest, the triggering of these starbursts and the onset of AGN activity are both the result of the same merger we would expect to detect substantial young stellar populations (YSP) in the host galaxies. Moreover, determination of the ages of starbursts in a large enough sample of AGN host galaxies has the potential to allow an understanding of the timing of the triggering of the AGN relative to the main merger event.

To fully utilise this information, it is important to understand how the spectral energy distribution (SED) of a starburst evolves with time. Figure 1.11[6] clearly demonstrates this evolution by showing a spectrum of an instantaneous burst of star formation at 10 Myr, 100 Myr, 1 Gyr and 10 Gyr. These spectra are overlain on a Hertzsprung – Russell diagram showing the stellar main sequence, which plots the luminosity of a star against its surface temperature. If it is assumed that all the stars are formed at the same time, then the spectrum of the stellar population will be dominated by the stars that are currently at the main sequence turn off, and the main sequence life-time, temperature and luminosity of a star is mostly dependent on its mass. Figure 1.11 shows that at

[6] http://cse.ssl.berkeley.edu/bmendez/ay10/2002/notes/lec13.html

10 Myr, hot O and B stars are dominating the spectrum of the population, with the flux peaking strongly in the ultra-violet (UV). As the population ages, these stars evolve off the main sequence, and by 100 Myr, is is the late type B and A type stars which dominate the flux. At these ages, the flux still peaks strongly in the UV, however, the 4000 Å break and Balmer absorption lines become more pronounced. By the time the population has reached 1 Gyr, the flux of the population is dominated by F type stars. Figure 1.11 shows that at this age, the peak in the flux has moved to the optical domain

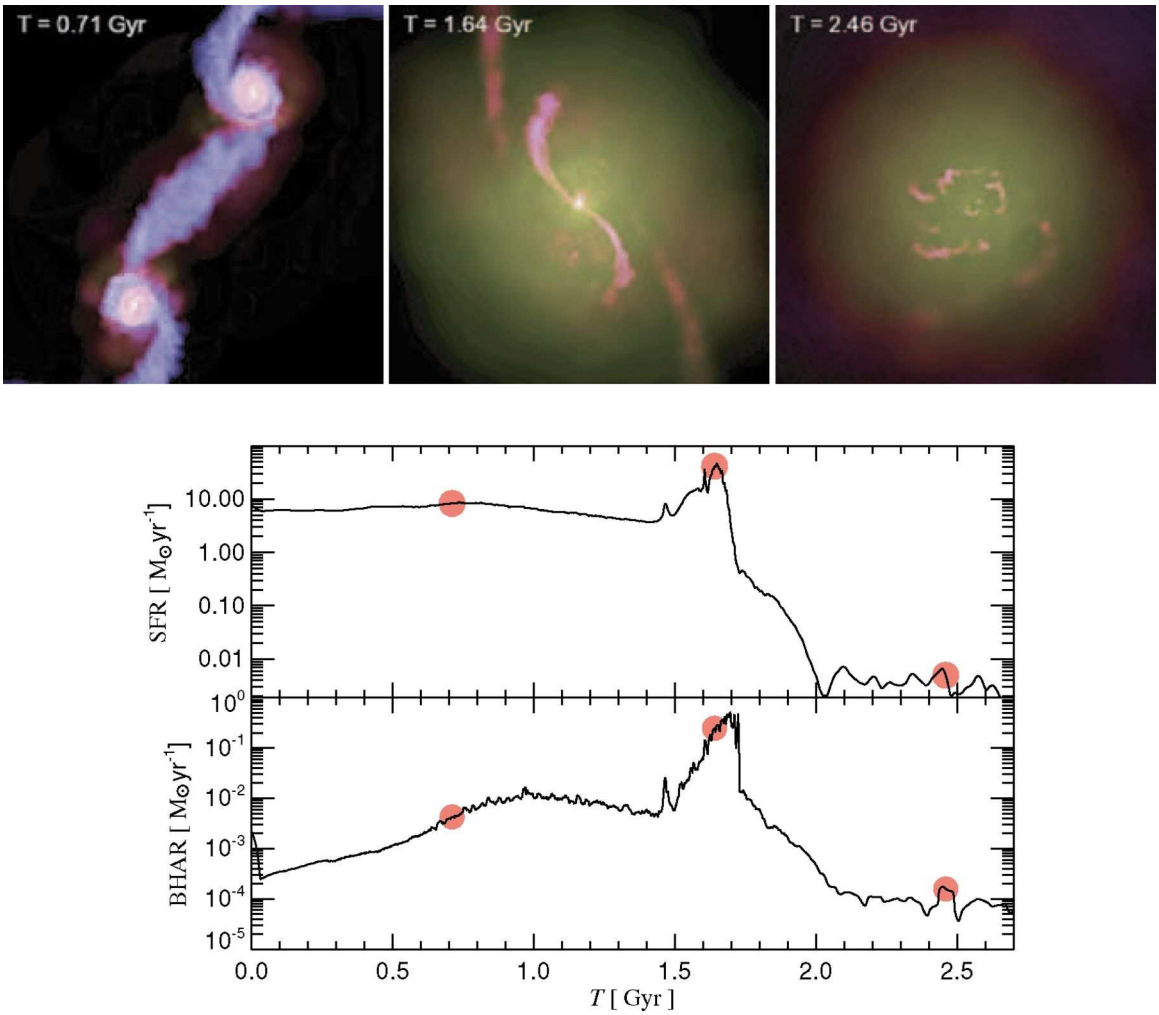

Figure 1.10: The results of a simulation between two disc galaxies showing the variation in both star formation rate and the SMBH accretion rate, taken from Springel et al. (2005). The three snap-shot images (top) show the distribution of gas at three different points in the merger, with the colour showing the temperature of the gas and the brightness denoting the density of the gas. The bottom panel shows the variation of the star formation rate (top) and SMBH accretion rate (bottom) with time. The red dots correspond to the snap-shot images shown above.

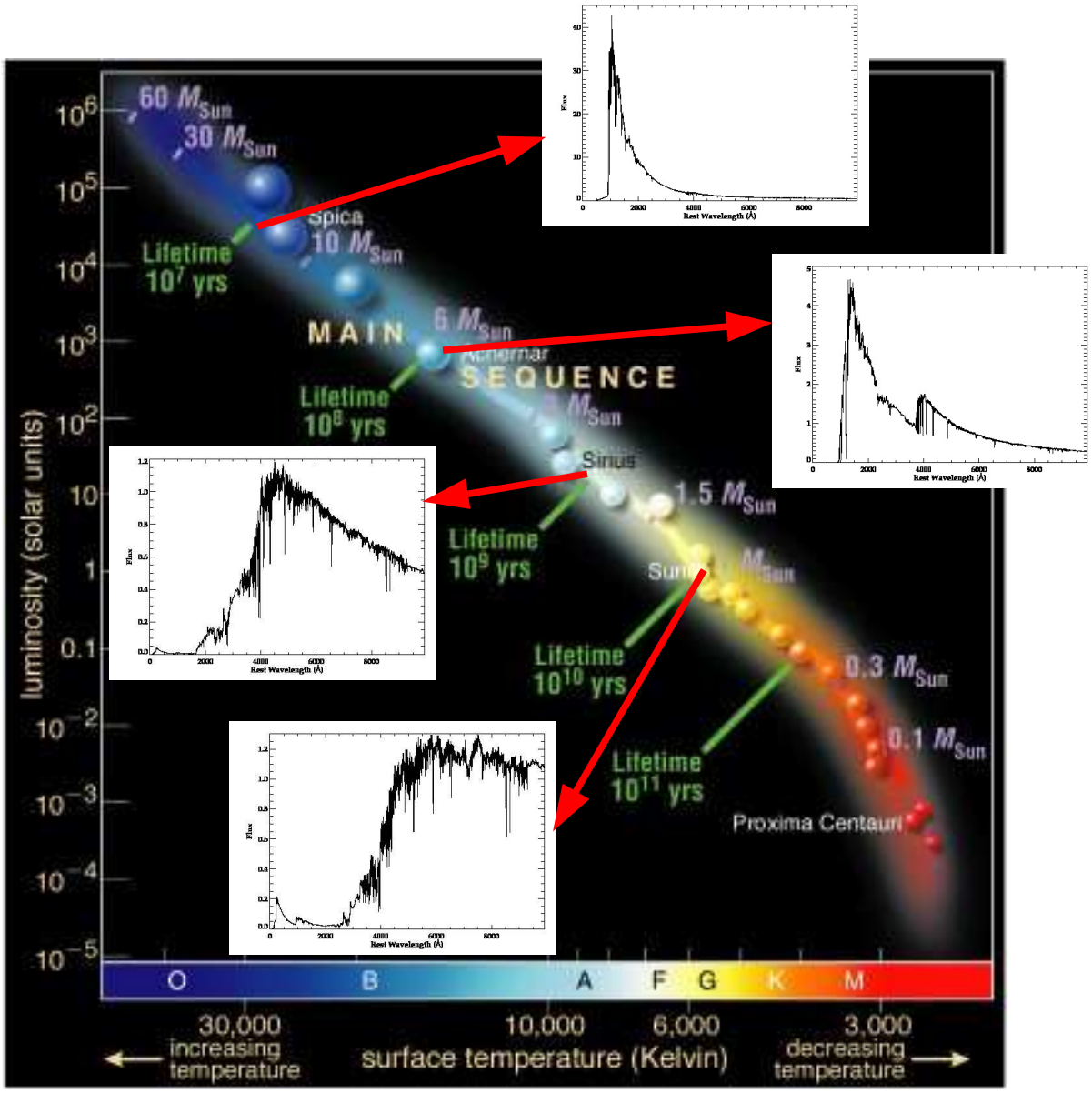

Figure 1.11: An H-R diagram of the stellar main sequence, showing stellar luminosity plotted against surface temperature. The mass stars at different temperatures is also shown. Overlain are spectra of an instantaneous burst of star formation at each of the main sequence life-times shown of the H-R diagram.

because the more massive, bluer stars have all evolved off the main sequence. At 10 Gyr, it will be stars similar to the Sun that dominate the SED, with the majority of the flux emitted longwards of 5000 Å.

Dating the stellar populations also allows evolutionary scenarios to be tested, such as that put forward by Sanders et al. (1988), in which mergers between gas rich galaxies lead to ULIRGs in which the IR luminosity is initially driven by rapid star formation. Later in the mergers, at the point of coalescence of the two SMBHs, the AGN begin to dominate the IR luminosity, eventually driving out the natal cocoon of dust and gas, and allowing them to become detectable at optical wavelengths (e.g. Springel et al. 2005; Hopkins et al. 2006). In this scenario, the peak of star formation would be expected to occur while the AGN are still deeply buried, and therefore, by the time the AGN become visible in the optical, the stellar population would be detected as an ageing starburst of several 100 Myr.

A number of studies focussed on characterising the stellar populations of AGN host galaxies have detected relatively old post-starburst populations with ages 100 Myr to a few Gyr (Tadhunter et al., 2005; Holt et al., 2007; Wills et al., 2008; Wild et al., 2010; Canalizo & Stockton, 2013) which, if a quasar lifetime of 1 – 100 Myr is assumed (Martini & Weinberg, 2001), implies a substantial delay between the merger-induced starbursts and the quasars being triggered/becoming visible. However, other studies have found clear evidence of quasi-simultaneous triggering of the luminous quasar and starburst (Heckman et al., 1997; Canalizo & Stockton, 2000; Brotherton et al., 2002; Davies et al., 2007; Wills et al., 2008; Tadhunter et al., 2011). Therefore, the question of whether luminous quasars are triggered at the peak of star formation in major, gas-rich mergers remains unresolved.

1.8 The outstanding issues

This thesis will address the issues of how and when luminous AGN (quasars) are triggered as their host galaxies evolve. This will be done through careful study of an homogeneous sample of type II quasars, which is introduced in Chapter 2. Type II quasars are ideal test beds to make progress in this field, because, unlike their type I counterparts, the nuclear point sources are hidden from direct view, allowing an unhindered study of their hosts. These key outstanding questions are as follows.

- **How are quasars triggered?**
- **When are quasars triggered?**

- **Are quasars only hosted by the most massive early-type galaxies?**

In Chapter 3, a morphological study of a sample of type II quasars is made, with the aim of determining their merger/interaction status. This is accomplished through the use of high quality optical imaging data. In isolation, this information lacks context in terms of galaxy evolution. Therefore, the images are compared with those of a matched control sample of quiescent galaxies. The results of this analysis were initially presented in Bessiere et al. (2012).

If major, gas-rich mergers are the catalyst for both quasar and starburst activity, by determining the ages of the young stellar populations, it is possible to investigate when the quasar activity was triggered, relative to the main merger-induced starburst. Therefore, in Chapters 4 and 5, high quality spectra of the type II quasars are used to perform stellar population synthesis modelling. Not only does this allow the dating of the stellar populations, but also provides information on the nature of the triggering mechanism, because the presence of a massive YSP also provides evidence of major, gas-rich mergers. The results presented in Chapter 4 can be found in Bessiere et al. (2014).

Although previous quasar host galaxy studies have provided evidence that quasar hosts are almost invariably giant elliptical galaxies in terms of their masses, such studies have generally assumed that the light of the host is dominated by a single, old stellar population. In Chapter 6, the results presented in Chapters 4 and 5 are used to determine the stellar masses of the type II quasar host galaxies, allowing full consideration of the contributions of both the young and old components to the total mass.

The data, results and analysis presented in this thesis provide clear insights into the triggering of luminous, quasar-like AGN, however, there is much scope for further studies in order to improve both the significance and robustness of this work. Possible future avenues of investigation are discussed in Chapter 7.

Throughout this work, a cosmology with $H_0 = 70$ km s^{-1} Mpc^{-1}, $\Omega_m = 0.27$ and $\Omega_\Lambda = 0.73$ is assumed.

Chapter 2

Sample selection, observations and data reduction

2.1 The Sample

The sample of 20 type II quasars used in this study was derived from the catalogue of candidate objects presented by Zakamska et al. (2003), who selected galaxies from the Sloan Digital Sky Survey (SDSS; York et al. 2000) with high ionisation, narrow emission lines, but no indication of broad permitted lines. To characterise the nature of the ionising source, they used diagnostic emission line ratios to demonstrate the energetic dominance of the AGN. Zakamska et al. (2003) provide full information on the criteria used to select type II objects based on emission line ratios.

Because the AGN is itself obscured in type II objects, the luminosity of the [OIII]λ5007 emission line ($L_{[OIII]}$) is used as a proxy for its bolometric luminosity (e.g. Heckman et al. 2005; LaMassa et al. 2009; Dicken et al. 2014). It is assumed that a type II object will have the same intrinsic AGN luminosity for a given $L_{[OIII]}$ as a type I object. Zakamska et al. (2003) make their cut between objects that are considered to be quasars, and those with Seyfert-like luminosities at $L_{[OIII]} > 10^{8.5} L_{\odot}$, which is roughly equivalent to an AGN absolute magnitude $M_B < -23$ mag.

Zakamska et al. (2003) selected their sample of 291 candidate type II quasars from the spectra obtained on 600 SDSS plates, considering objects targeted by a number of SDSS algorithms. Below, the criteria used to select targets for the various SDSS surveys are briefly outlined.

- **Galaxy:** This survey targeted resolved objects to a limiting magnitude of $r = 17.77$ and was the main priority of the SDSS spectroscopic survey (Strauss et al.,

2002). Figure 2.1(a) shows a flow diagram which outlines the decision making process for assessing whether an object should be target as part of the galaxy survey[1].

- **Quasar:** This survey targeted potential quasars by colour down to a limiting magnitude of $r = 19.1$ (Richards et al., 2002). The selection criteria required that the source should lie more than 4σ from either the *ugri* or *griz* stellar locus. Once again, the full selection criteria applied were complex, and are therefore best illustrated by the flowchart shown in Figure 2.1(a).

- **Luminous Red Galaxies:** These objects were also targeted based on their colours, down to a limiting magnitude of $r = 19.5$ (Eisenstein et al., 2001). The sample selection criteria were dependent on cuts in the colour–colour–magnitude cube of *g-r, r-i, r* and were also dependent on the redshift of the object.

- **Serendipity:** These sources were targeted as objects which lay outside the colour selection space of the algorithms described above. The majority of them are optical counterparts to objects detected by the FIRST (radio) (Becker et al., 1995) or ROSAT (x-ray) (Voges et al., 1999) surveys, with a limiting magnitude of $i = 20.5$.

- **Special:** These were small projects with varying selection criteria.

- **Deep Southern Equatorial Scan (DSES):** This survey used repeated scans of the same region and targeted objects using the same algorithms as described above, but to 1 magnitude dimmer than the main survey.

Table 2.1 shows the particular SDSS algorithm that resulted in each of the objects presented in this thesis being targeted. It is notable that a large proportion of these objects were targeted by the serendipity algorithm, which is consistent with the full sample presented in Zakamska et al. (2003). As discussed there, this fact means that neither this sample, nor the parent sample can be considered to be complete. This is due to the fact that fibres on the SDSS plates were only allocated to this algorithm if unallocated fibres remained after the main Galaxy and Quasar surveys had been targeted. Figure 2.2 is taken directly from Zakamska et al. (2003) and shows the number of objects selected by each algorithm in their full sample (solid line) and their high luminosity sample ($L_{[OIII]} > 3 \times 10^8$ $L_\odot$; dashed line).

[1] http://www.sdss.org/dr7/algorithms/target.html

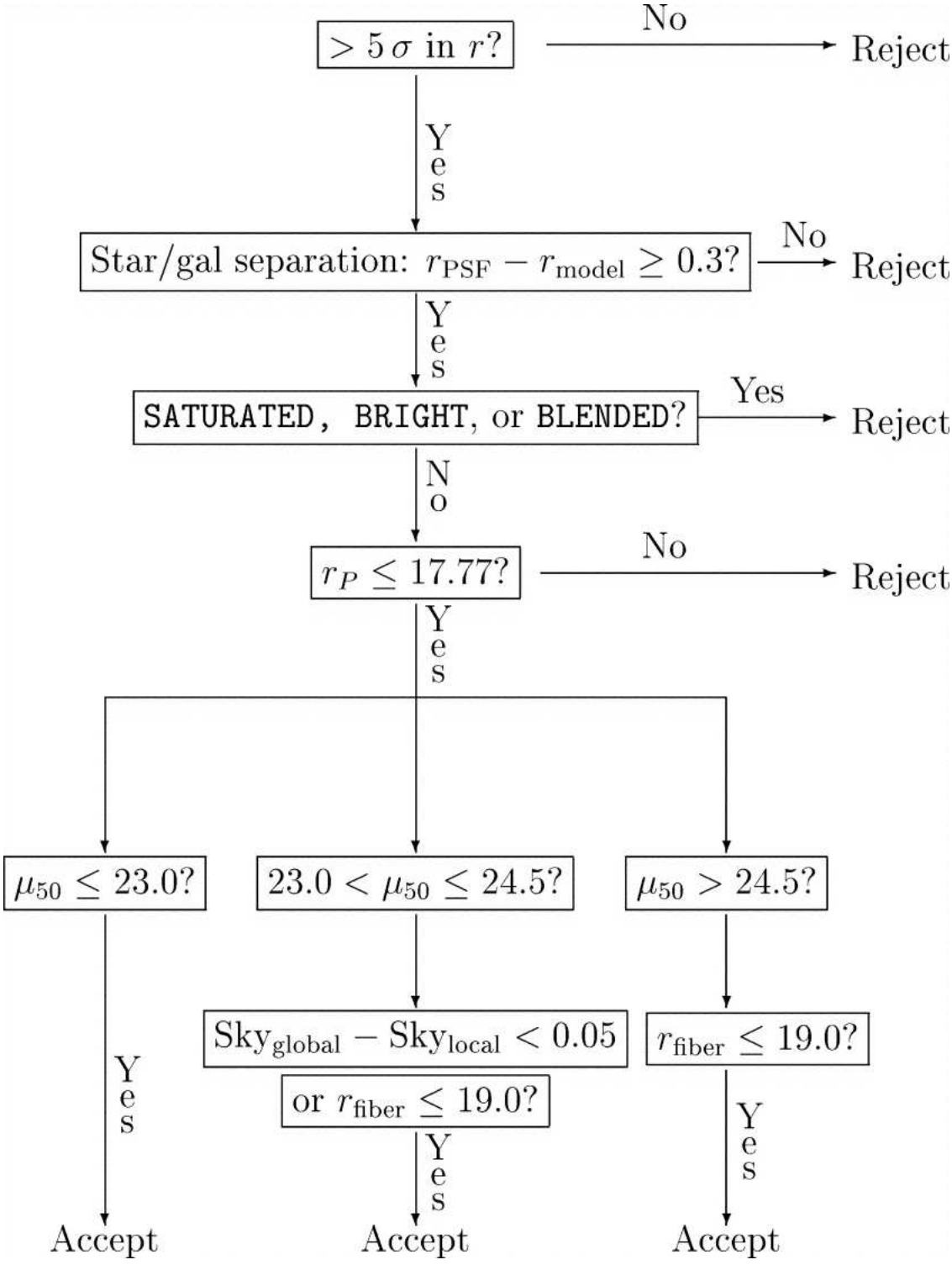

(a)

Figure 2.1: Flow charts showing the decision making process for selecting objects for spectroscopy for (a) the SDSS galaxy survey, and (b) Quasar survey. These flow charts, and further detailed information, can be found at the SDSS website.

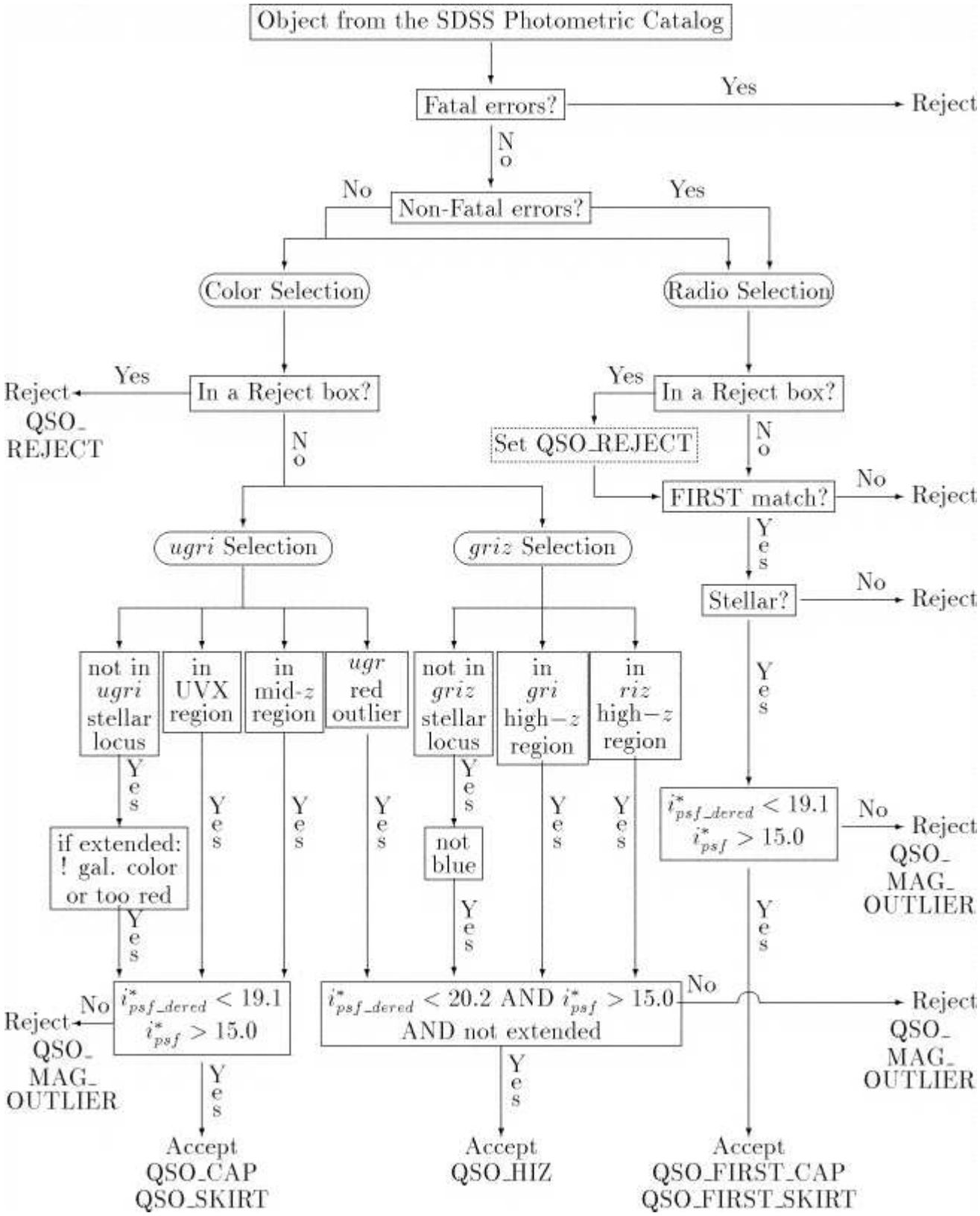

(a)

Figure 2.1: [continued]

The sample presented in this work comprises all 20 objects from Zakamska et al. (2003) with RAs in the range $23 < RA < 10$ hr, declinations $< +20$ degrees, redshifts in the range $0.3 < z < 0.41$ and [OIII] emission line luminosities $L_{[OIII]} > 10^{8.5} L_{\odot}$ (see Table 2.1). The redshift limits ensure that the objects are sufficiently close and bright for the detection of fainter, extended features to be possible. Using the cosmology assumed in this thesis, the redshift limits correspond to a light travel time of between 3.42 Gyr and 4.36 Gyr, or alternativley, the light was emitted when the age of the Universe was between 9.10 Gyr and 10.04 Gyr. The $L_{[OIII]}$ limit was chosen to ensure that the objects do indeed contain AGN with quasar-like bolometric luminosities. Subsequent updates to the emission line luminosities, based on changes to the technique used by SDSS to flux calibrate the spectra, were made by Reyes et al. (2008), and suggest that six objects from the original sample selection fall marginally below this $L_{[OIII]}$ cut. However, because the original sample selection was based on Zakamska et al. (2003), we choose to retain the full sample of 20 objects, although the updated $L_{[OIII]}$ values are included in Table 2.1 (bracketed values) as a matter of interest.

Due to the fact that one of the prime aims of this study is the evidence for morpho-

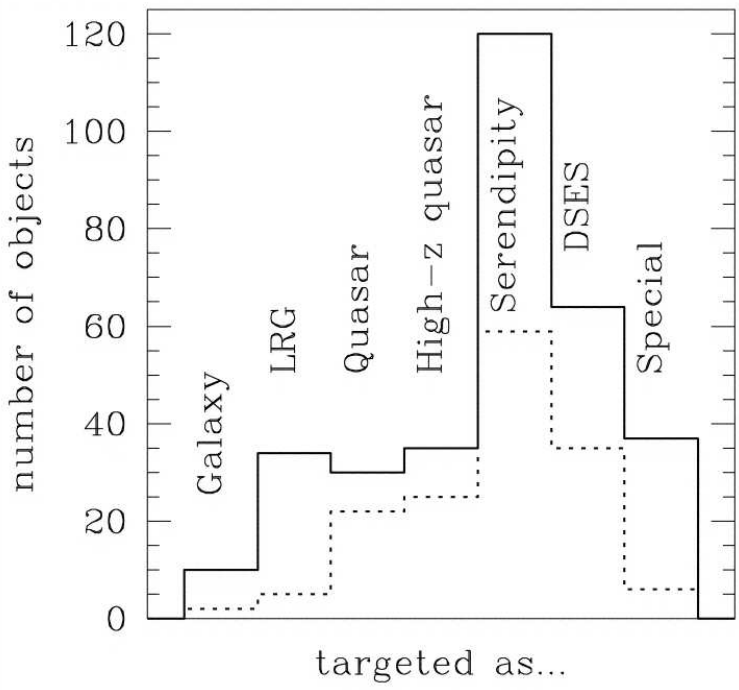

Figure 2.2: The distribution of SDSS algorithms used to target the 291 candidate type II quasars in the parent sample. The solid line includes all the objects, while the dotted line includes the high luminosity objects ($(L_{[OIII]} > 3 \times 10^8$ L$_{\odot}$) only. This figure is taken directly from Zakamska et al. (2003).

logical disturbance in the host galaxies of type II quasars, no selection criteria regarding the radio properties of the sample of type II quasars was imposed. However, given that a comparison in the rates of morphological disturbance between this sample and the powerful radio-galaxies (PRG) of Ramos Almeida et al. (2011) (introduced in Chapter 3) is made, the derived radio power, extrapolated to 5 GHz is given in Table 2.1. In order to derive these values, the February 2012 version of the Faint Images of the Radio Sky at Twenty-centimeters (FIRST)[2] catalogue was used. This survey is intended to cover 10,000 degrees^2 of the North and South Galactic caps, to a 5σ detection threshold of 1.0 mJy (Becker et al., 1995). The maps produced have 1.8 arcsec pixels, a typical rms of 0.15 mJy and a resolution of 5 arcsec.

Following the example of Zakamska et al. (2004), the catalogue was searched for any matches within 3 arcsec of each object, producing a total of 11 matches. This method allows for the matching of any core radio component associated with the source but does not include the flux associated with any extended lobes or jets. In order that all emission associated with an object is included, the search was extended to a 90 arcsec radius, which at the typical redshift of this sample equates to $\sim$0.5 Mpc, resulting in 6 further matches. These matches were then visually inspected to determine if they are associated with the sources. They were considered to be associated if they had a double lobed morphology centred on the core position, even if no core component is detected, or if they have an asymmetric radio component and a core component (Zakamska et al., 2004). Imposing this criteria left a total of 4 out of the 6 matches. The integrated flux at 1.4 GHz for each component associated with the source was summed to obtain the total flux.

Two objects in the type II quasar sample (J0142+14 and J0159+14) are not in the footprint of the FIRST survey. In order to ensure radio data was available for all the sources, the NVSS survey (Condon et al., 1998) also conducted at 1.4 GHz, but with a 5σ detection threshold of $\sim$2.5 mJy, was utilised. Neither of these objects had matches with 90 arcsec.

The total integrated fluxes were then converted to luminosities at 5 GHz (L_{5GHz}) using spectral indices taken from Zakamska et al. (2004). However, in most cases, the spectral index is unknown so, in these cases, a value of $\alpha = -0.75$ was assumed because this is a typical value for radio-loud AGN (Donnelly et al., 1987).

[2] http://sundog.stsci.edu/

Table 2.1: Full classification of the sample objects: Columns 1 and 2 give the SDSS identifier and abbreviated identifier that will be used throughout this thesis. Columns 3 and 4 list the spectroscopic redshift and cosmology corrected scale taken from the NED database. Column 5 corresponds to the value of $\log(L_{[OIII]}/L_{\odot})$ taken from Zakamska et al. (2003) upon which the original sample selection was based, while the values in brackets are updated values taken from Reyes et al. (2008). Column 6 corresponds to log L_{5GHz} W/Hz/Sr calculated using the integrated flux at 1.4 GHz from either the FIRST or NVSS surveys, assuming a spectral index of $\alpha = -0.75$ where it is unknown. If the object was undetected by either survey, then an upper limit is given corresponding to the detection limit of the survey. The final column gives the SDSS targeting algorithm used to select these sources for spectroscopic follow up (Zakamska et al., 2003). 1 = Quasar, 2 = High redshift quasar, 3 = Serendipity, 4 = DSES, 5 = Special (see text for details).

Name	Abbreviated name	z	Scale (kpc arcsec^{-1})	$\log(L_{[OIII]}/L_{\odot})$	log L_{5GHz} (W Hz^{-1} Sr^{-1})	SDSS Algorithm
J002531-104022	J0025-10	0.303	4.48	8.73(8.65)	22.08	1
J011429+000037	J0114+00	0.389	5.28	8.66(8.46)	24.70	4
J012341+004435	J0123+00	0.399	5.36	9.13(9.14)	23.27	4
J014237+144117	J0142+14	0.389	5.28	8.76(8.87)	< 22.58	1
J015911+143922	J0159+14	0.319	4.64	8.56(8.39)	< 22.38	2
J021757-011324	J0217-01	0.375	5.16	8.55(8.37)	22.35	4
J021758-001302	J0217-00	0.344	4.88	8.75(8.81)	22.15	3
J021834-004610	J0218-00	0.372	5.13	8.85(8.62)	< 22.13	4
J022701+010712	J0227+01	0.363	5.05	8.90(8.70)	< 22.11	5
J023411-074538	J0234-07	0.310	4.55	8.77(8.78)	22.35	3
J024946+001003	J0249+00	0.408	5.44	8.63(8.75)	22.14	3
J032029+003153	J0320+00	0.384	5.23	8.52(8.40)	< 22.17	1,5
J033248-001012	J0332-00	0.310	4.55	8.50(8.53)	23.36	3
J033435+003724	J0334+00	0.407	5.43	8.61(8.75)	< 22.23	4
J084856+013647	J0848-01	0.350	4.95	8.56(8.46)	24.00	3
J090414-002144	J0904-00	0.353	4.98	8.93(8.89)	23.52	1,3
J092318+010144	J0923+01	0.386	5.27	8.94(8.78)	22.09	3
J092356+012002	J0924+01	0.380	5.22	8.59(8.46)	23.33	3
J094836+002104	J0948+00	0.324	4.71	8.52(8.57)	22.35	3
J235818-000919	J2358-00	0.402	5.39	9.32(9.29)	< 22.21	1,4

2.2 Observations

2.2.1 Gemini Multi-Object Spectrograph

The primary optical imaging and spectroscopic data used in this thesis was obtained in service mode using the Gemini Multi-Object Spectrograph (GMOS-S) mounted on the 8.1m Gemini South telescope at Cerro Pachón, Chile.

The GMOS-S detector (Hook et al., 2004) consists of three adjacent 2048×4096 pixel CCDs separated by two gaps of approximately 2.8 arcsec. This gives a field of view of 5.5×5.5 arcmin^2 and a pixel scale of 0.146 arcsec pixel^{-1}.

2.2.2 Optical Imaging

The imaging observations were carried out in queue mode between August 2009 and September 2011 (semesters 2009B and 2011B), using the r' filter, in good seeing conditions, with a median seeing value of FWHM = 0.80 arcsec (ranging between 0.53 arcsec and 1.08 arcsec, see Table 2.2). To determine the seeing in each of the 20 images, measurements of 2-dimensional Gaussian fits to four foreground stars were averaged. Full details of the observations can be found in Table 2.2.

Between four and nine 250 second exposures (1000–2250 seconds total) were taken for each object, allowing for the detection of the low surface brightness tidal features that are indicative of merger events. The images were taken in a four point square dither pattern with a 10 arcsec step size. This technique allows for the removal of the gaps between the CCDs when the images are combined, improved removal of other image imperfections, and better flat fielding.

The data were reduced using the dedicated Gemini GMOS package within the IRAF[3] environment. The reduction was carried out it four steps. The separate images from the three CCDs that comprised each exposure were first combined into a single image which was then flat fielded and bias subtracted. These images were then mosaicked and finally co-added to produce the final image.

In order to calibrate the magnitude scale, calibration images of Landolt standard star fields taken with the r'-band filter at both the beginning and end of the 2009-2010 and 2010–2011 observing periods were used to determine the photometric zero points. Using these, it was determined that the photometric accuracy of the observations is ± 0.08 mag.

[3]IRAF is distributed by the National Optical Astronomy Observatory, which is operated by the Association of Universities for Research in Astronomy (AURA) under cooperative agreement with the National Science Foundation (http://iraf.noao.edu/).

Name	Exptime(s)	obs. date	Seeing	E(B-V)	Mag(AB)	Mag(corr)
J0025-10	250 × 4	2011-09-19	0.86	0.0312	18.32	17.84
J0114+00	250 × 4	2010-01-12	1.03	0.0277	19.22	18.56
J0123+00	250 × 8	2009-12-09	0.73	0.0336	19.73	19.03
J0142+14	250 × 4	2010-01-13	1.06	0.0501	18.85	18.13
J0159+14	250 × 9	2011-08-04	0.93	0.0566	19.98	19.40
J0217-01	250 × 4	2009-12-09	0.84	0.0327	19.19	18.55
J0217-00	250 × 4	2009-10-20	0.77	0.0341	18.87	18.30
J0218-00	250 × 4	2009-12-23	0.84	0.0366	18.91	18.27
J0227+01	250 × 4	2010-01-07	0.66	0.0294	19.19	18.59
J0234-07	250 × 4	2010-01-12	0.98	0.0401	19.67	19.16
J0249+00	250 × 8	2009-12-14	0.73	0.0561	20.08	19.30
J0320+00	250 × 4	2009-11-12	0.76	0.1016	19.13	18.29
J0332-00	250 × 4	2009-10-23	0.51	0.1084	18.53	17.83
J0334+00	250 × 8	2009-12-24	0.63	0.1201	20.10	19.15
J0848+01	250 × 4	2009-12-22	0.65	0.0368	19.14	18.55
J0904-00	250 × 4	2009-12-24	0.53	0.0376	18.74	18.14
J0923+01	250 × 4	2009-12-13	0.66	0.0275	19.18	18.52
J0924+01	250 × 7	2009-12-24	0.90	0.0420	20.08	19.40
J0948+00	250 × 4	2009-12-26	0.83	0.0774	19.44	18.80
J2358-00	250 × 4	2009-08-23	1.08	0.0362	19.08	18.37

Table 2.2: Details of the optical imaging observations carried out at Gemini South using the GMOS instrument: Column 1 gives the object name, column 2 the exposure times, columns 3 and 4 give the date of the observation and the seeing conditions (in arcsec) as measured from the final reduced images. Column 5 gives the Galactic extinction and column 6 gives the apparent magnitude of the object within a 30 kpc aperture, after the removal of any other bright objects that fall within the radius. Column 7 is the magnitude in the r' band corrected for Galactic extinction and k-corrected.

This calibration is more uncertain for the image of J0159+14, which was taken with the GMOS-S instrument mounted on the telescope in a different configuration. However, the magnitude derived from the Gemini image agrees with the SDSS Model r_{AB} magnitude for this object to within 0.2 magnitudes.

The apparent r'_{AB} magnitude of each object was measured within a 30 kpc diameter aperture, removing contamination from other sources that fell within the aperture (e.g. foreground galaxies or stars). This was done by measuring the counts associated with the extraneous object, within an aperture enclosing the visible extent of the contaminating source, and subtracting this from the total counts within the 30 kpc aperture. The derived r'_{AB} magnitudes are given in column 6 of Table 2.2. The images were then corrected for Galactic extinction using the E(B-V) values, given in Table 2.2, which

are available at the NASA/IPAC Infrared science archive[4], based on the dust maps of Schlegel et al. (1998). The extinction law of Cardelli, Clayton & Mathis (1989) was assumed. The objects in this sample are generally subject to low values of Galactic reddening, with values in the range $0.0275 \leq E(B-V) \leq 0.1201$.

To make the magnitudes consistent within this sample, and also to make them directly comparable to other samples, k-corrections using the values reported by Frei & Gunn (1994) and Fukugita, Shimasaku & Ichikawa (1995) were also applied. In making k-corrections (to the rest frame), values pertaining to elliptical galaxies were assumed, because previous studies (e.g. Dunlop et al. 2003) have found the quasars tend to reside in early type hosts. The apparent magnitude of each object, corrected for Galactic extinction and k-corrected, is given in column 7 of Table 2.2. The final, fully reduced images are presented in Chapter 3.

2.2.3 Optical Spectroscopy

Long-slit spectra were taken for 18 of the 20 objects in the full sample, during semesters 2010B and 2011B, in queue mode, also using the Gemini GMOS-S instrument. Due to the absence of an atmospheric dispersion compensator on GMOS-S, the objects were observed at low airmass and/or with the slit placed at the parallactic angle, in order to minimise the effects of differential refraction (see Table 2.3). The observations were made predominately in dark time (except for J0025-10, J0227+01, J0320+00, J0848+01, J0948+00 and J2358-00, which were observed in grey time), in photometric conditions, with good seeing ($0.53 < \mathrm{FWHM} < 1.58$ arcsec with a median of 0.81 arcsec FWHM) using a slit width of 1.5 arc seconds. The seeing was measured by averaging 2-dimensional Gaussian fits of a number of foreground stars in the acquisition images (depending on the number of stars in the field) for each of the objects. The observations, in the main, consist of 4×675 s exposures using the B600 grating with 600 groves mm^{-1} blazed at 461 nm, and 3×400 s exposures using the R400 grating with 400 groves mm^{-1} blazed at 764 nm. The exposures in the two wavelength ranges were interleaved in order to mitigate any changes in the atmospheric conditions throughout each observational run. The full details of the observations can be found in Table 2.3.

The data were reduced using a combination of the Gemini GMOS-S dedicated data reduction package within the IRAF environment, other standard IRAF routines, and the STARLINK FIGARO[5] package. Initially, the three CCD images, which comprise each

[4] http://irsa.ipac.caltech.edu/applications/DUST/

[5] The author acknowledges the data analysis facilities provided by the Starlink Project

Name	obs. date	PA (degrees)	Exposure Blue(s)	Exposure Red(s)	Airmass	Seeing (arcsec)
J0025-10	2010-11-30	230	4×675	3×400	1.07-1.13	0.84
J0114+00	–	–	–	–	–	–
J0123+00	2011-10-24	209	4×675	3×400	1.17-1.21	1.12
J0142+14	2011-12-23	155	1×675 1×461	–	1.53-1.56	0.73
J0159+14	–	–	–	–	–	–
J0217-01	2010-12-03	146	4×675	3×400	1.19-1.33	0.97
J0217-00	2011-10-23	222	4×675	3×400	1.25-1.45	0.86
J0218-00	2010-12-04	171	4×675	3×400	1.15-1.21	1.11
J0227+01	2011-01-26	138	4×675	3×400	1.40-1.73	0.53
J0234-07	2010-12-06	126	4×675	3×400	1.37-1.74	0.78
J0249+00	2010-12-05	0	4×675	3×400	1.16-1.20	0.73
J0320+00	2010-12-05	216	4×675	3×400	1.21-1.36	0.75
J0332-00	2010-12-06	32	4×675	3×400	1.16-1.17	0.83
J0334+00	2010-12-01	350	4×675	3×400	1.19-1.30	1.13
J0848+01	2011-01-25	174	4×675	3×400	1.18-1.26	0.72
J0904-00	2012-01-20	140	4×675	3×400	1.35-1.58	0.71
J0923+01	2011-11-30	222	4×675	3×400	1.28-1.50	0.67
J0924+01	2011-02-01	0	4×675	3×400	1.18-1.20	0.75
J0948+00	2011-01-25	145	4×675	3×400	1.23-1.40	0.89
J2358-00	2011-09-03	331	4×675	3×400	1.16-1.74	1.58

Table 2.3: Details of the long-slit spectroscopic observations carried out at Gemini South using the GMOS instrument: Column 1 gives the object name, column 2 and 3 the observation date and slit position angle, columns 4 and 5 give the exposure times in seconds using the blue and red grisms respectively. Column 5 gives the airmass throughout the exposures and column 6 gives the seeing for the observations in arcsec as measured from the acquisition image.

exposure, were mosaicked into a single image which was then bias subtracted using the over-scan region, before flat fielding. The flat fields were taken contemporaneously with the science exposures. In order to produce a master flat, the exposures were combined using an average or median combine (depending on the number of exposures taken). The shape of the detector response was then modelled across the detector (in the spectral direction), and then each row was divided by this model in order to remove this effect, after which, the flat field was normalised to the median pixel value. The science images were then either median or average combined, depending on the number of exposures taken, however, this was not completely successful in removing all cosmic rays and therefore, the remainder were removed manually using the FIGARO CLEAN package.

http://starlink.jach.hawaii.edu/starlink/WelcomePage.

The wavelength comparison arcs were taken using a copper argon lamp, for both the red and blue exposures. For the 2010B semester run, they were taken on the same night as the observations, using a 1.5 arc second slit. However, for the 2011B run, arcs were not always taken on the same night as the observations, and therefore, the arc that was most contemporaneous to the observation was used. The wavelength calibration was performed in four steps. Initially, spectral lines were manually identified in a 1–dimensional spectrum, extracted from the arc image. A function was fit to these coordinates as a function of pixel coordinate. This was then used as a reference spectrum to identify the same features in the remaining regions of the arc image. The arc image was then fit to these coordinates and then this solution was applied to the 2-dimensional science image. The wavelength calibration for each image was checked by extracting a 1 dimensional spectrum of the sky emission lines close to the target position along the slit, and fitting the position of the most prominent lines using a Gaussian profile. Using this technique, the uncertainty in the wavelength calibration was found to be ~ 0.3 Å and ~ 0.5 Å for the B600 and R400 exposures respectively. Using a 1.5 arcsec slit, the average spectral resolution in the blue wavelength range was 7.2Å and was 11.4Å in the red wavelength range, as measured from the strong sky lines in the 2D frames.

Once a satisfactory wavelength calibration had been achieved, the sky subtraction was performed before the resulting 2 dimensional spectrum was flux calibrated. Due to the fact that an accurate flux calibration is essential when attempting to model stellar populations, several standard stars were observed over the course of each semester. Flux calibration curves were derived for each star individually, which were then compared to each other (independently for each semester) across the full wavelength range. Clearly outlying curves (i.e. due to mis-identification of the standard star, non-photometric conditions etc.) were rejected before combining the curves into an average flux calibration curve, which was then applied to all the objects observed in that semester. In this way, the accuracy of the flux calibration can be considered to be $\pm$ 5%. There is also a large region of overlap between the red and blue spectra ($\sim$ 2080 Å), allowing a further check that the calibrations in the two parts matches well. In most cases, the agreement was excellent, and the red and blue spectra agreed in both shape and level across the full region of the overlap to within 5%. In three cases (J0217-00, J0249+00 and J0924+01), the difference in the flux calibration between the blue and red spectra were significant (8%, 13% and 22% respectively), although the shapes of the spectra in these cases agreed well. However, because this occurred in a limited number of cases, it was considered that this was due to changes in the atmospheric conditions between the observations made

using the blue and red grisms, rather than being an issue with the flux calibration. Therefore, either the blue or red spectrum was scaled to match its counterpart with the higher continuum flux level. The final step was to correct the spectra for any spatial distortions, using the IRAF APALL package. The useful observed wavelength range was 3940 – 9140 Å, although wavelengths longer than 8200 Å are strongly affected by fringes.

2.3 The Spectra

Below the 1D spectra extracted from the data, for the 18 objects for which Gemini GMOS-S data has been obtained, are presented. In the majority of cases, only one aperture was extracted from each object, which was centred on the peak continuum flux. This was derived from a 100 Å slice of the 2 dimensional spectrum in the observed 6400 – 6600 Å region (exact wavelength region depending on redshift). In all such cases, the aperture had a metric diameter of 8kpc and was centred on the nucleus of each target. However, it must be noted that the apertures were not exactly 8 kpc because of the finite pixel scale. The sizes of the apertures were 10–12 pixels, depending on the redshift of the object.

In three cases (J0025-10, J0218-00 and J0332-00), it was possible to extract more than one aperture from the 2 dimensional spectrum. In the cases of J0218-00 and J0332-00, two apertures were extracted, one with a spatial scale of 8 kpc and centred on the nuclear region of the quasar host galaxy, while the second aperture was extracted from an extended region and had a 5 kpc physical scale. The quality of the data obtained for J0025-10 allowed the extraction of three distinct apertures, the details of which are presented in Chapter 4, where this object is discussed in detail. Figure 2.3 shows the full spectrum from each aperture extracted, except J0025-10 (see Chapter 4), and where appropriate, a spatial slice across the 2 dimensional spectrum showing the extent and positioning of the apertures extracted. The SDSS spectrum of J0114+00 is also presented. The SDSS use a 3 arcsec diameter fibre for spectroscopy, which at the redshift of J0114+00 corresponds to a spatial scale of 15.8 kpc.

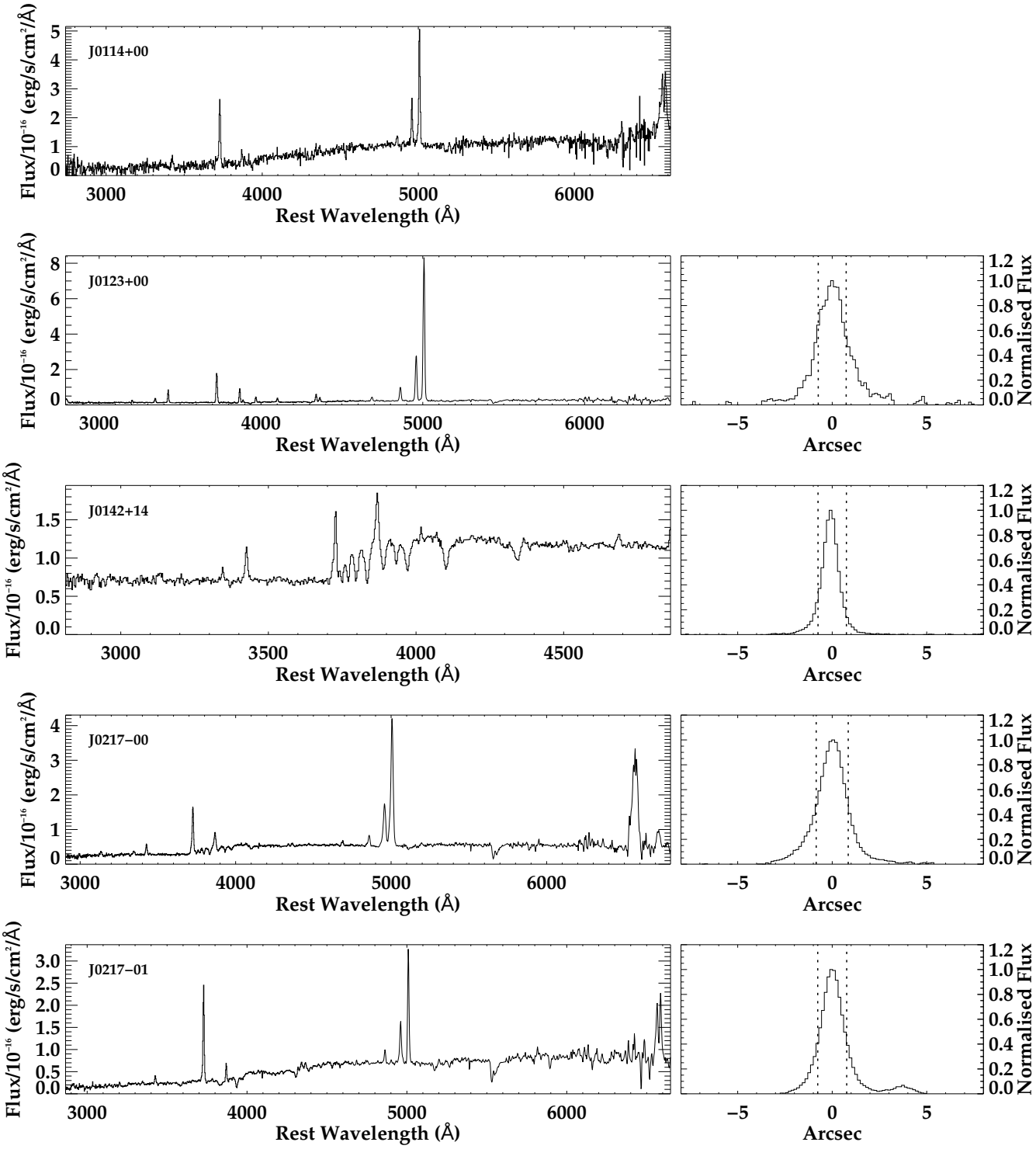

Figure 2.3: The Gemini GMOS-S spectra for 17 of the objects, and SDSS spectrum of J0114+00. Next to the spectra for each object is a spatial slice of the 2D spectrum detailing the aperture(s) used for the extraction.

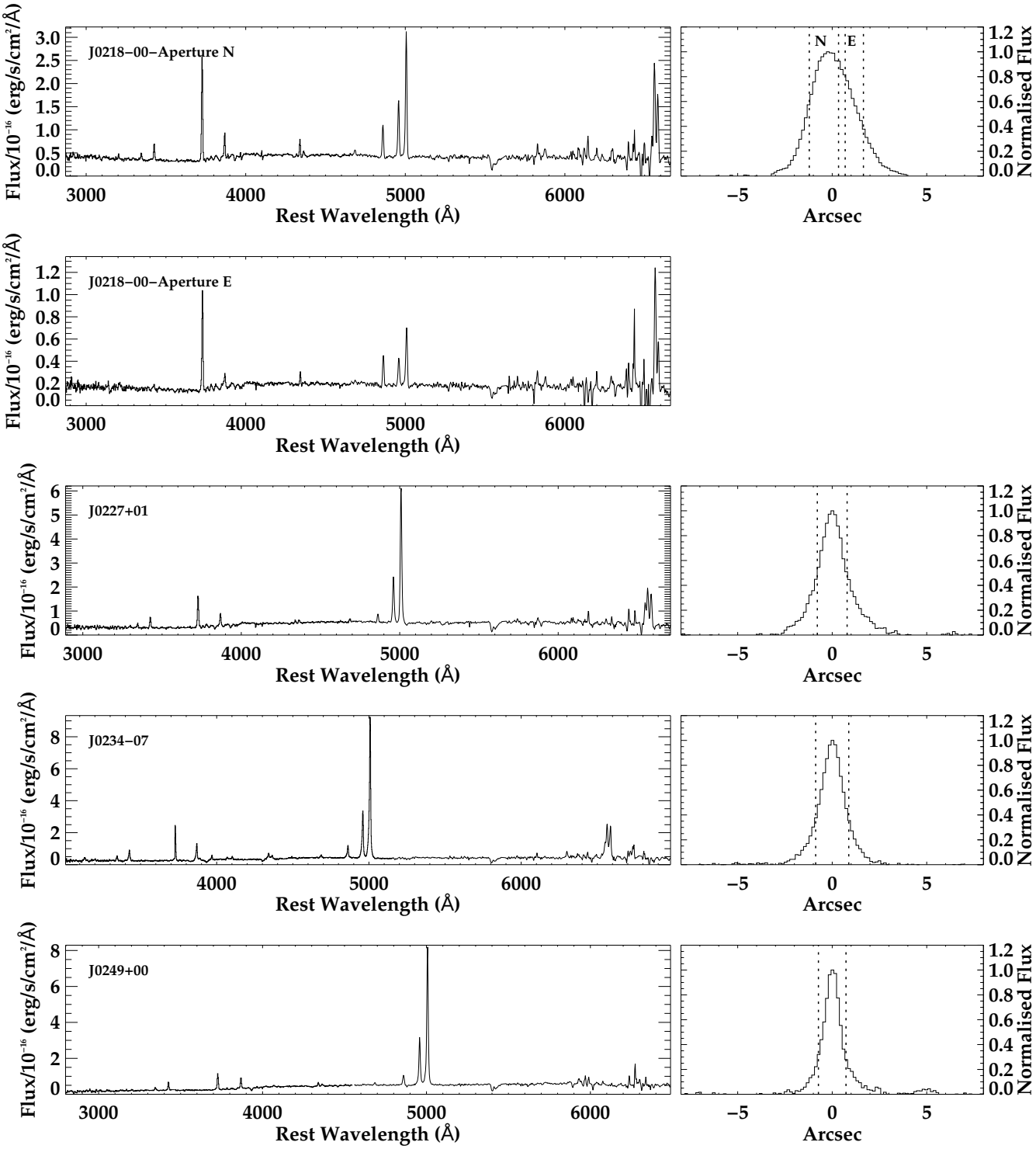

Figure 2.3: [continued]

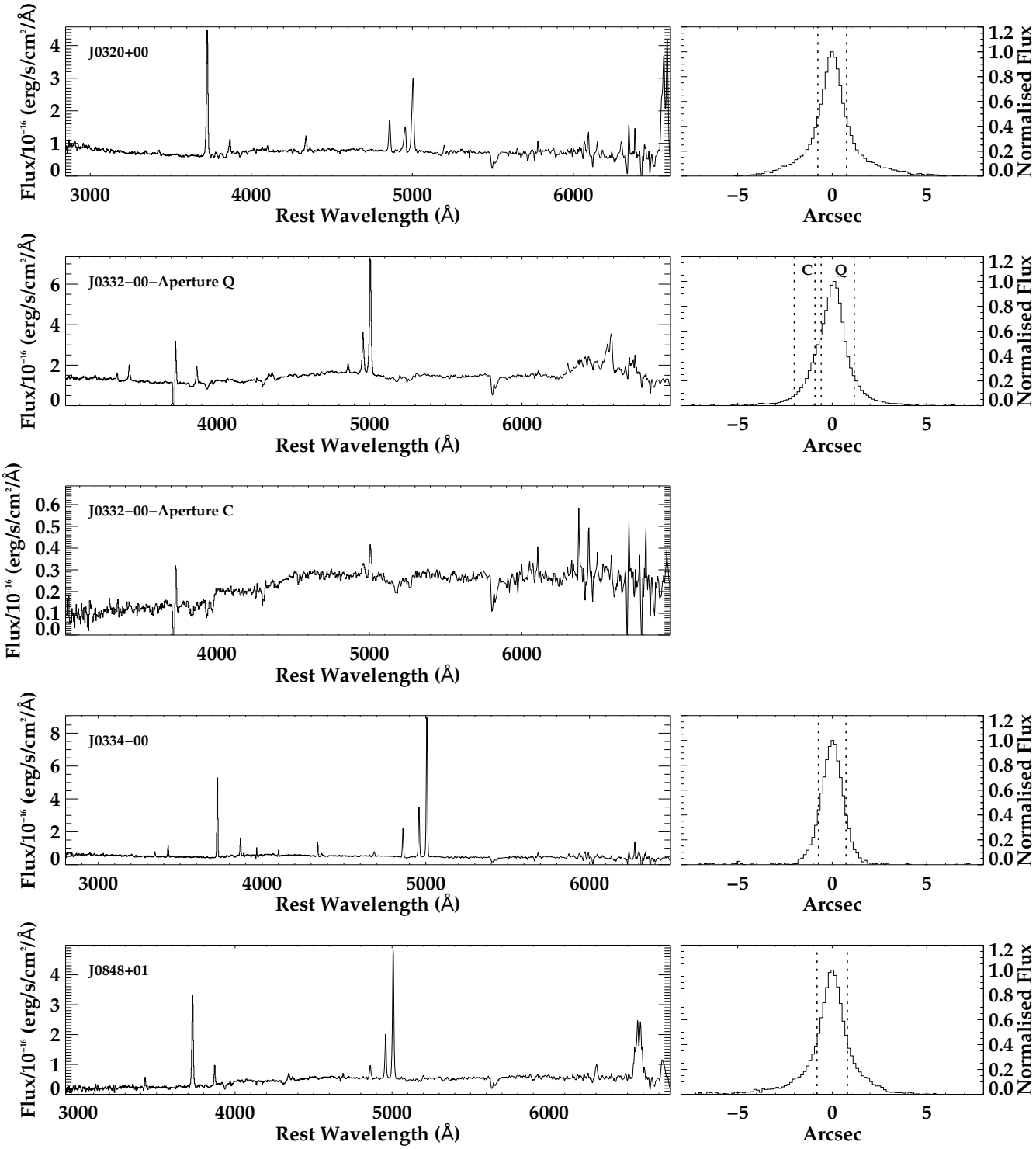

Figure 2.3: [continued]

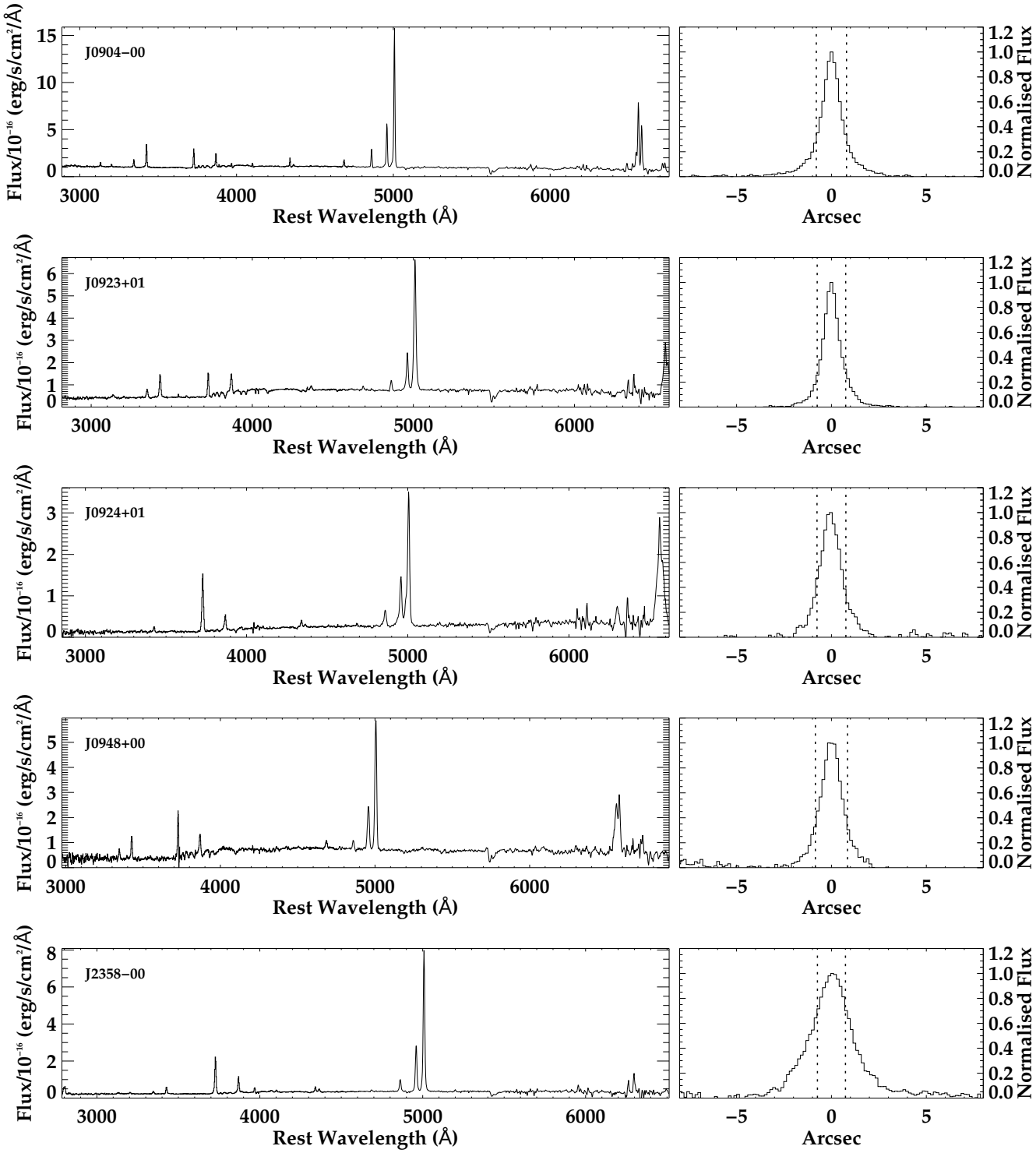

Figure 2.3: [continued]

2.4 Previous publications

In this section a brief outline of any previously published work for the 20 objects discussed in this thesis is given. A number of papers will be referred to several times, and therefore, for the rest of this section, the following abbreviations will be used: Z03 – Zakamska et al. (2003), R08 – Reyes et al. (2008), RA13 – Ramos Almeida et al. (2013).

RA13 have calculated spatial clustering amplitudes (B_{gq}) for each of the type II quasars investigated in this thesis. B_{gq} is a measure of how many galaxies are found within a fixed distance of the type II quasars (i.e. the counting radius), compared to the number expected from typical galaxy counts.

The objects that were counted as being associated with the target quasar are those that fall within the counting radius (in this case 170 kpc) and also fall within the apparent magnitude range $(m_* - 1) \leq m \leq (m_* + 2)$, where m_* is the typical apparent magnitude of a galaxy at the same redshift as the type II quasars (taking into account Galactic extinction). This counting process was repeated for dedicated offset fields, in order to determine the typical number of galaxies fulfilling the same criteria as adopted for the target objects. These two values were then compared to determine if the type II quasars lay in under-dense, over-dense or typical regions. Full details of how these calculations were made can be found in RA13.

J0025-10

J0025-10 is the most well studied object in this sample of type II quasars, and was identified for spectroscopy by the SDSS using the Quasar algorithm. Both Z03 and R08 determined that this source is luminous enough to conform to the quasar criterion imposed in this work ($\log(L_{[OIII]}/L_{\odot}) = 8.73$; Z03). Zakamska et al. (2004) also found that this source was detected by IRAS at 100 microns with a flux $F_{100\mu m} = 410 \pm 123$ mJy with a confidence of 0.50. The confidence level is calculated as 1 minus the probability that the match is a random background association. This probability is dependent on the correlation coefficient[6] and the offset of the match from the optical position of the source. Therefore, the confidence of this detection, and all of other IRAS detections presented in this section are low, but are included for completeness.

This source was also detected by the FIRST 1.4 GHz survey with a radio power (extrapolated to 5 GHz) $log(L_{5GHz}) = 22.08$ W Hz^{-1} Sr^{-1} (Table 2.1). The fluxes have been extrapolated to 5 GHz assuming a spectral index (radio) of $\alpha = -0.75$, because in

[6]For full information on this parameter and other information on IRAS, please consult the SCANPI help page at http://irsa.ipac.caltech.edu/applications/Scanpi/docs/overview.html

Chapter 3 a comparison of the radio properties of this sample of type II quasar is made with the 2 Jy sample of PRG, on the basis of their radio properties at 5 GHz.

It has also been shown by RA13 that J0025-10 is in a low density environment, with a spatial clustering amplitude $B_{gq} = -16 \pm 175$, suggesting this galaxy is in the field.

Villar-Martín et al. (2011) and Villar-Martín et al. (2013) present broad and narrow band ([OIII]) imaging, optical spectroscopy and CO observations of this object. They demonstrate that an extended tail and companion nucleus are both significantly more prominent in their broadband images (V-band) than in their [OIII] images, and therefore, most likely dominated by the continuum. They also find [OIII]/Hβ ratios in both these latter regions that are consistent with HII regions, and measure the velocity shift between the companion and quasar host to be $\Delta v = 0 \pm 70$ km s^{-1} , while the velocity shift between the tidal tail and quasar nucleus is $\Delta v = -15 \pm 70$ km s^{-1}. Their CO measurements show that there are two large reservoirs of cold gas present in this object, with a total mass of $M_{H_2} = (6 \pm 1) \times 10^9$ M$_\odot$, separated by ~ 9 kpc.

Using broadband (V-band; 4800–6000Å) measurements Zakamska et al. (2006) show that J0025-10 has a low degree of linear polarization of $P = 1.24 \pm 0.62\%$, with a polarization position angle of $\theta = 110 \pm 14$ degrees. However, it must be noted that this polarization, and those presented below, have all been detected at a level of 2σ or less, but once again, are presented here for completeness

J0114+00

J0114+00 was selected for spectroscopic follow up by SDSS from the DSES as an optical counterpart to a FIRST source, using the Serendipity algorithm, and although determined by Z03 to have a quasar-like luminosity ($\log(L_{[OIII]}/L_\odot) = 8.66$), R08 find that it falls slightly below the lower limit imposed in this thesis ($\log(L_{[OIII]}/L_\odot) = 8.46$). RA13 find that $B_{gq} = 254 \pm 272$, which suggests that it is in a low density field or group environment. Extrapolating the 1.4 GHz flux, using the measured spectral index of $\alpha = -0.670$ ($S \propto \nu^\alpha$) (Reid et al., 1999), J0114+00 has a radio power at 5 GHz of $log(L_{5GHz}) = 24.70$ W Hz^{-1} Sr^{-1}, making it the most powerful radio source in the sample. Figure 2.4 is taken directly from Reid et al. (1999) and shows a map of the double-lobed radio structure associated with J0114+00, made at 5 GHz using the VLA. This map indicates that the radio structure is edge brightened, which is consistent with an FRII morphology.

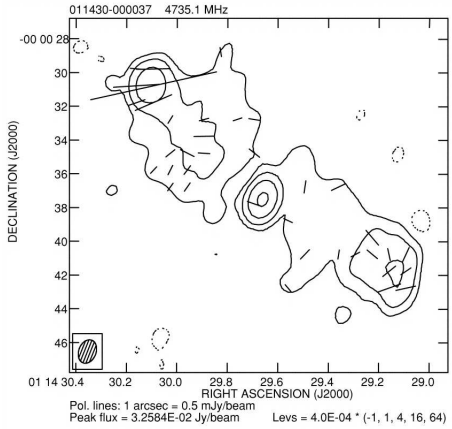

Figure 2.4: A radio map of J0114+00 taken at 5 GHz using the VLA and showing the double lobed structure of the radio emission from this object. This radio map is taken directly from Reid et al. (1999)

.

J0123+00

J0123+00 was targeted for spectroscopy by the SDSS as part of the DSES, as the optical counterpart to a FIRST object using the Serendipity algorithm, and is considered by both Z03 and R08 to have an [OIII] luminosity consistent with what would be expected for a quasar ($\log(L_{[OIII]}/L_{\odot}) = 9.13$; Z03), in fact, it has one of the highest [OIII] luminosities in this sample. This source is detected by the FIRST survey and has a radio power, extrapolated to 5 GHz, of $log(L_{5GHz}) = 23.27$ W Hz^{-1} Sr^{-1}. This object is found by RA13 to reside in a moderately dense environment, with $B_{gq} = 676 \pm 348$, which corresponds to Abell class 0 – 1, which is one of the densest environments found for this sample of type II quasars.

J0123+00 has also been found to have a very large extended emission line nebula (Villar-Martín et al., 2010), extending up to $\sim$ 180 kpc, making it one of the largest ionised nebulae associated with an active galaxy ever detected.

Zakamska et al. (2006) also present broadband polarisation measurements for this object, obtaining a value of $P = 3.47 \pm 2.21\%$ at a position angle of $\theta = 8 \pm 18$ degrees. Once again, this polarisation is detected at less than the 2σ level.

J0142+14

This object was selected by SDSS for spectroscopy using the Quasar algorithm and was classified by both Z03 and R08 as a quasar, with $\log(L_{[OIII]}/L_{\odot}) = 8.76$ (Z03). J0142+14 was also detected at 100 microns using IRAS data at $F_{100\mu m} = 410 \pm 67$ mJy with a

0.5 confidence level Zakamska et al. (2004). Zakamska et al. (2006) present broadband polarization measurements (V-filter) for J0142+14 and find a value of $P = 0.66 \pm 0.76\%$, however the polarization angle is undefined due to the fact that $P < 1.5\ \sigma(P)$, where $\sigma(P)$ is the uncertainty in the polarisation measurement. RA13 derive a spatial clustering amplitude of $B_{gq} = 149 \pm 251$, which suggests that this galaxy is in a low density field or group environment.

J0159+14

J0159+14 was targeted for spectroscopy using the High redshift quasar algorithm by SDSS. Although Z03 found this object to have quasar-like luminosity ($\log(L_{[OIII]}/\ L_{\odot}) = 8.56$), R08 determine a value slightly below the quasar cut off used here ($\log(L_{[OIII]}/\ L_{\odot}) = 8.39$). RA13 find a spatial clustering amplitude of $B_{gq} = 169 \pm 227$, which suggests that this galaxy is in a field or group environment.

J0217-00

J0217-00 was selected by the SDSS for spectroscopy from the DSES using the Serendipity algorithm, as an optical counterpart to a FIRST detected source. Both Z03 and R08 determine this object to have quasar-like luminosity ($\log(L_{[OIII]}/\ L_{\odot}) = 8.56$; Z03). This object has been detected by the FIRST survey with a radio power extrapolated to 5 GHz $log(L_{5GHz}) = 22.15$ W Hz^{-1} Sr^{-1}. Zakamska et al. (2004) also detect J0217-00 at both 60 and 100 microns, using IRAS survey data at $F_{60\mu m} = 140 \pm 43$ and $F_{100\mu m} = 490 \pm 103$ mJy respectively, with a confidence level of 0.75 and 0.50. RA13 derive a spatial clustering amplitude of $B_{gq} = 63 \pm 212$, indicative of this galaxy being in the field. Zakamska et al. (2006) also present broadband polarization measurements for this object, and find a value of $P = 1.53 \pm 0.97\%$ with a polarization angle $\theta = 145 \pm 18$ degrees.

Villar-Martín et al. (2011) present a narrow band ([OIII]) image of this object, as well a long-slit spectroscopy (PA 60), which passes through a prominent tidal feature. They find that this tidal tail is continuum dominated, and also that the quasar has a star-forming knot in its halo in which the gas is photo-ionised by young stars.

J0217-01

This source was targeted by SDSS for spectroscopy using the Serendipity algorithm as the optical counterpart to a FIRST detected object. Although Z03 determine this object to have quasar-like luminosity ($\log(L_{[OIII]}/\ L_{\odot}) = 8.55$), R08 find that it falls below

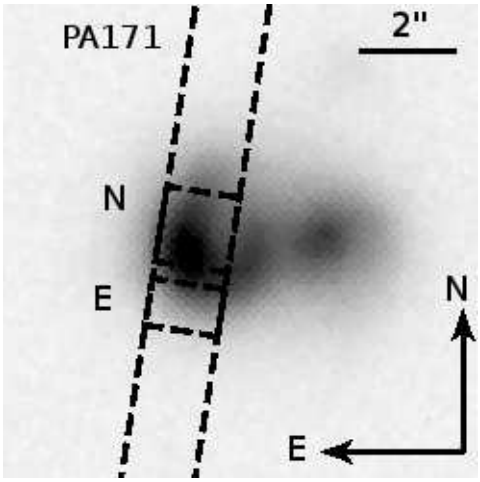

Figure 2.5: An optical image of J0218-00 showing the approximate positions of the two apertures that were extracted from the 2 dimensional spectra. Aperture N is centred on the nuclear region of the galaxy, while aperture E is centred on an extended region of the host galaxy

the quasar cut off adopted here ($\log(L_{[OIII]}/L_{\odot}) = 8.37$). J0217-01 was detected by the FIRST radio survey and has a radio power at 5 GHz of $log(L_{5GHz}) = 22.35$ W Hz^{-1} Sr^{-1}. This source is also found by RA13 to be in a low density environment, with a spatial clustering amplitude of $B_{gq} = -153 \pm 170$

J0218-00

This object was selected for SDSS spectroscopy from the DSES and is classified by both Z03 and R08 as being luminous enough to be considered a quasar, with $\log(L_{[OIII]}/L_{\odot}) = 8.85$) (Z03). RA13 find that J0218-00 is in a low density environment, with a spatial clustering amplitude of $B_{gq} = -49 \pm 199$. J0218-00 is one of the few objects from which more than one aperture has been extracted from the spectra. Figure 2.5 shows the approximate positions of these apertures against the Gemini GMOS-S optical image. These apertures are discussed in more detail in Chapter 5.

J0227+01

J0227+01 was targeted by SDSS for spectroscopy on a Special plate and has been selected using a wide selection of algorithms including FIRST and ROSAT matches, and has been determined by both Z03 and R08 to have a quasar-like luminosity ($\log(L_{[OIII]}/L_{\odot}) = 8.90$; Z03). This source is found by RA13 to be in a low density environment, with a spatial clustering amplitude of $B_{gq} = 159 \pm 241$.

J0234-07

J0234-07 was selected for spectroscopic follow up by the SDSS using the Serendipity algorithm as an optical counterpart to a FIRST source, and has a radio power at 5 GHz of $log(L_{5GHz}) = 22.35$ W Hz^{-1} Sr^{-1}. Both Z03 and R08 find that this source has a quasar-like luminosity ($\log(L_{[OIII]}/L_{\odot}) = 8.77$; Z03). RA13 find a spatial clustering amplitude of $B_{gq} = -115 \pm 152$, suggesting that this object in a low density environment.

J0234-07 has also been observed by Villar-Martín et al. (2011), where they present narrow band imaging centred on [OIII] for this source, as well as long slit spectroscopy (PA 171), with the intention of attempting to detect extended emission line structures, which they conclude are not present in this object.

Greene & Ho (2007) use SDSS data-release 4 spectra to classify this quasar as a type I object on the basis of the detection of a broad Hα component, a feature which is not evident in the data presented here. This is illustrated in Figure 2.6, which shows a zoom of the region around both the Hβ + [OIII] lines and the Hα + [NII] lines from the stellar continuum subtracted spectrum. This figure clearly demonstrates that in both cases, the hydrogen lines can be well fit using only the same kinematic components as necessary to fit each [OIII] line (assuming the same kinematic components for the [NII] lines). Greene & Ho (2007) employ a careful selection technique in order to avoid contamination of their sample of type I objects, and therefore it unclear how this discrepancy arises. Nevertheless, Greene & Ho (2007) determine a FWHM of 1820 km s^{-1} for the broad Hα component and derive a black hole mass of $\log(M_{BH}/M_{\odot}) = 6.7$.

J0249+00

This object was selected by SDSS for spectroscopy using the Serendipity algorithm as the optical counterpart to a FIRST source, which has a radio power at 5 GHz of $log(L_{5GHz}) = 22.14$ W Hz^{-1} Sr^{-1}. J0249+00 is classified by both Z03 and R08 as having quasar-like luminosity ($\log(L_{[OIII]}/L_{\odot}) = 8.63$). RA13 find a spatial clustering amplitude of $B_{gq} = -177 \pm 180$, which means that this object is in a low density environment.

J0320+00

J0320+00 was selected for spectroscopy by SDSS using the Quasar algorithm, and also as part of a Special plate. The $L_{[OIII]}$ derived by Z03 for this object indicates that it is luminous enough to be considered a quasar ($\log(L_{[OIII]}/L_{\odot}) = 8.52$), however, according to the analysis performed by R08, J0320+00 falls slightly below the value adopted in

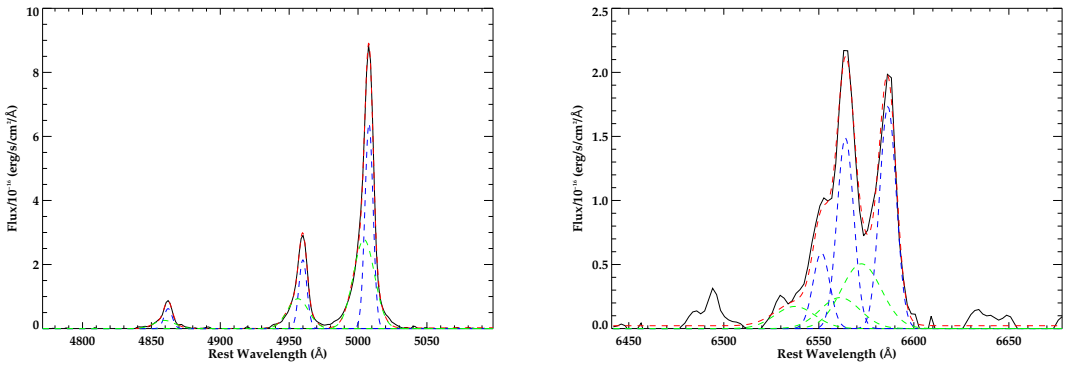

(a) Hβ + [OIII] lines (b) Hα + [NII] lines

Figure 2.6: The fits to (a) the Hβ + [OIII] lines and (b) the Hα + [NII] lines for J0234-07 demonstrating that both the Hβ and Hα lines can be well fit using only the same kinematic components as the [OIII] lines. In both panels, the black line shows the data, the red line shows the overall fit to the data, the blue lines show the narrow components for each line, whilst the green lines show the broad components for each line.

this work ($\log(L_{[OIII]}/L_{\odot}) = 8.40$). Zakamska et al. (2004) have used IRAS 100 micron data to derive a flux of $F_{100\mu m} = 550 \pm 98$ mJy, with a confidence of 0.50. This is also one of the few objects in this sample to be considered part of a cluster, with a spatial clustering amplitude of $B_{gq} = 1297 \pm 425$, which is corresponds to Abell class 2 (RA13).

J0332-00

J0332-00 was targeted for spectroscopic follow up by the SDSS using the Serendipity algorithm as the optical counterpart to a ROSAT source, and has been characterised by both Z03 and R08 as having a quasar-like luminosity ($\log(L_{[OIII]}/L_{\odot}) = 8.50$; Z03). This object has also been detected by the FIRST 1.4 GHz survey, and has a radio power at 5 GHz of $log(L_{5GHz}) = 22.14$ W Hz^{-1} Sr^{-1}. Zakamska et al. (2004) also find an IRAS match at 60 microns, with a flux of $F_{60\mu m} = 90 \pm 27$ mJy at a confidence level of 0.75. RA13 find that this source is in a low density environment with a spatial clustering amplitude of $B_{gq} = -19 \pm 222$.

Since its classification as a type II quasar, it has emerged that this object is, in fact, a type I object, as can clearly be seen from the extremely broad Hα component in Figure 2.3. This has also been recognised by Barth et al. (2014), who present a Keck spectrum showing an obvious broad Hα component in the total light spectrum. Shen et al. (2011) presented measurements of the FWHM of this broad Hα component (FWHM = 13360 $\pm$7819 km s^{-1}) and also estimate the black hole mass to be $\log(M_{BH}/M_{\odot}) = 8.82$, with

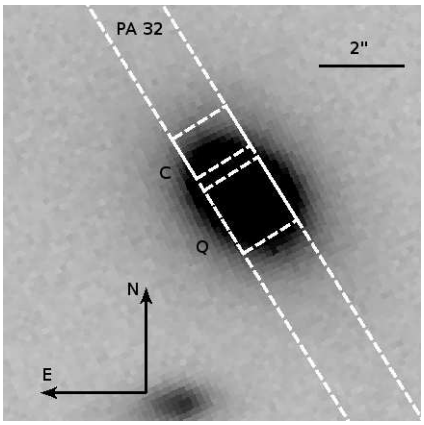

Figure 2.7: An optical image of J0332-00 showing the approximate positions of the two apertures that were extracted from the 2 dimensional spectra. Aperture Q is centred on the quasar host galaxy, whilst aperture C encompasses a merging companion host galaxy.

an Eddington ratio $\log(L_{Bol}/L_{Edd}) = -1.71$, indicating a moderately low accretion rate.

J0332-00 is one of the few objects for which more than one aperture was extracted from the 2-dimensional spectra. The main aperture was centred on the quasar host galaxy (Q), while a narrower aperture was extracted in the region of a companion nucleus (C), which can be seen more clearly in the images presented in Chapter 3. Figure 2.7 shows the approximate location of these apertures against the Gemini GMOS-S optical image.

J0334+00

This object was selected by SDSS for spectroscopy from the DSES and was targeted using multiple algorithms. Both Z03 and R08 identify this object as a type II quasar candidate with $\log(\mathrm{L}_{[OIII]}/\mathrm{L}_{\odot}) = 8.61$ (Z03). RA13 find J0334+00 to be in a low density environment with a spatial clustering amplitude of $B_{gq} = 36 \pm 235$.

J0848+01

J0848+01 was selected for follow up spectroscopy by the SDSS using the Serendipity algorithm as an optical counterpart to a FIRST source, with a radio power (extrapolated to 5 GHz) of $log(\mathrm{L}_{5GHz}) = 24.00$ W Hz^{-1} Sr^{-1}. Z03 classify this object as a quasar with $\log(\mathrm{L}_{[OIII]}/\mathrm{L}_{\odot}) = 8.56$, although R08 find $\log(\mathrm{L}_{[OIII]}/\mathrm{L}_{\odot}) = 8.46$, which puts this object slightly below the quasar cut off value that has been adopted here. This object is classified by RA13 as having a spatial clustering amplitude of $B_{gq} = 159 \pm 237$, which

means that it is in a low density environment.

J0904-00

J0904-00 was selected using both the Quasar algorithm and the Serendipity algorithm as the optical counterpart to a FIRST source, which has a radio power at 5 GHz $log(L_{5GHz}) = 23.52$ W Hz^{-1} Sr^{-1}. Both Z03 and R08 find that this source has a quasar-like luminosity with Z03 deriving a value $\log(L_{[OIII]}/L_{\odot}) = 8.93$. J0904-00 has also been detected by IRAS at both 60 and 100 microns with fluxes of $F_{60\mu m} = 110 \pm 47$ mJy (confidence of 0.8) and $F_{100\mu m} = 250 \pm 85$ mJy (confidence of 0.5) respectively (Zakamska et al., 2004). RA13 find J0904-00 to be in a cluster environment, with a spatial clustering amplitude of $B_{gq} = 463 \pm 295$, which is equivalent to Abell class 0.

Bian et al. (2006) use stellar absorption features in the host galaxy to derive a stellar velocity dispersion of $\log(\sigma) = 2.52$ km s^{-1}, from which they derive a black hole mass of $\log(M_{BH}/M_{\odot}) = 9.01$ and thus an Eddington ratio of $\log(L_{Bol}/L_{Edd}) = -0.91$, suggesting a moderate accretion rate.

J0923+01

J0923+01 was selected by the SDSS for spectroscopy using the Serendipity algorithm as an optical counterpart to a FIRST source, which has a radio power at 5 GHz $log(L_{5GHz}) = 22.09$ W Hz^{-1} Sr^{-1}. Both Z03 and R08 determine that it has a luminosity above the lower quasar luminosity limit imposed in this work($\log(L_{[OIII]}/L_{\odot}) = 8.94$; Z03). J0923+01 is found by RA13 to be in a low density field or group environment with $B_{gq} = 256 \pm 271$.

Bian et al. (2006) measure the stellar velocity dispersion to be $\log(\sigma) = 2.40$ km s^{-1}, and from this derive a black hole mass of $\log(M_{BH}/M_{\odot}) = 8.53$ and Eddington ratio $\log(L_{Bol}/L_{Edd}) = -0.34$, suggesting a moderately high accretion rate.

J0924+01

This source was selected using the Serendipity algorithm for SDSS spectroscopy as an optical counterpart to a FIRST source, which has a radio power, extrapolated to 5 GHz of $log(L_{5GHz}) = 23.33$ W Hz^{-1} Sr^{-1}. Although Z03 derive a luminosity consistent with quasars $\log(L_{[OIII]}/L_{\odot}) = 8.59$, R08 find that it falls below the cut off enforced in this thesis of $\log(L_{[OIII]}/L_{\odot}) = 8.5$, with a derived value of $\log(L_{[OIII]}/L_{\odot}) = 8.46$. RA13 have determined that this object is in a low density field environment, with $B_{gq} = -55 \pm 200$.

J0948+00

J0948+00 was targeted for spectroscopic follow up by the SDSS using the Serendipity algorithm as an optical counterpart to a FIRST source, which has a radio power at 5 GHz of $log(\mathrm{L}_{5GHz}) = 22.35$ W Hz^{-1} Sr^{-1}. Both Z03 and R08 derive a quasar-like luminosity ($\log(\mathrm{L}_{[OIII]}/\,\mathrm{L}_{\odot}) = 8.52$; Z03) for this object. RA13 find that J0948+00 is in a low density environment with $B_{gq} = -123 \pm 155$, which is characteristic of the field.

Bian et al. (2006) also report a stellar velocity dispersion of $\log(\sigma) = 2.05\,\mathrm{km\ s^{-1}}$, from which they derive a black hole mass of $\log(M_{BH}/\,\mathrm{M}_{\odot}) = 7.10$ and Eddington ratio $\log(L_{Bol}/L_{Edd}) = 0.62$, implying super Eddington accretion. Therefore caution should be exercised when interpreting this result.

J2358-00

J2358-00 was selected for spectroscopy by the SDSS using the Quasar algorithm. This is the most luminous quasar in the sample with $\log(\mathrm{L}_{[OIII]}/\,\mathrm{L}_{\odot}) = 9.13$. RA13 find that this source inhabits a low density region with a spatial clustering amplitude $B_{gq} = 40 \pm 231$. Broadband polarisation measurements are presented in Zakamska et al. (2006), where they find a value of $P = 3.30 \pm 1.75\%, \theta = 154 \pm 15$ degrees.

Villar-Martín et al. (2011) have shown that this object has an extended emission line nebula which is photo-ionised by the quasar, with a maximum extent of ~ 64 kpc. J2358-00 is also a clearly merging system (Chapter 3), and they have shown that the shift in velocity between the two components $\Delta v = +300 \pm 80$ km s^{-1}, which is well within the range expected for merging systems. Using emission line ratios, they determine that it is likely that the companion is also a star forming object.

In this Chapter, the Gemini GMOS-S imaging and spectroscopic observations and data reduction that form the basis of the work presented in this thesis have been presented. A brief summary of previously published papers including the objects in this sample has also been presented. In the next Chapter, an investigation of the optical morphology of this sample of type II quasars, based on the optical imaging data discussed above, is presented.

Chapter 3

The optical morphologies of type II quasar host galaxies

The work presented in this Chapter is based on that originally presented in Bessiere et al. (2012). Bessiere was responsible for reducing, analysing and interpreting the data, with suggestions and guidance from her co-authors

3.1 Introduction

If galaxy mergers are indeed the trigger for quasar activity, then the interaction will be accompanied by morphological disturbance of the host galaxy in the form of tidal tails, fans, shells etc., as well as close pairs which have yet to coalesce, manifesting as double nuclei or linked by bridges. In a gas-rich merger, such features are expected to be visible on a time-scale of $\sim$1 Gyr (Lotz et al., 2008), while the quasar activity is expected to last $\sim$1 – 100 Myr (Martini & Weinberg, 2001). This means that the quasar activity will be concurrent with the presence of tidal features and morphological disturbance of the host galaxy. If this is the case, then by attempting to detect these features in the host galaxies of quasars, it is possible to determine whether they have been involved in interactions.

The analysis of the morphologies of this homogeneous sample of type II quasars also provides the opportunity for comparison with radio-loud quasar host galaxies. Currently the relationship between luminous radio-loud and radio-quiet AGN is uncertain, and it is not clear whether the two types are triggered in the same manner. For example, it has been suggested that each episode of quasar activity might cycle through radio-loud and radio-quiet phases (Nipoti et al., 2005), in which case, the triggering mechanism

and galaxy morphologies would be similar for the two types. Therefore, the optical morphologies of the type II quasars presented in this thesis are compared with those of the 2 Jy sample of PRG presented in Ramos Almeida et al. (2011) (hereafter RA11).

However, in order to truly quantify the significance of mergers in the triggering of AGN, it is also important to compare the rate of interaction with a suitable sample of quiescent galaxies. Ramos Almeida et al. (2012) (hereafter RA12) provide just such a comparison, with a control sample selected to match the PRG in morphology, luminosity and redshift.

In Section 3.2, the techniques used to analyse the images are discussed, and the images themselves are presented in Section 3.3, along with detailed notes on the individual objects. In Section 3.4 the results of the analysis are presented, which are then discussed in section 3.5, including a comparison of the results with those of RA11 and RA12.

3.2 Data analysis

The fully reduced GMOS-S images were used for the detection of tidal features which provide evidence that the quasar host galaxy has been involved in an interaction or merger with another galaxy. The scheme used to classify the tidal features is based on that first used by Heckman et al. (1986) and is identical to that of RA11 and RA12. Summarising the different features, a tail (T) is a long, thin, usually radial structure (e.g. J2358-00 shown in Figure 3.1(d)), whilst a fan (F) is shorter and broader than a tail (e.g. J0923+01 shown in Figure 3.1(a)). A shell (S) is a curved feature that is tangential to the main body of the galaxy (e.g. J0848+01 shown in Figure 3.1(e)) and an amorphous halo (A) indicates an asymmetric halo with no definitive structure (e.g. J0123+00 and J0227+01 shown in Figures 3.1(c) and 3.1(e)). Bridges (B) extend between two galaxies linking them in tidal interactions and can extend over large distances (e.g. J2358-00 in Figure 3.1(d)). Irregular (I) features do not fit into any of the above categories and can include features such as knots (e.g. J0217-00 in Figure 3.1(b)). Double nuclei (2N) are those objects that have two brightness peaks within a projected separation of 10 kpc (e.g. J0332-00 in Figure 3.1(c)).

Simulations have shown that the presence of all these features can be attributed to the host galaxy being involved in some kind of tidal encounter with another. This can take the form of mergers, both major and minor, or gravitational interactions that will not necessarily result in the coalescence of the two objects involved (Quinn 1984; Hernquist & Spergel 1992; Cattaneo et al. 2005; Lotz et al. 2008; Feldmann et al. 2008).

The detection of the features was made by eye, independently by three different people, and the results of each individual were then compared to confirm the detection of these features. This was necessary as, in the case of fainter features, detection and classification can be subjective. In all cases it was found that all three classifiers agreed on the presence or absence of tidal features. However, it was not always the case that all three agreed on the detailed classification of the feature (e.g. fan or shell). In such cases, the author of this thesis determined the final classification.

One of the main aims of this study is to compare the results obtained for type II quasars with those of the control sample of intermediate redshift, early-type galaxies presented in RA12 and the PRG of RA11. Therefore, in order that results be directly comparable, the surface brightnesses of the detected features of the type II quasar host galaxies have been measured in an identical manner to that applied in the latter study. The average number of counts for each feature were first calculated by taking several measurements using small apertures, the size of which was dependent on the extent of the feature. Using the same aperture, exactly the same process was repeated in several regions local to the feature in order to subtract the contribution from the sky and the diffuse light from the galaxy. Because the results obtained from this technique are somewhat dependent on the exact placement of the apertures, the reliability of the technique was tested by two people making independent measurements of the same features for a number of the quiescent early types of RA12. In these cases, the difference in the surface brightness obtained was below 0.1 mag. The results were then corrected for Galactic extinction, $(1+z)^4$ surface brightness dimming and then k-corrections were applied. The derived values of surface brightness are given in Table 3.1. The purpose of measuring the surface brightness of the features is to determine the nature of the merger. For example, simulations show that morphological signatures produced in gas rich interactions are brighter than those produced in gas poor ones (Naab et al. 2006; Bell et al. 2006; McIntosh et al. 2008).

Once the initial classification was made, three separate enhancement techniques were applied to the images, using the Interactive Development Language (IDL), for the purposes of confirming the features detected in the original images, and detecting fainter features that were not evident in the unprocessed images. Note however, the detection and classification of the tidal features listed in Table 3.1 is based purely on the unenhanced images. The three techniques employed were unsharp masking, image filtering and smoothed galaxy subtraction. Full details of how these techniques were applied can be found in RA11.

3.3 Notes on Individual Objects & Type II Quasar Images.

In order to improve the presentation of the images, all three image enhancement techniques mentioned in Section 3.2 have been applied to the Gemini GMOS-S images. Figure 3.1 shows the best resulting image for each object. Each main image is 35×35 arcsec and the inserts are to the same scale. The captions for the sub-figures give details of the enhancement technique, if any, used in each case. The scale adopted for the image stretching is also given for each object, and the key is given in the main caption for the figure.

3.3.1 J0025-10

In Figure 3.1(a), the Gemini GMOS-S image shows that this system is clearly interacting, since it has a double nucleus, which can be seen more clearly in the insert, with a projected separation of 4.5 kpc. The north eastern nucleus is the quasar host. The galaxy also has two distinct tails, with the shorter, brighter tail pointing towards the north east and a longer tail pointing towards the south east.

3.3.2 J0114+00

The deep Gemini GMOS-S image of this object, displayed in Figure 3.1(b), shows that this system has a second fainter nucleus to the north west at a projected separation of 8.0 kpc, which can be seen more clearly in the insert. There is also a shell extending to the south east with a surface brightness of $\mu_r^{corr} \simeq 23.1$ mag arcsec^{-2}.

3.3.3 J0123+00

The deep image, displayed in Figure 3.1(c), clearly reveals that this quasar host galaxy is involved in an interaction. It can be seen that there is a secondary nucleus at a projected separation of 7.6 kpc from the centre of the host galaxy. However, on the basis of the long-slit spectroscopy published in Villar-Martín et al. (2010), it is likely that this feature is dominated by strong [OIII] line emission. There is also a tidal tail/bridge feature extending to the east with a surface brightness $\mu_r^{corr} \simeq 24.7$ mag arcsec^{-2} to a distance of 62 kpc from the centre of the host galaxy. Villar-Martín et al. (2010) also detect this extended feature in their narrow-band image centred on [OIII] λ5007, demonstrating that it leads to a companion galaxy at the same redshift as J0123+00,

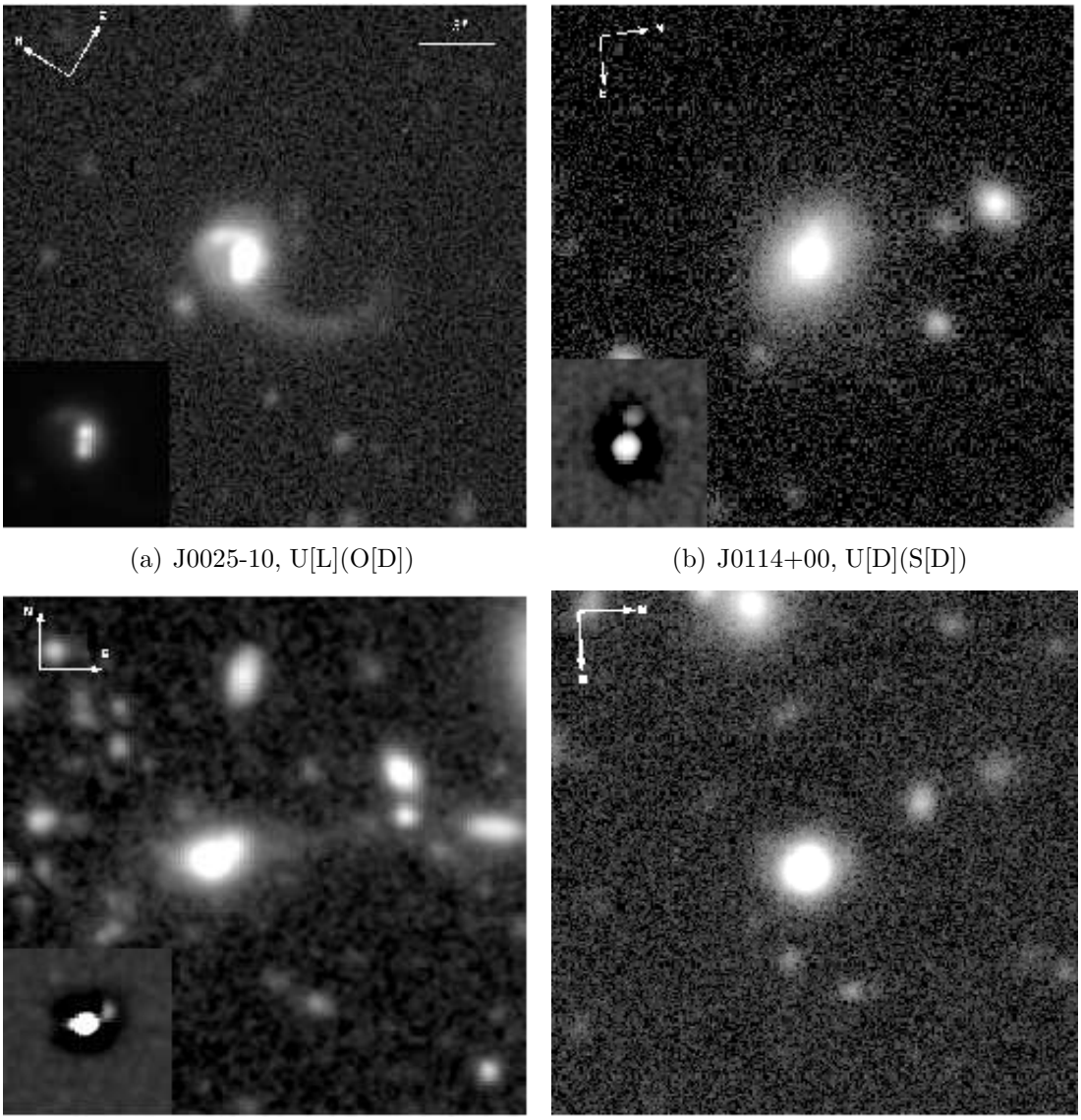

(a) J0025-10, U[L](O[D])

(b) J0114+00, U[D](S[D])

(c) J0123+00, M[L](S[D])

(d) J0142+14, O[L]

Figure 3.1: Gemini GMOS-S images of all 20 type II quasar host galaxies in this sample. All the images are 35 × 35 arcsec, and the first image on each page shows the scale bar. All insert images are also to the same scale. The image processing technique used, if any, is given by the code beneath the image along with its abbreviated name. O: Original, unprocessed image, U: Unsharp mask, M: Median Filtered and S: Smoothed galaxy subtracted. For those images that include inserts, the code is given in brackets. The scale used for the image stretching is given in square brackets, L: log scale and D: default linear scale. The reader is advised that the images are best viewed on a computer screen.

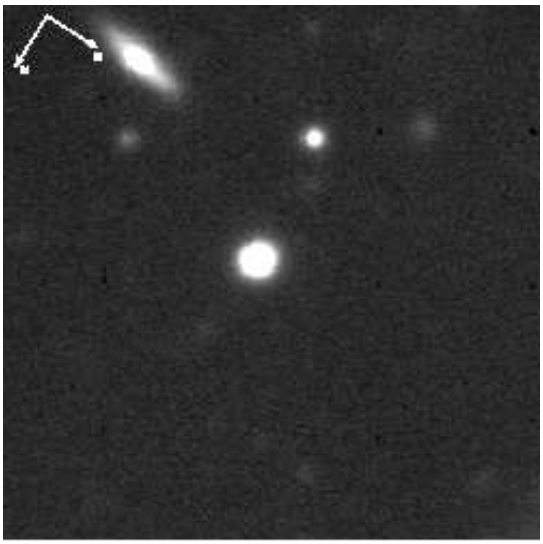

(a) J0159+14, O[L]

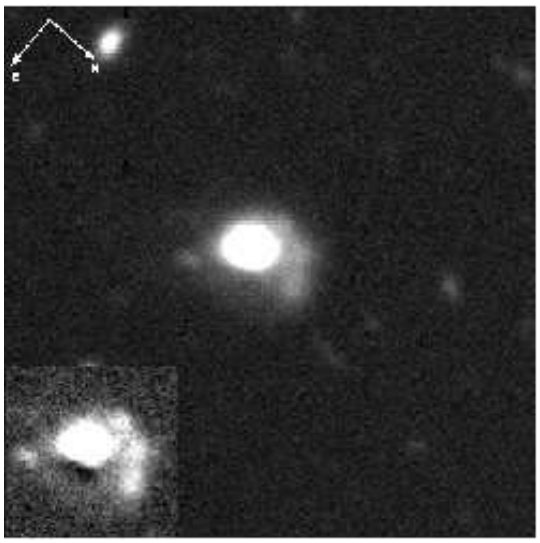

(b) J0217-00, O[L](U[L])

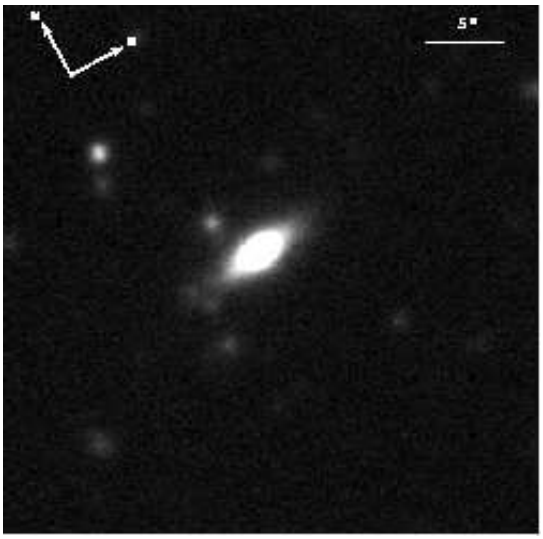

(c) J0217-01, O[D]

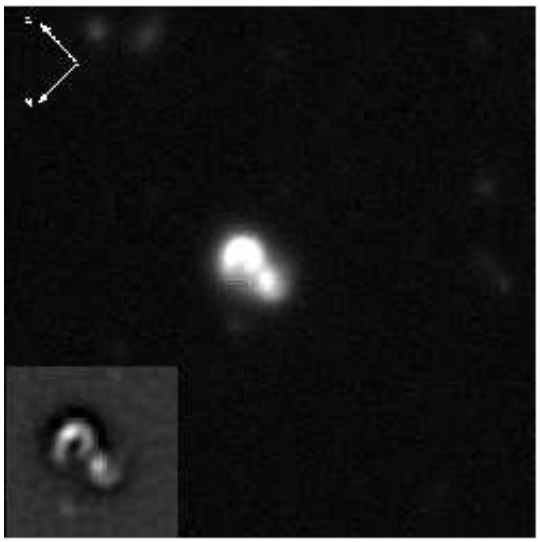

(d) J0218-00, O[D](M[D])

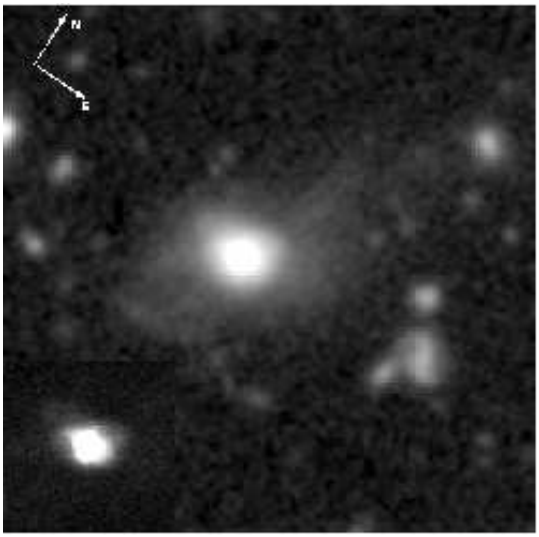

(e) J0227+01, M[D](U[D])

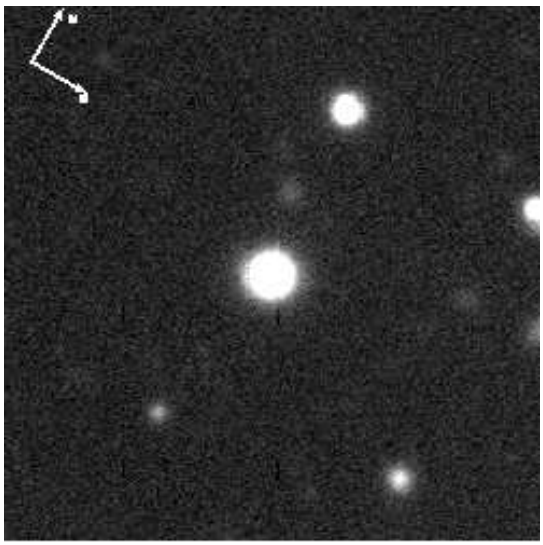

(f) J0234-07, O[L]

Figure 3.1: [continued]

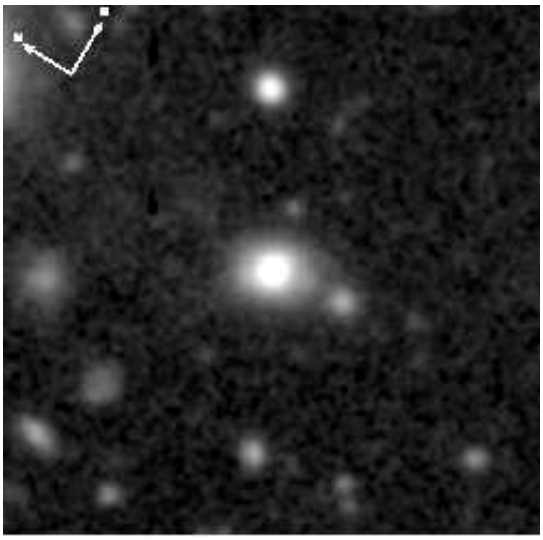

(a) J0249+00, M[L]

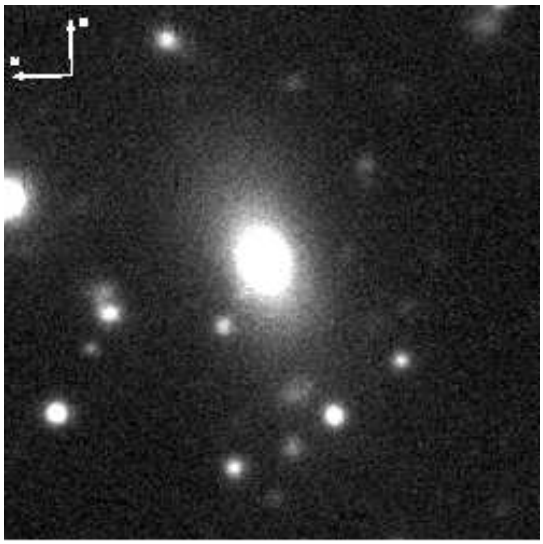

(b) J0320+00, O[L]

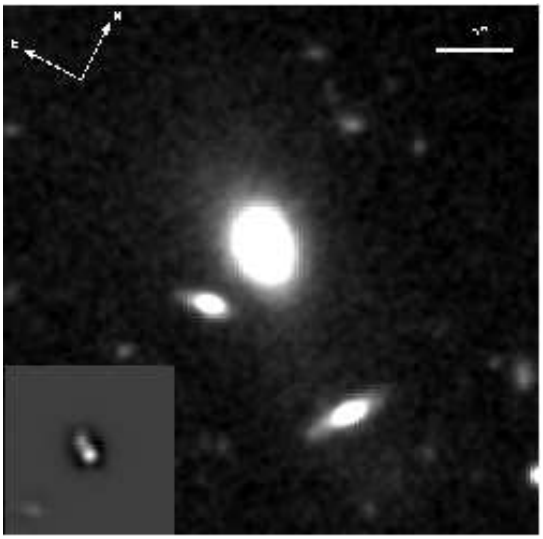

(c) J0332-00, M[L](S[D])

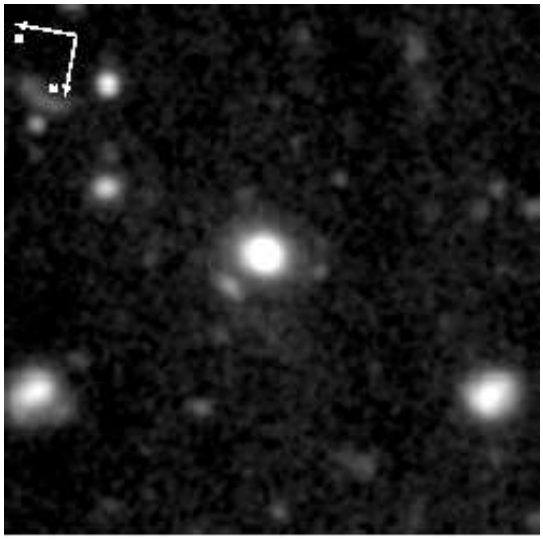

(d) J0334+00, M[L]

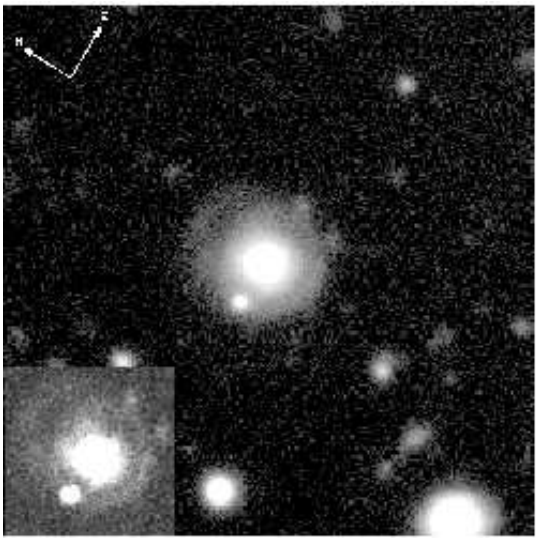

(e) J0848+01, O[L](U[L])

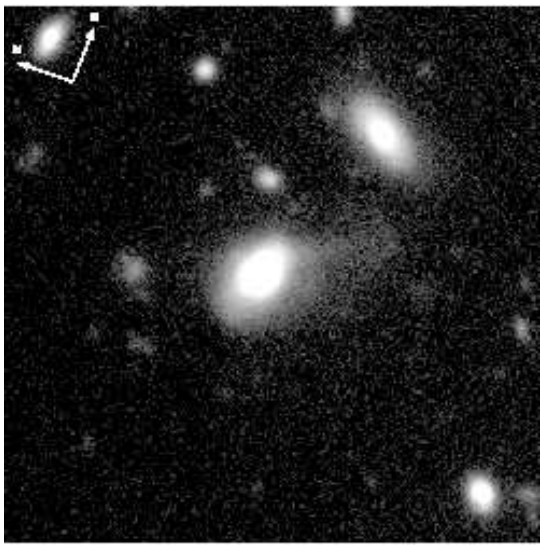

(f) J0904-00, O[L]

Figure 3.1: [continued]

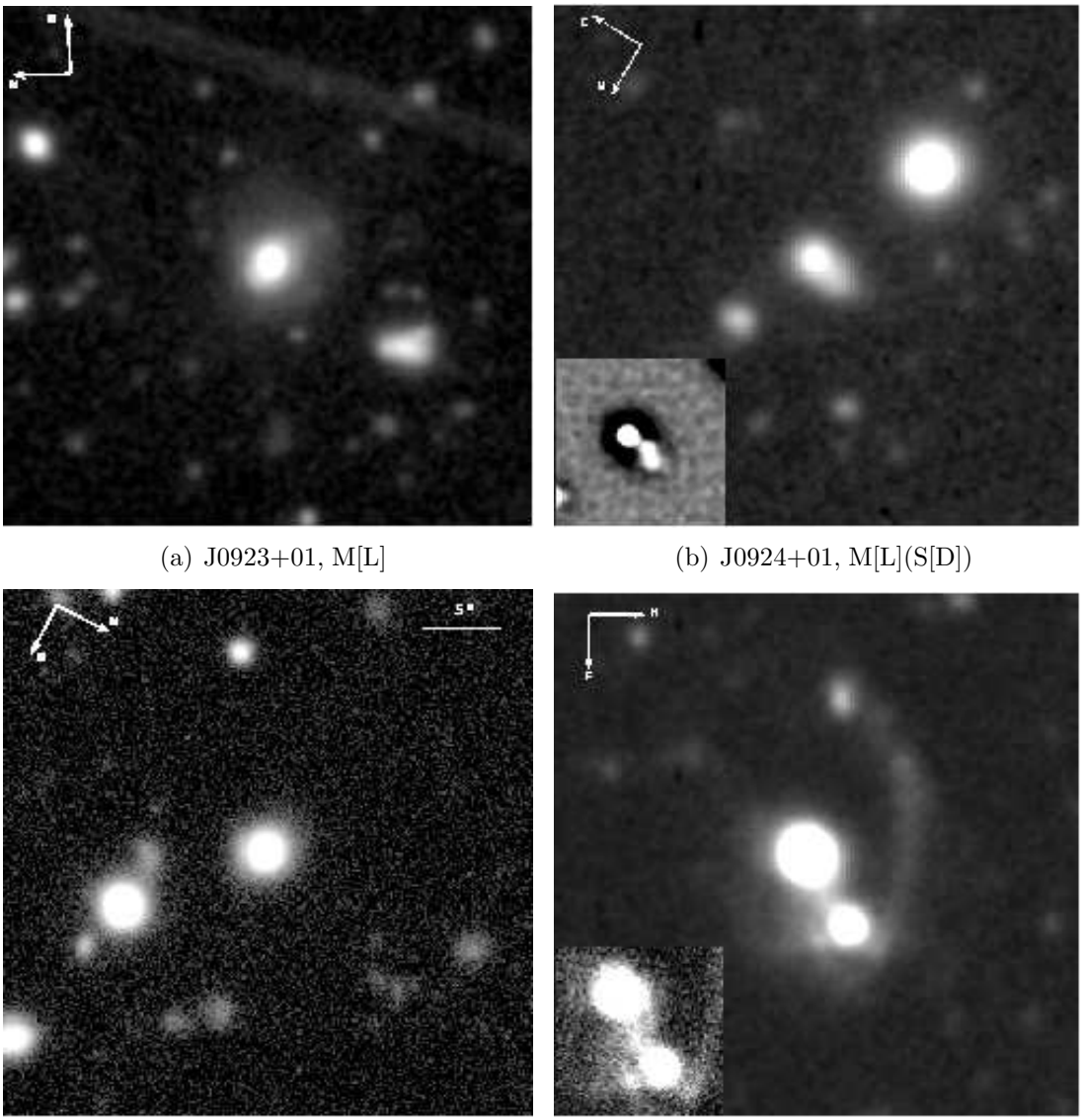

(a) J0923+01, M[L]

(b) J0924+01, M[L](S[D])

(c) J0948+00, O[L]

(d) J2358-00, M[D](U[D])

Figure 3.1: [continued]

and 100 kpc from its nucleus. In this object it is possible that all the extended tidal features are emission-line rather than continuum dominated.

3.3.4 J0142+14

The deep Gemini GMOS-S image of this object, presented in Figure 3.1(d), shows that this quasar is hosted by a compact galaxy with no signs of morphological disturbance attributable to interactions or merger activity.

3.3.5 J0159+14

Figure 3.1(a) shows the deep Gemini GMOS-S image of this object, which does not reveal any clear evidence of an interaction or merger event, suggesting that the quasar is hosted by a compact galaxy. However, the median filtered image does show some evidence for a low surface brightness tail/bridge feature linking J0159+14 to a faint companion galaxy 27 kpc to the north. Note however that as this feature was not detected in the unprocessed image, it is not include it in the classification.

3.3.6 J0217-00

This object is amongst the most spectacular in the sample, with clear signs of morphological disturbance indicating a merger or interaction (Figure 3.1(b)). In the north west there is a tidal tail which appears to comprise of three knots, with a measured surface brightness of $\mu_r^{corr} \simeq 22.1$ mag arcsec^{-2}. The long-slit VLT spectroscopy of Villar-Martín et al. (2011) along PA116 shows that this is a continuum emitting feature. There is also an irregular feature in the south-east, with a surface brightness of $\mu_r^{corr} \simeq 22.6$ mag arcsec^{-2}, that also seems to take the form of a knot. Villar-Martín et al. (2011) confirm that this knot is at the same redshift as the galaxy and is quite probably a knot of star formation. The faintest feature is the shell on the north-east side which has a surface brightness of $\mu_r^{corr} \simeq 23.7$ mag arcsec^{-2}.

3.3.7 J0217-01

It can be seen from the image presented in Figure 3.1(c) that the quasar appears to reside in an undisturbed disc galaxy. No signs of interactions or mergers are detected, apart from what may be some faint companion galaxies at the western end of the disc. It appears that the galaxy is viewed close to edge-on.

3.3.8 J0218-00

Figure 3.1(d) clearly shows that this quasar host galaxy is one of the most tidally disturbed in the sample, with a shape reminiscent of a question mark. The quasar is hosted by the larger eastern galaxy of the pair, which has a projected separation of 12 kpc, and appears to be stretched and curled around itself. This arc-like tidal feature is the brightest in the sample with a mean surface brightness of $\mu_r^{corr} \simeq 20.6$ mag arcsec^{-2} There is also an irregular feature in the north west with a surface brightness $\mu_r^{corr} \simeq$

22.6 mag arcsec^{-2}. The Gemini long-slit spectrum of this object (PA171) passes through the eastern AGN and associated arc feature, which is found to be continuum- rather than emission-line dominated.

3.3.9 J0227+01

This quasar host galaxy, shown in Figure 3.1(e), has a highly distorted appearance, with an amorphous halo and two overlapping shells, one in the east and the other in the south. The halo is the brightest feature and extends to 30 kpc from the centre of the galaxy, with surface brightness $\mu_r^{corr} \simeq 22.4$ mag arcsec^{-2}. The southern shell has surface brightness $\mu_r^{corr} \simeq 24.1$ mag arcsec^{-2} and the eastern $\mu_r^{corr} \simeq 24.4$ mag arcsec^{-2}. There is also a tail pointing towards the north to a projected distance of 55 kpc with a surface brightness $\mu_r^{corr} \simeq 24.6$ mag arcsec^{-2}.

3.3.10 J0234-07

This quasar appears to be hosted by a compact galaxy. The deep Gemini GMOS-S image, (Figure 3.1(f)), shows no signs of morphological disturbance that could be attributed to an interaction or merger.

3.3.11 J0249+00

The deep GMOS-S image (Figure 3.1(a)) of this object shows a shell to the south of the host galaxy with surface brightness $\mu_r^{corr} \simeq 23.1$ mag arcsec^{-2}, that extends in the direction of a companion object. The companion is also to the south, with a projected separation of 28 kpc, and the two galaxies are linked by a faint tidal bridge of $\mu_r^{corr} \simeq$ 24.0 mag arcsec^{-2}. The Gemini long-slit spectrum (PA0) cuts through both the southern arc and the edge of the companion galaxy, but shows no strong [OIII] emission associated with either of these features, which are likely to be continuum-dominated.

3.3.12 J0320+00

This quasar host galaxy, shown in Figure 3.1(b), has an extended asymmetric halo in the north east/south west direction, with mean surface brightness $\mu_r^{corr} \simeq 23.5$ mag arcsec^{-2}. It is not possible to define any clear structure within the halo itself, although there is a hint of a shell to the north east. This latter feature appears more prominent in the enhanced images, although it is not used for the purposes of classification. There is no

evidence that the brighter knot in the north west, which appears to be within the halo, is associated with the galaxy.

3.3.13 J0332-00

Figure 3.1(c) clearly shows that this object has a double nucleus, with the quasar hosted by the western nucleus, and the second at a projected separation of 4 kpc to the east. There is a shell to the south west and also a fan in the north east direction that have surface brightnesses of $\mu_r^{corr} \simeq 22.3$ mag arcsec^{-2} and $\mu_r^{corr} \simeq 24.2$ mag arcsec^{-2} respectively, as well as what may be a diffuse tidal tail/bridge that extends in the direction of a disc galaxy in the south west, which is at a projected separation of 53 kpc. However, the latter galaxy does not appear to be tidally distorted, and there is no evidence that it is at the same redshift as J0332-00. The Gemini long-slit spectrum (PA32), centred on the western nucleus, cuts through the shell to the south west as well as edge of the fainter nucleus to the east, but neither of these structures shows strong emission lines, suggesting that they are dominated by continuum emission.

3.3.14 J0334+00

The deep image of this object (Figure 3.1(d)), reveals a faint shell to the west of the host galaxy with $\mu_r^{corr} \simeq 24.1$ mag arcsec^{-2}. There is also an object at a projected separation of 18 kpc to the north east, but because there is no obvious sign of co-aligned tidal features or a bridge, it is not considered to be a companion.

3.3.15 J0848+01

The Gemini GMOS-S image of this object, shown in Figure 3.1(e), reveals two clear shells, the brighter in the north with $\mu_r^{corr} \simeq 23.2$ mag arcsec^{-2} and the slightly dimmer in the south east with $\mu_r^{corr} \simeq 23.5$ mag arcsec^{-2}. There is also a smaller object to the west at a projected separation of 14 kpc, but there is no independent evidence that this is associated with the host galaxy. The Gemini long-slit spectrum (PA174) shows no strong [OIII] emission associated with the northern shell, which is dominated by continuum emission.

3.3.16 J0904-00

This object, shown in Figure 3.1(f), has a tail in the south east direction, extending from the centre of the galaxy to a distance of 45 kpc. This tail becomes more diffuse along its length, and has a kink at its end pointing towards the east. The mean surface brightness taken along the entire length of the feature is $\mu_r^{corr} \simeq 23.2$ mag arcsec^{-2}. There is also a shell that appears to start at the base of the tail and wraps ∼180 degrees around the galaxy. At its brightest, to the north west of the galaxy, this shell feature has a surface brightness of $\mu_r^{corr} \simeq 22.2$ mag arcsec^{-2}. The Gemini long-slit spectrum (PA280) shows no strong [OIII] emission specifically associated with the latter feature, which is likely to be continuum dominated.

3.3.17 J0923+01

The Gemini GMOS-S image (Figure 3.1(a)) shows that this is a morphologically disturbed host galaxy with a tail/fan feature to the south east that terminates in a shell ($\mu_r^{corr} \simeq 24.0$ mag arcsec^{-2}) 27 kpc from the nucleus. There is also a shell feature to the south west of the nucleus with surface brightness $\mu_r^{corr} \simeq 23.4$ mag arcsec^{-2}. The Gemini long-slit spectrum (PA0) shows no strong [OIII] emission associated with the latter feature, which is likely to be continuum dominated.

3.3.18 J0924+01

The image of this host galaxy (Figure 3.1(b)), has a prominent tidal tail pointing south to a projected distance of 17 kpc, with a surface brightness $\mu_r^{corr} \simeq 21.6$ mag arcsec^{-2}. Interestingly, the median filtered-image shown in Figure 3.1(b), reveals a faint bridge connecting J0924+01 to a companion galaxy 34 kpc to the north, which itself has a tidal tail that points away from the quasar host. However, since the latter features are not visible in the unenhanced image, they have not been included in the morphological classification presented in Table 3.1.

3.3.19 J0948+00

Figure 3.1(c) shows that the deep Gemini GMOS-S image of this object does not reveal any indication of morphological disturbance in the host galaxy of this type II quasar. It appears to be an undisturbed elliptical galaxy.

3.3.20 J2358-00

The image of this system (Figure 3.1(d)) reveals what is, without a doubt, the most spectacular quasar host galaxy in the sample. This image shows clear evidence of an interaction, possibly leading to a merger, with the two galaxies at a projected separation of 30 kpc. The quasar is hosted by the western galaxy in the pair and the two galaxies are linked by a bridge with a measured surface brightness of $\mu_r^{corr} \simeq 22.7$ mag arcsec^{-2}, which can be seen more clearly in the insert. There is a long tidal tail extending from the companion to a projected distance of 80 kpc in the north west with a measured surface brightness of $\mu_r^{corr} \simeq 23.3$ mag arcsec^{-2}, and also a fan in the south with surface brightness $\mu_r^{corr} \simeq 23.4$ mag arcsec^{-2}. These features are also detected in *HST* images presented by Zakamska et al. (2006), which show more detail within the main structures.

VLT long-slit spectroscopy by Villar-Martín et al. (2011) along PA60 and PA83, shows that the companion galaxy and tidal bridge are dominated by continuum emission. Moreover, the Gemini long-slit spectrum (PA331) shows no significant [OIII] emission where the slit intercepts the tidal tail to the north west of the quasar host galaxy.

3.4 Results

In this thesis, the example of RA11 and references therein have been used to classify the detected features. Table 3.1 gives the full classification of all the host galaxies.

The main result of this study is that, of the 20 type II quasar host galaxies in this sample, fifteen ($75 \pm 20\%$) show clear evidence of morphological disturbance at relatively high levels of surface brightness, $\tilde{\mu}_r^{corr} = 23.37$ mag arcsec^{-2} with a range $\Delta\mu_r^{corr} \simeq [20.64,\ 24.65]$ mag arcsec^{-2}.

Following the example of RA11, the galaxies have been grouped by morphology (Tables 3.1 & 3.2), though the scheme has been changed slightly. RA11 used five groups while here, it was found that four are sufficient, since none of the quasar host galaxies in this sample have detected dust features. The groupings are as follows.

1. Galaxies involved in tidal encounters that will not necessarily lead to mergers (B).
2. Galaxies that show evidence of morphological disturbance due to interactions or mergers such as shells, fans and amorphous halos (A,I,S,F).
3. Galaxies that have two nuclei within 10 kpc (2N).
4. Isolated galaxies that are not disturbed.

Table 3.1: Full classification of the sample objects and the surface brightness of the detected morphological features: Column 1 gives the abbreviated SDSS identifier. Columns 2 gives the surface brightness dimming (mag arcsec^{-2}) taken from the NED database. Column 3 shows the morphological classification, with the features shown in square brackets not being considered as secure detections. These features are not considered in any of the analysis and are for information only. The morphological classification are 2N: double nuclei, T: tail, S: shell, A: amorphous halo, F: fan, B: bridge, I: irregular feature. Column 4 shows the surface brightness measured from the images and column 5 shows the surface brightness corrected for Galactic extinction, surface brightness dimming and k-corrected. Finally, column 6 indicates the morphological group that each object is classified into. The groups are defined as 1) The quasar host is part of a galaxy pair involved in a clear tidal interaction. 2) Other signs of morphological disturbance such as fans, shells and tails 3) A system with multiple nuclei, i.e. those within 10 kpc of each other. 4) An isolated galaxy with no signs of any morphological disturbance.

Object	Dimming	Morphology	μ_{AB} (mag arcsec^{-2})	μ_{AB}^{corr}(mag arcsec^{-2})	Group
J0025-10	1.15	2N, 2T	22.53, 24.91	20.90, 23.28	2,3
J0114+00	1.42	2N, S	25.2	23.12	2,3
J0123+00	1.46	2N, B, [A]	26.8	24.65	2,3
J0142+14	–	–	–	–	4
J0159+14	–	[B]	–	–	4
J0217-00	1.28	T, I, F	23.91,24.41, 25.56	22.06, 22.56, 23.71	2
J0217-01	—	–	–	–	4
J0218-00	1.37	I, A, [B]	22.65, 24.66	20.64, 22.65	1,2
J0227+01	1.34	A, 2S, T	24.31,26.05, 26.33, 26.33	22.37, 24.11, 24.39, 24.63	2
J0234-07	–	–	–	–	4
J0249+00	1.48	S, B	25.40, 26.22	23.13, 23.95	1,2
J0320+00	1.41	I, [S]	25.74	23.49	2
J0332-00	1.17	2N, S, F, [B]	24.21, 26.15	22.34, 24.28	2,3
J0334+00	1.48	S	26.59	24.16	2
J0848+01	1.31	2S	25.08, 25.41	23.18, 23.51	2
J0904-00	1.32	T, S	25.08, 25.28	23.17, 23.37	2
J0923+01	1.42	S, F, [T]	25.47, 26.06	23.42, 23.99	2
J0924+01	1.41	T, [B]	23.70	21.63	2
J0948+00	–	–	–	–	4
J2358-00	1.46	B, T, F	24.84, 25.45, 25.58	22.66, 23.27, 23.40	1,2

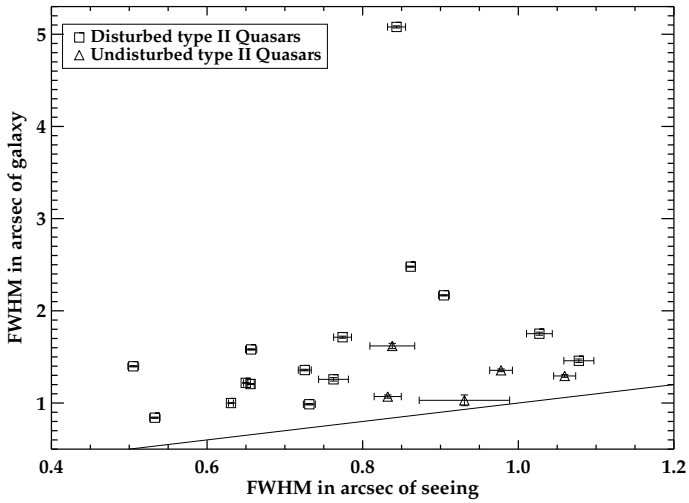

Figure 3.2: Shows the FWHM of the type II quasar host galaxies broken down into morphologically disturbed (open squares) and undisturbed (open triangles), measured assuming a Gaussian core, against the FWHM of the stars measured from the same images. The line shows the seeing of the image.

The classification of each of the host galaxies into the morphological groups is given in Table 3.1. It should be noted that the above categories are not exclusive, and a host galaxy may be classified into more than one group. It was found that for the type II sample, 7 ($35 \pm 13\%$) are in the pre-coalescence phase of a galaxy interaction and are classified in either group 1 or 3. Another 8 ($40 \pm 14\%$) are in the coalescence or post coalescence phase of a merger and are classified only into group 2. The remaining 5 ($25 \pm 11\%$) show no signs of interaction and are classified into group 4.

These findings indicate that, if an interaction/merger event is responsible for the triggering of the nuclear activity, there is no preferred phase in which it occurs. AGN activity is seen to occur both before, during and after the coalescence of the black holes, although it must be kept in mind that there may be more than one phase of quasar activity. This is in accordance with the results of RA11 (Table 3.2) for the SLRG, where they find that the radio activity is seen to occur at all phases of the interaction/merger, with roughly equal proportions categorised as pre- and post-coalescence.

Note that the 25% of objects that appear undisturbed are potentially interesting in their own right. Of these five objects, one (J0217-01, Figure 3.1(c)) is an apparently undisturbed edge on disc, while the other four (J0142+14 Figure 3.1(d), J0159+14 Figure 3.1(a), J0234-07 Figure 3.1(f) and J0948+00 Figure 3.1(c)) appear to be spatially compact objects. In order to determine if there is any real difference between the host galaxies of the disturbed majority and these four undisturbed quasars, other than the

Morphology	Group	Type II Quasars	SLRG	Comparison	Comparison + discs	EGS Sample
Pre-coalescence	1, 3	35%	50%	28%	20%	21%
Coalescence or post-coalescence	2	40%	45%	39%	29%	33%
No sign of interaction	4	25%	5%	33%	51%	46%
Any sign of disturbance	1,2,3	$75 \pm 20\%$	$95^{+5}_{-21}\%$	$67 \pm 14\%$	$49 \pm 10\%$	$54 \pm 7\%$

Table 3.2: A morphological classification of the galaxies in the type II quasar sample, the PRG at $z > 0.2$ of RA11, and quiescent galaxies of the $0.3 < z < 0.41$ EGS comparison sample, the comparison sample including discs and the full EGS sample of RA12 in the same absolute magnitude range as the type II host galaxies(104 galaxies). The galaxies are grouped by morphology with groups 1 & 3 being pre-coalescence systems, group 2 being coalescing or post-coalescence systems and group 4 being non interacting systems. Column 1 & 2 give the morphology and the group respectively. Columns 3, 4 & 5 give the percentage of the sample of type II quasars, SLRG and quiescent galaxies that are classified in each group. Please note that if a galaxy is classified in group 2 but is also in groups 1 or 3, it is considered to be a pre-coalescence system.

lack of tidal features, 2-D Gaussian fits have been used to determine the FWHM of the cores of the type II quasar images, which were then compared with values for foreground stars in the same image. Figure 3.2 shows the results of the analysis, with the black line marking the seeing and the type II sample broken down into disturbed and undisturbed host galaxies. As can be seen from Figure 3.2, the four undisturbed galaxies have a FWHM close to the seeing of the images, demonstrating that they are barely resolved. However, because these are the images with some of the worst seeing, it may not be possible to detect faint tidal features on larger scales if they are present.

3.5 Discussion

3.5.1 Comparison with quiescent early-type sample

In this section the results obtained in this thesis are compared with those found for a comparison sample of quiescent galaxies taken from deep Subaru images of the Extended Groth Strip (EGS). The full criteria used to select objects as suitable for the full control sample are given in RA12, who made use of the *Rainbow Cosmological Surveys database*[1],

[1] https://rainbowx.fis.ucm.es/Rainbow_Database

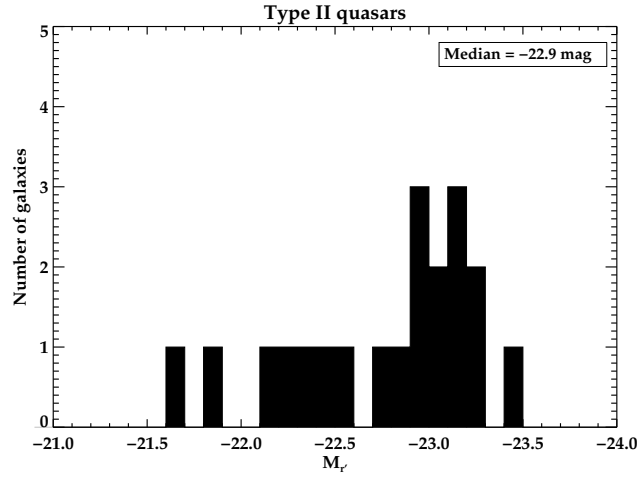

(a)

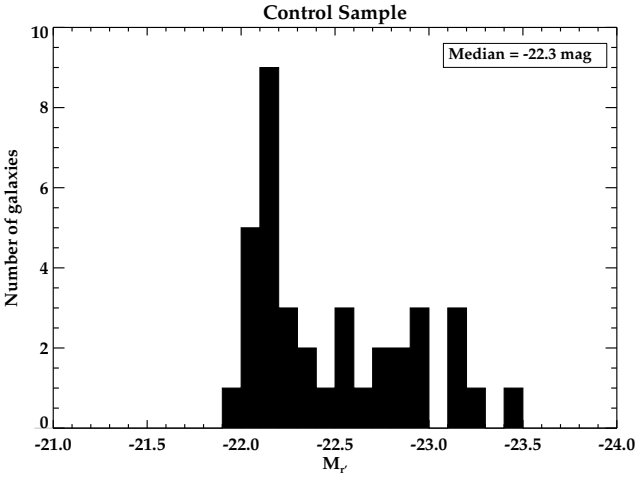

(b)

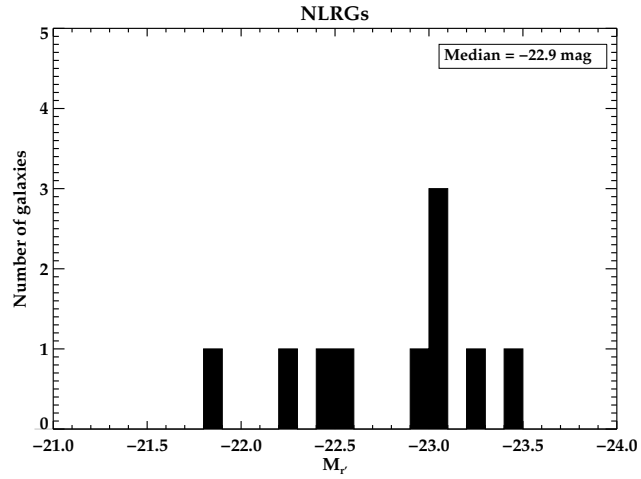

(c)

Figure 3.3: The distribution of the absolute magnitudes of (a) the type II quasar host galaxies, (b) the $0.3 < z < 0.41$ part of the EGS comparison sample and (c) the $0.2 < z < 0.7$ 2Jy NLRG. The median value of $M_{r'}$ is given for the portion of sample used for the comparison in each panel.

which includes a compilation of photometric and spectroscopic data, along with value-added products such a photometric redshifts, stellar masses, star formation rates, and synthetic rest-frame magnitudes for several deep cosmological fields (Pérez-González et al. 2008; Barro et al. 2009, 2011). To summarise, galaxies were first selected by colour to isolate those that are on the 'red sequence' using the colour selection criterion (M_u-M_g) > 1.5 (Blanton, 2006). They were then further selected to be early-types, which involved visual inspection of the images to determine whether the galaxies were discs or ellipticals. The galaxies that were considered to be definite discs were disregarded, and those that were classified as possible discs were maintained. The reason for making this distinction is that the vast majority of PRG, which the full control sample was selected to match, are associated with elliptical galaxies. The full EGS control sample was also selected to have the same host luminosity and redshift range as the $0.2 < z < 0.7$ portion of the 2Jy sample. The Subaru images were considered to be suitable because they have similar filter, depth and resolution to the Gemini GMOS-S images of RA11.

The 2Jy sample extends over a greater redshift range than the type II quasars studied here, and this is reflected in the redshift range of the EGS quiescent galaxies. Therefore, for comparison with the type II quasar host galaxies, it was decided to use only the galaxies from the parent EGS sample that are in the redshift range $0.3 < z < 0.41$, to reflect the distribution of the sample studied here. This leaves a comparison sample of 36 quiescent galaxies, classified as either ellipticals or possible discs, within the same absolute magnitude (Figures 3.3(a) & 3.3(b)) and redshift range (Figure 3.4) as the type II quasars.

The results of the morphological analysis of the $0.3 < z < 0.41$ EGS comparison sample are presented in Table 3.2. These show that there is no statistically significant difference in the rate of disturbance detected in the type II quasars and the comparison sample, with $75 \pm 20\%$ of the type II quasars and $67 \pm 14\%$ of the comparison sample showing evidence of tidal features. If only features in the comparison sample that fall within the same range of surface brightness as the type II quasars are considered, the proportion of tidally disturbed early-type galaxies in the comparison sample falls to $50 \pm 6\%$. When considering the classification of the galaxies into the different morphological groups, no significant difference between the type II quasars and comparison sample was found (see Table 3.2).

The values for the surface brightnesses of the detected features of the comparison sample are taken from RA12 and are summarised in Table 3.3 and Figure 3.5(b), converted to r' magnitudes using colours for elliptical galaxies taken from Fukugita et al. (1995). It

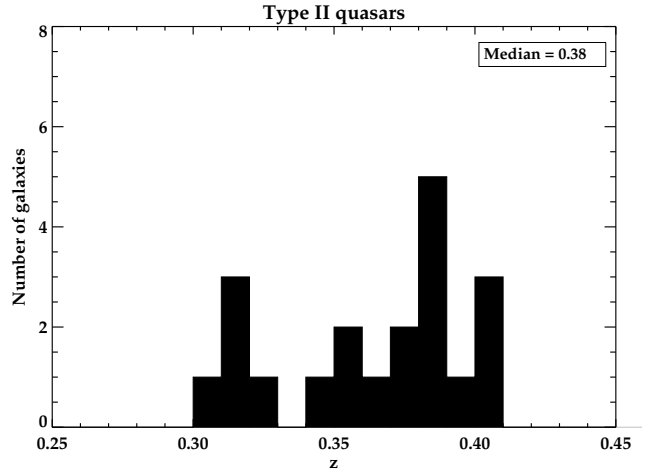

(a)

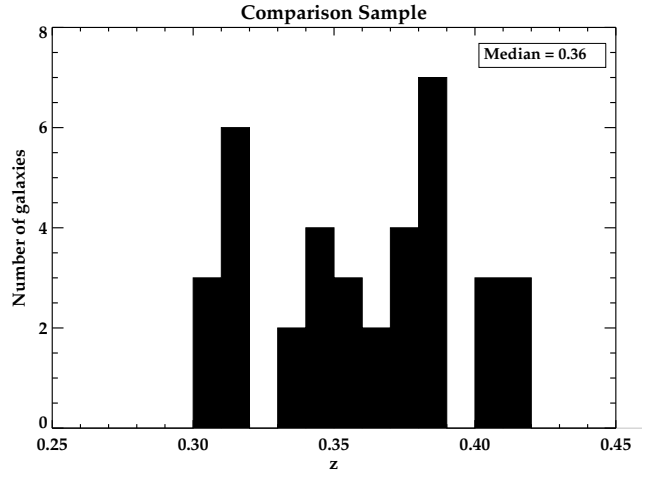

(b)

Figure 3.4: A comparison of the redshift distribution of (a) the type II quasars and (b) the comparison sample. The median redshift for each sample is shown in the appropriate panel. A K-S test returns the probability P=0.643 that the redshift distribution is drawn from the same parent population.

can be seen that, the median value of surface brightness for the features in the comparison sample is almost a magnitude fainter than the type II sample ($\tilde{\mu}_r^{corr} = 24.3$ mag arcsec^{-2} compared with $\tilde{\mu}_r^{corr} = 23.4$ mag arcsec^{-2} for the type II quasars), the range of surface brightness also extends to fainter values than the type II quasars, with the comparison sample having a range $\Delta\mu_r \simeq [22.11, 26.06]$ mag arcsec^{-2}. Therefore, the features detected in the type II quasars are up to 2 magnitudes brighter than those detected in the comparison sample. The distribution of the surface brightnesses in these two samples can be compared by performing a Kolmogorov-Smirnov (K-S) test. This returns a prob-

ability P=0.002 that the two distributions are drawn from the same parent population, which is significant at the 99.8 % ($> 3\sigma$) level, strongly indicating that the two samples are drawn from different populations. Figure 3.5 clearly demonstrates this difference between distributions, with Figure 3.5(b) shifted towards fainter magnitudes in relation to Figures 3.5(a) and 3.5(c).

The criteria that the control sample should be made up of early-type, red galaxies was thought to be suitable for comparison with the type II quasars because some previous studies (e.g. Dunlop et al. 2003) have found that these types of galaxies are typical of quasar hosts. However, another possible approach is to match the control sample and the type II quasars in colour space. This, in effect, is an approximate means of matching the star formation rates between the quasar host galaxies and quiescent control sample. Adjusting the selection criteria to account for star formation rate has the potential to effect the result found here, because some studies of lower luminosity AGN have found that, when star-formation rate is taken into account, the host galaxies of AGN and quiescent galaxies become indistinguishable (Li et al., 2008; Reichard et al., 2009).

Including the discs

A possible weakness of the comparison made in the previous section is that only ellipticals and possible discs have been included in the EGS comparison sample. While such a comparison sample selection is appropriate for PRG, which are almost invariably associated with giant elliptical galaxies, it is not clear whether it is so appropriate for luminous radio-quiet AGN, because some (albeit a low fraction) of the latter are known to be hosted by disc galaxies (Dunlop et al. 2003; Greene et al. 2009). Indeed one of the type II quasar objects discussed in this thesis (J0217-01) is a clear disc galaxy. Therefore, the comparison of the previous section is repeated, but reinstating the quiescent galaxies that were rejected from the EGS control sample of RA12 because they were visually classified by the authors as discs. This leads to the inclusion of an extra 15 quiescent galaxies with $0.3 < z < 0.41$ and absolute magnitudes in the same range as the type II quasar host galaxies, bringing the total sample to 51 quiescent galaxies. Visual inspection suggests that the vast majority of the discs are early-type (S0) and therefore all magnitudes have been converted to r' using colours for S0 galaxies from Fukugita et al. (1995).

Of these 15 galaxies, only one displays any sign of morphological disturbance, which is in the form of a fan. This galaxy was therefore classified into group 2 and the remaining 14 into group 4. When including the discs, it was found that $49 \pm 10\%$ of the full sample

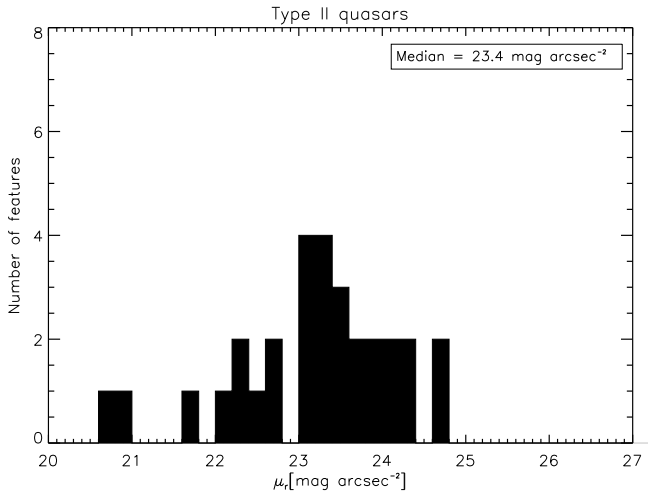

(a)

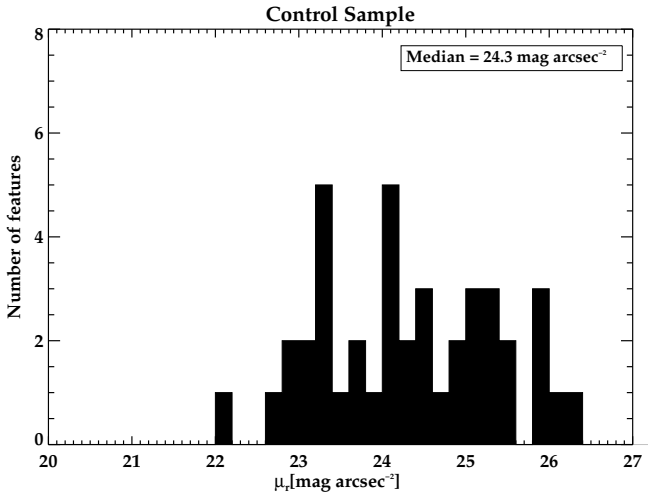

(b)

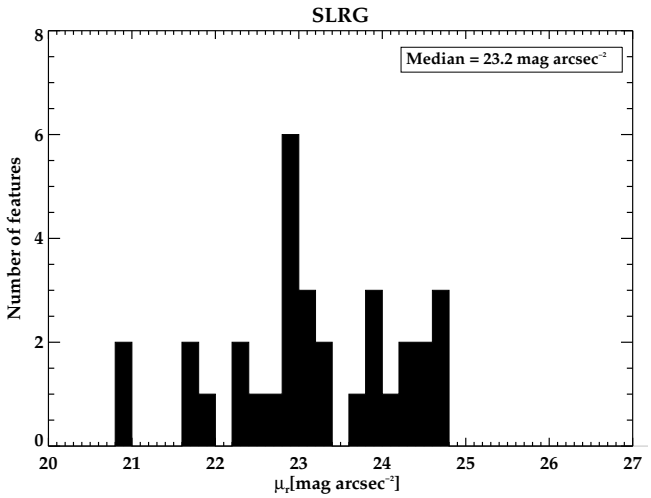

(c)

Figure 3.5: A comparison of the distribution of the surface brightness of the detected features in the r' band of (a) the type II quasar sample, (b) the comparison sample of quiescent early type galaxies, and (c) the $0.2 < z < 0.7$ 2Jy SLRG. The median value of $\mu_{r'}$ (mag arcsec^{-2}) is given in each panel for that sample.

of 51 show evidence for morphological disturbance. Again, if only those galaxies with at least one feature as bright as the dimmest type II feature (and double nuclei) is included, this figure falls to $36 \pm 9\%$. Moreover, inclusion of the measured surface brightness of the one feature associated with the disc galaxies does not change the statistics of the distribution of the surface brightnesses for the comparison sample.

Table 3.2 shows clearly that only including quiescent galaxies that have been visually classified as early-types (Section 3.5.1) leads to a conservative comparison between the rates of disturbance found in the type II quasars and those found in the quiescent red sequence galaxies.

This is also true if the detected rates of disturbance in the type II quasars are compared with those for the 104 early-type galaxies from the complete EGS control sample that are in the same absolute magnitude range. In this case, it was found that $54 \pm 7\%$ show signs of interaction (Table 3.2), falling to $45 \pm 7\%$ if only those with a feature in the same surface brightness range as those detected in the type II quasars are considered. The median and range of surface brightnesses remains very similar (Table 3.3) to that for the comparison sample. This comparison emphasises the fact that, by considering only early-type galaxies in the same redshift range as the type II quasars, the comparison between the rates of disturbance may be a conservative one.

Surface brightnesses

The fact that, in all the quiescent samples considered here, the surface brightness of the detected features is up to 2 magnitudes fainter than in the type II quasar host galaxies could indicate that the interactions experienced by these quiescent early-type galaxies are different in nature to those being experienced by both the type II quasars and PRG. Examples of these differences may be that they are gas poor interactions rather than gas rich ones, or minor mergers instead of major ones. In such cases, the interaction would not be expected to lead to luminous AGN activity if major, gas-rich mergers are required to trigger and sustain such activity.

Alternatively, the difference in the surface brightness of the features between the two groups could be due to the fact that, for the comparison sample, the interaction events are being viewed at later stages in the merger than in the type II quasar and 2 Jy groups. Simulations (e.g. Springel et al. 2005; di Matteo et al. 2005; Hopkins et al. 2008) suggest that, if major mergers and interactions between galaxies were the triggering event for luminous AGN activity, then this would preferentially occur close to the peak of the process, around the point of coalescence of the SMBH. However, considering the

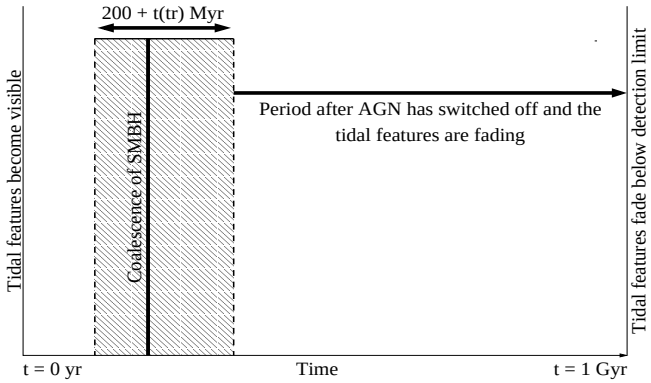

Figure 3.6: A representation of the time scales over which the morphological features will be visible in comparison to the period in which the quasar will be active. The shaded area is the period around the coalescence of the SMBH which simulations suggest is when the AGN is most likely to be triggered. The AGN is then switched off fairly early in the process of the merger and then the features gradually fade until they fall below the detection limit.

separation of the two nuclei in the pre-coalescence systems, such as J2358-00 shown if Figure 3.1(d), it is possible that the type II objects in this sample are being observed 100-200 Myr before coalescence (though it could be even earlier for J0123+00), although it is not clear how long after the coalescence they might be observed. Although there is evidence for substantial time delays in lower luminosity PRG and AGN (Wild et al., 2010; Tadhunter et al., 2011), it is not clear that this applies to high luminosity AGN, and it remains uncertain how long after the merger it is possible for quasar-like AGN activity to be triggered. If it is assumed that there is a period after the coalescence of the SMBH in which the AGN activity can be triggered (t_{tr}), then this means that there is a limited window of $\sim 200 + t_{tr}$ Myr in which the activity can occur.

Assuming that the tidal features will gradually fade over the lifetime of the interaction until they fall below detection limits, the morphological features associated with galaxies that are hosting a quasar should appear brighter at the time that the quasar is active, fading as time progresses until the AGN switches off. Figure 3.6 shows a visual representation of this scenario, with the shaded area indicating the time around the coalescence of the SMBH in which the AGN is expected to be triggered. It also shows that, for a significant proportion of the time over which the interaction signatures are visible, the system would not be be capable of hosting a quasar. It must be kept in mind that an AGN phase is a snapshot in time in the history of a galaxy and it may be that, in the comparison sample, these interaction events are being viewed at a time before AGN activity has commenced or after it has waned, leaving the fading tidal debris of a

historic, merger induced AGN.

3.5.2 Comparison with the 2Jy sample

It is also interesting to compare the results derived here for the type II quasars with those presented in RA11 for the 2 Jy sample of PRG, as it may be possible to identify any common factors between the two samples which may isolate a single triggering mechanism. To summarise the selection criteria, they required that all objects had $S_{2.7GHz} > 2.0$ Jy, steep radio spectra indices $\alpha_{2.7}^{4.8} > 0.5$ ($F_\nu \propto \nu^{-\alpha}$), declinations $\delta < +10°$ and redshifts $0.05 < z < 0.7$. For further details on the criteria used for selection and completeness, refer to Tadhunter et al. (1993, 1998) and RA11.

To allow a direct comparison between the two, only the $0.2 < z < 0.7$ portion of the 2Jy sample has been used. This gives a sub-sample of 22 PRG comprising 21 SLRG and 1 WLRG. The latter object was discounted from consideration because it has an emission line luminosity that is almost two orders of magnitude lower than the 2 Jy radio galaxies of similar redshift and radio power, and is therefore not comparable to the powerful quasars studied here. This leaves a final sub-sample of 21 SLRG at $0.2 < z < 0.7$. Note that the lower redshift limit corresponds to the redshift at which, due to the correlations between radio power, emission line luminosity and redshift, the radio galaxies have a similar lower limit to their emission line luminosity as the type II quasars in the sample.

Figure 3.7 shows the comparison of radio power for both the PRG (open squares) and type II quasars (solid symbols). The values of both L_{5GHz} and $L_{[OIII]}$ for the PRG are taken from Dicken et al. (2009) and references therein, whilst the corresponding values for the type II quasars are given in Table 2.1. Using the correlation found by Xu et al. (1999) between radio-power and emission line luminosity, the line represents the boundary between their definition of radio-loud and radio-quiet AGN. As can be seen from Figure 3.7, the majority of the type II sample can be considered to be radio-quiet, with only one object falling squarely in radio-loud territory (J0114+00) and one on the border-line between the two groups (J0848-01). This is in accordance with the Zakamska et al. (2004) findings that ∼10% of type II quasars are radio-loud.

Figure 3.7 also demonstrates that the [OIII] luminosities of the SLRG, which are indicative of the AGN luminosities, extend to higher values than those of the type II quasars. However, in this thesis, the link between *quasar* activity and the rates of interactions/mergers is under investigation, so in that respect, the real concern is that the lower limit of $L_{[OIII]}$ of the two samples should be consistent with each other and with all the objects having quasar-like luminosities. Although there are no hard and fast

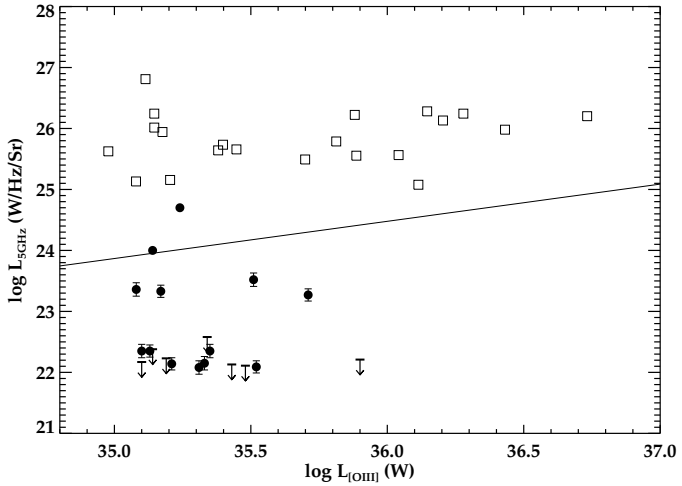

Figure 3.7: The values of L_{5GHz} (W Hz^{-1} Sr^{-1}) plotted against $L_{[OIII]}$ (W) for the full sample of type II quasars (solid symbols) and PRG from RA11 (open squares). For those type II quasars that were detected by the FIRST survey (circles), L_{5GHz} was calculated from the total integrated flux at 1.4 GHz. If the spectral index is known, this value was used for making the calculations, and no error bars are shown. In all other cases a value of $\alpha = -0.75$ was used and the error bars were derived by calculating L_{5GHz} using $\alpha = -0.5$ and $\alpha = -1$. The horizontal lines represent those objects that were undetected by either FIRST or NVSS. In these cases, the detection threshold of the survey (1.0 mJy for FIRST and 2.3 mJy for NVSS) was used as an upper limit. The squares represent the 21 SLRG used as a comparison to the type II quasars. The line represents the boundary between radio-loud and radio-quiet AGN.

Sample	Redshift Range	Median Value $\tilde{\mu}_r^{corr}$(mag arcsec^{-2})	Range $\Delta\mu_r^{corr}$(mag arcsec^{-2})
Type II	0.3, 0.41	23.37	20.90, 24.65
EGS Comparison	0.3, 0.41	24.30	22.11, 26.06
EGS Comparison incl. discs	0.3, 0.41	24.17	22.11, 26.06
EGS Complete	0.2, 0.7	23.95	22.03, 26.06
2Jy PRG	0.2, 0.7	23.18	20.94, 24.78

Table 3.3: A comparison of the surface brightnesses of the tidal features detected in the type II quasars, the EGS comparison sample, the EGS comparison sample including discs, the complete EGS sample of RA12 in the same absolute magnitude range as the type II quasar host galaxies, and the $0.2 < z < 0.7$ portion of the 2 Jy SLRG sample of RA11. Column 1 gives the sample, column 2 lists the median of the surface brightness of the features and column 3 corresponds to the range of surface brightness of the detected features. All values of surface brightness are given in the r' band and have been corrected for Galactic extinction, surface brightness dimming and have been k-corrected to the rest-frame.

rules regarding the boundary between what constitutes a Seyfert and a quasar, in this thesis, the distinction is made at $L_{[OIII]} > 10^{8.5} L_{\odot}$ W. Figure 3.7 demonstrates that all the objects studied here fulfil this criteria, except for 1 SLRG (PKS 0859-25) which has $L_{[OIII]} = 10^{8.4} L_{\odot}$. This object was maintained for the purpose of comparison, however, as it is on the borderline of the original selection criteria.

In terms of the aims of this work, which is to study the rates of interaction in *powerful quasars*, the SLRG provide a good comparison in terms of optical luminosity, as they fulfil the criteria for the lower limit to the AGN power.

In order to determine whether the host galaxies of the two types of AGN are of similar luminosity, the apparent r' band magnitudes of the samples are plotted against redshift. Figure 3.8 shows both the type II quasars (open squares) and the entire 2Jy sample split into the various optical classifications given in RA11. This was done to aid the comparison between the two, since BLRG are likely to be inherently more luminous due to the unobscured AGN contribution to their global brightness. As can be seen from Figure 3.8, if those PRG in which the central engine is directly visible are discounted (i.e BLRG), the type II quasars have similar apparent magnitudes to PRG in the same redshift range. It can clearly be seen that the inclusion of these unobscured PRG would artificially push the entire sample to brighter magnitudes, and therefore they are not included in further comparison of the luminosities of the host galaxies.

Figure 3.3(a) and 3.3(c) shows the distribution of $M_{r'}$ for the type II quasars and NLRG of the 2Jy sample. Only the 10 NLRG are used for the purposes of comparison

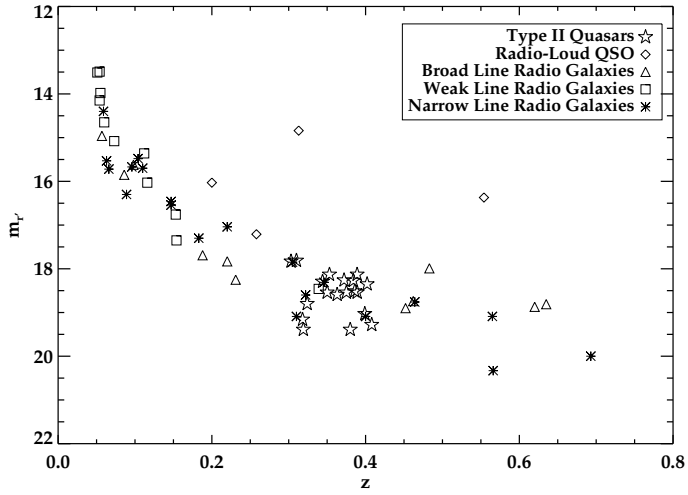

Figure 3.8: A comparison of the 30 kpc magnitude of this sample of type II quasars compared to the 30 kpc magnitude of the 2Jy radio galaxy sample of RA11. The type II quasars are shown as open stars with the PRG sample broken down into their optical classifications of radio-loud quasars (open diamonds), BLRG (open triangles), WLRG (open squares) and NLRG (asterisks). Both samples have been corrected for Galactic extinction and k-corrected.

because, in this way, it is probable that the intrinsic luminosities of the host galaxies are being compared, without needing to account for the direct quasar light as mentioned above. Carrying out a K-S test on these two populations returns a probability of P=0.275, implying that the null hypothesis that the two distributions are drawn from the same parent population cannot be rejected. The two groups have the same median $M_{r'}$ magnitude (-22.9 mag), while the range of magnitudes is $\Delta M_{r'} \simeq [-23.4, -21.6]$ mag for the type II quasars and $\Delta M_{r'} \simeq [-23.4, -21.8]$ mag for the NLRG. This demonstrates that no significant difference between the absolute magnitudes of the host galaxies of radio-loud and radio-quiet quasars was detected, which is contrary to the findings of some previous studies such as Kirhakos et al. (1999), Dunlop et al. (2003) and Hyvönen et al. (2007) who detected differences in host galaxy absolute magnitude of up to ∼1 mag.

Considering the $0.2 < z < 0.7$ 2Jy sample of RA11, the median surface brightness of the detected features in the r' band is $\tilde{\mu}_r^{corr} = 23.18$ mag arcsec^{-2} with a range $\Delta\mu_r^{corr} \simeq [20.94, 24.78]$ mag arcsec^{-2} (Table 3.3). These values of surface brightness are in the same range as those found for the type II quasar sample, with a very similar median (23.4 mag arcsec^{-2} for the type II quasars and 23.2 mag arcsec^{-2} for the 2Jy PRG). The probability returned by the K-S test when comparing the surface brightness of all the detected features of the 2Jy PRG sub-sample and the type II quasars is P =

0.517, indicating that the distribution of surface brightnesses of the detected features may be drawn from the same parent distribution. This comparison is shown in Figures 3.5(a) and 3.5(c), and the similarity in both the median value and range of surface brightness of the detected features support the hypothesis that the two types of AGN may be triggered by the same type of merger events, since the surface brightness and type of features present will be dependent on the characteristics of the progenitor galaxies and the parameters of the merger.

The proportions of the two samples classified into the different morphological groups described above were also compared. It can be seen from Table 3.2 that similar rates of disturbance were found in the two samples, with a higher proportion of the 2Jy sample of RA11 showing signs of morphological disturbance, although the small sample sizes must still be considered when making this comparison. Moreover, in both cases there is no single phase of the interaction in which the nuclear activity has been triggered. The similarities between the rates of disturbance and the range of features observed in the two samples are consistent with the idea that the two types are triggered in a similar manner.

3.5.3 The volume density of type II quasars, disturbed early-type galaxies and 2Jy PRG

The idea that all interacting early-type galaxies will, at some point in the encounter, go through a quasar phase can be tested by following the methodology of RA12. In this case, the volume density of quasars (ρ_{QSO}) is related to the volume density of morphologically disturbed ellipticals (ρ_{DE}) by the equation:

$$\frac{\rho_{QSO}}{\rho_{DE}} = 0.01 \left(\frac{t_{QSO}}{10Myr}\right) \left(\frac{t_{DE}}{1Gyr}\right)^{-1}, \tag{3.1}$$

where t_{QSO} is the typical lifetime of a quasar, and t_{DE} is the time-scale on which interaction signatures will remain visible. If it is assumed that a quasar lifetime is $\sim 10^7 - 10^8$ years (Martini & Weinberg, 2001) and that the features will remain visible above the surface brightness detection limit of the images for $\sim 10^9$ years (Lotz et al., 2008), then it is expected that quasars will make up a fraction of 0.01-0.1 of the total population of disturbed ellipticals.

A value for the volume density of type II quasars can be determined by integrating the $L_{[OIII]}$ luminosity function of Bongiorno et al. (2010) above the lower $L_{[OIII]}$ limit

of this sample, ($\log(L_{[OIII]}/L_{\odot}) = 8.50$) and assuming a redshift of $z = 0.3$[2]. This yields a result for the volume density of type II quasars of $N_{QSO2} = 2.7 \times 10^{-7}$ Mpc^{-3}. Multiplying this by the fraction of type II quasar host galaxies in the sample that show evidence of tidal disruption ($f_{DQSO2} = 0.75$), and applying the results of Reyes et al. (2008), who find a ratio of ∼1.2:1 of type II to type I quasars in this luminosity and redshift range, the total volume density of morphologically disturbed quasars in this redshift range, including both type I and type II quasars is $\sim 4.5 \times 10^{-7}$ Mpc^{-3}.

If the luminosity function for red early-type galaxies of Faber et al. (2007) is then integrated above the lowest B band luminosity ($M_B = -20.4\, mag$) of the type II quasars at $z = 0.3$, a volume density of 8.6×10^{-4} Mpc^{-3} is found. Multiplying this figure by the proportion of galaxies from the comparison sample that have morphological features above the minimum surface brightness of the type II quasar morphological features ($f_D \sim 0.62$) gives a volume density of disturbed early-type galaxies of $\rho_{DE} \sim 5.3 \times 10^{-4}$ Mpc^{-3}. Then, by comparing the latter volume density with that of quasars at similar redshifts, $\frac{\rho_{QSO}}{\rho_{DE}} = 8.5 \times 10^{-4}$ is obtained, which is at least a factor of 10 less than expected under the simple assumption that all merging galaxies go through a quasar phase. One explanation for this result is that not all disturbed early-type galaxies are capable of hosting a quasar. As mentioned before, apart from merger phase, other factors are likely to have a strong influence on the outcome of the merger and the gas flows into the nuclear region. These include whether the galaxies are gas-rich or gas-poor, the mass ratio of the two galaxies, and the masses of the black holes.

Type II quasars and 2Jy PRG

As shown in Section 3.5.2, the similarities in the rates of morphological disturbance, the mix of tidal features of the PRG and quasar II objects, and the host galaxy magnitudes support the idea that both classes are triggered in a similar way. The idea that quasars cycle through radio-loud and radio-quiet phases during a particular triggering event (e.g. Nipoti et al. 2005) can also be tested by making use of the correlation between radio power and emission line luminosity, found to exist for PRG (Baum & Heckman 1989; Tadhunter et al. 1998; Rawlings et al. 1990). This correlation can be used to ensure that only PRG of comparable optical luminosity to the type II quasars are considered, thereby allowing a comparison of the volume densities of the two classes of AGN, and thus testing the possibility that all quasars go through at least one radio-loud phase.

[2]This z is assumed rather than the median of the sample because, in order to determine the volume density of disturbed ellipticals, the work of Faber et al. (2007) is used, who provide figures for z=0.3. Therefore, to be directly comparable, this redshift was assumed for all the samples analysed here.

To determine the volume density of PRG (ρ_{PRG}), the radio luminosity function of Willott et al. (2001) was integrated above the radio luminosity limit of the 2Jy radio sample at $z > 0.2$, which is $P_{151MHz} \simeq 2.0 \times 10^{26}$ W Hz^{-1} sr^{-1}. This corresponds approximately to the same emission line luminosity as the lowest $L_{[OIII]}$ value in the type II sample[3], allowing a comparison of quasars of the same intrinsic emission line luminosity. The matching in emission line luminosity is important when comparing the space densities of the two groups, because it allows for the testing of the hypothesis that each individual quasar will cycle through both radio-loud and radio-quiet phases. This makes the implicit assumption that the quasar will maintain the same optical luminosity throughout the entire active phase. It was found that, the volume density of powerful radio galaxies at $z = 0.3$ is 7.0×10^{-9} Mpc^{-3}.

The integration of this luminosity function was also performed in RA12, however, they used a lower limit of $P_{151MHz} \simeq 1.3 \times 10^{25}$ W Hz^{-1} sr^{-1} at $z = 0.5$ and obtained a volume density of 1×10^{-6} Mpc^{-3}. Table 3.4 clearly demonstrates that the volume density of radio galaxies is highly sensitive to the lower radio power limit used. This is due to the fact that the radio luminosity function falls very steeply at the highest luminosities: an increase of a factor of 10 in the lower radio power limit leads to a decrease in the volume density by a factor of 100. Table 3.4 demonstrates this clearly by showing the volume densities derived for the different samples considered, with the different lower limits used.

Type II quasars and early-type galaxies

Using the results derived above for the volume densities of type II quasars and PRG of similar emission line luminosity, it was found that $\frac{\rho_{RG}}{\rho_{QSO}} = 0.015$ or $\sim$2%. Utilising this result, it is possible to apply time scale arguments to test whether radio-loud AGN and quasars are the same objects seen at different phases in their evolution. If it is assumed that the typical time-scale of a radio-loud phase is $\sim 10^7 - 10^8$ years (Blundell et al. 1999; Shabala et al. 2008), and that $\sim$0.7% of quasars of comparable luminosity are currently in a radio-loud phase, this would imply that the lifetime of the radio-quiet phase is $\sim 10^9 - 10^{10}$ years. However, this is much larger than the currently favoured typical lifetime of radio-quiet quasars which is thought to be $\sim 10^7 - 10^8$ years (Norman & Scoville 1988; Kauffmann & Haehnelt 2000; Martini & Weinberg 2001; Kelly et al. 2010), similar to that of PRG. Therefore, based on their relative volume densities and

[3]The lowest [OIII] emission line luminosity measured for the SLRG in the $z \geq 0.2$ 2Jy sample is $L_{[OIII]} = 9.4 \times 10^{34}$ W

Sample	Work	Lower Limit	Assumed redshift	Volume Density (Mpc^{-3})
Type II	This	$L_{[OIII]} \simeq 1.2 \times 10^{35}$ W	0.3	3×10^{-7}
PRG	RA12	$P_{151MHz} \simeq 1.3 \times 10^{25}$ W Hz^{-1} sr^{-1}	0.0	2×10^{-7}
PRG	This	$P_{151MHz} \simeq 2.0 \times 10^{26}$ W Hz^{-1} sr^{-1}	0.3	7×10^{-9}
PRG	RA12	$P_{151MHz} \simeq 1.3 \times 10^{25}$ W Hz^{-1} sr^{-1}	0.5	1×10^{-6}
Control	RA12	$M_B = -20.3$ mag	0.1	4×10^{-4}
Comparison	This	$M_B = -20.4$ mag	0.3	9×10^{-4}
Control	RA12	$M_B = -20.3$ mag	0.5	8×10^{-4}

Table 3.4: The volume density of the type II quasar sample. The volume density of both the PRG and comparison samples as derived in this work and that of RA12 are also included. Columns 1 and 2 list the sample under consideration and the work in which the volume density was derived. Column 3 corresponds to the lower luminosity limit used to derive the volume density. Column 4 gives the assumed redshift at which the volume density is derived and Column 5 gives the volume density when considering these lower luminosity limits and assumed redshifts.

estimated duty cycles, it is unlikely that most radio-quiet quasars go through a radio-loud phase during a particular quasar triggering event. This result may instead indicate that other factors, apart from accretion history, are important in determining whether an AGN is radio-loud, for example the spin of the SMBH (e.g. Baum et al. 1995; Sikora et al. 2007).

3.6 Conclusions

In this chapter the results of a morphological study of a complete sample of 20 type II quasars at intermediate redshifts ($0.3 < z < 0.41$), selected from the catalogue of candidate objects of Zakamska et al. (2003) were presented. The derived results were then compared with those obtained for a comparison sample of quiescent red galaxies (RA12) and a sample of PRG (RA11). These results were interpreted in the context of triggering quasar activity, and understanding the relationship between radio-quiet and radio-loud quasars. The main results are:

- $75 \pm 20\%$ of the complete sample of type II quasars analysed in this study show evidence of morphological disturbance at relatively high levels of surface brightness. The median value of surface brightness of the features is $\tilde{\mu}_r^{corr} = 23.4$ mag arcsec^{-2} and the range is $\Delta\mu_r^{corr} \simeq [20.6, 24.7]$ mag arcsec^{-2}.

- 35% of the host galaxies are in the pre-coalescence phase of a merger or are involved in a gravitational interaction that will not necessarily lead to a merger. 40% of the host galaxies are in the coalescence or post-coalescence phase of a merger. The remaining 25% of the host galaxies show no morphological signs of mergers or interaction. These results indicate that, if a merger is responsible for triggering the AGN activity, this can happen before, during or after the merging of the SMBH

- When comparing the rates of morphological disturbance found in the type II quasars ($75 \pm 20\%$) and a sample of quiescent red galaxies ($68 \pm 14\%$), similar rates of interaction were found in both samples. However, the morphological features detected in the comparison sample are up to 2 magnitudes fainter than those found in the type II quasars, which may highlight a fundamental difference in the types of mergers that the two groups are undergoing.

- When comparing to the SLRG of RA11, it was found that the detected morphological features have a very similar range and median value of surface brightness, indicating that in both radio-loud and radio-quiet AGN, the host galaxies may be undergoing the same types of mergers.

- It is unlikely that a single triggering event will lead to a quasar that cycles through both radio-loud and radio-quiet phases. This is because, from the values derived in Section 3.5.3, only $\sim$2% of quasars of comparable emission line luminosity are radio-loud, suggesting a lifetime for the radio-quiet phase of $\sim 10^9 - 10^{10}$ years — much larger than current observationally based estimates.

These results are consistent with the idea that powerful quasars are triggered in galaxy mergers/interactions, although it is evident that not all morphologically disturbed early-type galaxies are capable of hosting a powerful quasar-like AGN. Clearly the detailed nature of the interaction (e.g. major/minor, gas-rich/gas-poor) is likely to have an influence on the outcome. It is also evident that mechanisms other than major, gas-rich mergers must also be capable of triggering quasar activity, because it was found that $25 \pm 11\%$ of the quasar host galaxies show no signs of tidal interactions.

In order to further characterise the host galaxies of the type II quasars in this sample, and determine at which point in the merger process the AGN is triggered, spectral synthesis modelling of 19 of the objects presented here is carried out in Chapters 4 and 5.

Chapter 4

Clear evidence for the early triggering of a luminous quasar-like active galactic nuclei in a major, gas-rich merger

The work presented in this Chapter is based on that originally presented in Bessiere et al. (2014), but includes more extensive spectral synthesis modelling of the data, and considers the uncertainties in the modelling in greater depth.Bessiere was responsible for reducing, analysing and interpreting the data, with suggestions and guidance from her co-authors

4.1 Introduction

In Chapter 3, deep optical imaging data were used to demonstrate that a large proportion of type II quasar host galaxies show evidence of involvement in merger events. However, quasar activity is not the only consequence of such merger events. In order to clarify the sequence and timing of the events surrounding the triggering of luminous AGN, a campaign of optical spectroscopy of a sample of type II quasars (defined as having $L_{[OIII]} > 10^{8.5} L_{\odot}$, Zakamska et al. 2003) has been undertaken, for which a full morphological study, based on deep Gemini GMOS-S r' imaging, was presented in the previous chapter. Here long-slit spectroscopic observations of one of the objects in this sample – J0025-10 – which shows some remarkable properties that make it worthy of note in the context of the evolutionary scenarios described above, are presented. The

spectra are used to determine the ages, reddening and masses of the stellar populations in the host galaxy.

J0025-10 is one of the objects in the sample whose spectrum shows the clearest evidence for a dominant young stellar population (YSP). This, coupled with the quality of the spectroscopic data, allows three distinct spatial apertures to be extracted from the 2 dimensional spectrum. This also makes J0025-10 an ideal test bed to rigorously assess the stellar modelling techniques, before going on to apply them to the rest of the sample, where the YSP is less dominant.

This Chapter is constructed as follows. Section 4.2 describes the data used in this Chapter, while in Section 4.2.1, the modelling technique employed to fit the stellar population is described and tested. In Section 4.3, the results of the stellar population modelling are presented, and in Section 4.4, these results are discussed in the broader context of AGN triggering. Finally, the work presented in this chapter is summarised in Section 4.5.

4.2 J0025-10 – The Data

The F775W Hubble Space telescope (HST) image presented in Figure 4.1(a)[1], shows the J0025-10 host galaxy overlayed with the 1.5 arcsec slit used for the spectroscopy at a PA of 230 °. J0025-10 is at a redshift of z=0.3203 and is undergoing a major merger event, with the two distinct nuclei separated by ~ 5 kpc (Chapter 3), and with a velocity shift of only $|\Delta v| = 20 \pm 20$ km s^{-1} (Villar-Martín et al., 2011) between them. There are also two distinct tidal tails, the brighter of which is clearly visible curving to the north of the nucleus in Figure 4.1(a). CO measurements made by Villar-Martín et al. (2013) reinforce the idea that this is a gas rich merger, showing that J0025-10 contains a total of $(6 \pm 1) \times 10^9$ M$_\odot$ of molecular gas in two reservoirs, with 60% in the central region and 40% associated with the northern tidal tail.

The data reduction techniques used to prepare these data for analysis have been described in detail in Chapter 2. The analysis presented in this Chapter is based on 1 dimensional spectra extracted from three different components of the system (Figure 4.1(b)), where each aperture covers a projected region of 1.5×1.1 arcsec^2 (6.7×5.0 kpc^2). Apertures Q and G are centred on the nuclei of the quasar host galaxy and the merging companion galaxy respectively, whilst aperture T is centred on the tidal tail associated

[1]This image of J0025-10 is taken from the Hubble Legacy Archive. It was taken as part of proposal no. 10880 (P.I. Schmitt) using ACS/WFC with the F775W filter

with the quasar host galaxy. The spectra have been corrected for Galactic reddening (E(B - V) = 0.03), as derived from the dust map of Schlegel, Finkbeiner & Davis (1998), using the extinction law of Cardelli et al. (1989).

Figure 4.1(a) shows the spatial location of each aperture, while Figure 4.1(b) shows the location of the apertures plotted on a spatial profile of the 2 dimensional spectrum. The extracted 1 dimensional spectra are shown in Figure 4.2, and in each of the apertures the presence of the higher order Balmer stellar absorption lines is clearly visible along with the Balmer break. These features alone indicate that significant young stellar populations must be present.

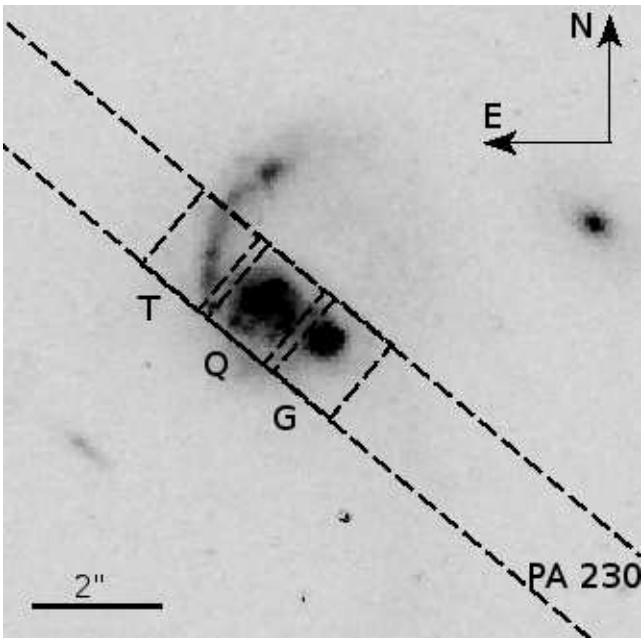

(a)

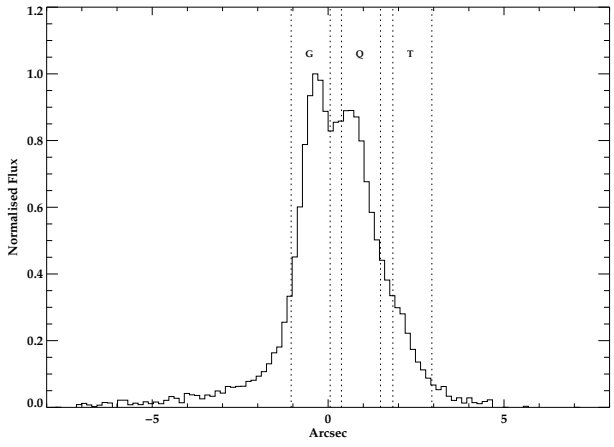

(b)

Figure 4.1: (a) HST image of J0025-10 showing the position of the 1.5 arcsec slit used for the long slit spectroscopy. The image also shows the approximate spatial locations of the three 5 kpc apertures used in this analysis. (b) A spatial profile of the 2D spectrum of J0025-10 in the observed wavelength range 5370 – 5553 Å indicating the regions from which the three apertures were extracted.

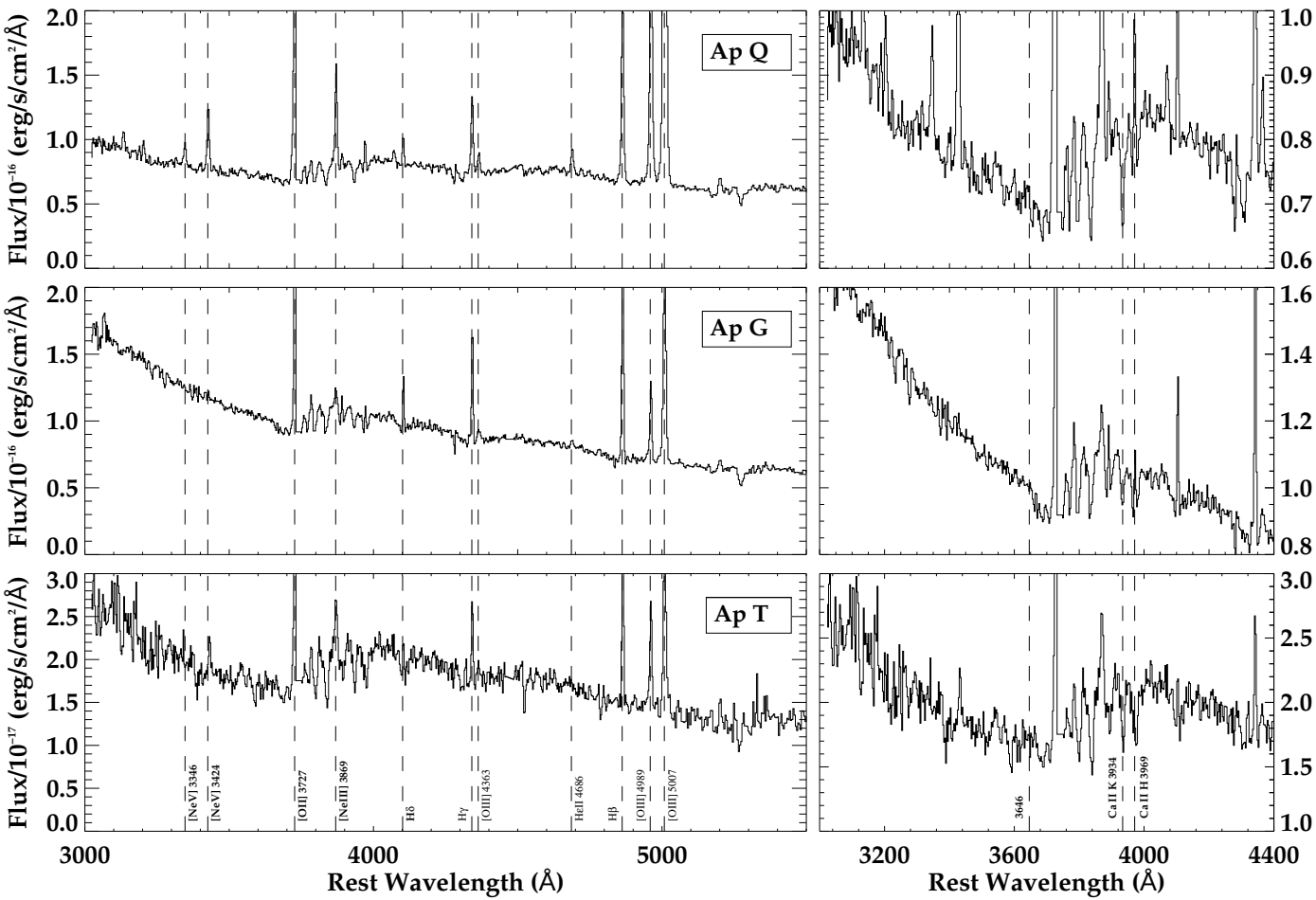

Figure 4.2: The 1D spectra extracted from the three distinct spatial regions of J0025-10. Each spectrum is shown in a separate panel on the left, with the top panel showing the quasar host galaxy component (Q), the middle panel showing the companion galaxy component (G), and the bottom panel showing the spectrum for the northern tidal tail (T). The most significant emission lines are highlighted. The right hand panels show a zoom of the short wavelength end of the spectrum of the same spatial region with prominent features highlighted. Region G shows the detection of the Balmer edge in emission, which indicates the presence of a significant population of young stars, and also demonstrates the importance of an accurate nebular subtraction when modelling the stellar populations.

Aperture	OSP Age (Gyr)	OSP Flux (%)	YSP Age (Gyr)	E(B-V)	YSP FLux (%)
Q	8	33	0.006	0.1	67
G	1	17	0.01	0.0	83
T	8	16	0.03	0.0	82

Table 4.1: The best fitting stellar models subtracted from the spectra for the three spatial regions of J0025-10 before the continuum modelling. Colum 1 gives the aperture modelled, whilst columns 2 and 3 give the age of the OSP component and it contribution to the total flux in the normalising bin. Columns 4, 5 and 6 denote the age, reddening and contribution to the total flux in the normalising bin of the YSP component.

4.2.1 Continuum Modelling

In order to model the stellar continuum, a purpose written IDL routine was used (CONFIT; Robinson et al. 2000; Robinson 2001), which attempts to fit up to three components to the observed spectrum. These three components can comprise of up to two different stellar populations and, in addition, a power-law component which has the form $F_\lambda \propto \lambda^\alpha$ ($-15 < \alpha < 15$). The routine fits the required number of components to the observed spectra using various combinations of flux, to compute the reduced minimum χ^2 value for each combination. The spectra have been modelled using 77 wavelength bins of 30 Å width below a rest-frame wavelength of 6000 Å, and 60 Å width at longer wavelengths; the wider bins at longer wavelength were necessary due to strong sky residuals and fringing. These bins were evenly distributed across the wavelength range, avoiding strong emission lines, atmospheric absorption bands, chip gaps and bad columns. A normalising bin of 4583–4613 Å was selected, because this region is free of any significant emission or absorption features.

Before fitting, the higher order Balmer lines and a nebular continuum were also subtracted, using the procedure outlined in Dickson et al. (1995) and Holt, Tadhunter & Morganti (2003). The necessity of subtracting the nebular continuum in this case is demonstrated by Figure 4.2, which shows clear evidence of the Balmer continuum edge in emission (at 3646 Å) in the companion galaxy component. The process of generating the nebular continuum involved several processes. Initially, the best fitting stellar model was subtracted from the spectrum to account for any underlying stellar absorption of Hβ, which can be significant in young stars (Table 4.1). The Hβ flux was then measured from this stellar-subtracted spectrum. In order to do this as accurately as possible, it was assumed that the Hβ line could be modelled using the same kinematic components as the strong [OIII] emission lines. Therefore, all three lines were modelled simultaneously using

Gaussian profiles, fixing the width of Hβ to be the same as those of the [OIII]λ4959, 5007 lines, which were themselves fixed to a ratio of 3/1. The lines were fit using the least number of kinematic components possible, and in this case, only one narrow component per line was deemed necessary to produce an adequate fit.

Once the Hβ flux and width had been measure, a spiketrum[2] of the Balmer higher order lines (H $\geq$ 8) was generated using the STARLINK FIGARO package, assuming case B recombination. This, of course, means that the ratio of each Balmer line in relation to Hβ has a fixed value. This spiketrum was then convolved with Gaussians of the measured width of Hβ, producing a model of the Balmer emission lines.

The next step was to generate a nebular continuum which accounts for the free-free, free-bound and two photon decay continua associated with the nebula. This model was produced using the STARLINK DIPSO package, assuming an electron temperature of $T = 10000$ K and electron density of $N_e = 1000$ cm^{-3}. However, it should be noted that the resulting nebular model is not particularly sensitive to the assumed temperature and density. The model of the Balmer emission lines and the continuum nebular emission were then combined to form the final nebular model. Measuring the contribution of the total nebular continuum that was generated using this method, to the total flux just below the Balmer edge (3450–3550Å), it was found that the nebular continuum contributes 2.7%, 9.6% and 8.8% in apertures Q, G and T respectively. In order to determine whether it was necessary to apply a reddening correction to the subtracted nebular continuum, the Balmer decrements were measured from the stellar-continuum-subtracted spectra. Unfortunately, because of the strong sky residuals and fringing above 6000 Å (rest-frame), it was not possible to accurately measure the Hα flux, and therefore the Hγ/Hβ and Hδ/Hβ ratios were measured instead. The results, shown in Table 4.2, are consistent at the 2σ level with the ratios expected from Case B recombination theory (Hγ/Hβ = 0.47, Hδ/Hβ = 0.27; Osterbrock & Ferland 2006). This implies little to no intrinsic reddening in the various apertures, and therefore, no correction to the nebular component was applied. Careful examination of the nebular subtracted spectra in the region of the Balmer edge confirmed the accuracy of the subtraction.

The stellar templates used here were generated using STARBURST 99 (Version 6.0.4) [3] (Leitherer et al., 1999; Vázquez & Leitherer, 2005; Leitherer et al., 2010). Two different sets of assumptions were made about the star formation history when generating the

[2] A spectrum where all the elements except for those at the tablulated values are zero. In this case, the tabulated values are the expected fluxes of the higher order Balmer lines, considering the measured Hβ flux.

[3] http://www.stsci.edu/science/starburst99/docs/default.htm

Aperture	Hγ/Hβ	Hδ/Hβ
Q	0.41 ± 0.03	0.22 ± 0.02
G	0.47 ± 0.04	0.25 ± 0.02
T	0.51 ± 0.04	0.29 ± 0.03

Table 4.2: The Hγ/Hβ and Hδ/Hβ ratios measured in each of the three apertures, following subtraction of a continuum model. Column one denotes which aperture the measurement applies to, columns two and three give the value of the Hγ/Hβ and Hδ/Hβ ratio respectively.

templates. Firstly it was assumed that the star formation took place in an instantaneous burst, with an initial mass of 10^6 $M_\odot$, which was allowed to evolve for 5 Gyr. The second assumption was that of a continuous star formation history, with a constant star formation rate, which was allowed to proceed for 0.2 Gyr. It should be noted that in these two cases, the concept of the age of the stellar population is different. When considering the burst model, the age of the population defines the time that has passed since the initial burst, and therefore, traces the age of stars at the main sequence turn off. In the case of continuous formation, the age of the population refers to the period of time elapsed since the star formation episode began.

For both sets of models, the Padova evolutionary tracks including the AGB phase were used (Bressan et al., 1993; Fagotto et al., 1994a,b; Girardi et al., 2000), because they allow the inclusions of stars of the widest range of masses and ages to be included in the stellar population model, which was considered to be advantageous because the composition of the stellar population is unkown. Solar metallicity and a Kroupa IMF (Kroupa, 2001), using two mass intervals (0.1 $M_\odot$, 0.5 $M_\odot$, 100 $M_\odot$), with exponents 1.3 and 2.3 were assumed. Reddening in the range $0 \leq E(B-V) \leq 2.0$ in steps of $\Delta E(B-V) = 0.1$ was then applied to these template spectra using the extinction curve of Calzetti et al. (2000).

The strategy that was adopted for the stellar synthesis modelling was to use the minimum number of components required to produce an acceptable fit. In this way, the issue of degeneracies inherent in fitting larger numbers of components is somewhat mitigated. For each aperture the model was run with a series of combinations of components, which represent plausible evolutionary scenarios for the host galaxies, and included the following.

1. An unreddened old stellar population (OSP) of age 8 Gyr combined with a burst model young to intermediate stellar population (YSP/ISP) with age in the range 0.001 – 5 Gyr and reddening in the range $0 \leq E(B-V) \leq 2.0$.

2. An unreddened ISP of age 2 Gyr combined with a burst model YSP/ISP with age in the range 0.001 – 2 Gyr and reddening in the range $0 \leq E(B-V) \leq 2.0$.

3. An unreddened ISP of age 1 Gyr combined with a burst model YSP/ISP with age in the range 0.001 – 1 Gyr and reddening in the range $0 \leq E(B-V) \leq 2.0$.

4. An unreddened YSP of age 0.5 Gyr combined with a burst model YSP with age in the range 0.001 – 0.5 Gyr and reddening in the range $0 \leq E(B-V) \leq 2.0$.

5. An unreddened OSP of age 8 Gyr combined with a continuous formation model stellar population with age in the range 0.001 – 0.2 Gyr and reddening in the range $0 \leq E(B-V) \leq 2.0$.

6. An unreddened ISP of age 2 Gyr combined with a continuous formation model stellar population with age in the range 0.001 – 0.2 Gyr and reddening in the range $0 \leq E(B-V) \leq 2.0$.

7. An unreddened ISP stellar population of age 1 Gyr combined with a continuous formation model stellar population with age in the range 0.001 – 0.2 Gyr and reddening in the range $0 \leq E(B-V) \leq 2.0$.

8. An unreddened YSP of age 0.5 Gyr combined with a continuous formation model stellar population with age in the range 0.001 – 0.2 Gyr and reddening in the range $0 \leq E(B-V) \leq 2.0$.

9. For the quasar nucleus component only, an 8 Gyr unreddened OSP combined with a power-law component. This would represent the case in which no significant star formation is present, and the strong blue component is produced by scattered light from the hidden quasar nucleus (Tadhunter et al., 2002).

10. In addition, for the quasar host galaxy aperture (Q), fits 1- 8 are run including a power-law component, which could be representative of scattered quasar light.

An 8 Gyr underlying population was thought to be a reasonable assumption, due to the fact that quasar host galaxies are often found to be early-types (Dunlop et al., 2003; Tadhunter et al., 2011) which, evidence suggests, formed the majority of their stars at high redshift. Therefore, considering the age of the Universe at the typical redshift of the sample of type II quasars presented here (9-10 Gyr, assuming $H_0 = 70\,\mathrm{km\ s^{-1}\ Mpc^{-3}}$), 8 Gyr would be a reasonable estimate for the age of the dominant (in terms of mass) stellar population.

However, this assumption may not hold true, and the host galaxies may have had a different underlying population before the quasar/star formation activity was initiated. Therefore, the spectra are also modelled using an ISP of 0.5, 1 or 2 Gyr.

Therefore, for the galaxy nucleus and tidal tail, 8 possible combinations of components are explored, while for the quasar nucleus, 17 possible combinations of components are explored.

4.3 Results

For each successful combination of components, a contour plot was produced (see Figures 4.3 and 4.4) which shows the contours of reduced minimum χ^2 (χ^2_{red}) values for the various combinations of OSP/ISP and YSP with various ages and reddening, the results of which are summarised in Tables 4.3 and 4.4 separately for the burst and continuous formation histories. Taking into consideration previous experience with such fits, any combination with $\chi^2_{red} \leq 1$ was deemed to be a possible acceptable fit (e.g. Tadhunter et al. 2005; Holt et al. 2007). Further discrimination was then made on the basis of visual inspection of how well some of the age-sensitive absorption lines, including the Ca II K absorption feature, the higher order Balmer lines and G band, were fitted. Figure 4.5, shows examples of the overall fits to the spectra and the fits around the Balmer absorption features, produced by CONFIT, for apertures Q, G and T respectively, for particular combination of stellar populations.

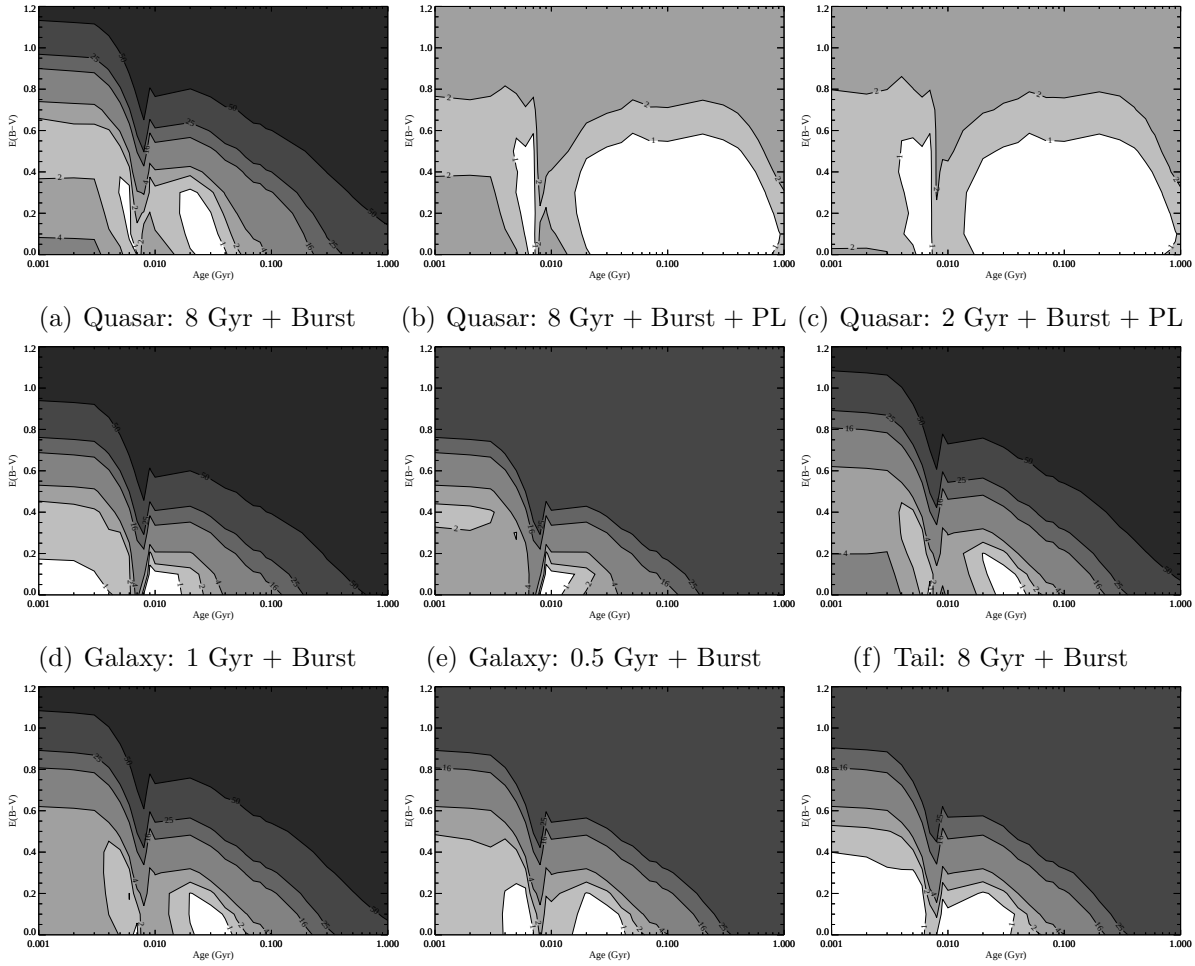

(a) Quasar: 8 Gyr + Burst (b) Quasar: 8 Gyr + Burst + PL (c) Quasar: 2 Gyr + Burst + PL

(d) Galaxy: 1 Gyr + Burst (e) Galaxy: 0.5 Gyr + Burst (f) Tail: 8 Gyr + Burst

(g) Tail: 2 Gyr + Burst (h) Tail: 1 Gyr + Burst (i) Tail: 0.5 Gyr + Burst

Figure 4.3: The reduced minimum χ^2 contour plots for each of the successful CONFIT runs which included a burst model of star formation. Each plot shows the region of χ^2 space in which possible acceptable fits may be found ($\chi^2 < 1$). The numbers give the reduced minimum χ^2 value of the contour and the area in which $\chi^2_{red} < 1$ is shown in white.

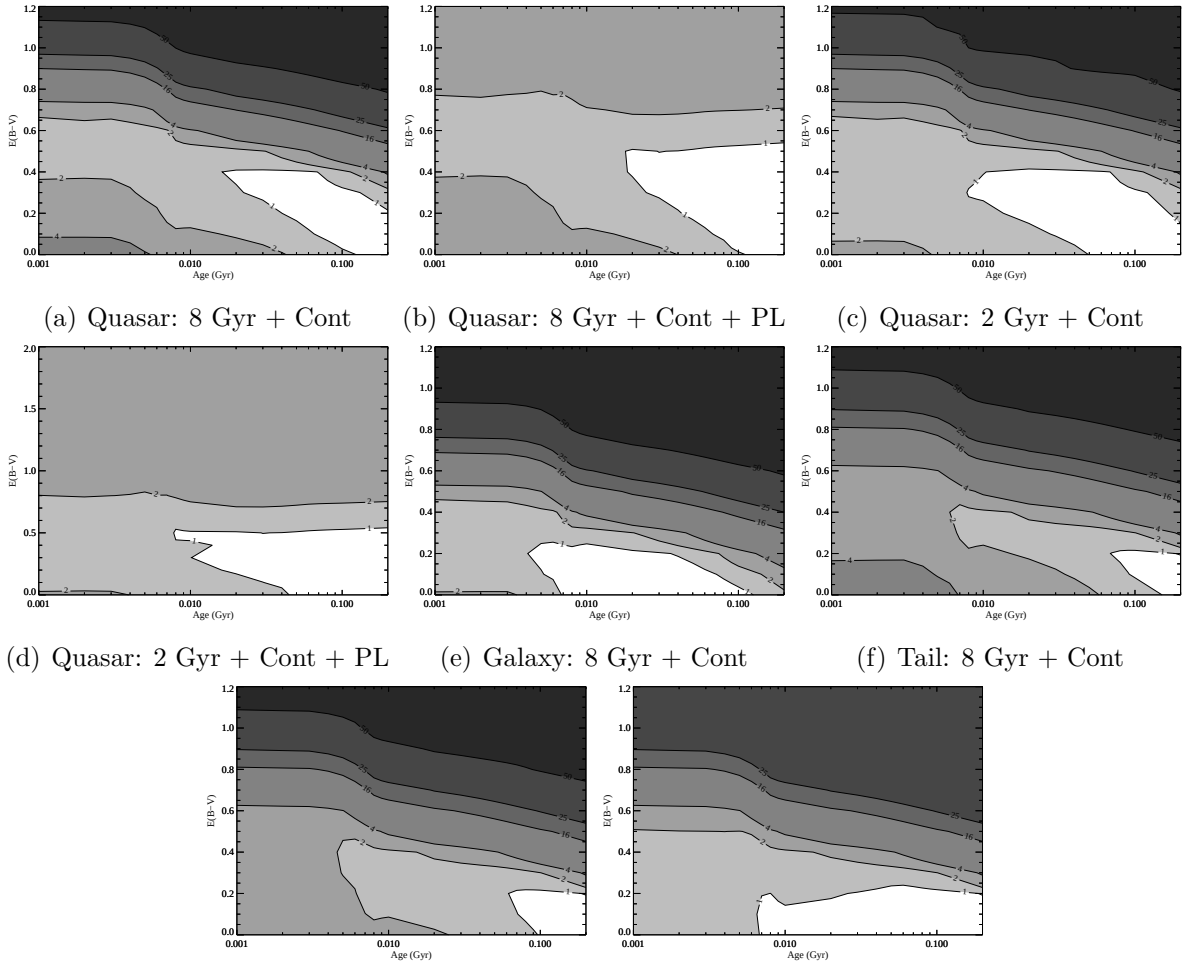

(a) Quasar: 8 Gyr + Cont (b) Quasar: 8 Gyr + Cont + PL (c) Quasar: 2 Gyr + Cont

(d) Quasar: 2 Gyr + Cont + PL (e) Galaxy: 8 Gyr + Cont (f) Tail: 8 Gyr + Cont

(g) Tail: 2 Gyr + Cont (h) Tail: 1 Gyr + Cont

Figure 4.4: The reduced minimum χ^2 contour plots for each of the successful CONFIT runs which included a continuous star formation model. Each plot shows the region of χ^2 space in which possible acceptable fits may be found ($\chi^2 < 1$). The numbers give the reduced minimum χ^2 value of the contour and the area in which $\chi^2_{red} < 1$ is shown in white.

Table 4.3: The results of the various combinations of stellar populations which included a burst star formation history used in the Confit runs. Column 1 gives the aperture that is being modelled. Columns 2 to 4 show the age of the OSP/ISP population used in the fit, whether a power-law component was also included, and whether an acceptable fit was achieved based on visual inspection of the overall fit and the age sensitive stellar absorption features. Columns 5 and 6 denote the age and reddening of the YSPs that allow an acceptable fit. Columns 7 to 9 give the percentage contribution to the total flux in the aperture of the OSP, YSP and, if it is included, the power-law component respectively.

Aperture	OSP/ISP (Gyr)	Power law component	Acceptable fit ?	YSP (Gyr)	E(B-V)	OSP/ISP flux %	YSP flux %	Power Law flux %
Q	8	No	Yes	0.02–0.04	0–0.2	19 –37	63–79	–
Q	2	No	No	–	–	–	–	–
Q	1	No	No	–	–	–	–	–
Q	0.5	No	No	–	–	–	–	–
Q	8	Yes	Yes	0.02 – 0.3	0–0.5	0–39	34–79	4–39
Q	2	Yes	Yes	0.02–0.4	0–0.4	0–42	39–94	0–42
Q	1	Yes	No	–	–	–	–	
Q	0.5	Yes	No	–	–	–	–	–
G	8	No	No	–	–	–	–	–
G	2	No	No	–	–	–	–	–
G	1	No	Yes	0.009 –0.01	0–0.1	0–32	67–97	–
G	0.5	No	Yes	0.009–0.01	0–0.1	0–37	65–96	
T	8	No	Yes	0.03–0.04	0–0.1	5–20	77–92	–
T	2	No	Yes	0.03–0.04	0–0.1	6–24	73–91	–
T	1	No	Yes	0.02–0.04 (0.006)	0–0.1	7–44	53–90	–
T	0.5	No	Yes	0.001–0.006 (0.009–0.03)	0–0.3	7–66	34–90	–

Table 4.4: The results of the various combinations of stellar populations which included a continuous star formation history used in the Confit runs. Column 1 gives the aperture that is being modelled. Columns 2 to 4 show the age of the OSP/ISP population used in the fit, whether a power-law component was also included, and whether an acceptable fit was achieved based on visual inspection of the overall fit and the age sensitive stellar absorption features. Columns 5 and 6 denote the age and reddening of the YSPs that allow an acceptable fit. Columns 7 to 9 give the percentage contribution to the total flux in the aperture of the OSP, YSP and, if it is included, the power-law component respectively.

Aperture	OSP/ISP (Gyr)	Power law component	Acceptable fit ?	YSP (Gyr)	E(B-V)	OSP/ISP flux %	YSP flux %	Power Law flux %
Q	8	No	Yes	0.02–0.2	0–0.4	0–39	61–97	–
Q	2	No	Yes	0.02–0.2	0.1–0.4	10–43	58–89	–
Q	1	No	No	–	–	–	–	–
Q	0.5	No	No	–	–	–	–	–
Q	8	Yes	Yes	0.02–0.2	0.1–014	0–35	62–96	0–18
Q	2	Yes	Yes	0.02–0.2	0.1–0.4	0–41	55–98	0–18
Q	1	Yes		0.007–0.2	0.2–0.4	0–42	10–98	0–24
Q	0.5	Yes		0.001–0.2	0–0.8	0–40	32–87	0–34
G	8	No	Yes	0.04–0.08	0–0.1	18–23	74–83	–
G	2	No	No	–	–	–	–	–
G	1	No	No	–	–	–	–	–
G	0.5	No	No	–	–	–	–	–
T	8	No	Yes	0.2	0.1	7–22	75–90	–
T	2	No	Yes	0.1–0.2	0–0.1	9–27	71–88	–
T	1	No	Yes	0.03–0.2	0–0.2	9–41	56–87	–
T	0.5	No	Yes	0.001–0.2	0–0.3	6–62	38–90	–

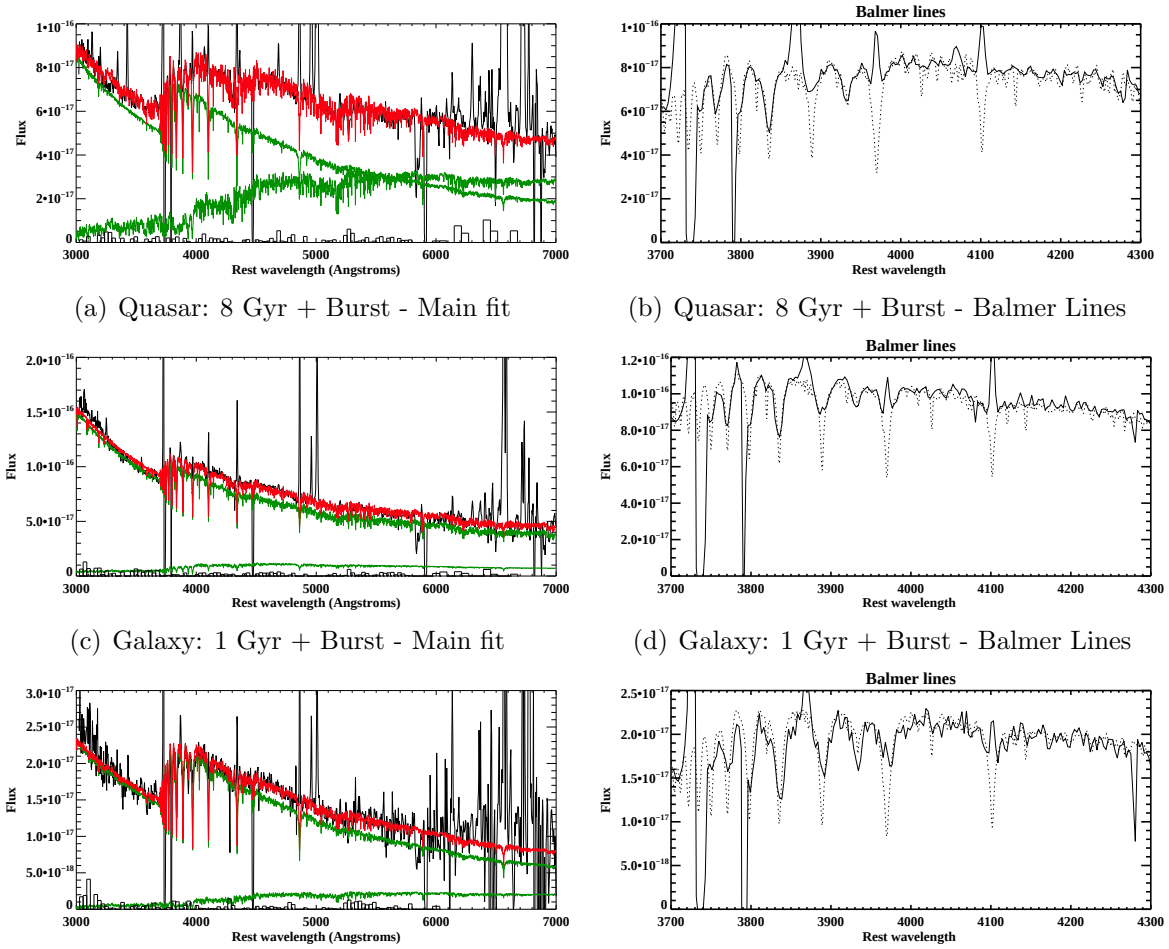

(a) Quasar: 8 Gyr + Burst - Main fit

(b) Quasar: 8 Gyr + Burst - Balmer Lines

(c) Galaxy: 1 Gyr + Burst - Main fit

(d) Galaxy: 1 Gyr + Burst - Balmer Lines

(e) Tail: 8 Gyr + Burst - Main fit

(f) Tail: 8 Gyr + Burst - Balmer Lines

Figure 4.5: Examples of stellar population fitting results produced by CONFIT for each of the spatial apertures extracted from J0025-10. The left-hand panels show the overall fit to the spectra, with the green lines representing the model OSP and YSP, while the red line shows a linear combination of the two. The histogram show the residuals in each of the continuum bins used for the modelling. The right-hand panels show a zoom of the age sensitive Balmer and Ca II K absorption features, where the solid line represents the data and the dotted line represents the fit. Panels (a) and (b) show a fit to the quasar component and includes a combination of an 8 Gyr OSP and an unreddened YSP with $t_{YSP} = 0.03$ Gyr. Panels (c)-(d) show the fit to the Galaxy component and include a 1 Gyr ISP combined with an unreddened YSP with $t_{YSP} = 0.009$ Gyr. Finally, panels (e)-(f) show a CONFIT fit associated with the tail aperture which includes an 8 Gyr OSP combined with an unreddened YSP with $t_{YSP} = 0.04$ Gyr.

4.3.1 The quasar host galaxy

Figure 4.3(a) shows the contour plot of χ^2_{red} values for the combination of an 8 Gyr OSP with a burst model YSP/ISP for the bulge of the quasar host galaxy. It is clear that there are two regions in which $\chi^2_{red} < 1$ (4-8 Myr and 20-40 Myr), however, although the fit to the general shape of the continuum with YSPs of age 4-8 Myr are reasonable, closer inspection of the fit in the region of the higher order Balmer lines allows these to be disregard as acceptable solutions. This conclusion is reinforced by the fact that the prominent, very broad He II λ4686 emission feature associated with Wolf-Rayet stars is not detectable. If a substantial population of age 4–8 Myr were present, this feature should be clearly visible in the spectum. Therefore, if a power-law component is not included, acceptable fits are achieved with an OSP of 8 Gyr, combined with a YSP component with age between 20 and 40 Myr, and low reddening in the range $0 \leq E(B-V) \leq 0.2$. Table 4.3 shows that, for all combinations for which an acceptable fit is achieved, the flux is dominated by the YSP, which contributes 63 – 79 % of the total flux in the normalizing bin (4538Å–4613Å).

With the inclusion of a power-law component (Figure 4.3(b) & 4.3(c)), acceptable fits can be achieved for both an 8 Gyr OSP and a 2 Gyr ISP combined with a YSP. Again, there are two regions for each combination in which $\chi^2_{red} < 1$. The younger region has ages in the range 5 – 7 Myr but closer inspection of the detailed fits to the Ca II K line allows these younger ages to be disregarded because the model substantially over-predicts the strength of this absorption feature.

The inclusion of the power-law component, which in this case could be representative of either a scattered AGN component or the continuum associated with very young stellar population (VYSP), results in a wider range of ages that provide acceptable fits (Table 4.3). The YSP/ ISP ages range between 0.02 and 0.4 Gyr, with reddening $0 \leq E(B-V) \leq 0.5$. In these cases, the YSP contributes up to 94 % of the total flux, while the power-law component contributes a maximum of 42%. Unsurprisingly, as the contribution to the flux from the power law increases, the age and reddening of the YSP/ISP components that provide acceptable fits also increases. At the oldest ages and highest reddening, the power-law contributes $\sim 40\%$ of the total flux in the normalising bin, which, if due to scattered light from the hidden quasar, would be detectable as broad wings to Hβ.

In order to determine a reasonable upper limit for a contribution from scattered quasar light, Gaussian components have been added to the model-subtracted data with values of broad Hβ equivalent width and FWHM that are typical of quasars (78Å and

5000 km s^{-1} respectively)[4]. It is found that, if a scattered quasar component were present, this would be clearly detectable if the quasar contributed 20% or more of the total flux in the normalising bin. Taking this into account rules out YSPs older than 100 Myr when considering both a 2 and 8 Gyr underlying OSP/ISP. Although these findings suggest that there is unlikely to be a major contribution from a scattered quasar component (associated with older age YSP), these observations do not allow a lower level scattered quasar contribution to be ruled out. Spectropolarimetry observations are required to accurately quantify the true level of any scattered light component. This issue will be discussed in depth in the following chapter.

When considering the results for the continuous star formation models, it is clear from the results shown in Table 4.4 and the contour plots presented in Figure 4.4 that, for combinations which include an 8 or 2 Gyr population, very similar results are achieved, with ages $0.02 \leq t_{YSP} \leq 0.2$ and reddenings $E(B-V) \leq 0.4$ found. However, this does not provide a true upper limit to the age of the YSP because the upper age range is truncated by the maximum age of the model. The continuous models also allow for possible solutions that include 0.5 and 1 Gyr underlying populations, as well as a power-law component. The latter combinations were not successful when using the burst models. However, in these cases, nearly all combinations of components have $\chi^2_{red} < 1$, therefore, the associated contour plots have not been included in Figure 4.4 because they do not convey any useful information. Visual inspection of a representative sample of these solutions allows the majority, in both cases, to be discarded because they over-predict the Ca II K absorption feature. In terms of reddening, the continuous models are mostly consistent with the burst models (except for 0.5 Gyr fits), however, the continuous star-formation model does allow for older ages than the burst models.

4.3.2 The companion galaxy nucleus

Figure 4.3(d) & 4.3(e) show the contours of χ^2_{red} for the combinations of components (including a burst YSP component) that produce acceptable fits for the nucleus of the companion galaxy. These clearly demonstrate that a much narrower range of YSP ages produces acceptable fits. In fact, it is apparent from Table 4.4 that it is only fits including ISPs of both 0.5 or 1 Gyr and a YSP component of 9 – 10 Myr with $0 \leq E(B-V) \leq 0.1$ that produce acceptable results. In both cases, the flux is dominated by

[4]These values were derived from 'A Catalog of Quasar Properties from SDSS DR7'(Schneider et al., 2010; Shen et al., 2011), by selecting all objects that have $L_{OIII} > 10^{45}$ erg s^{-1} and taking the median values of broad Hβ equivalent width and FWHM.

the YSP component, which contributes between 65% and 97 % of the total flux in the normalizing bin. Note that the presence of a YSP of relatively young age is consistent with the detection of strong emission lines in this region with H II-region-like line ratios (Villar-Martín et al., 2011). Indeed, comparison of the equivalent width of the Hβ line (log(W(Hβ)Å)=1.27) with the instantaneous burst models of Leitherer et al. (1999) implies $t_{ysp} \sim 6$ Myr, although older ages are possible if the star formation history is more extended. Note however, that if the population were younger than this, we would expect to detect the broad He II$\lambda\lambda$4686, 5411 features associated with Wolf-Rayet stars, which is not the case (Leitherer et al., 1999).

Table 4.4 shows that, when considering the continuous formation models, it is only possible to achieve an acceptable fit for combination 5, which includes an 8 Gyr OSP. This is in contrast to the results presented above for the burst models (Table 4.3), where it is only models that consider the combination of an ISP and YSP that produce acceptable fits. However, in both the case of a burst and a continuous star formation history, it is the YSP that dominates the flux, contributing a maximum of 74 % of the total flux in the normalising bin for the continuous star formation case.

When using these continuous models, older ages for the YSP are found than for the burst models ($0.04 \leq t_{YSP} \leq 0.08$), but the same low values for reddening ($E(B-V) \leq 0.1$) is found in both cases.

4.3.3 The tidal tail

The northern tidal tail can be fit with an underlying OSP of 8 Gyr or ISPs of 0.5, 1 and 2 Gyr, all combined with a burst model YSP. Table 4.3 shows that, for all except the fits with a 0.5 Gyr underlying population, a YSP of 20–40 Myr with reddening $0 \leq E(B-V) \leq 0.1$ is required, comparable with the YSP population required for the quasar host galaxy component. For an ISP of 0.5 Gyr, there a two possible regions in χ^2_{red} space that produce acceptable fits. These have YSP ages 1–6 Myr ($0 \leq E(B-V) \leq 0.3$) and 9–30 Myr ($0 \leq E(B-V) \leq 0.1$). Table 4.3 shows that, when considering fits with an 8 or 2 Gyr component, it is the YSP that dominates the flux in the aperture. For ISPs of 0.5 and 1 Gyr, the ISP flux makes a more significant contribution to the total flux. Although visual inspection of the fits does not allow for discrimination between the older and younger combinations, the equivalent width of the detected Hβ line suggests a starburst age of ~ 6 Myr (Leitherer et al., 1999), favouring the 0.5 Gyr + 1-6 Myr population fits. However, all OSP/ISP plus YSP combinations that provide an acceptable fit to the data require a contribution from a YSP with low reddening.

Table 4.4 shows that all combinations which include a continuous formation model produce acceptable results. In the case of combination 5 (Figure 4.4(f)), it is only the oldest ages (0.2 Gyr) and the lowest reddenings ($E(B-V) \leq 0.1$) that produce acceptable results, with younger ages and higher reddenings for which $\chi^2_{red} < 1$ producing fits that over-predict Ca II K. For combination 6 (Figure 4.4(g)), fits with $t_{YSP} < 0.1$Gyr and $E(B-V) > 0.1$ and be discounted, as can fits for combination 7 with $t_{YSP} < 0.3$Gyr and $E(B-V) > 0.2$ for the same reason. For combination 8, fits with the youngest ages and lowest reddenings do not produce an acceptable fit. Therefore, for the tidal tail, it appears that the younger the unreddened underlying component is, the less constraint is placed on the age of the YSP component.

4.3.4 Stellar Masses

The relationship between quasar host galaxies and quiescent galaxies remains unclear: are quasars hosted predominantly by massive ellipticals (e.g. Dunlop et al. 2003; Tadhunter et al. 2011), or can they be hosted by galaxies across the stellar mass range? One approach to answering this question involves determining the total stellar masses of the host galaxies using broad-band photometry at a single wavelength (e.g K-band Inskip et al. 2010). However, when doing so it is important to account for the mix of stellar populations present, because the assumptions made can have a significant impact on the result. This is emphasised by the modelling results which show that, while the companion galaxy component has a similar total flux at ~ 5500Å to the quasar host, its stellar mass is a factor of $\sim 5-10$ times lower.

The accuracy of our modelling allows the calculation of the masses of the stellar populations within each aperture, accounting for the OSP/ISP and YSP separately. In addition, by using the photometry from the Gemini GMOS-S imaging data, presented in the previous chapter, it is possible to account for the extended flux that is not contained within the slit.

The possible range of masses for each aperture has been calculated separately by first assuming that the OSP makes the maximum acceptable contribution to the total flux in that aperture, and then repeating the process for the maximum acceptable YSP flux. This has been done because, although the YSP dominates the flux in all three apertures, it is the OSP, particularly when an 8 Gyr OSP is assumed, that will most likely dominate the mass of the system. Table 4.5 shows the stellar masses derived for the OSP and YSP components separately and also the total stellar mass in each spatial region. Clearly the total stellar mass of the system is dominated by the 8 Gyr OSP

Aperture	OSP/ISP	YSP	Total
Q	31–54	0.84–1.9	32–54
G	0.32–5.7	0.39–0.86	1.1–6.0
T	0.24–6.8	0.20 –0.37	0.61–7.1
Total Mass			33 – 67

Table 4.5: The stellar masses derived from each of the 5 kpc apertures. Column 1 gives the aperture, while columns 2 to 4 show the derived mass of the OSP, YSP and total mass respectively. All the values are given in units of 10^9 $M_\odot$. The results shown in this table correspond to the minimum and maximum contribution to the flux from an OSP/ISP. The mass estimates assume a Kroupa IMF.

that is detected in the quasar component (Q). In the companion galaxy region (G), the maximum mass is contributed by a 0.5 Gyr underlying ISP component, and therefore, this part of the system only contributes $\sim 3-8\%$ of the total stellar mass.

The results in Table 4.5 include only the flux contained within the 1.5 arcsec slit, which corresponds to an area of 5×6.7 kpc^2 per aperture in the assumed cosmology. In order to correct for this, the deep GMOS-S r' images were used to determine an apparent magnitude of $r_{AB} = 18.40$, (corrected for Galactic extinction), within a 30 kpc aperture. From this value, it was found that 59% of the flux at the central wavelength of the r' filter is accounted for by the three apertures in the slit.

To calculate the total mass of the system it was assumed that starlight not accounted for by the apertures comprises the same mix of populations as apertures Q, G and T, in turn, both for a minimum and maximum contribution from an OSP. Therefore, the minimum mass is derived by assuming the minimum OSP contribution to the models for each aperture and assuming the same mix of stellar populations as in aperture G for the flux excluded from the slit. The maximum mass is determined by summing the masses found from the models assuming the largest possible contribution from an OSP/ISP, and that the flux excluded from the aperture can be modelled with the same mix of populations as aperture Q. This leads to a total stellar mass for the system in the range $3.7 \times 10^{10} M_\odot < M < 1.7 \times 10^{11} M_\odot$ which, if adopting the characteristic mass derived from the mass function of Cole et al. (2001) ($m_* = 1.4 \times 10^{11} \mathrm{M}_\odot$), is around the characteristic mass, with a range $0.3m_* - 1.2m_*$.

A number of previous studies of the host galaxies of both radio-loud and radio-quiet quasars have concluded that they tend to be hosted by massive elliptical galaxies. Scaling the derived values to a Kroupa IMF for ease of comparison, Dunlop et al. (2003) and Tadhunter et al. (2011) found median stellar masses of $4.1m_*$ and $2.5m_*$ respectively for radio-loud quasars and radio galaxies. Dunlop et al. (2003) also derived masses for

a sample of radio-quiet quasars finding a slightly lower median stellar mass of $1.8m_*$. The stellar mass calculations presented above, which take into account the dominant contribution to the flux from the YSP, show that J0025-10 will not evolve into a massive elliptical through *this* merger[5]. In fact, the total stellar mass derived for this system is consistent with that found for the sample of nearby ULIRGs presented in Rodríguez Zaurín et al. (2010) (median mass $0.5m_*$).

4.4 Discussion

4.4.1 Testing the modelling

The impact of changing the wavelength bins

In order to test how important the placement of the wavelength bins was to the results obtained, five tests were performed which involved taking a random sample of 39 of the original wavelength bins plus the original normalising bin (total of 40 bins) in order to perform the continuum fitting. The sample of bins was randomised by assigning each of the 77 bins a number, and then using a random number generator (using IDL) to generate a list of 38 unique numbers (using a different seed each time), which were then removed from the list. The normalising bin was then added manually. For all the tests, the nebular subtracted quasar spectrum was used, and the modelling assumed an 8 Gyr OSP with a burst YSP component.

The aim of the tests was to determine whether the relative weighting of the bin distribution has an impact on the regions of age–reddening space in which $\chi^2_{red} < 1$. The results of these tests, along with the original results for the quasar nebular subtracted spectrum are shown in Table 4.6. These tests show that the placement of the bins has little affect on the results, although in the cases of tests 1 and 2, where a larger proportion of the wavelength covered by the bins is in the reddest part of the spectrum, the possible solutions associated with region 1 are far more restricted. However, it must be noted that visual inspection of the original run led to these younger ages being rejected for providing poor fits in the region of the age sensitive stellar absorption lines. Table 4.6 shows that, in the case of region 2, in which acceptable solutions are found, the distribution of the bins makes little difference to the results achieved.

[5]We note that, although there is some cold molecular gas remaining in this system – as evidenced by the CO observations – its mass is not sufficient to significantly boost the total stellar mass, even if completely converted in to stars.

	Original	Test 1	Test 2	Test 3	Test 4	Test 5
Region 1 Age (Gyr)	0.005–0.007	0.006	0.006	0.005–0.007	0.005–0.007	0.004–0.007
Region 1 E(B-V)	0–0.3	0.1–0.2	0.1–0.2	0–0.4	0–0.4	0–0.4
Region 2 Age (Gyr)	0.02–0.04	0.02–0.04	0.02–0.03	0.02–0.04	0.02–0.04	0.02–0.04
Region 2 E(B-V)	0–0.3	0–0.3	0–0.3	0–0.3	0–0.3	0–0.3
3027–3858(%)	25	18	24	31	16	23
3891–4703(%)	25	22	26	16	28	26
4703–5589(%)	25	29	17	26	35	30
5589–6680(%)	25	31	33	17	21	21

Table 4.6: The results of various tests carried out in order to identify what the affects (if any) are of using different wavelength bins for the continuum modelling. Each column shows the results for the various tests carried out. Region 1 refers to the younger region in which $\chi^2_{red} < 1$ and region 2 refers to the older. The first and second rows give the range of ages in Gyr and E(B-V) which produce results with $\chi^2_{red} < 1$ in region 1, while rows 3 and 4 give the same for region2. Rows 4-8 give the percentage of the total wavelength covered by the bins used in that run in the wavelength range shown.

The impact of applying a nebular subtraction

In order to quantify the effect subtracting the nebular continuum has on the resulting continuum modelling, the minimum nebular (no subtraction) and maximum nebular (unreddened nebular continuum subtraction) are compared for both the quasar and galaxy components. The tail component is not considered here, because the lower signal-to-noise of the spectrum results in the continuum modelling being less well constrained.

It can be seen from Table 4.7 that, in the case of the quasar component, the subtraction of the nebular continuum has little effect on the resulting possible solutions ($\chi^2_{red} < 1$). This is unsurprising given the small contribution to the total flux from the nebular continuum in this case ($\sim$ 3% in the range 3450–3550Å). In the case of the galaxy component however, the nebular contributes $\sim$ 10% of the total flux blue-wards of the Balmer edge, and correspondingly, the subtraction of this nebular component has a much more significant impact on the results of the continuum modelling. Table 4.7 shows that the range of possible ages is significantly reduced after the subtraction. In the unsubtracted case, ages up to 0.1 Gyr are allowed by the modelling, however in the subtracted case, this is reduced to 0.01 Gyr.

Although the subtraction of the nebular continuum has had an impact on the range

Aperture	Unsubtracted		Subtracted	
	Age (Gyr)	E(B-V)	Age (Gyr)	E(B-V)
Quasar	0.004–0.006	0–0.3	0.005–0.007	0–0.3
	0.02–0.03	0–0.2	0.02–0.04	0–0.3
Galaxy	0.001–0.03	0–0.1	0.001–0.004	0–0.1
	0.08–0.1	0–0.1	0.008–0.01	0–0.1

Table 4.7: The results of performing the stellar continuum modelling before and after the subtraction of the model nebular continuum, for both the quasar host galaxy and the companion galaxy. In the case of the quasar host galaxy, an 8 Gyr + burst YSP model was used, and in the case of the galaxy, a 1 Gyr + burst YSP was used. Column 1 shows the aperture modelled, while columns 2 and 3 give the regions of age and reddening in which $\chi^2_{red} < 1$, for the unsubtracted spectrum. Columns 4 and 5 give the same values for the subtracted values. Note that the values shown here are for regions which produce $\chi^2_{red} < 1$, and have not been visually inspected for goodness of fit.

of ages that produce $\chi^2_{red} < 1$, in both the cases of the quasar and galaxy components, it has very little impact on the allowed values of reddening.

These results demonstrate that, as the contribution of the nebular component becomes more significant, the importance of performing a subtraction before continuum modelling also increases.

4.4.2 Sources of uncertainty

There are a number of factors which can have a significant impact on both the ages and masses derived for a stellar population using this technique of stellar population fitting. In this section, the main factors that will impact the results are outlined.

The initial mass function

One of the main sources of uncertainty in any attempts to derive stellar masses in this manner is the dependence of the results on the form of the initial mass function (IMF) assumed. This is because, as shown above, the total mass of the system is, in a large part, dependent on the significance of the OSP. This is true even when a large proportion of the flux is attributable to the YSP. In this work, a Kroupa (Kroupa, 2001) IMF is assumed, which takes the form of a broken power-law, such that $\xi(m) \propto m^{-\alpha_i}$, where:

$$\alpha_1 = +1.3, \quad 0.1 \leq m/\,\mathrm{M}_\odot < 0.5$$

$$\alpha_2 = +2.3, \quad m/\,\mathrm{M}_\odot \geq 0.5$$

and $\xi(m)\mathrm{d}m$ is the number of single stars in the mass interval m to $m + \mathrm{d}m$.

In comparison, the widely used Salpeter IMF comprises a constant power-law form, with $\alpha = 2.35$. If the two are compared, it can be seen that, for masses greater than 0.5 $\mathrm{M}_{\odot}$, both the Kroupa and Salpeter IMF predict a similar proportion of stars at each mass. However, below this limit, the Salpeter IMF predicts significantly more stars at a given mass then the Kroupa IMF. This is illustrated in Figure 4.6, where the distribution of stars predicted by both IMFs in the range $0.1 \leq m/\,\mathrm{M}_{\odot} \leq 3$ is plotted. It can be seen that at lower masses ($m/\,\mathrm{M}_{\odot} < 0.5\,\mathrm{M}_{\odot}$) the two functions diverge significantly. This divergence is important in determining the total mass of the system, because a significant proportion of the total stellar mass is contributed by the low mass stars. For a Kroupa IMF, this will be around 32 % of the total mass, but will be higher for a Salpeter IMF.

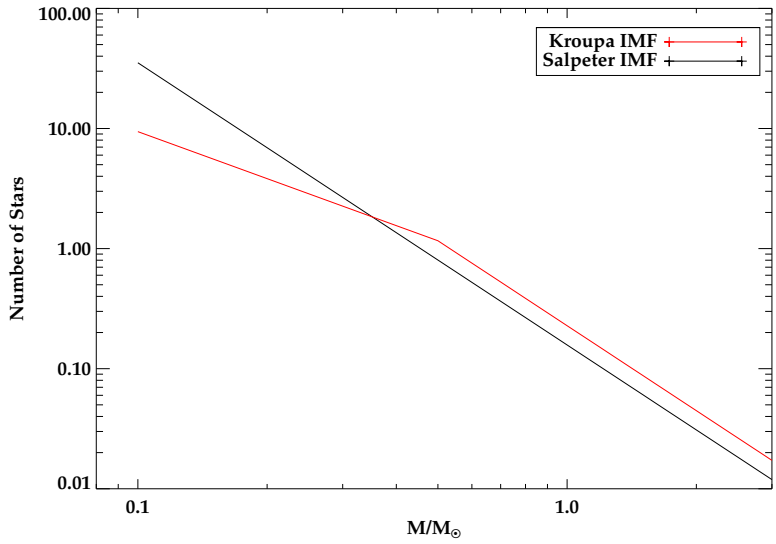

Figure 4.6: A comparison of the number of stars at a given mass predicted by both a Salpeter (black line) and Kroupa (red line) IMF. The distribution in each case is normalised to 1 $\mathrm{M}_{\odot}$.

Many previous studies have assumed a Salpeter IMF in their mass derivations. Therefore to facilitate direct comparisons between this work and other studies (particularly Rodríguez Zaurín et al. (2009) and Tadhunter et al. (2011)), an empirical conversion between the two IMFs has been derived. In order to do this, the stellar templates of Bruzual & Charlot (2003) (hereafter BC03) have been utilised, because these are the templates used in the studies mentioned previously. To establish a conversion factor, the masses derived for the remainder of the sample, presented in the next two chapters were used, as well as the results presented above for the mass of J0025-10. It should be

noted that it may not be the case that the combinations of components would provide acceptable fits using these BC03 templates (in terms of some of the age-sensitive absorption features), however, the matter of interest here is the overall shape of the continuum, rather than the finer details. Figure 4.7 shows the results of this comparison, with the total mass predicted within the spectroscopic apertures by the STARBURST99 templates using a Kroupa IMF plotted against that predicted by the BC03 templates using a Salpeter IMF. In both cases, the fitting was performed using an 8 Gyr unreddened OSP combined with a burst YSP model. The masses shown refer to the total stellar mass within the spectroscopic aperture. It can be seen that, as expected, the mass derived using the BC03 templates with the Salpeter IMF is higher, with an empirically derived conversion factor of 1.36±0.1. This is slightly lower than the standard value of 1.6 found in the literature.

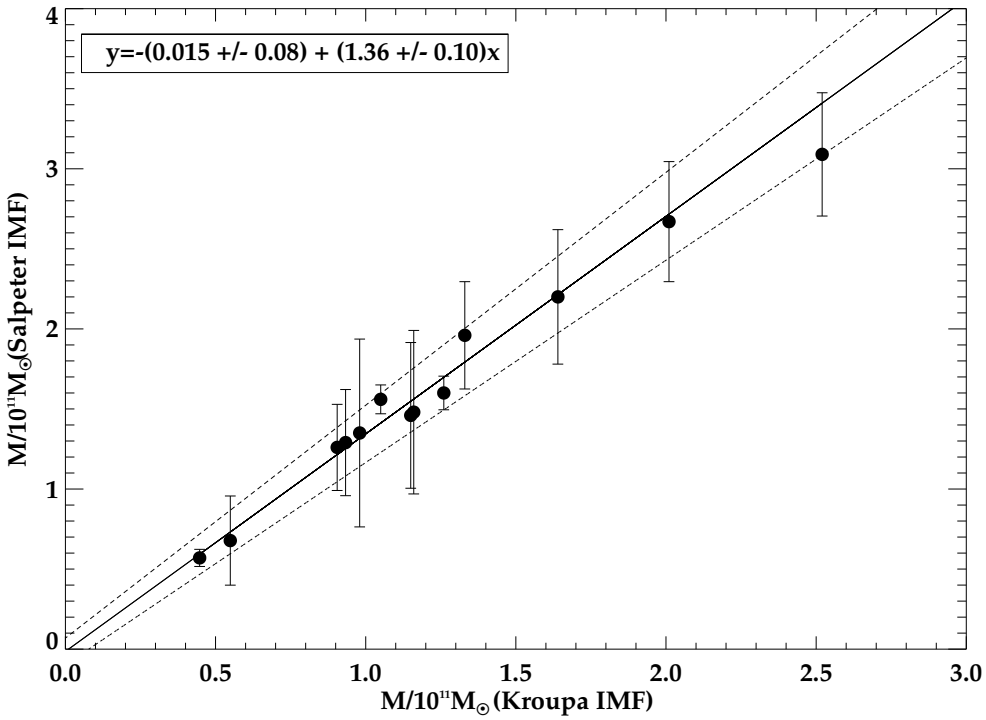

Figure 4.7: The mass derived by assuming a Salpeter IMF plotted against the mass obtained using a Kroupa IMF. The uncertainty is derived by calculating the minimum and maximum mass for each object. The solid line shows the best fit, while the dotted lines show the 1σ uncertainties associated with assuming the minimum and maximum mass for each object.

Evolutionary Tracks

Another crucial factor in the outcome of the population synthesis modelling is the stellar evolutionary models used. These will impact the masses derived in two main forms: the first of these is that different possible assumptions about how hydrogen burning in the core will proceed, will affect the rate at which stars evolve off the main sequence. Because it is the light of the stars at the main sequence turn off that dominates the integrated light of the spectrum, particularly in the simple stellar populations used here, this can lead to a different age determination for the YSP. However, due to the redshifts of the type II quasars studied in this thesis, solar metallicity is a reasonable assumption because the light travel time is ~ 4 Gyr. Therefore, a gas-rich massive galaxy at this epoch would plausibly have a similar composition to that of the Milky Way at the time the Sun was formed.

Once stars have moved off the main sequence, the (fairly uncertain) modelling of highly evolved giant stars becomes important. This is because these stars can contribute a disproportionately large fraction of the total luminosity of the population (Maraston et al., 2006). Therefore, variations in assumptions about their evolutionary time scales and surface temperatures can lead to differences in ages derived from populations synthesis modelling. Both these issues will in turn lead to different mass determinations, because the technique relies on converting the light-weighted age to a stellar mass using a derived mass-to-light ratio, which in turn is dependent on the age of the stellar population.

Metallicity

The assumed metallicity of the population will also impact on the final mass found through population synthesis, because of the effect it will have on the temperature of a star at any given mass. Stars of higher metallicity will be cooler than stars with equivalent mass but with lower metalicity, because of their higher opacity, which also means that they will remain on the main sequence for longer.

All these issues are sources of uncertainty in determining the masses of the population and are difficult to overcome. We cannot know the true IMF in distant galaxies and therefore must assume that it is comparable with that found in our own. Although this does appear to be the case, there is some evidence suggesting that the IMF may vary (e.g. van Dokkum & Conroy 2010; Cappellari et al. 2013). We also do not know the metallicity of the populations, or how it might vary within a population.

4.4.3 J0025-10 in an evolutionary context

The results presented above make it clear that in all three regions of J0025-10 a YSP of age $t_{ysp} < 40$ Myr with low reddening ($0 \leq E(B-V) \leq 0.3$) contributes a large proportion of the total flux. It is striking that similar ages and reddenings are found for these YSPs across the entire system, suggesting that J0025-10 is currently undergoing a galaxy-wide burst of star formation. This finding is interesting in the context of evolutionary scenarios, such as that of Sanders et al. (1988), in which galaxy mergers lead to ULIRGs which then eventually become observable quasars. Such models predict that, at the peak of star formation activity, associated with the time of the coalescence of the two BHs (e.g. di Matteo et al. 2005; Springel et al. 2005; Hopkins et al. 2006), we should observe a dust enshrouded system containing a highly reddened YSP (i.e. a ULIRG), in which any quasar activity that may have been triggered is too deeply embedded for us to detect directly. It is only with the onset of AGN and/or starburst related feedback processes, as the AGN begins to dominate, that the gas and dust are removed, resulting in the quenching of star formation activity. Thus, in the Sanders et al. (1988) scenario, when the quasar becomes directly detectable, it should be hosted by a system in which the two nuclei have coalesced and also have an ageing starburst population.

The properties of J0025-10, displays a number of traits that are contradictory to the evolutionary view of Sanders et al. (1988) in many ways. To begin with, its two nuclei have not yet coalesced and are still separated by ~ 5 kpc. Despite this, J0025-10 already hosts a luminous quasar, clearly detectable in the optical narrow lines, whilst at the same time hosting a massive YSP of $t_{ysp} < 40$ Myr. This strongly implies that the AGN and star formation activity were triggered quasi-simultaneously. However, it cannot be ruled out that at some future point, an even more intense periods of star formation and BH accretion will occur.

It should further be noted that this system appears to have very little (if any) reddening affecting the YSP or narrow emission lines, a result supported by both continuum and emission line modelling. In other words, there is a lack of dust in the regions in which a significant proportion of the YSP currently reside. The obvious implication of this is that the dust in these regions has already been efficiently removed by some process, most likely outflows powered by the AGN or starburst. If this is the case, then this process has been triggered earlier in the merger process than simulations have thus far suggested.

A full discussion of the wider context of AGN triggering and any associated star

burst activity will be deferred to the next Chapter, where the analysis and results for the remainder of the type II quasars, with spectroscopic data (18) are presented in full.

4.5 Summary

Gemini GMOS-S long-slit data have been used to determine the ages and masses of the stellar populations in apertures extracted from three distinct regions of the merging type II quasar system J0025-10. The stellar continuum modelling technique used to determine the ages of the stellar populations in these three apertures has also been tested. The following results have been found.

- The quasar host galaxy component of the system is well fit with a combination of an unreddened 8 Gyr population combined with a YSP of between 20 and 40 Myr with reddenings in the range $0 \leq E(B-V) \leq 0.2$.
- The companion galaxy is well fit with an ISP of 0.5-1 Gyr with a YSP of between 6 and 10 Myr (taking into account the Hβ line equivalent width) and reddenings in the range $0 \leq E(B-V) \leq 0.1$.
- The north eastern tail component is well fit by an OSP/ISP and a YSP of 20–40 Myr with reddenings in the range $0 \leq E(B-V) \leq 0.1$. It is also well fit by an ISP of 0.5 Gyr with a YSP of 1 - 6 Myr. Though we cannot discriminate by the quality of the fit alone, the measured equivalent width of the Hβ line favours this latter combination.
- The total stellar mass of the system is $3.7 \times 10^{10} M_{\odot} <$ M$< 1.7 \times 10^{11} M_{\odot}$ ($0.3m_{*} - 1.2m_{*}$), which is lower than the stellar masses previously found for quasar host galaxies.
- The regions of age–reddening in which values of $\chi^2_{red} < 1$ are found is not strongly dependent on the positioning of the continuum bins used for modelling.
- The importance of subtracting the nebular continuum from the data before modelling the stellar components is dependent on the proportion of the total flux it contributes just below the Balmer edge.

The young ages of the stellar populations in all three regions of J0025-10 probed by these high quality spectra, unambiguously demonstrate that the luminous quasar-like

nucleus in J0025-10 has been triggered at around the same time as a major episode of star formation, immediately prior to the coalescence of the nuclei in a gas-rich merger. The low reddening deduced for all three apertures using the YSP continuum and the narrow line emission measurements clearly indicate that, even at this early stage of the merger, outflows driven either by the AGN or starburst have been effective in driving much of the dust and gas from the visible star formation regions. These results are fully consistent with the trend found by Tadhunter et al. (2011), that luminous quasars host starburst populations with $t_{ysp} < 0.1$ Gyr.

Chapter 5

The stellar populations of type II quasar host galaxies

5.1 Introduction

In Chapter 4, the stellar population synthesis modelling results for the merging system J0025-10 were presented. It was shown that, in this case, the starburst and quasar activity have been triggered quasi-simultaneously, a finding which is contrary to evolutionary scenarios such as that presented by Sanders et al. (1988), and simulations of galaxy mergers/AGN feedback (di Matteo et al., 2005; Springel et al., 2005; Hopkins et al., 2006; Johansson et al., 2009). However, in order to properly establish whether this is a common occurrence for type II quasars, or whether it is more often the case that a substantial delay is detected between the triggering of the starburst and AGN activity, the techniques described in depth in Chapter 4 have been applied to the remainder of the type II quasar sample, which was outlined in Chapter 2. Thus, by establishing whether a detectable YSP is present in these type II quasar host galaxies, and if so, whether the ages of these populations are coincident with those expected for a typical quasar lifetime (1-100 Myr; Martini & Weinberg 2001), it will be possible to establish the timing of the quasar activity in relation to the merger.

The modelling techniques and results are presented in this chapter in the following way. In Sections 5.2 and 5.3, the modelling techniques and strategies, which were described in depth in Chapter 4 Section 4.2.1, are briefly recapped. In section 5.4, the results of the stellar population synthesis modelling is presented for each of the objects individually. The main uncertainties inherent in the modelling process are then discussed in Section 5.5, and then results for the full sample are summarised in Section 5.6. In

Section 5.7, these results are discussed in the context of evolutionary scenarios and also compared with results derived for other classes of merging/active objects, and finally, the main findings of this chapter are summarised is Section 5.9.

5.2 Nebular Subtraction

The method used for the nebular subtraction was described in detail in Chapter 4. As described there, as a first step, it is imperative to subtract a stellar model from the spectra, in order to account for the underlying stellar absorption. The flux of the Hβ emission line can then be measured and thus, it is possible to construct the nebular model. In Table 5.1 the ages, reddenings and total flux contributions of the different components of the initial stellar models subtracted are given.

After performing the subtraction of the stellar template, the flux of the Hβ line was measured from the resulting spectrum. Although it would obviously be preferable to measure any reddening of the nebular continuum by using the Hα/Hβ ratio, because these are the strongest lines and also have a greater wavelength separation, the strong fringing at the longest wavelengths does not allow reliable measurements of the Hα flux. In the case of the higher redshift objects in the sample, Hα is shifted out of the spectral range altogether. Therefore, in order to make some estimate of the amount of reddening that the nebular continuum is subjected to in each object, the fluxes of the Hγ and Hδ lines were also measured. However, due to the lower equivalent widths of the lines, in some cases the errors were larger than the value of the ratio. In such cases the values were disregarded.

Table 5.2 shows that, in the majority of cases, it was not possible to make a reliable measurement of the Balmer decrements either because the Hγ and Hδ lines were too faint and/or because no reliable measurement of the Hα flux could be made. Therefore, in order to maintain a consistent approach, a maximum nebular subtraction (i.e. applying no reddening to the model nebular continuum) was attempted first. The resulting nebular subtracted spectrum was then inspected in order to determine if this resulted in a non-physical step in the spectrum around the region of the Balmer edge (3646 Å). If this was the case, reddening that was consistent with the Balmer decrement measured from the stellar-subtracted spectrum was applied. However, in the cases where no Balmer decrement could be measured, no reddening was applied to the model nebular continuum. In all cases where this was necessary, this procedure produced an acceptable results, with no clear over-subtraction at the Balmer edge. This is not unexpected, because the fact

that the higher order Balmer emission lines are too weak to measure accurately, implies a weaker nebular continuum. Inspection of Table 5.2 demonstrates that, when the nebular continuum contributes $< 20\%$ of the flux below the Balmer edge, it was not possible to measure the Balmer decrements. This weaker nebular continuum means that the result of the subtraction will not be too sensitive to any reddening correction applied.

The results presented in column 5 of Table 5.2 make it clear that it is important to consider the effects of the nebular continuum before embarking on the modelling process. In the vast majority of cases, the nebular continuum accounts for over 15% (ranging from 3–28%) of the total flux just below the Balmer edge, measured in the wavelength range 3540–3640Å (where the contribution from the nebular continuum will be most pronounced). Failure to account for this component could lead to underestimations of the true ages of the YSPs, because the stellar spectrum will appear bluer than it actually is. The proportion of the UV flux attributed to the nebular continuum in these type II quasars host galaxies, is in good agreement with that found for the 2 Jy PRG (Tadhunter et al., 2002), where values ranging from 3–28%, are found, and the majority of the sample also has contributions above 15% over the same wavelength range.

Table 5.1: The details of the stellar models subtracted from the spectra in order to measure the Hβ flux. Column 1 gives the name of the object, whilst column 2 denotes the normalising bin that was used for the modelling. Columns 3 and 4 show the age and flux contribution of the OSP. Columns 5-8 give the assumed formation history, the age in Gyr, the percentage contribution to the total flux in the normalising bin and the reddening of the YSP component respectively. For the models that required a power-law component, the percentage contribution to the flux in the normalising bin and the spectral index α ($F_\lambda \propto \lambda^\alpha$), are given in columns 9 and 10.

Name	Normalising Bin (Å)	OSP Age (Gyr)	OSP Flux (%)	Formation History	YSP Age (Gyr)	YSP Flux (%)	E(B-V)	Power-law (%)	α
J0114+00	4395–4455	8	69.0	B	0.04	36.7	0.8	–	–
J0123+00	4725–4785	8	49.0	B	5	24.3	0.6	31.2	-0.89
J0142+14	4593–4653	–	–	–	–	–	–	–	–
J0217-00	4518–4578	8	19.1	B	0.05	82.8	0.5	–	–
J0217-01	4502–4562	8	59.4	B	0.02	32.3	0.9		–
J0218-00(Q)	4410–4470	8	35.9	B	0.03	62	0.1	–	–
J0218-00(E)	4410–4470	8	28.0	B	0.03	69.2	0.2	–	–
J0227+01	4423–4483	8	26.7	C	0.04	68.7	0.6	–	–
J0234-07	4510–4570	8	83.1	B	0.001	16.7	0.1	–	–
J0249+00	4420–4480	8	31.2	B	0.03	69.1	0.7		–
J0320+00	4427–4487	8	40.6	B	0.02	56.5	0.1	–	–
J0332-00(Q)	4475–4535	8	24.6	B	4	34.3	0.2	38.2	-2.03
J0332-00(C)	4475–4535	8	58.0	B	0.9	21.7	0	16.2	-0.03
J0334+00	4405–4465	8	23.0	B	0.03	78.1	0.1	–	–
J0848+01	4523–4583	8	56.7	B	0.05	39.2	0.4	–	–
J0904-00	4760–4820	8	14.8	B	0.02	87.0	0.3	–	–
J0923+01	4415–4475	8	7.4	B	0.04	90.8	0.5	–	–
J0924+01	4423–4483	2	32.0	B	0.003	65.8	1.1	–	–
J0948+00	4520–4580	2	41.6	B	0.1	55.6	0.3	–	–
J2358-00	4417–4477	8	21.7	B	0.02	79.1	0.5	–	–

Name	Hγ/Hβ	Hδ/Hβ	Hα/Hβ	Nebular Continuum (%)	E(B-V)
J0025-10(Q)	0.41 ±0.03	0.22 ±0.02	–	3	–
J0025-10(G)	0.47 ±0.04	0.04 ±0.02	–	10	–
J0025-10(T)	0.51 ±0.04	0.29 ±0.03	–	9	–
J0114+00	–	–	–	14	–
J0123+00	0.43 ±0.03	0.22 ±0.02	–	20	0.2
J0142+14	–	–	–	–	–
J0217-00	–	–	–	14	–
J0217-01	–	–	–	20	–
J0218-00(Q)	0.37 ±0.02	–	–	17	–
J0218-00(E)	0.32 ±0.02		–	17	–
J0227+01	–	–	–	11	–
J0234-07	0.42 ±0.12	–	2.41 ±0.12	25	0.25
J0249+00	0.35 ±0.14	–	–	25	–
J0320+00	0.43 ±0.17	–	–	8	0.2
J0332-00(Q)	–	–	–	4.1	–
J0332-00(C)	–	–	–	3.3	–
J0334+00	0.38 ±0.02	0.21 ±0.01	–	23	–
J0848+01	–	–	–	19	–
J0904-00	0.46 ±0.17	–	3.82 ±1.3	13	–
J0923+01	–	–	–	14	–
J0924+01	0.33 ±0.09	–	4.26 ±1.43	14	0.3
J0948+00	–	–	–	15	–
J2358-00	0.39 ±0.08	0.23 ±0.07	–	28	–

Table 5.2: The Balmer decrements measured from each of the apertures extracted from the full sample of type II quasars. Column 1 gives the name of the object and if appropriate, which aperture is being referred to. Column 2, 3 and 4 give the Hγ/Hβ Hδ/Hβ and Hα/Hβ ratios respectively along with the associated fitting error. Column 5 gives the percentage contribution of the nebular continuum to the total flux in the wavelength range 3540–3640Å and the final column gives the E(B-V) value of reddening applied to the model nebular continuum before subtraction from the data. In the cases in which a reddening correction was applied before subtraction, the value shown in column 5 refers to the percentage of the total flux contributed by the model after the reddening correction has been applied. No value was calculated for J0142+14 due to the fact that Hβ fell outside the spectral range.

5.3 Modelling Strategy

In this section, the modelling strategy adopted, which was described in depth in Chapter 4, is recapped. The stellar population models used here were generated using the STARBURST99 code of Leitherer et al. (1999), assuming both an instantaneous burst star formation history, with an initial mass of $10^6\,M_\odot$, and a continuous star formation history, assuming a star formation rate of $100\,M_\odot\ yr^{-1}$. In both cases, solar metallicity and a Kroupa IMF were assumed. The burst models were allowed to run until 5 Gyr, because this is mapping the passive ageing of a simple stellar population, while the continuous formation models were allowed to run until 200 Myr, because it is unlikely that the starburst could be sustained over longer periods of time (e.g. Springel et al. 2005; Johansson et al. 2009). For the purposes of the modelling, nine combinations of components, outlined below, were adopted, which reflect viable possibilities for the various components which contribute to the observed spectrum.

1. An unreddened, 8 Gyr OSP combined with a power-law component, accounting for the case of an OSP plus a scattered or direct AGN component.

2. An unreddened, 8 Gyr underlying population, combined with an instantaneous burst star formation model, with ages $0.001 < t_{YSP}\ (\mathrm{Gyr}) < 5.0$ and reddening $0 \leq E(B-V) \leq 2.0$.

3. An unreddened, 2 Gyr underlying population, combined with an instantaneous burst star formation model, with ages $0.001 < t_{YSP}\ (\mathrm{Gyr}) < 2.0$ and reddening $0 \leq E(B-V) \leq 2.0$.

4. An unreddened, 8 Gyr underlying population, combined with a continuous star formation model, with ages $0.001 < t_{YSP}\ (\mathrm{Gyr}) < 0.2$ and reddening $0 \leq E(B-V) \leq 2.0$.

5. An unreddened, 2 Gyr underlying population, combined with a continuous star formation model, with ages $0.001 < t_{YSP}\ (\mathrm{Gyr}) < 0.2$ and reddening $0 \leq E(B-V) \leq 2.0$.

6. The same as 2 with the addition of a power-law component.

7. The same as 3 with the addition of a power-law component.

8. The same as 4 with the addition of a power-law component.

9. The same as 5 with the addition of a power-law component.

In the majority of cases in which the aperture has been extracted from the nuclear region of the quasar host galaxy, all nine modelling combinations were applied to the nebular subtracted spectra. In the majority of cases where the aperture has been extracted from an extended region of the quasar host galaxy or a companion nucleus, only combinations 2 to 5 have been applied. This is because it is unlikely that there will be a significant contribution to the flux from scattered quasar light in these apertures.

In order to perform the modelling, a normalising bin in the region of 4400 – 4800 Å was selected, avoiding strong emission lines, chip gaps, dead columns and other cosmetic defects. The normalising bin used for each object is shown in column 2 of Table 5.1. A flux calibration error of ±5% was assumed (see Chapter 2).

5.4 Results For Individual Objects

In the following section, the results are presented for each of the objects for each of the successful combination of components discussed in Section 5.3. In all cases, the overall shape, higher order Balmer lines, Ca II K and G-band fits for solutions that produce $\chi^2_{red} < 1$ were visually examined, in order to determine if they could be deemed acceptable. If any of these regions of the spectrum produced a very poor fit, then the combination of components was rejected as an acceptable solution. Due to the limitations of CONFIT, this inspection must be made by eye. However, in future it would be preferable to automate the rejection of solutions with poor fits around the stellar features, by updating the fitting routine to give more weight to bins in these regions. This is particularly true around Ca II K because this stellar absorption feature is not in-filled by any emission lines related to either the AGN or to star forming processes. Automating the process will make the rejection of solutions with $\chi^2_{red} < 1$ more objective. In cases where a large number of combinations produce $\chi^2_{red} < 1$, a representative sample of combinations were examined, taking account of the allowed values of YSP/ISP ages and associated reddenings.

5.4.1 J0114+00

Unfortunately, no Gemini GMOS-S spectrum is available for J0114+00 and therefore, the SDSS database has been utilised instead. Although this spectrum has a lower signal-to-noise (S/N) than the Gemini GMOS-S data, it is still of adequate quality and covers

OSP Age (Gyr)	PL	Model	OSP Flux (%)	YSP Age (Gyr)	YSP Flux (%)	E(B-V)	Power-law (%)
8	No	B	53–82	0.004–0.007	17–44	0.8–1.3	–
			51–81	0.02–0.4	19–48	0.6–1.0	–
		C	63–78	0.008	20–33	1.2	–
			57–79	0.06–0.2	20–41	0.9–1.1	–
	Yes	B	50–82	0.004–0.007	17–47	0.9–1.3	0–10
			47–84	0.03–0.2	8–51	0.3–1.1	0–16
		C	53–80	0.08–0.2	18–44	1.0–1.1	0–7
2	No	B	0–71	0.5–2	30–98	0.2–1.0	–
		C	–	–	–	–	–
	Yes	B	0–71	0.5–2	28–100	0.2–1.0	0–10
		C	–	–	–	–	–

Table 5.3: Results of the stellar population synthesis modelling for J0114+00. Column 1 gives the age of the assumed underlying, unreddened old/intermediate age stellar population. Column 2 denotes whether a power-law component was included in the fit and column 3 gives the star-formation history model used (Burst or Continuous). Column 4 shows the range of OSP fluxes that are allowable for each fitting combination, while columns 5, 6 and 7 show the range of YSP ages, fluxes and reddenings produced by that combination of components. The final column gives the range of power-law contribution for that combination of components, if included.

a sufficient wavelength range to perform spectral synthesis modelling.

After performing the initial run (combination 2), the stellar model, which included a YSP with t_{YSP}= 0.04 Gyr and E(B-V)= 0.8 (see Table 5.1), was subtracted. The nebular continuum generated from the stellar-subtracted spectrum contributes $\sim$ 15% of the total flux blue-ward of the Balmer edge (Table 5.2). In this case, it was not possible to make a reliable estimate of the Balmer decrements, because of the intrinsically low equivalent widths of the Hγ and Hδ emission lines, and the low S/N of these data. Therefore, no reddening correction was applied to the model nebular continuum before subtraction.

Table 5.3 shows that, it was possible to achieve acceptable fits for all combinations that include an unreddened 8 Gyr OSP, however, acceptable fits were only achieved for combinations including an unreddened 2 Gyr population when a burst model was used.

Figure 5.1 shows contour plots for the six combinations in which the fitting produced solutions with $\chi^2_{red} < 1$. For combination 2 (Figure 5.1(a)), there are three regions with $\chi^2_{red} < 1$, and for combination 6 (Figure 5.1(c)), there are two. Visual inspection of the fits in the regions around age-sensitive stellar absorption features allows the conclusion that these are all viable solutions.

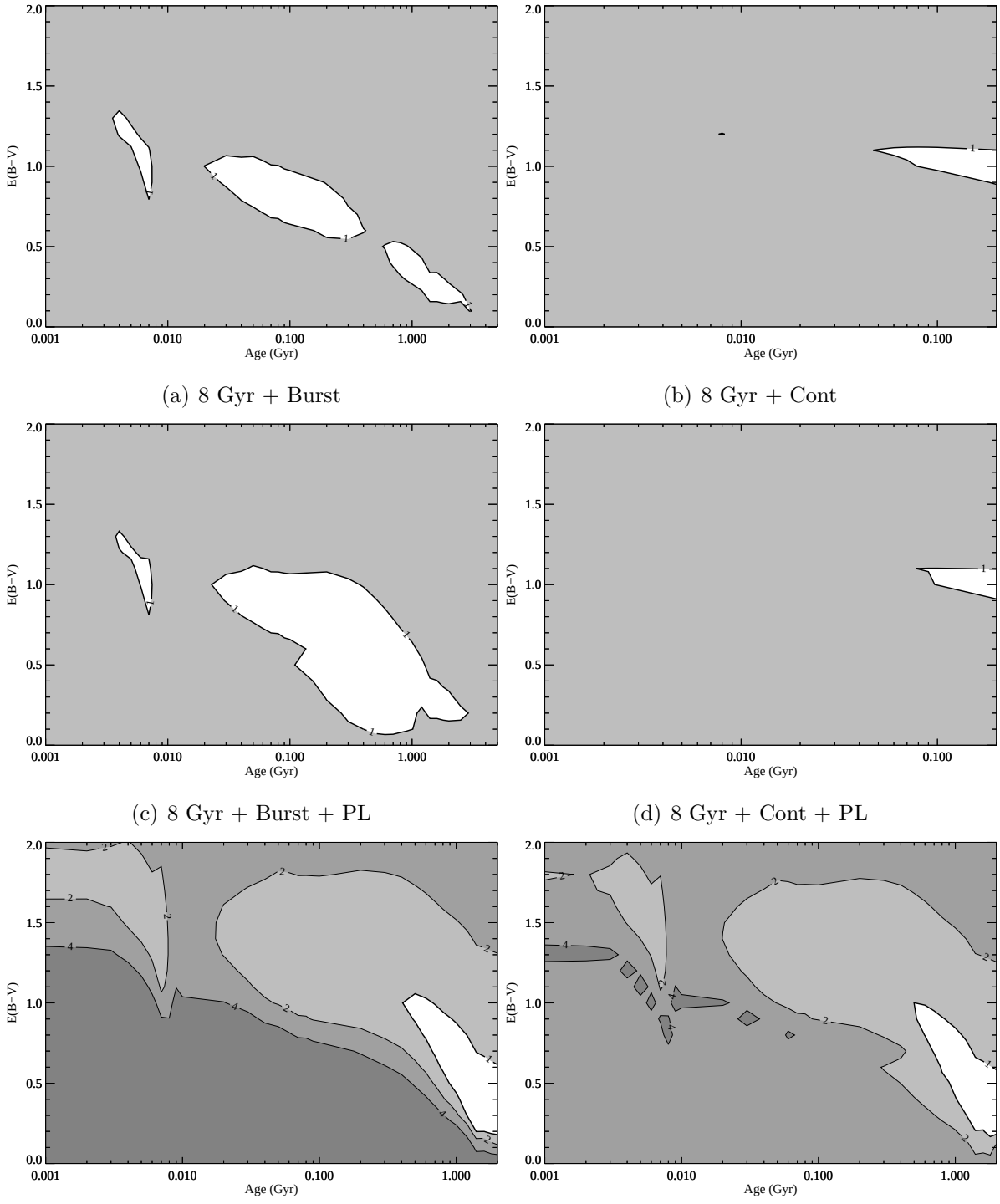

(a) 8 Gyr + Burst

(b) 8 Gyr + Cont

(c) 8 Gyr + Burst + PL

(d) 8 Gyr + Cont + PL

(e) 2 Gyr + Burst

(f) 2 Gyr + Burst + PL

Figure 5.1: Plots showing the contours of χ^2_{red} for the various combination of components that produce an acceptable fit for J0114+00. The particular combination used is given in the sub-caption for the plot. The region in which $\chi^2_{red} < 1$ is shown in white, and the values of χ^2_{red} are given on the contour lines.

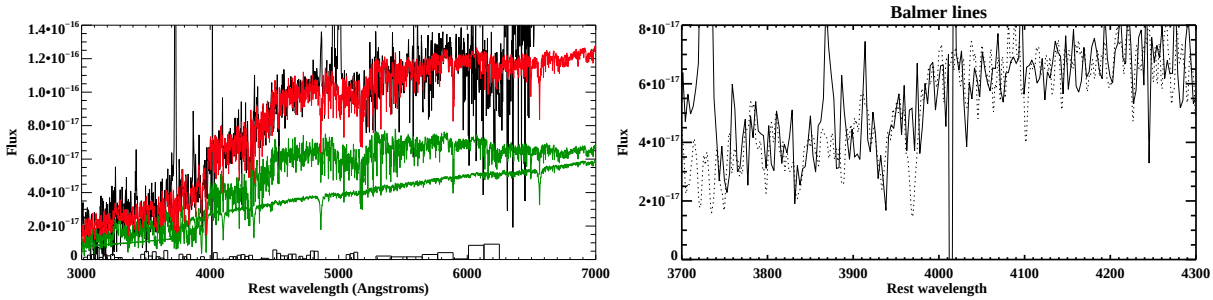

(a) 8 Gyr + Burst - Main fit

(b) 8 Gyr + Burst - Balmer Lines

Figure 5.2: An example of an acceptable fit produced by CONFIT for J00114+00. This fit is produced by combination 2 and includes a YSP with t_{YSP}= 0.06 Gyr and E(B-V)= 0.9.

Table 5.3 demonstrates that for this particular object, the OSP dominates the flux in the normalising bin, which leads to the models being relatively unconstrained. Therefore, the fits for the burst models produce a wide range of ages and reddenings ($0.004 \leq t_{YSP}$ (Gyr) ≤ 0.4 and $0.6 \leq E(B-V) \leq 1.3$) for combination 2).

Figure 5.2 shows an example of an acceptable fit generated by combination 2 with t_{YSP}= 0.06 Gyr and E(B-V)= 0.9. Further examples of acceptable fits for each combination can be found in Appendix A, Section A.2

5.4.2 J0123+00

The initial modelling for J0123+00 was performed using combination 6, because it was not possible to obtain acceptable fits without the inclusion of a power-law component. However, this resulted in a wide range of ages and reddenings producing acceptable fits ($2 \leq t_{ISP}$ (Gyr) ≤ 5 and $0.4 \leq E(B-V) \leq 1.2$), which, based on age-sensitive stellar features, were impossible to differentiate between. Therefore, the stellar model that produced the lowest χ^2_{red} value was subtracted, which included an ISP with $t_{ISP} = 5.0$ Gyr, $E(B-V) = 0.6$ and a power-law component, the details of which can be found in Table 5.1.

The nebular continuum model generated for J0123+00 from the stellar-subtracted spectrum produces a large contribution to the total flux blue-wards of the Balmer edge ($\sim$ 48%), and subtraction of this model without first applying reddening of the value derived from the Balmer line ratios (Table 5.2), results in an unphysical step in the spectrum. Therefore, the model continuum was reddened using a value of E(B-V)= 0.2, which is the mean value of reddening derived from the Hγ/Hβ and Hδ/Hβ ratios. The

OSP Age (Gyr)	PL	Model	OSP Flux (%)	YSP Age (Gyr)	YSP Flux (%)	E(B-V)	Power-law (%)
8	No	B	–	–	–	–	–
		C	–	–	–	–	–
	Yes	B	52–81	0.001 –0.01	3–26	0.0–0.2	12–40
			0–67	0.001–5	1–96	0.2–2.0	2–35
		C	58–82	0.001–0.05	3–19	0.0–0.4	8–40
			55–86	0.001–0.2	3–46	1.1–2.0	2–33
2	No	B	–	–	–	–	–
		C	–	–	–	–	–
	Yes	B	–	–	–	–	–
		C	–	–	–	–	–

Table 5.4: The results of the stellar population synthesis modelling for J0123+00. The definitions for each of the columns is the same as that given in the caption for Table 5.3.

reddened nebular continuum contributes $\sim 20\%$ of the flux just below the Balmer edge, and does not result in an over subtraction of the nebular continuum component.

Table 5.4 and Figure 5.3 show that, when an 8 Gyr population is combined with either a burst or continuous star formation model and a power-law component, it is possible to achieve an acceptable fit to the spectra. In both cases, there are two regions in Figure 5.3 that have $\chi^2_{red} < 1$ however, it was not possible to determine from the fits which one provides the better solution, and thus the importance of the power-law component, which Table 5.4 shows can range from $2 \leq \mathrm{PL}\% \leq 40$.

When attempting to perform the stellar population modelling for J0123+00, it has proven difficult to constrain the ages of the YSP/ISP component. Once again (as for J0114+00), this may be due to the fact that the flux is dominated by the OSP for nearly all possible acceptable solutions, making it difficult to accurately model the lower level YSP contribution.

Figure 5.4 shows an example of an acceptable fit using combination 6, which in this case include a young component of t_{ISP}= 4 and E(B-V)= 0.3. Further examples of acceptable fits can be found in Appendix A Section A.3

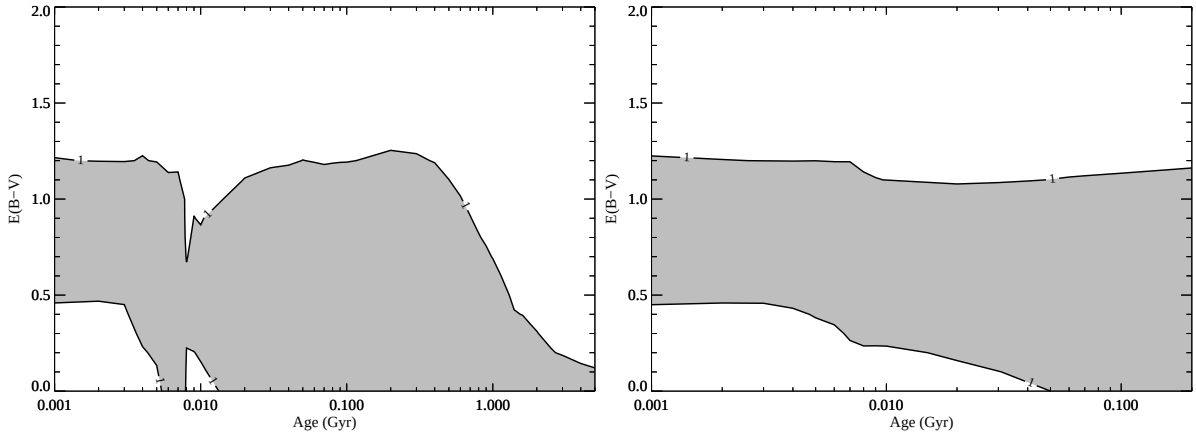

(a) 8 Gyr + Burst + PL

(b) 8 Gyr + Cont + PL

Figure 5.3: Plots showing the contours of χ^2_{red} for the various combination of components that produce an acceptable fit for J0123+00. The particular combination used is given in the sub-caption for the plot. The region in which $\chi^2_{red} < 1$ is shown in white, and the values of χ^2_{red} are given on the contour lines.

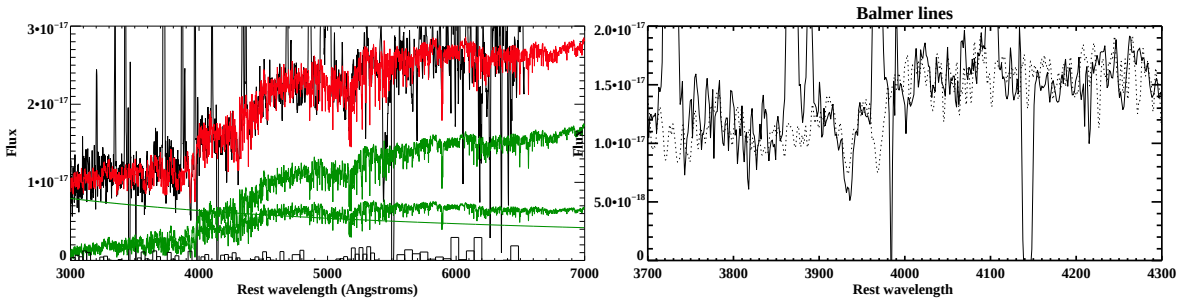

(a) 8 Gyr + Burst + PL - Main Fit

(b) 8 Gyr + Burst + PL - Balmer Lines

Figure 5.4: An example of an acceptable fit produced by CONFIT for J0123+00. This fit is generated by combination 6 and includes an ISP with t_{ISP}= 4 and E(B-V)= 0.3.

5.4.3 J0142+14

Unlike the other objects for which GMOS-S spectroscopic data is available, for J0142+14 only a relatively limited spectral range was observed, with only the blue grism (Chapter 2) being utilised in this case. However, modelling of this object is still well constrained because the spectrum has a high S/N as well as strong Balmer absorption lines, which are an unambiguous feature of a young population of stars. The rest-frame spectral range covered by this spectrum is 2813 – 4863 Å, which means that the majority of the Hβ flux falls outside of the spectrum, thus preventing the nebular from being subtracted before the modelling.

Table 5.5 shows that, it was only possible to achieve acceptable fits to the spectrum

OSP Age (Gyr)	PL	Model	OSP Flux (%)	YSP Age (Gyr)	YSP Flux (%)	E(B-V)	Power-law (%)
8	No	B	2–32	0.05–0.1	72–98	0.2–0.4	–
		C	–	–	–	–	–
	Yes	B	0–20	0.04–0.4	52–104	0.1–0.5	0–48
		C	–	–	–	–	–
2	No	B	0–22	0.04–0.1	70–99	0.2–0.5	–
		C	–	–	–	–	–
	Yes	B	0–42	0.04–0.1	62–104	0.2–0.5	0–45
		C	–	–	–	–	–

Table 5.5: The results of the stellar population synthesis modelling for J0142+14. The definitions for each of the columns is the same as that given in the caption for Table 5.3.

when using a burst model of star formation, both with and without the inclusion of a power-law component. In all cases, where an adequate fit was achieved, the allowable ages are very similar ($0.04 \leq t_{YSP}$ (Gyr) ≤ 0.1), except in the case of combination 6, where the maximum allowable age is 0.4 Gyr. In all cases, the reddening of the YSP is $0.1 \leq E(B-V) \leq 0.5$, and the flux of the YSP dominates the total flux of the system, in some cases accounting for 100 % of the flux.

Figure 5.5 shows the contours of χ^2_{red} for the combinations of components that produced reasonable fits. In all four cases, there are a few fits with $t_{YSP} = 0.007$ Gyr that have $\chi^2_{red} < 1$ but in all cases, visual inspection of the fits shows that they are not acceptable due to the fact that they strongly over-predict the absorption at Ca II K. In the cases that also include a power-law component, solutions with older ages and higher values of reddening also have $\chi^2_{red} < 1$, however, the highest ages and reddenings can be ruled out because they produce a poor overall fit to the shape of the spectrum.

It is interesting to note that J0142+14 is classified as undisturbed in terms of its morphology, and appears to be relatively compact in the deep r'-band image presented in Chapter 3, Figure 3.1(d). However, the modelling results presented here combined with the clearly detectable Balmer absorption lines in the spectrum (illustrated in Figure 5.6(b)), make it clear that there has been a powerful episode of star formation within the last 0.4 Gyr. This suggests that J0142+14 may be an 'E+A' galaxy, which is thought to be a short lived phase in which a galaxy transforms from star-forming to passively evolving (Tran et al., 2003, 2004). These galaxies are characterised by weak nebular lines (associated with star formation) such as [OII]λ3727 and strong absorption lines, such a Hδ, characteristics which are clearly visible in the spectrum of J0142+14 (Chapter 2 Figure 2.3).

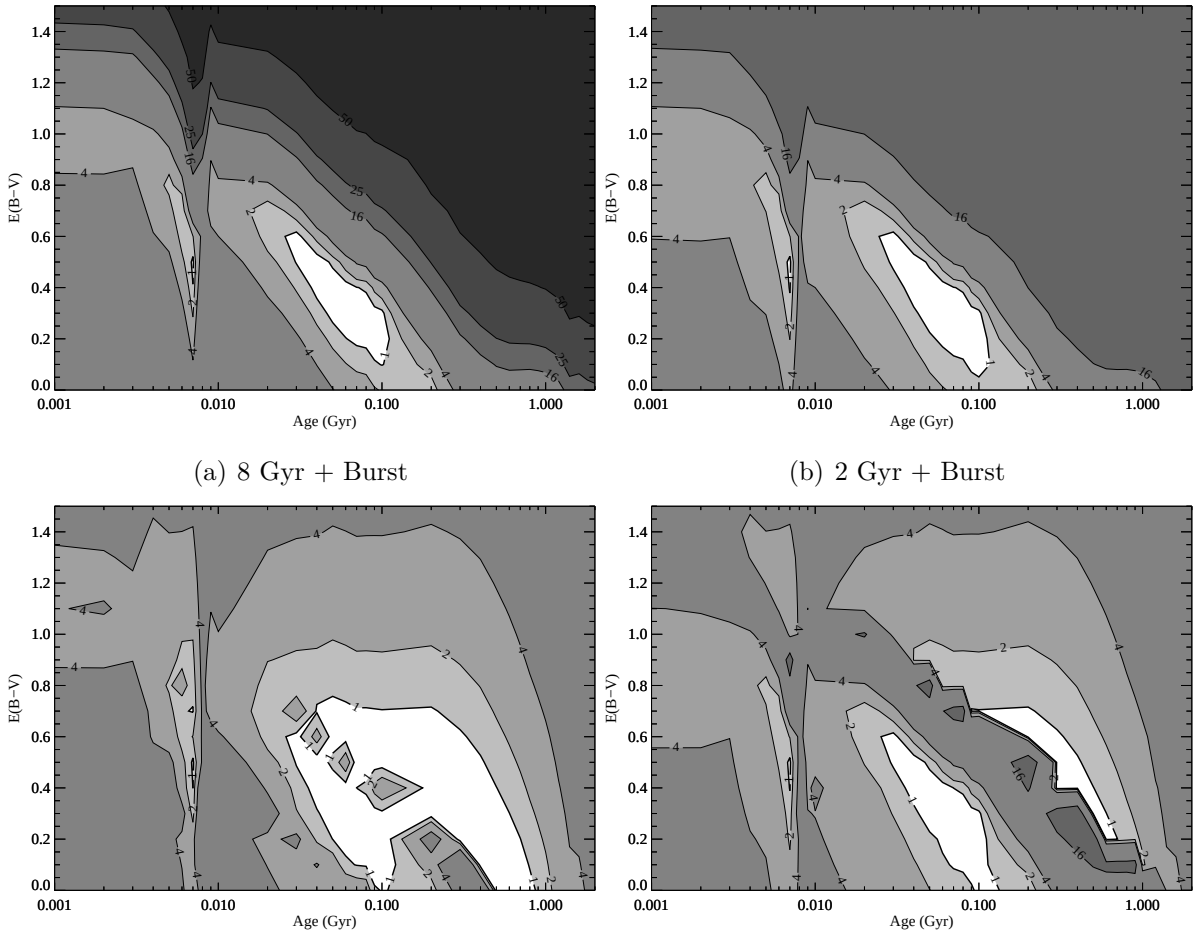

(a) 8 Gyr + Burst

(b) 2 Gyr + Burst

(c) 8 Gyr + Burst + PL

(d) 2 Gyr + Burst + PL

Figure 5.5: Plots showing the contours of χ^2_{red} for the various combination of components that produce an acceptable fit for J0142+14. The particular combination used is given in the sub-caption for the plot. The region in which $\chi^2_{red} < 1$ is shown in white, and the values of χ^2_{red} are given on the contour lines.

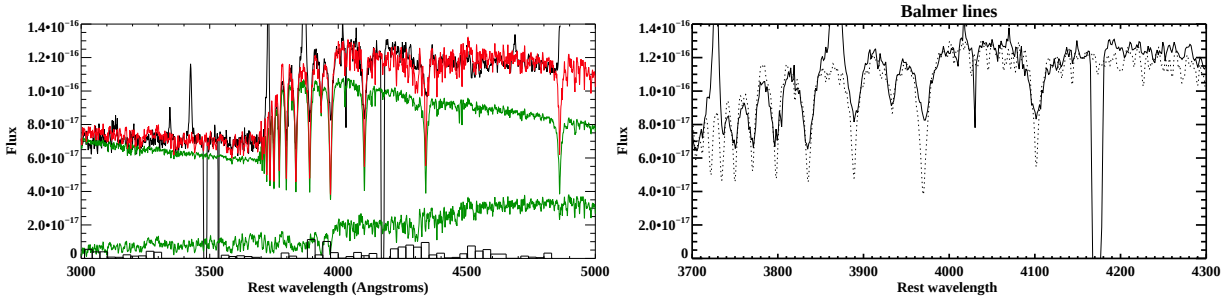

(a) 8 Gyr + Burst - Main Fit

(b) 8 Gyr + Burst - Balmer Lines

Figure 5.6: An example of an acceptable fit produced by CONFIT for J0142+14. This fit is produced by combination 2 and includes a YSP with $t_{YSP} = 0.08$ Gyr with $E(B-V) = 0.2$.

Swinbank et al. (2012) present integral field unit (IFU) observations for 11 E+A galaxies ($0.07 < z < 0.12$) and find that 90% of their sample have residual rotational motion, with the A type stars spread throughout the galaxy, a finding which they attribute to previous minor/major merger activity. It is plausible that this is also the case for J0142+14 implying that, even though no evidence of a recent merger is detected, it is likely that one has occurred fairly recently.

Figure 5.6 shows an example of a fit produced using combination 2, which includes a YSP of $t_{YSP} = 0.08$ Gyr with $E(B-V) = 0.2$. Further examples of fits for the successful combinations can be found in Appendix A Section A.4

5.4.4 J0217-00

After the initial modelling of J0217-00 (using combination 2), a stellar model with a YSP $t_{YSP} = 0.05$ Gyr and $E(B-V) = 0.5$ was selected for subtraction, and the nebular continuum generated from the stellar-subtracted spectrum contributes $\sim$ 14% of the total flux just below the Balmer edge (3540 - 3640 Å). In this case, it was not possible to determine any values for the Balmer decrements because Hγ falls directly adjacent to a chip gap, and the low equivalent width of Hδ results in uncertainties which are larger than the measured values. Therefore, it was not possible to apply a reddening correction to the nebular continuum before subtracting it from the spectrum, however this did not result in an unphysical step at the Balmer edge.

OSP Age (Gyr)	PL	Model	OSP Flux (%)	YSP Age (Gyr)	YSP Flux (%)	E(B-V)	Power-law (%)
8	No	B	0–26	0.06–0.1	75–100	0.5–0.6	–
		C	–	–	–	–	–
	Yes	B	0–37	0.06–0.4	62–92	0.1–0.6	0–33
		C	–	–	–	–	–
2	No	B	0–37	0.06–0.1	65–100	0.5–0.6	–
		C	–	–	–	–	–
	Yes	B	0–40	0.06–0.4	52–100	0.2–0.6	0–32
		C	–	–	–	–	–

Table 5.6: The results of the stellar population synthesis modelling for J0217-00. The definitions for each of the columns is the same as that given in the caption for Table 5.3.

Table 5.6 shows that, it was only possible to achieve acceptable fits when a burst component was included in the model. Figure 5.7, shows that in all cases, there are two regions where $\chi^2_{red} < 1$, however, inspection of the fits associated with these younger

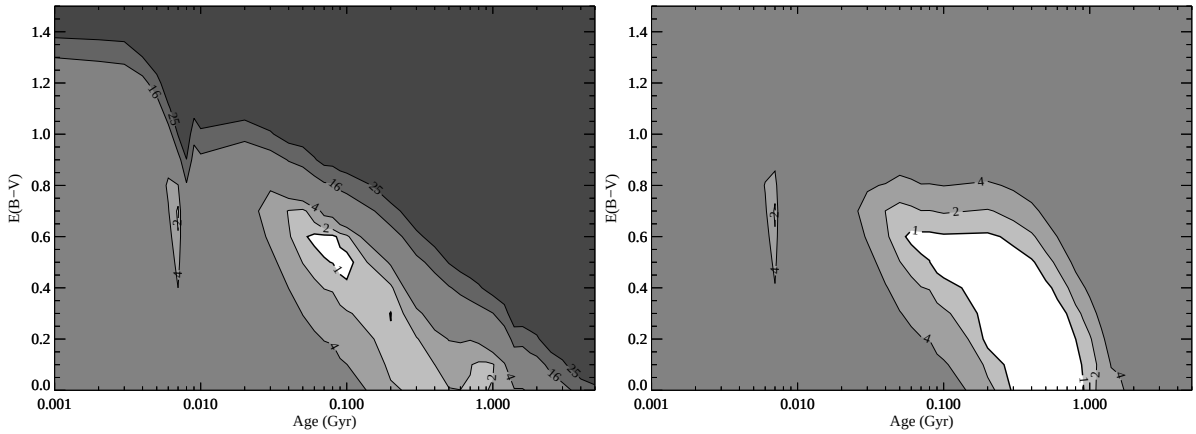

(a) 8 Gyr + Burst

(b) 8 Gyr + Burst + PL

(c) 2 Gyr + Burst

(d) 2 Gyr + Burst + PL

Figure 5.7: Plots showing the contours of χ^2_{red} for the various combination of components that produce an acceptable fit for J0217-00. The particular combination used is given in the sub-caption for the plot. The region in which $\chi^2_{red} < 1$ is shown in white, and the values of χ^2_{red} are given on the contour lines.

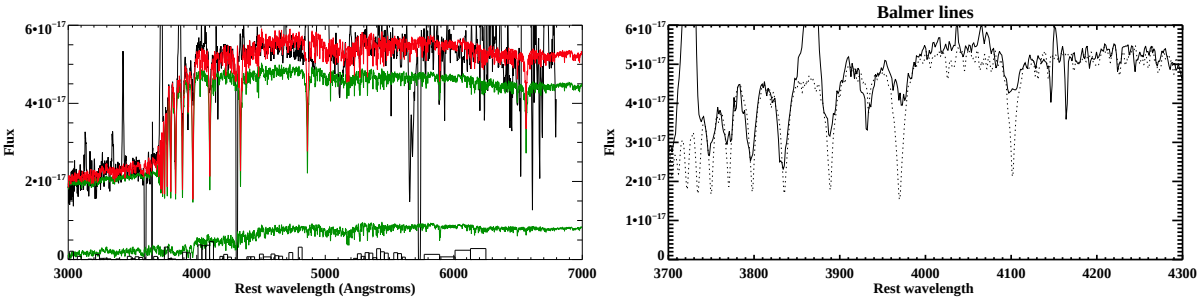

(a) 8 Gyr + Burst - Main fit

(b) 8 Gyr + Burst - Balmer Lines

Figure 5.8: An example of an acceptable fit produced by CONFIT for J0217-00. This fit was produced by using combination 2 and includes a YSP with $t_{YSP} = 0.1$ and $E(B-V) = 0.5$.

regions showed that these models provide a poor fit for Ca II K because they strongly over-predict the strength of the absorption, and therefore, these solutions were discarded.

Table 5.6 shows that for both cases in which the spectrum was modelled with no power-law component (combinations 2 and 3), the acceptable ages are in the range $0.06 \leq t_{YSP}$ (Gyr) ≤ 0.1 and the associated values of reddening are in the range $0.5 \leq E(B-V) \leq 0.6$. When a power-law component was also included, the range of acceptable ages in both cases is extended to 0.4 Gyr.

Figure 5.8 shows an example of an acceptable fit generated by combination 2. The fit includes a YSP of $t_{YSP} = 0.1$Gyr and $E(B-V) = 0.5$. Further examples of acceptable fits for J0217-00 can be found in Appendix A Section A.5.

5.4.5 J0217-01

The initial modelling of J0217-01 was performed using combination 2, and produced a best fitting model which included a YSP of age $t_{YSP} = 0.2$ and $E(B-V) = 0.9$ (Table 5.1). Subtracting this model from the data, and measuring the Hβ flux from the resulting spectrum, produced a nebular continuum model which contributes $\sim 5\%$ of the total flux just below the Balmer edge. Attempting to derive the Balmer decrements proved unsuccessful because of the large errors associated with the Hγ and Hδ measurements, which are ultimately due to this weak nebular continuum.

All nine combinations of components outlined in Section 5.3 were applied. Of these, only combinations that include an 8 Gyr unreddened component (combinations 2,4,6 & 8) produced acceptable fits, the details of which are outlined in Table 5.7.

Figure 5.9(a) shows that, for combination 2, there are three region in which solutions

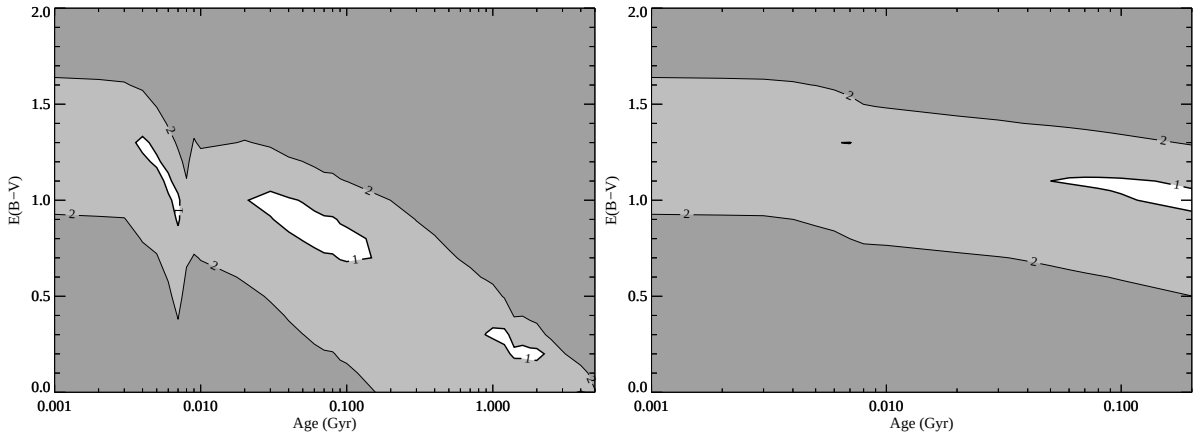

(a) 8 Gyr + Burst

(b) 8 Gyr + Cont

(c) 8 Gyr + Burst + PL

(d) 8 Gyr + Cont + PL

Figure 5.9: Plots showing the contours of χ^2_{red} for the various combination of components that produce an acceptable fit for J0217-01. The particular combination used is given in the sub-caption for the plot. The region in which $\chi^2_{red} < 1$ is shown in white, and the values of χ^2_{red} are given on the contour lines.

OSP Age (Gyr)	PL	Model	OSP Flux (%)	YSP Age (Gyr)	YSP Flux (%)	E(B-V)	Power-law (%)
8	No	B	64–79	0.004–0.007	20–32	0.9–1.3	–
			63–82	0.03–0.1	22–25	0.7–1.1	–
		C	65–76	0.007	20–30	1.3	–
			63–76	0.06–0.2	20–32	1–1.1	–
	Yes	B	61–82	0.004–0.007	13–32	0.9–1.3	0–11
			33–85	0.03–1.4	11–57	0.3–1.1	0–17
		C	61–79	0.06–0.2	15–34	1–1.1	0–8
2	No	B	–	–	–	–	–
		C	–	–	–	–	–
	Yes	B	–	–	–	–	–
		C	–	–	–	–	–

Table 5.7: The results of the stellar population synthesis modelling for J0217-01. The definitions for each of the columns is the same as that given in the caption for Table 5.3.

with $\chi^2_{red} < 1$ can be found, spread over a wide range of ages. However visual inspection of age sensitive stellar absorption lines allowed the oldest region to be discarded. In the case of combination 6, Figure 5.9(c) shows that there are two regions in which $\chi^2_{red} < 1$, which cover the same overall range of ages as do the results for combination 2, although with much of the intervening area between the two older regions now also being possible solutions. In this case, all ages provided acceptable fits, however solutions with $E(B-V) < 0.3$ can be discarded. Combinations 4 and 8, which include continuous star-formation models, produce broadly similar results, with ages in the range $0.06 \leq t_{YSP} \leq 0.2$ and $1 \leq E(B-V) \leq 1.1$. However, combination 4 also allows for a fit with $t_{YSP} = 0.007$ Gyr.

In the majority of cases where acceptable solutions are found, regardless of whether a burst or continuous model of star formation is included, the flux in the aperture is dominated by the OSP component.

Figure 5.10 shows an example of an acceptable fit to J0217-01, produced by combination 2, which includes a YSP of $t_{YSP} = 0.007$ Gyr and $E(B-V) = 0.9$. Further examples of acceptable fits for all the successful combinations can be found in Appendix A Section A.5.1

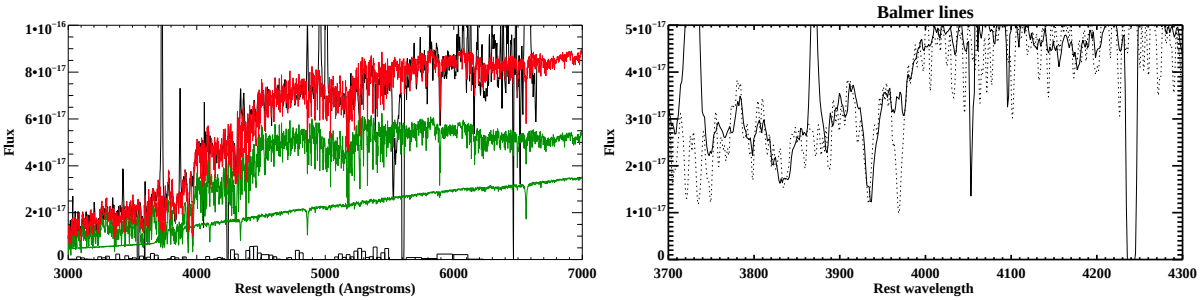

(a) 8 Gyr + Burst - Main fit

(b) 8 Gyr + Burst - Balmer Lines

Figure 5.10: An example of an acceptable fit produced by CONFIT for J0217-01. This fit was produced by combination 2 and incorporates a YSP with t_{YSP}= 0.007 Gyr and E(B-V)= 0.9.

5.4.6 J0218-00

J0218-00 is a complex system, with two distinct nuclei which have a projected separation of $\sim$ 12kpc (Figure 3.1(d)). This interaction has left the quasar host galaxy in what appears to be a ring-like configuration. Unfortunately, the spectroscopic slit does not pass through both nuclei, however, it was still possible to extract two distinct apertures from the quasar host galaxy. The main aperture is centred on the region containing the active nucleus (with a spatial scale of 8 kpc) and a second, narrower aperture is centred on an extended region of the ring like structure (with a spatial scale of 5kpc). The details of how the apertures were extracted can be found in Chapter 2 (Figure 2.5). Each of the extracted apertures was modelled independently, and the results are presented separately below.

Nuclear aperture

The initial fit for the nuclear aperture was performed using combination 2, and a best fitting model, which included a YSP t_{YSP} = 0.03 Gyr and $E(B-V)$ = 0.1 (Table 5.1), was selected. After subtracting the stellar model, the nebular continuum generated from the measured Hβ flux contributes $\sim$ 16% of the total flux in the 3540–3640 Å range. The Hγ/Hβ ratio was measured to be 0.37 $\pm$0.02 (Table 5.2), and this value was initially applied to the nebular continuum before subtraction. However, this resulted in an under-subtraction in the region of the Balmer edge, and therefore, an unreddened nebular continuum was subtracted instead, which produced a reasonable result. The failure of the technique in this case is most likely due to the relatively low equivalent width of the Balmer emission lines and strong underlying Balmer absorption lines. It is

probably the case that the true value of reddening is somewhere between these extreme cases. However, it is difficult to judge what the most appropriate value is by visual inspection alone.

OSP Age (Gyr)	PL	Model	OSP Flux (%)	YSP Age (Gyr)	YSP Flux (%)	E(B-V)	Power-law (%)
8	No	B	13–39	0.03–0.09	60–87	0.1–0.3	–
		C	–	–	–	–	–
	Yes	B	0–37	0.03–0.4	51–96	0–0.5	0–42
		C	0–5	0.2	91–98	0.5	0–0.4
2	No	B	–	–	–	–	–
		C	–	–	–	–	–
	Yes	B	0–41	0.04–0.4	43–99	0.1–0.5	0.1–37.0
		C	0–10	0.2	87–98	0.5	0–0.5

Table 5.8: The results of the stellar population synthesis modelling for J0218 – Nuclear Aperture. The definitions for each of the columns is the same as that given in the caption for Table 5.3.

All nine combinations of components were run for the nuclear aperture, the results of which are given in Table 5.8. These result show that, when no power-law component is included, it was only possible to achieve acceptable fits for combination 2. Figure 5.11(a) displays the contour plot for this combination of components, and shows that there are two possible regions of interest ($\chi^2_{red} < 1$). Visual inspection of age sensitive stellar absorption features allowed the younger solutions to be discounted, leaving a range of acceptable solutions with ages $0.03 \leq t_{YSP} \leq 0.09$ and reddenings in the range $0.1 \leq E(B-V) \leq 0.3$.

Combinations that included a power-law component all produced acceptable fits (combinations 6-9). Combination 6 has two regions in which $\chi^2_{red} < 1$ (Figure 5.11(b)), however, the younger region was once again rejected on the basis of the finer detail. In the case of combinations 5 and 6, the ages and reddenings are very similar and in all acceptable combinations, the YSP dominates the flux in the aperture. However, it is notable that the power-law component can contribute up to $\sim 40\%$ of the flux in the normalising bin.

Figure 5.12 shows an example of an acceptable fit produced by combination 2 which has a YSP of $t_{YSP} = 0.04$ Gyr and $E(B-V) = 0.2$. Further examples of acceptable fits for the successful combinations can be found in Appendix A Section A.6.1

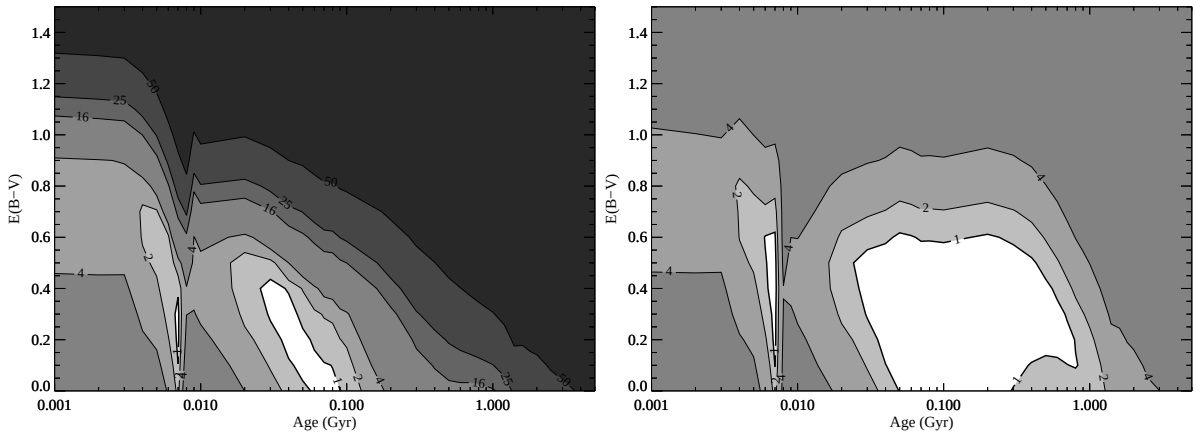

(a) 8kpc 8 Gyr + Burst

(b) 8kpc 8Gyr + Burst + PL

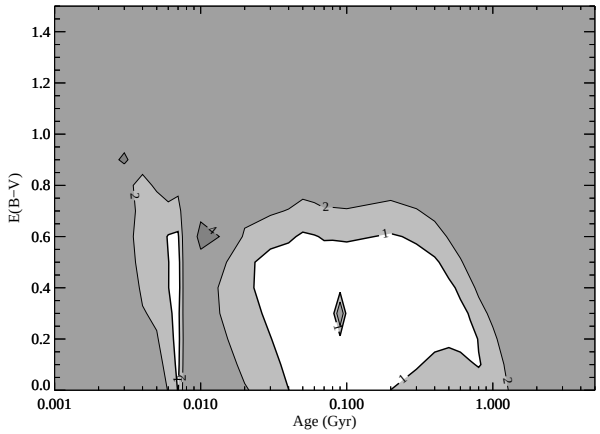

(c) 8kpc 2Gyr + Burst + PL

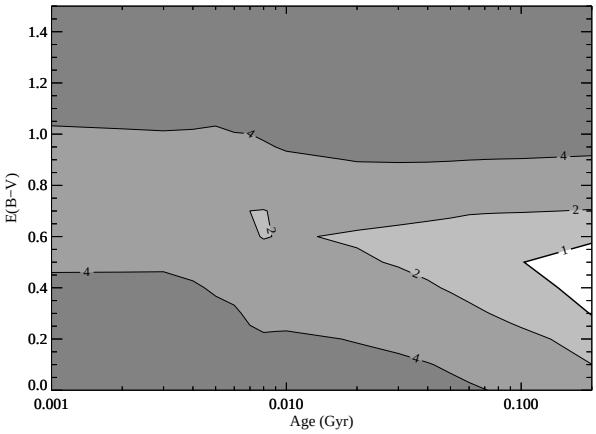

(d) 8kpc 8 Gyr + Cont + PL

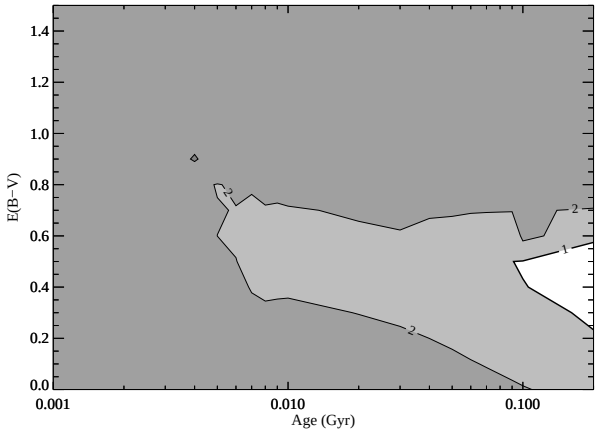

(e) 8kpc 2Gyr + Cont + PL

Figure 5.11: Plots showing the contours of χ^2_{red} for the various combination of components that produce an acceptable fit for J0218-00 – Nuclear aperture. The particular combination used is given in the sub-caption for the plot. The region in which $\chi^2_{red} < 1$ is shown in white, and the values of χ^2_{red} are given on the contour lines.

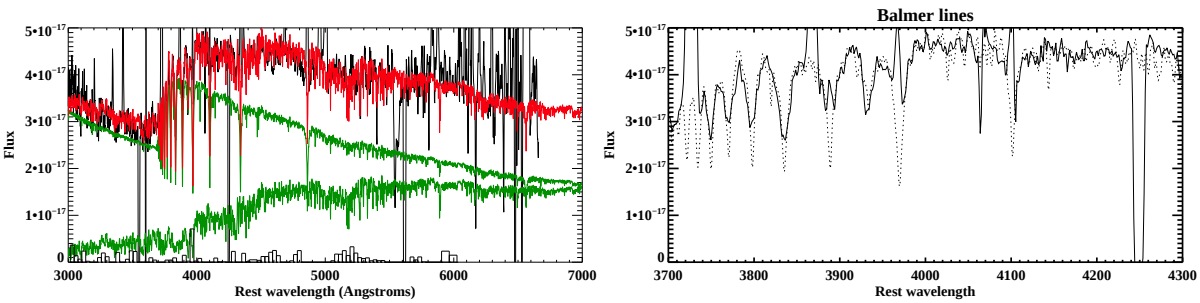

(a) 8Gyr + Burst - Main Fit

(b) 8Gyr + Burst - Balmer Lines

Figure 5.12: An example of an acceptable fit produced by CONFIT for J0218-00 – Nuclear aperture. This fit was generated using combination 2 and includes a YSP with $t_{YSP} = 0.04$ Gyr and $E(B-V) = 0.2$.

Extended aperture

The initial modelling for the extended aperture extracted from J0218-00 was performed using combination 2, which resulted in a best-fitting model with $t_{YSP} = 0.03$ and $E(B-V) = 0.2$ (see Table 5.1). This is very similar in terms of the components used, and their contribution to the total flux as for the nuclear aperture. The model nebular continuum was then constructed, using the Hβ flux measured from the stellar subtracted spectrum, which contributes $\sim$ 16% of the total flux in the 3540Å – 3640 Å range. The Balmer decrements were measured from the stellar-subtracted spectrum and produced a value of Hγ/Hβ = 0.32 $\pm$0.02. This suggests that the nebular continuum is slightly more reddened in the extended region than in the nuclear region (see Table 5.2). However, when the continuum was reddened before subtraction, the same issues was encountered as described for the nuclear aperture. Therefore, an unreddened continuum was subtracted before continuing with the full modelling process.

The extended aperture is centred on a non-active, extended region of the galaxy and

OSP Age (Gyr)	PL	Model	OSP Flux (%)	YSP Age (Gyr)	YSP Flux (%)	E(B-V)	Power-law (%)
8	No	B	10–33	0.02–0.04	67–81	0.1–0.4	–
		C	4–31	0.05–0.2	66–94	0.2–0.4	–
2	No	B	26–37	0.004–0.006	56–74	0.3–0.5	–
			15–44	0.02–0.04	56–81	0.1–0.4	–
		C	0–42	0.006–0.2	55–96	0.2–0.6	–

Table 5.9: The results of the stellar population synthesis modelling for J0218 – Extended Aperture. The definitions for each of the columns is the same as that given in the caption for Table 5.3.

therefore, only combinations 2 to 5 (no power-law component) were used for the modelling process. This is because it is unlikely that there will be any significant contribution to the flux from scattered quasar light.

Figures 5.13(a) and 5.13(c) show that, when including a burst population in the fit, there are two possible regions of interest, where $\chi^2_{red} < 1$. In the case where an 8 Gyr population was assumed, it is only fits within the older region ($0.02 \leq t_{ysp} \leq 0.04$), that are acceptable. Fits in the younger region under predict the flux blue-wards of the Balmer break, resulting in an incorrect shape for the overall model spectrum. When assuming a 2 Gyr underlying population, the same region provides acceptable fits, with a very similar proportion of the flux attributed to the YSP component. However, in this case the younger region ($0.004 \leq t_{ysp} \leq 0.006$) also produces acceptable fits.

Figures 5.13(b) and 5.13(d) show the contours of χ^2_{red} for the models that included a continuous star formation model. This shows that in both cases, the possible age range of acceptable fits is greater, although it extends over a greater range for the models that include a 2 Gyr population. For combination 4, there is also a small region at younger ages, but this does not produce an acceptable fit. In both cases where continuous star formation was assumed, Table 5.9 shows that the flux ascribed the YSP and OSP in each case is very similar.

Figure 5.14 shows an example of an acceptable fit for combination 2, which includes a YSP $t_{YSP} = 0.04$ Gyr and E(B-V) = 0.1. It can be seen by comparison with Figure 5.12 that the overall shape and the age sensitive absorption lines in the region of the higher order Balmer lines are very similar, which may suggest that the burst of star-formation induced by this obvious merger was initiated across the entire galaxy. Further examples of acceptable fits produced by successful combinations are shown in Appendix A Section A.6.2.

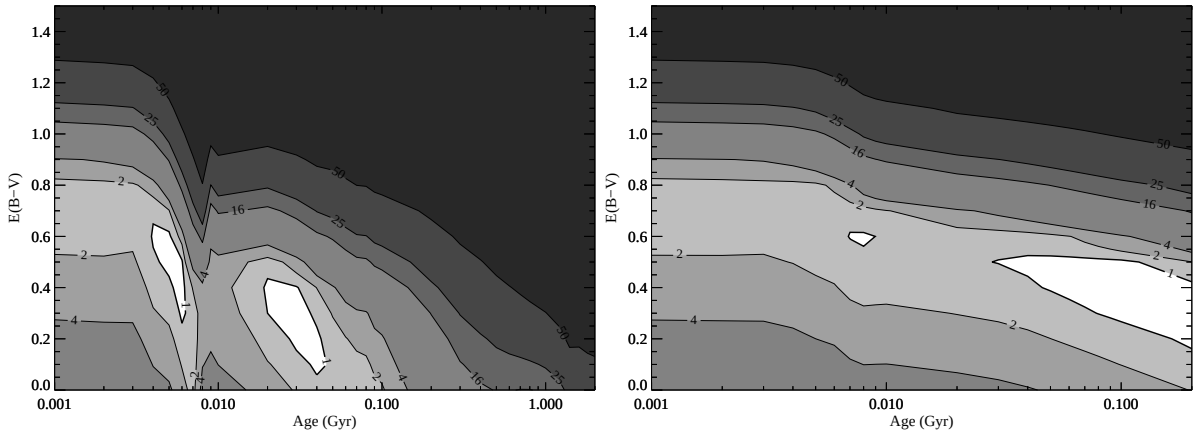

(a) 8 Gyr + Burst

(b) 8 Gyr + Cont

(c) 2 Gyr + Burst

(d) 2 Gyr + Cont

Figure 5.13: Plots showing the contours of χ^2_{red} for the various combination of components that produce an acceptable fit for J0218-00 – Extended aperture. The particular combination used is given in the sub-caption for the plot. The region in which $\chi^2_{red} < 1$ is shown in white, and the values of χ^2_{red} are given on the contour lines.

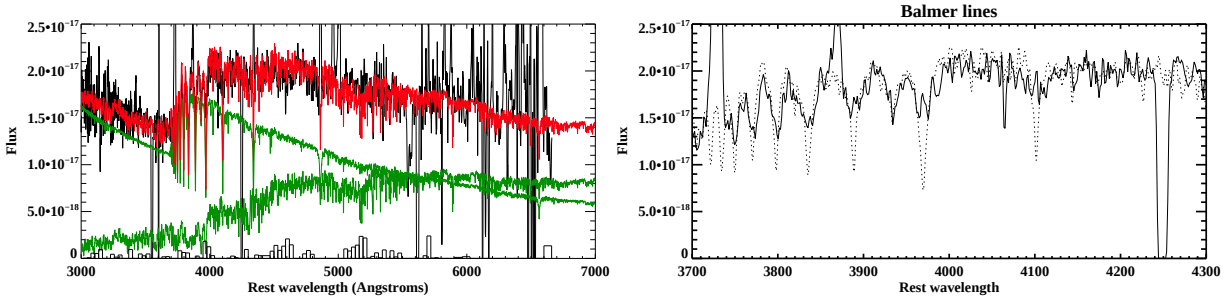

(a) 8 Gyr + Burst - Main Fit

(b) 8 Gyr + Burst - Balmer Lines

Figure 5.14: An example of an acceptable fit produced by CONFIT for J0218-00 – Extended aperture. This model was generated using combination 2 and includes a YSP with t_{YSP}= 0.04 and E(B-V)= 0.1.

5.4.7 J0227+01

The initial modelling for J0227+01 was performed using combination 4, which resulted in a best fitting model with $t_{YSP} = 0.04$ Gyr and $E(B-V) = 0.6$ (Table 5.1). This model was then subtracted from the spectrum before measuring the Hβ flux, in order to construct the nebular continuum model. This resulted in a model that contributes $\sim 11\%$ of the total flux just below the Balmer edge at 3646 Å (Table 5.2). Unsurprisingly, with such a comparatively weak nebular continuum, both the Hγ and Hδ emission lines are weak, preventing a reliable measurement of the nebular reddening, via the Balmer decrements, being made. In light of this, it was not possible to apply a reddening correction to the nebular component before subtraction. However, the resulting nebular subtracted spectrum produced an acceptable result.

All nine combination of components, outlined in Section 5.3, were then run for J0227+01, and the results, presented in Table 5.10, show that the full range of combinations which include a YSP produce an acceptable fit.

The combinations which include a burst star formation history (Figures 5.15(a), 5.15(c), 5.15(a) and 5.15(c)) all produce two regions in which $\chi^2_{red} < 1$. However, in all these cases, the younger ages can be discounted due to the fact that these models over-predict the Ca II K absorption.

When combinations which do not include a power-law component are used, the range of ages that produce acceptable fits is $0.03 \leq t_{YSP} \leq 0.1$, with reddenings in the range $0.1 \leq E(B-V) \leq 0.5$ and the YSP component contributing up to 85% of the flux in the normalising bin. When a power-law component is also included, the ages move to older values ($0.09 \leq t_{YSP} \leq 0.2$) and a larger range of reddenings is allowed ($0 \leq E(B-V) \leq$

OSP Age (Gyr)	PL	Model	OSP Flux (%)	YSP Age (Gyr)	YSP Flux (%)	E(B-V)	Power-law (%)
8	No	B	15–52	0.03–0.1	46–82	0.1–0.5	–
		C	27–32	0.2	63–69	0.5	–
	Yes	B	0–49	0.09–0.7	29–89	0–0.6	0–41
		C	10–33	0.2	61–85	0.5–0.6	0-7
2	No	B	26–52	0.03–0.04	46–72	0.4–0.5	–
		C	21–50	0.09–0.2	47–75	0.5–0.6	–
	Yes	B	12–71	0.03–0.2	20–80	0–0.7	0–34
		C	25–52	0.1–0.2	38–67	0.5–0.6	0–9

Table 5.10: The results of the stellar population synthesis modelling for J0227+01. The definitions for each of the columns is the same as that given in the caption for Table 5.3.

0.6).

For the models that include a continuous formation history (Figures 5.15(b), 5.15(d), 5.15(b) and 5.15(d)), it is only the oldest ages ($0.09 \leq t_{YSP} \leq 0.2$) allowed by the modelling that produce acceptable results.

Figure 5.16 shows an example of an acceptable fit, using combination 2, which includes a YSP with $t_{YSP} = 0.05$ Gyr and $E(B-V) = 0.3$. Further examples of acceptable fits for combinations 3 – 9 can be found in Appendix A, Section A.7.

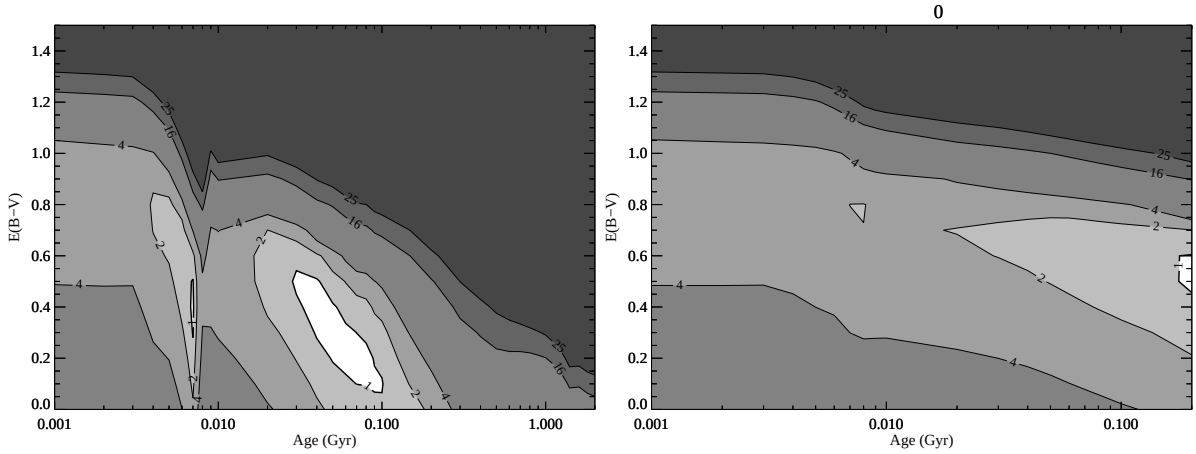

(a) 8 Gyr + Burst

(b) 8 Gyr + Cont

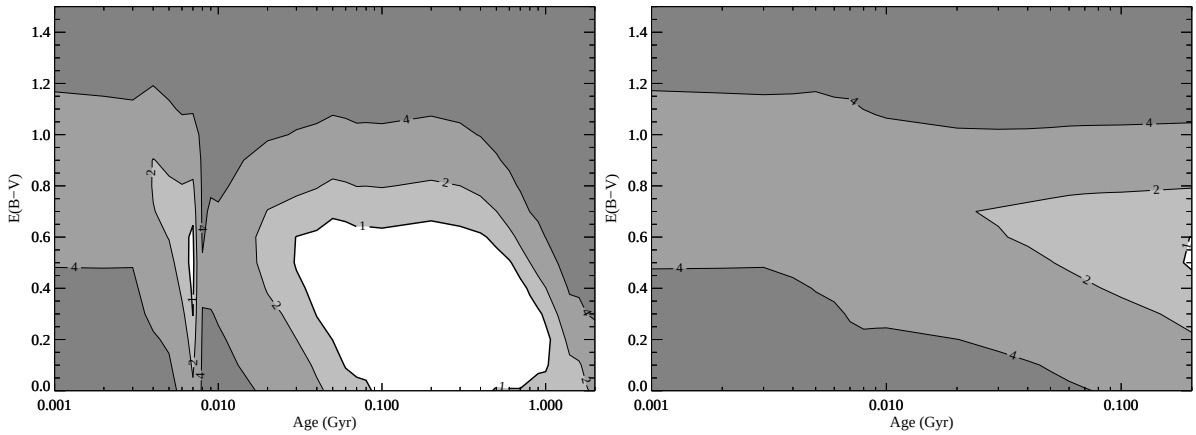

(c) 8 Gyr + Burst + PL

(d) 8 Gyr + Cont + PL

Figure 5.15: Plots showing the contours of χ^2_{red} for the various combination of components that produce an acceptable fit for J0227+01. The particular combination used is given in the sub-caption for the plot. The region in which $\chi^2_{red} < 1$ is shown in white, and the values of χ^2_{red} are given on the contour lines.

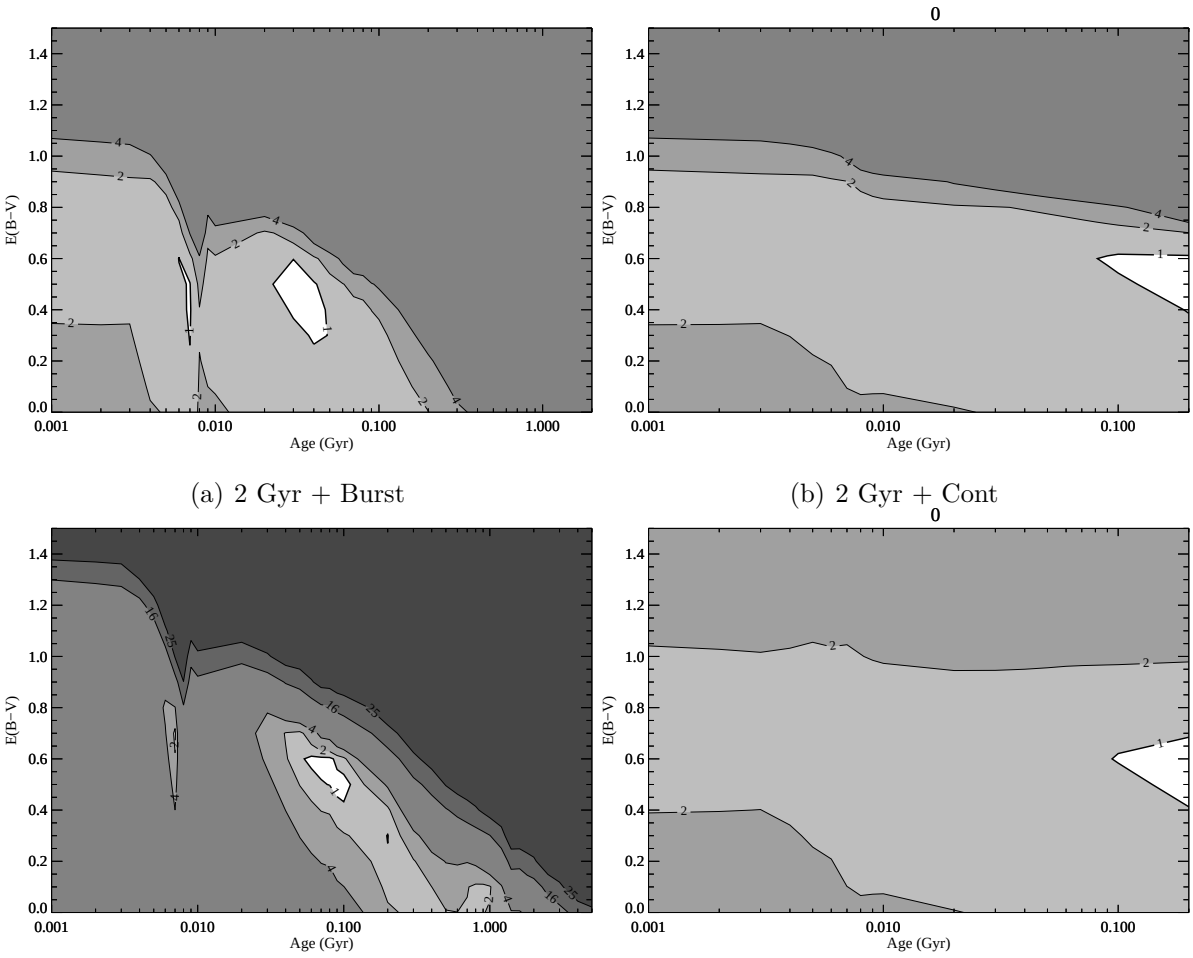

(a) 2 Gyr + Burst

(b) 2 Gyr + Cont

(c) 2 Gyr + Burst + PL

(d) 2 Gyr + Cont + PL

Figure 5.15: [continued]

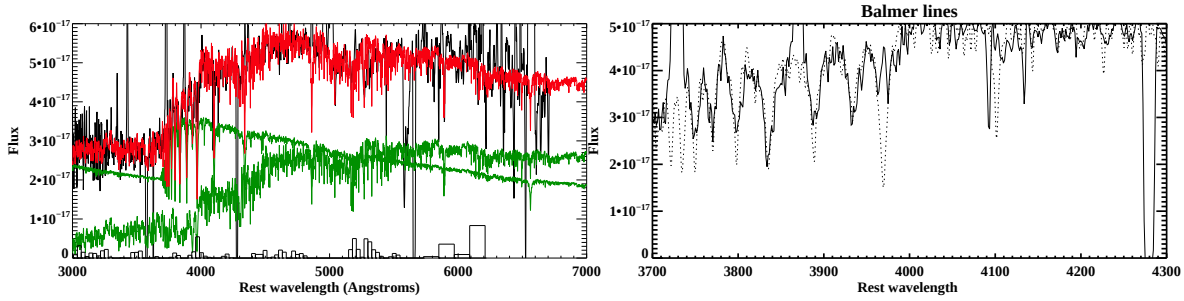

(a) 8 Gyr + Burst - Main fit

(b) 8 Gyr + Burst - Balmer Lines

Figure 5.16: An example of an acceptable fit produced by CONFIT forJ0227+01. This fit was generated using combination 2 and consists of and 8 Gyr OSP combined with a YSP of t_{YSP}= 0.05 Gyr and E(B-V)= 0.3.

5.4.8 J0234-07

The initial modelling for J0234-07 was performed using combination 2 and resulted in a wide range of possible solutions that have $\chi^2_{red} < 1$. An inspection of the overall shape of the continuum and regions around age sensitive stellar absorption lines showed the best fit to have a YSP $t_{YSP} = 0.001$ and E(B-V) = 0.1. However, Table 5.1 shows that the OSP dominates the flux, which is also the case for all other possible solutions for combination 2. This means that the resulting stellar model is not strongly dependent on the choice of YSP component.

OSP Age (Gyr)	PL	Model	OSP Flux (%)	YSP Age (Gyr)	YSP Flux (%)	E(B-V)	PL Flux (%)
8	No	B	41–85	0.001–0.02	15–55	0–0.7	–
		C	57–85	0.001–0.2	15–42	0–0.6	–
	Yes	B	0–82	0.001–5	0–100	0–2	0–33
		C	54–81	0.001–0.2	0–42	0–2	0–33
2	No	B	–	–	–	–	–
		C	–	–	–	–	–
	Yes	B	68–88	0.001–0.003	6–11	0–0.1	3–20
			59–91	0.001–0.3	4–34	0.7–1.6	0.7–14
			0–83	1.2–2	9–83	0.2–0.5	6–20
		C	69–88	0.001–0.004	6–9	0	3–21
			60–91	0.001–0.2	9–80	0.9–1.7	1–12

Table 5.11: The results of the stellar population synthesis modelling for J0234-07. The definitions for each of the columns is the same as that given in the caption for Table 5.3.

This model was subtracted from the spectrum before the Hβ flux was measured. This produced a nebular continuum that contributes $\sim$ 24% of the flux in the 3540–3640 Å range. Table 5.2 shows the Balmer decrement measured from the stellar-subtracted spectrum. Initially, to remain consistent with the technique of maximum nebular subtraction applied in the majority of cases, no reddening was applied to the nebular continuum before subtraction. However, this resulted in a step in the resulting stellar continuum at 3646 Å. To resolve this issue, reddening of E(B-V) = 0.25 was applied to the nebular continuum before subtraction, (the value derived from the Hγ/Hβ ratio), which produced a much improved result.

All nine combinations were then run for J0234-07, and Table 5.11 shows that all but combinations 3 and 5 produce acceptable results. Figure 5.17 shows the contour plots of χ^2_{red} for combinations 2,4,7 and 9 respectively, however, no contour plots for combinations 5 and 7 have been included because all combinations of components produce a result

with $\chi^2_{red} < 1$ and therefore, these plots do not convey any useful information.

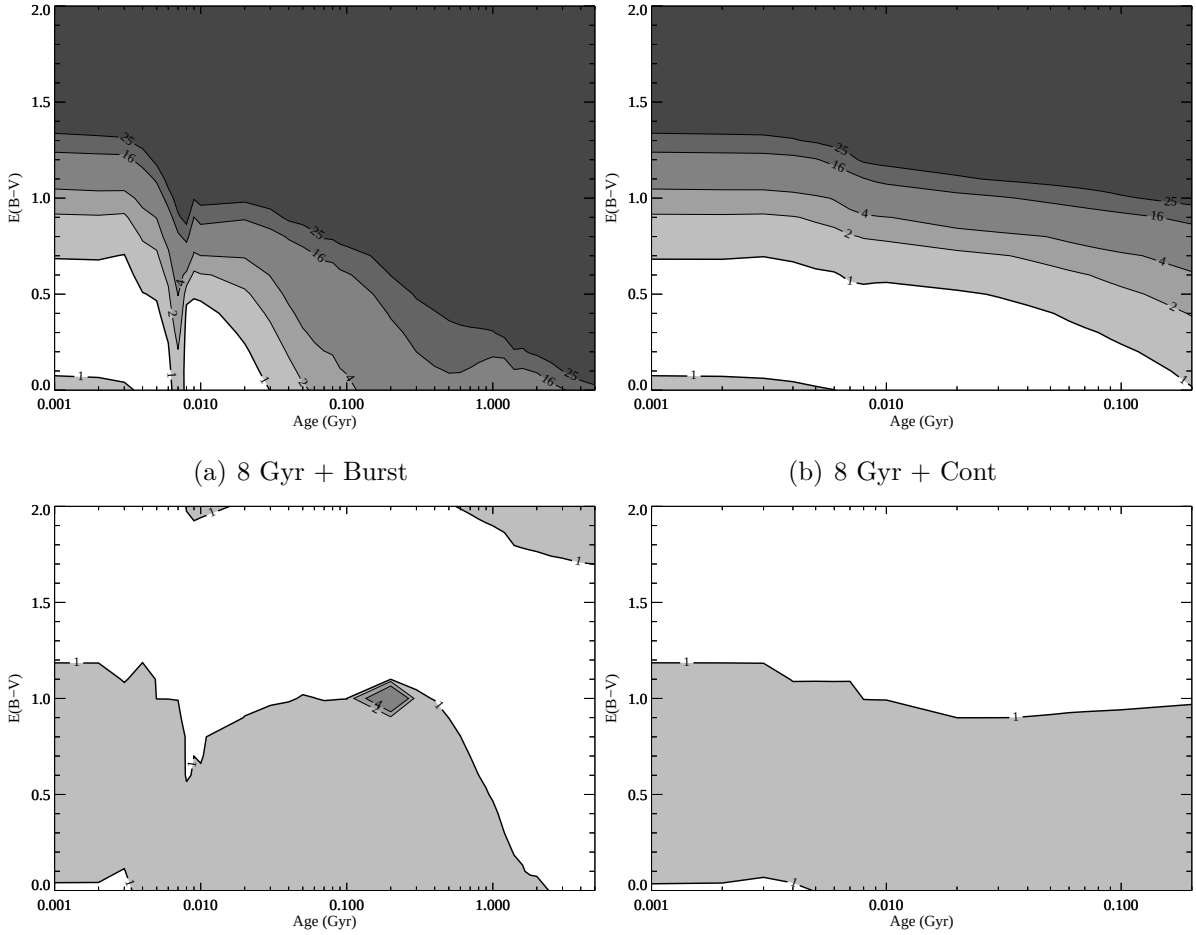

(a) 8 Gyr + Burst

(b) 8 Gyr + Cont

(c) 2 Gyr + Burst + PL

(d) 2 Gyr + Cont + PL

Figure 5.17: Plots showing the contours of χ^2_{red} for the various combination of components that produce an acceptable fit for J0234-07. The particular combination used is given in the sub-caption for the plot. The region in which $\chi^2_{red} < 1$ is shown in white, and the values of χ^2_{red} are given on the contour lines.

It must be noted that, in addition to combinations which include a YSP, the spectrum of J0234-07 can also be fit using only an 8 Gyr, unreddened population combined with a power-law component, making it unclear whether a YSP component is at all necessary. Table 5.11 and Figure 5.18 show that the combinations which do not include a power-law component, tend to include very young or young components at a low level of contribution to the total flux in the normalising bin. This means that in these cases, the VYSP/YSP could, in fact, be taking the form of a power-law, as illustrated in Figure 5.18(a), where the VYSP ($t_{YSP} = 0.003$, $E(B-V) = 0.2$) has an approximately power-law form. This is also demonstrated by the fits shown in Appendix A Section

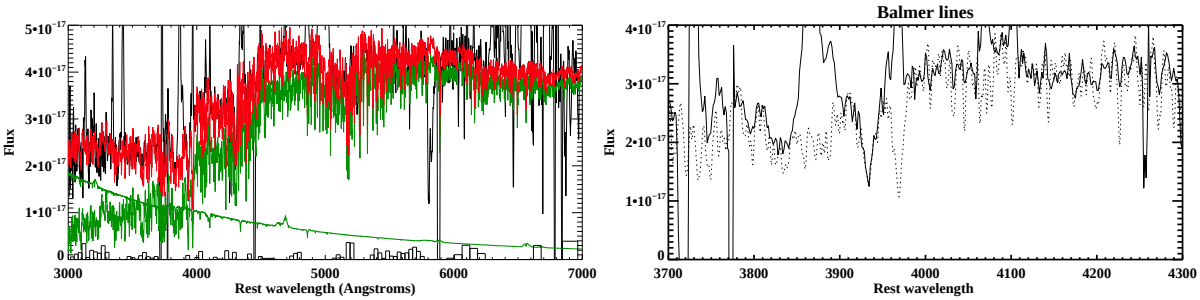

(a) 8 Gyr + Burst - Main fit

(b) 8 Gyr + Burst - Balmer Lines

Figure 5.18: An example of an acceptable fit produced by CONFIT for J0234-07. The fit shown here was generated using combination 2 and includes a YSP with t_{YSP}= 0.003 Gyr and E(B-V)= 0.2.

A.8.

With such a wide range of possible solutions and such young ages producing acceptable fits to these data, as well as an 8 Gyr plus power-law combination, it is not possible to discriminate between the various possibilities. However, it should be noted that there is little evidence for the Balmer absorption lines, associated with young stars, in the spectrum (Figure 5.18(b)), although these are also weak at the youngest model ages.

5.4.9 J0249-00

In order to produce a model stellar spectrum, the initial run was performed using combination 2. This resulted in a best fitting model with t_{YSP} = 0.03 and E(B-V) = 0.7 (see Table 5.1). After subtracting the model from the data and measuring the Hβ flux from the stellar-subtracted spectrum, the resulting model nebular continuum contributes

OSP Age (Gyr)	PL	Model	OSP Flux (%)	YSP Age (Gyr)	YSP Flux (%)	E(B-V)	Power-law (%)
8	No	B	12–35	0.05–0.1	65–88	0.7–0.8	–
		C	–	–	–	–	–
	Yes	B	0–24	0.05–0.7	47–89	0.4–0.8	0–30
		C	–	–	–	–	–
2	No	B	19–59	0.05–0.2	44–81	0.6–0.9	–
		C	–	–	–	–	–
	Yes	B	1–61	0.06–0.6	41–84	0.5–0.8	0..26
		C	–	–	–	–	–

Table 5.12: The results of the stellar population synthesis modelling for J0249+00. The definitions for each of the columns is the same as that given in the caption for Table 5.3.

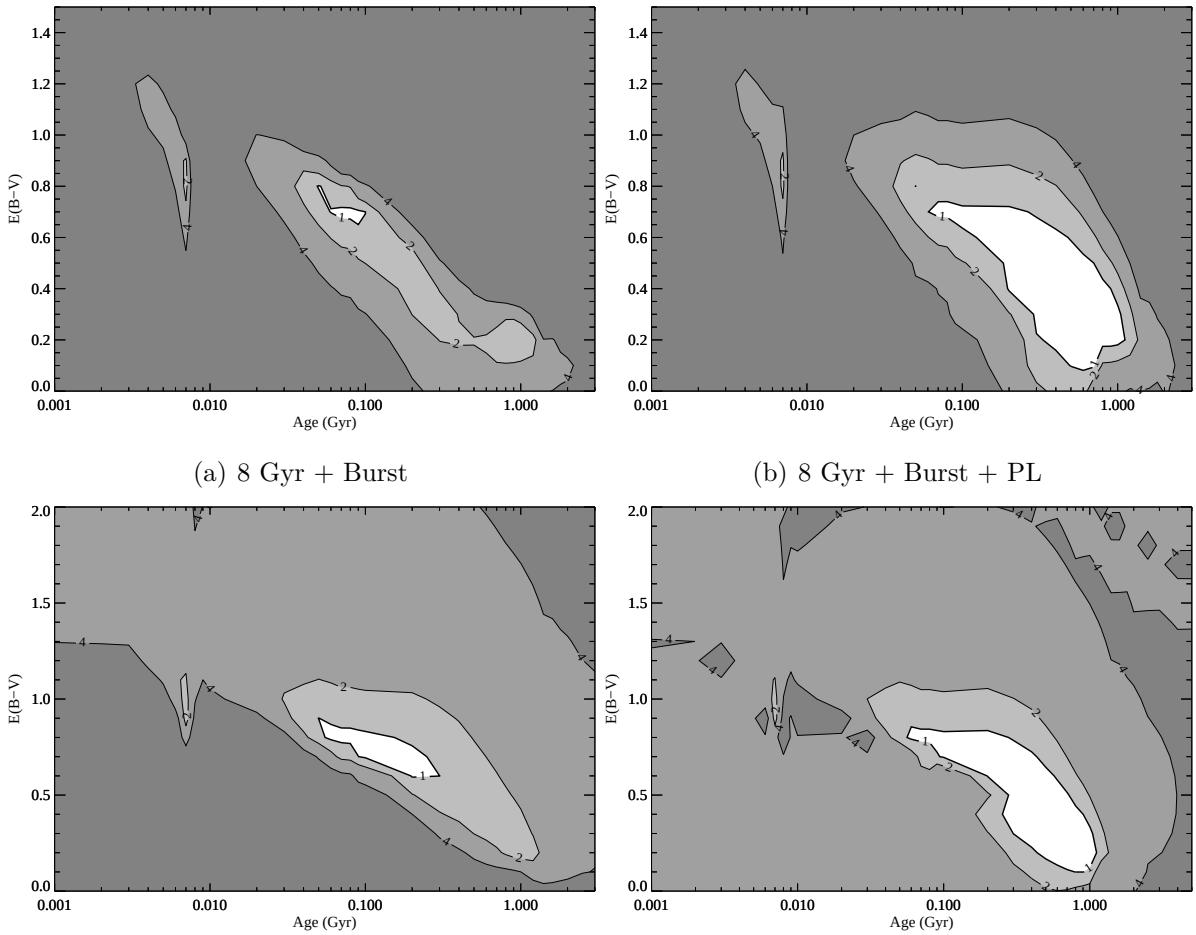

(a) 8 Gyr + Burst

(b) 8 Gyr + Burst + PL

(c) 2 Gyr + Burst

(d) 2 Gyr + Burst + PL

Figure 5.19: Plots showing the contours of χ^2_{red} for the various combination of components that produce an acceptable fit for J0249-00. The particular combination used is given in the sub-caption for the plot. The region in which $\chi^2_{red} < 1$ is shown in white, and the values of χ^2_{red} are given on the contour lines.

$\sim 25\%$ of the flux in the 3540–3640Å range. No reddening was applied to this continuum because, as is shown in Table 5.2, the uncertainty associated with measuring the Hγ/Hβ ration is large in comparison to the measured value, and thus is consistent with reddenings of $0 \leq E(B-V) \leq 1.7$ (assuming case B recombination). Therefore, because the value of reddening is poorly constrained, and also because subtracting an unreddened nebular continuum provides an acceptable result, a maximum nebular subtraction was performed before proceeding with the fitting.

Of the nine combinations of components specified in section 5.3, only those that include a burst model of star formation produce acceptable results. Table 5.12 and Figure 5.19 show that in all cases, only one region produces solutions with $\chi^2_{red} < 1$. In

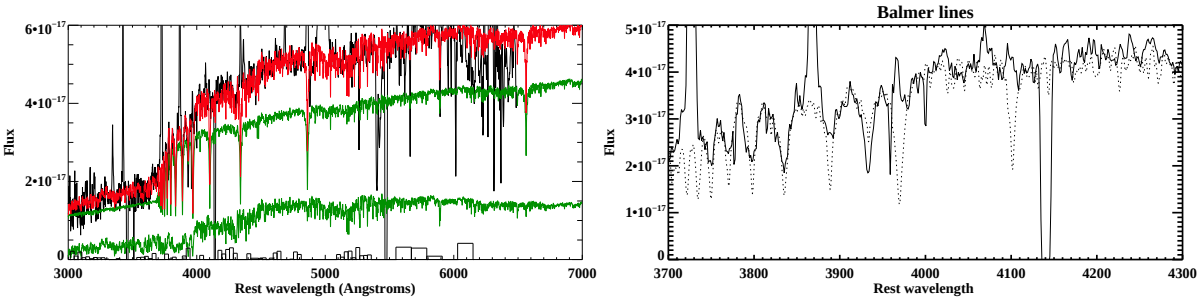

(a) 8 Gyr + Burst - Main fit

(b) 8 Gyr + Burst - Balmer Lines

Figure 5.20: An example of an acceptable fit produced by CONFIT for J0249-00. The fit shown here was generated by combination 2 and shows a YSP with $t_{YSP} = 0.07$ Gyr and $E(B-V) = 0.7$.

the case of combinations 2,3, and 7, all fits that produce $\chi^2_{red} < 1$ are acceptable, however, for combination 6 (Figure 5.19(b)), it is only combinations with $E(B-V) > 0.3$ that are acceptable solutions. This is because solutions with lower reddenings produce a poor fit to the overall shape of the continuum, with the power-law component rising too steeply towards the red, and thus over-predicting the total flux in the reddest part of the spectrum. This is reflected in the results presented for this combination (8 Gyr + Burst + PL) in Table 5.12. In the cases of combinations 2 and 3, the ages and reddenings allowed are broadly similar, with combination 3 allowing a slightly older age and larger range of reddenings. As is typical, when a power-law component is included, significantly older ages provide acceptable fits at a wider range of reddenings.

Figure 5.20 shows an example of an acceptable fit using combination 2, and includes a YSP of $t_{YSP} = 0.07$ Gyr and $E(B-V) = 0.7$. Examples of fits for the other successful combinations can be found in Appendix A Section A.9

5.4.10 J0320+00

The initial modelling for J0320+00 was performed using combination 2, and the resulting best-fit model includes a YSP of $t_{YSP} = 0.02$ Gyr and E(B-V) = 0.1. After subtracting this stellar model from the spectrum, the model nebular continuum generated from the Hβ flux contributes $\sim$ 14% of the flux between in the 3540Å – 3640Å range. The Balmer decrements were measured using Hβ and Hγ (Table 5.2) but because of the large uncertainty associated with the measured value, which allows for reddenings in the range $0 \leq E(B-V) \leq 1.3$ (assuming case B recombination), and the fact that the maximum subtraction produces a good result around the Balmer edge, no reddening correction has

been applied to the nebular continuum model before subtraction.

OSP Age (Gyr)	PL	Model	OSP Flux (%)	YSP Age (Gyr)	YSP Flux (%)	E(B-V)	Power-law (%)
8	No	B	37–47	0.005–0.006	50–61	0.1–0.3	–
			33–46	0.02–0.03	52–64	0.0–0.2	–
		C	26–47	0.007–0.2	50–70	0–0.4	–
	Yes	B	18–25	0.001	69–77	0.7	< 1
			11–47	0.004–0.006	53–100	0.1–0.6	0–23
			4–48	0.02–0.4	18–27	0–0.6	0–46
		C	7–46	0.003–0.2	33–88	0–0.6	0–31
2	No	B	–	–	–	–	–
		C	–	–	–	–	–
	Yes	B	10–49	0.001–0.006	27–82	0.6–0.8	0–22
			11–55	0.009–0.4	14–76	0.3–0.7	0–42
		C	8–52	0.001–0.2	28–85	0.4–0.7	0–26

Table 5.13: The results of the stellar population synthesis modelling for J0320+00. The definitions for each of the columns is the same as that given in the caption for Table 5.3.

The results of running combinations 2–9 are presented in Table 5.13, which shows that all combinations, except for 3 and 5, produce solutions with $\chi^2_{red} < 1$. In the cases of combinations 2 and 7 (Figures 5.21(a) and 5.21(e)), there are two regions containing possible solutions, whilst in the case of combination 6 (Figure 5.21(c)) there are three. For combinations 4, 8 and 9, (Figures 5.21(b), 5.21(d) and 5.21(f)) there is one extended region in which possible solutions are found.

In the case of combination 2, all the fits associated with both regions are acceptable, whilst in the case of combination 6, fits that include a YSP with $t_{YSP} > 0.4$ Gyr were rejected, because they result in strongly over-predicted the Ca II Kabsorption. For combination 7, fits associated with the younger regions that have $E(B-V) < 0.6$ were rejected, and also those in the older region with $E(B-V) < 0.3$ and/or $t_{YSP} > 0.4$ Gyr. This was because they either strongly over-predict the Ca II K absorption feature or they do not result in a good fit to the overall shape of the continuum. For combination 8, solutions with t_{YSP} 0.003 $<$ Gyr were discounted , and for combination 9, solutions that have $E(B-V) < 0.4$ were also rejected.

Columns 4 and 6 of Table 5.13 demonstrate that, when no power-law is included in the model, the YSP contributes a slightly higher proportion of the flux than the OSP, and that when a power-law component is included, this difference becomes more pronounced.

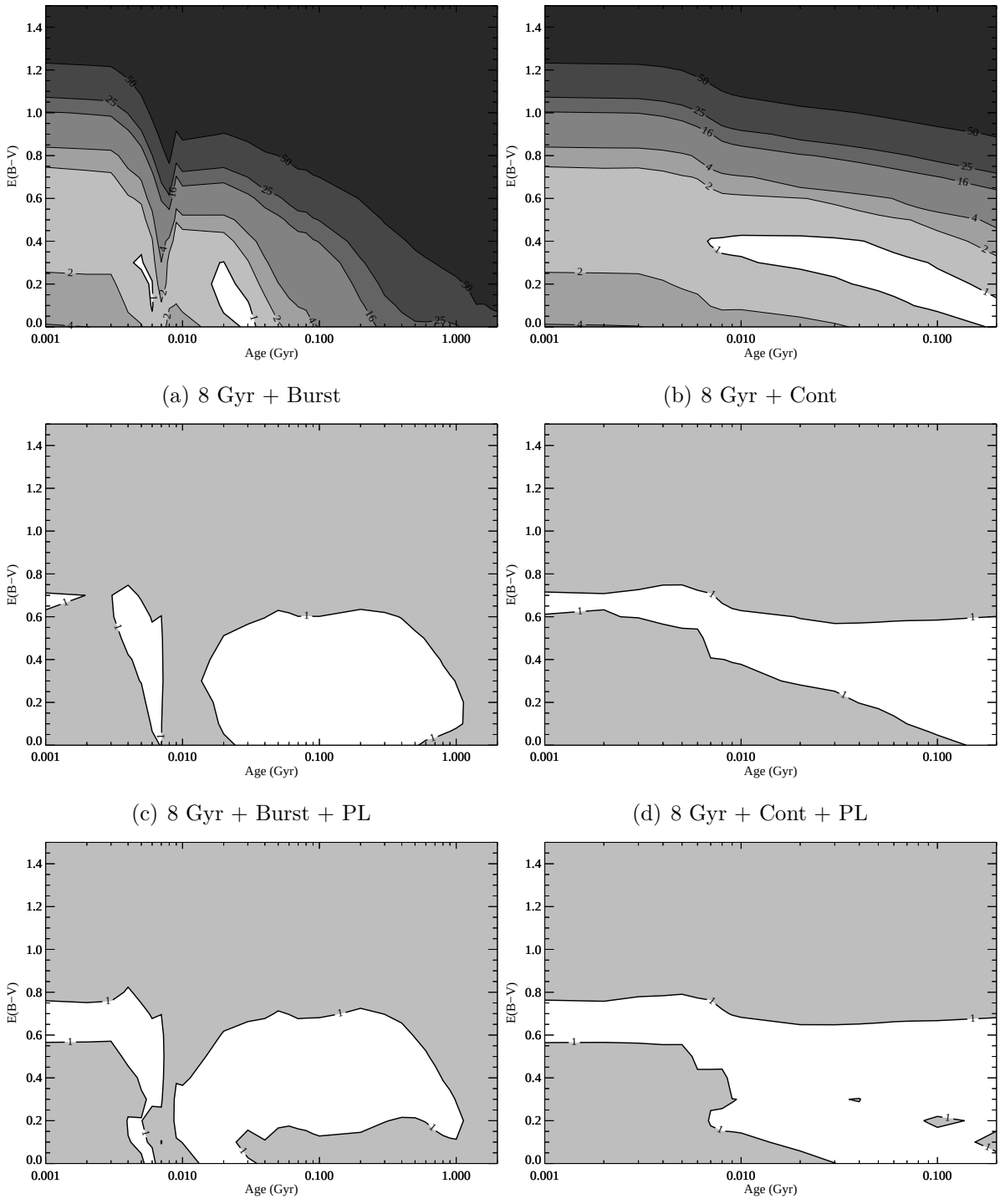

(a) 8 Gyr + Burst

(b) 8 Gyr + Cont

(c) 8 Gyr + Burst + PL

(d) 8 Gyr + Cont + PL

(e) 2 Gyr + Burst + PL

(f) 2 Gyr + Cont + PL

Figure 5.21: Plots showing the contours of χ^2_{red} for the various combination of components that produce an acceptable fit for J0320-00. The particular combination used is given in the sub-caption for the plot. The region in which $\chi^2_{red} < 1$ is shown in white, and the values of χ^2_{red} are given on the contour lines.

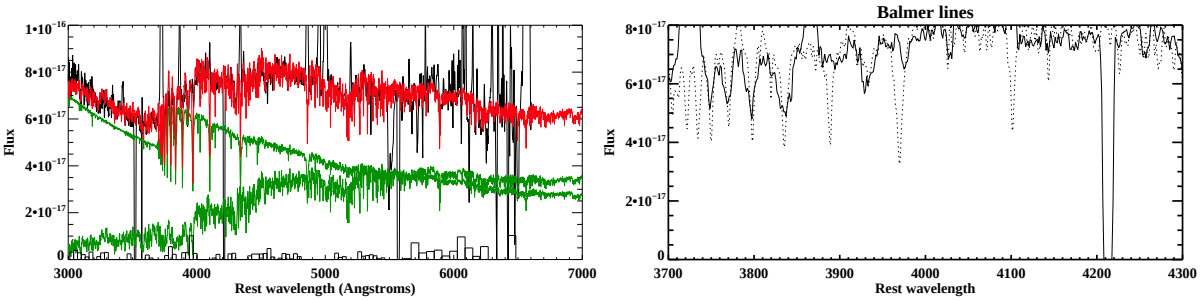

(a) 8 Gyr + Burst - Main Fit

(b) 8 Gyr + Burst - Balmer Lines

Figure 5.22: An example of an acceptable fit produced by CONFIT for J0320-00. The fit shown here was generated using combination 2, and includes a YSP with $t_{YSP} = 0.02$ and E(B-V) = 0.2.

Figure 5.22 shows an example of an acceptable fit using combination 2, including a YSP of $t_{YSP} = 0.02$ and E(B-V) = 0.2. Example of fits for all other acceptable combinations can be found in Appendix A Section A.10

5.4.11 J0332-00

Although this object was originally classified by Zakamska et al. (2003) as a type II quasar, the Gemini GMOS-S spectrum presented in Figure 2.3 clearly shows, on the basis of a very broad Hα component, that J0332-00 is, in fact, a type I AGN. This finding is confirmed by Barth et al. (2014), who also find clear evidence for a broad Hα component in their data. Despite this, an attempt was made to fit the stellar populations in the same manner as the other objects presented in this section.

In Chapter 3, J0332-00 (Figure 3.1(c)) was classified as a double nucleus, with the two components separated by 4 kpc. In this case, the 1.5 arc second slit passes directly through both nuclei, allowing the extraction of two distinct spatial apertures centred on each of the components (i.e. the quasar host galaxy and the companion nucleus). Full details of the aperture extractions can be found in Chapter 2. Each aperture is modelled independently and discussed individually below.

Quasar nucleus

The initial modelling for the quasar nucleus component was performed using combination 6. This is because there can be no doubt that a significant fraction of the flux will be attributable to the unobscured quasar nucleus, and the power-law component is assumed to account for this contribution. The best fitting model was deemed to include an ISP

OSP Age (Gyr)	PL	Model	OSP Flux (%)	YSP Age (Gyr)	YSP Flux (%)	E(B-V)	Power-law (%)
8	Yes	B	0–76	0.001–5	0–51	0–2	0–47
		C	32–77	0.001–0.2	0–43	0–2	0–47
2	Yes	B	46–71	0.001–0.003	19–28	0–0.1	3–27
			40–73	0.001–0.004	14–47	1–1.3	5–20
			26–73	0.008–0.1	13–63	0.5–0.9	4–22
		C	–	–	–	–	–

Table 5.14: The results of the stellar population synthesis modelling for J0332-00 – Quasar Nucleus. The definitions for each of the columns is the same as that given in the caption for Table 5.3.

with t_{ISP}= 4 Gyr and E(B-V)= 0.2, as well as the OSP and power-law components (Table 5.1). In order to construct the nebular model, this stellar model was subtracted from the spectrum and the Hβ flux was then measured. This resulted in a nebular model that contributes $\sim$ 4% of the total flux in the 3540Å–3640Å range (Table 5.2). Due to the low equivalent widths of the Hγ and Hδ lines, it was not possible to determine a reliable value for the Balmer decrements, and therefore no reddening was applied to the nebular continuum before subtraction. This did not result in an unphysical step in the spectrum at the Balmer edge, and was thus considered acceptable.

The nuclear aperture extracted from the nuclear region of J0332-00 is one of the few cases which can be fit using combination 1, and thus does not *require* the inclusion of a YSP in order to produce acceptable fits. This means that it is not possible to place any meaningful constraints on the ages and reddenings of the YSP/ISP components, if one is indeed present. This conclusion is reinforced by the results presented in Table 5.14, which shows that, for combinations which include an 8 Gyr OSP (6 and 8), all ages and reddenings provide acceptable solutions. No contour plots of χ^2_{red} for these combinations are presented here because they do not convey any useful information.

Figure 5.23 shows the contour plot for combination 7, which is the only combination which provides *any* constraint on the reddenings of the YSP/ISP component, although nearly all ages are still acceptable. In the case of combination 9 (2 Gyr + Cont + PL), regions in which $\chi^2_{red} < 1$ were achieved, however, in all cases the Ca II K absorption feature was strongly over predicted by the models and therefore, these solutions were rejected.

It is interesting to note that, the quasar appears to be relatively unreddened given the slope of the power-law component ($\alpha = -2.24$) in the combination 1 fit shown in Figure 5.24(b). This would imply that, if no YSP component is present, the quasar nucleus has

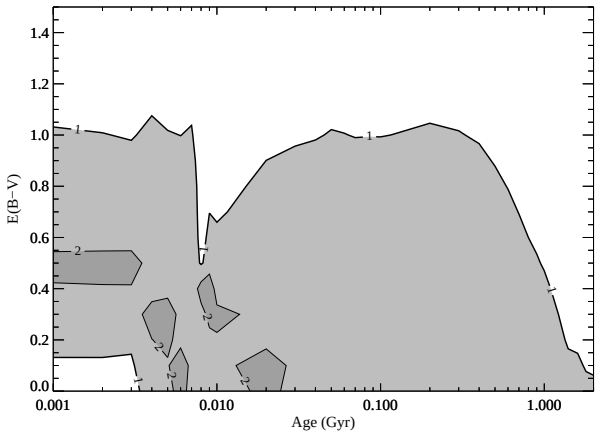

(a) 2 Gyr + Burst + PL

Figure 5.23: Plots showing the contours of χ^2_{red} for the various combination of components that produce an acceptable fit for J0332-00 – Quasar Host Galaxy. The particular combination used is given in the sub-caption for the plot. The region in which $\chi^2_{red} < 1$ is shown in white, and the values of χ^2_{red} are given on the contour lines.

a relatively low luminosity considering the high [OIII] luminosity. In order to determine if this is the case, an attempt to fit the broad Hα and Hβ components has been made, in order to determine the Balmer decrements in the BLR. This is complicated by the fact that, due to the strong fringing and residuals from the sky subtraction, the spectrum is very noisy at wavelengths greater than 6000 Å. This object also has a double peaked broad emission line profile which requires a minimum of two broad components, further complicating the fitting process. The Balmer decrements were derived for each of these components separately, and in both cases it was found that Hα/H$\beta \sim 10 \pm 2 - 4$, which is substantially larger than expected for case B recombination. This is likely due to the poor quality of the data in the region of Hα.

Figure 5.24 shows the fit generated by combination 1, and it can be seen that the combination of an 8 Gyr OSP and a power-law component provides and adequate fit. Further examples of acceptable fits which include a YSP/ISP component can be found in Appendix A Section A.11.1.

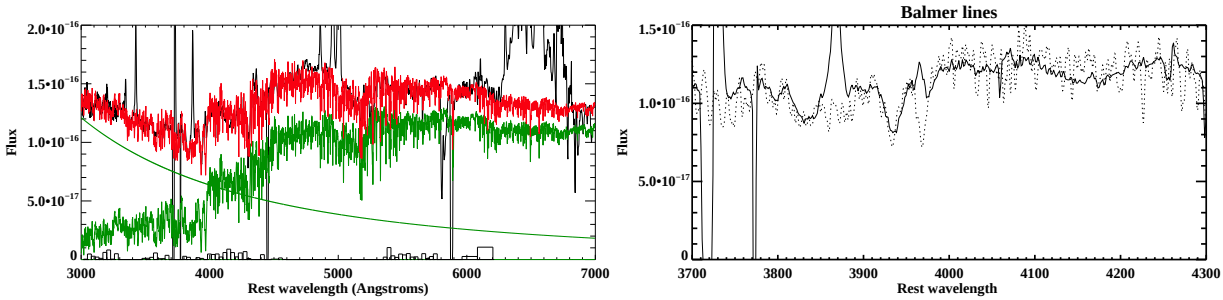

(a) 8 Gyr + PL - Main Fit

(b) 8 Gyr + PL - Balmer Lines

Figure 5.24: An example of an acceptable fit produced by CONFIT for J0332-00 – Quasar Host Galaxy. The fit shown here was produced using combination 1 and comprises an 8 Gyr population and a power-law component with $\alpha = -2.24$.

Companion nucleus

The initial modelling for the companion nucleus was performed using combination 2, and resulted in a best fitting model which included an unreddened YSP with t_{YSP}= 0.9 Gyr. Measuring the Hβ flux from the resulting stellar-subtracted spectrum generated a nebular continuum model which contributes $\sim$ 3% of the flux just below the Balmer edge. This is consistent with the value found for the aperture centred on the quasar nucleus. Once again, it was not possible to obtain a reliable estimate for the Balmer decrements, and therefore, an unreddened nebular continuum was subtracted before proceeding with the stellar synthesis modelling.

For the companion nucleus, all nine combinations of components outlined in Section 5.3 were run because, even though this nucleus does not itself host an AGN, its proximity to the type I quasar host nucleus means that, the extent to which this aperture will be contaminated by scattered light from the quasar is unclear. Table 5.15 shows that only combinations which include an 8 Gyr component produce acceptable fits. All combinations that include a 2 Gyr ISP do produce solutions with $\chi^2_{red} < 1$, however, these invariably over-predict the Ca II K absorption feature and were therefore rejected.

Figure 5.25 shows the contour plots of χ^2_{red} for the combinations which provide acceptable fits. This figure shows that, when no power-law component is included, there are three regions in which $\chi^2_{red} < 1$ (Figures 5.25(a) and 5.25(b)), and in both cases, all three regions provide acceptable solutions. However, when a power-law is included (Figures 5.25(c) and 5.25(d)), this is reduced to two regions on interest, although in the case of combination 6, the older region extends over a much wider range of ages and reddenings than for combination 2. In the case of combination 6, all solutions that have $\chi^2_{red} < 1$ are acceptable, but in the case of combination 8, only the fits in the older region

OSP Age (Gyr)	PL	Model	OSP Flux (%)	YSP Age (Gyr)	YSP Flux (%)	E(B-V)	Power-law (%)
8	No	B	64–70	0.001–0.002	25–29	0.8	–
			59–75	0.004–0.006	22–35	0.4–0.8	–
			65–75	0.03–0.05	23–31	0.2–0.4	–
		C	58–70	0.001–0.002	25–35	0.8–0.9	–
			57–73	0.004–0.009	23–36	0.7–0.8	–
			56–71	0.05–0.2	25–38	0.4–0.6	–
	Yes	B	57–76	0.004–0.007	11–36	0.3–0.8	0–18
			0–78	0.03–4	8–85	0–0.6	0–25
		C	57–73	0.09–0.2	14–35	0.4–0.5	0–14
2	No	B	–	–	–	–	–
		C	–	–	–	–	–
	Yes	B	–	–	–	–	–
		C	–	–	–	–	–

Table 5.15: The results of the stellar population synthesis modelling for J0332-00 – Companion nucleus. The definitions for each of the columns is the same as that given in the caption for Table 5.3.

are acceptable.

Figure 5.26 shows an example of an acceptable fit produced using combination 2. In this case, the YSP has age t_{YSP}= 0.005 Gyr and E(B-V)= 0.6. Examples of acceptable fits for all other successful combinations can be found in Appendix A Section A.11.2.

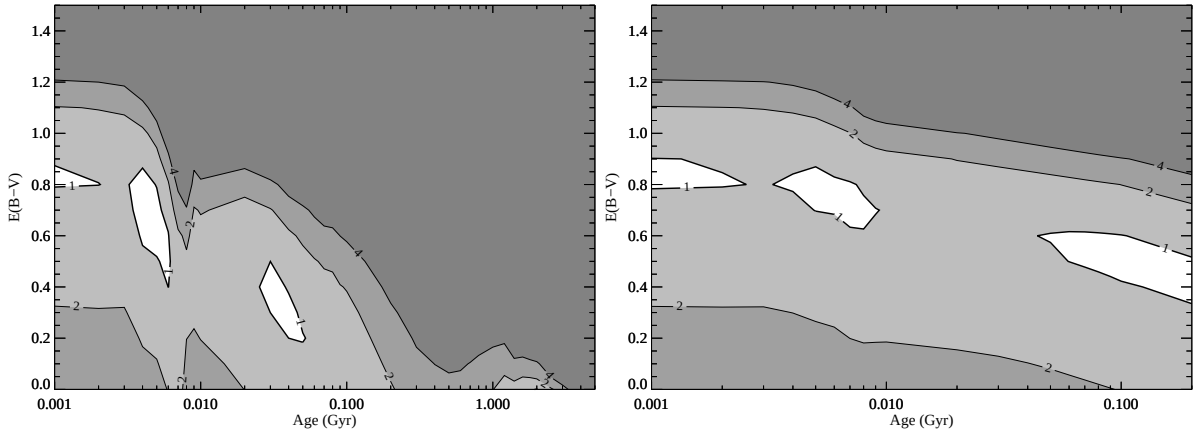

(a) 8 Gyr + Burst

(b) 8 Gyr + Cont

(c) 8 Gyr + Burst + PL

(d) 8 Gyr + Cont + PL

Figure 5.25: Plots showing the contours of χ^2_{red} for the various combination of components that produce an acceptable fit for J0332-00 – Companion nucleus. The particular combination used is given in the sub-caption for the plot. The region in which $\chi^2_{red} < 1$ is shown in white, and the values of χ^2_{red} are given on the contour lines.

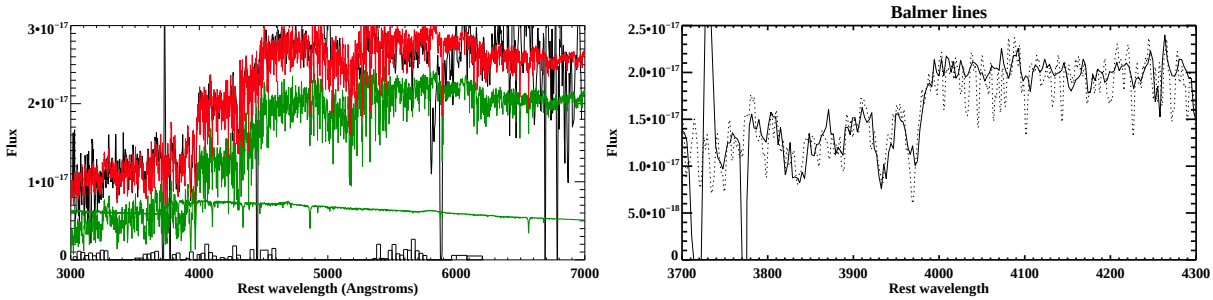

(a) 8 Gyr + Burst - Main fit

(b) 8 Gyr + Burst - Balmer Lines

Figure 5.26: An example of an acceptable fit produced by CONFIT for J0332 – Companion nucleus. This particular fit was generated using combination 2 and incorporates a YSP with t_{YSP}= 0.005 Gyr and E(B-V)= 0.6.

5.4.12 J0334+00

The initial modelling for J0334+00 was performed using combination 2, and resulted in a best fitting model with $t_{YSP} = 0.03$ Gyr and E(B-V) = 0.1. The nebular continuum model produced from measuring the Hβ flux from the stellar-subtracted spectrum contributes $\sim 22\%$ of the flux in the 3540 Å – 3640 Å region. The Balmer decrements were measured using both the Hγ/Hβ and Hδ/Hβ ratios (Table 5.2). The two measurements result in different ranges of possible reddenings, and therefore a value of E(B-V) = 0.36 was assumed because this is the average value of the region in which the values overlap. However, this resulted in slightly poorer fits than was achieved in the initial run, and therefore an unreddened nebular model was subtracted before proceeding with the modelling.

OSP Age (Gyr)	PL	Model	OSP Flux (%)	YSP Age (Gyr)	YSP Flux (%)	E(B-V)	Power-law (%)
8	No	B	6–27	0.04–0.09	74–97	0–0.2	–
		C	–	–	–	–	–
	Yes	B	0–27	0.04–0.3	65–94	0–0.3	0–32
		C	–	–	–	–	–
2	No	B	9–32	0.04–0.08	71–95	0–0.2	–
		C	–	–	–	–	–
	Yes	B	0–39	0.04–0.4	49–100	0–0.4	0–34
		C	–	–	–	–	–

Table 5.16: The results of the stellar population synthesis modelling for J0334+00. The definitions for each of the columns is the same as that given in the caption for Table 5.3.

Table 5.16 shows that it was only possible to achieve acceptable fits when a burst YSP model is included. Models that utilise a continuous star formation component instead do not produce acceptable results. Figures 5.27(a) and 5.27(c)) show that, for combinations 2 and 3, there are two possible regions of interest ($\chi^2_{red} < 1$) for the ages of the YSP. However, in both cases, inspection of the fits in the region of the Balmer lines allows the younger regions to be discounted as a possibility, because, in both cases, they strongly over-predicts the Ca II K absorption. When no power-law component is included in the fit, the upper age is always less that 100 Myr, with low values of reddening for the YSP population ($0 \leq E(B-V) \leq 0.2$). The inclusion of a power-law allows a wider spread of ages and reddenings, (Figures 5.27(b) and 5.27(d)), with a maximum age of 0.4 Gyr and reddening in the range $0 \leq E(B-V) \leq 0.4$. In all cases for which successful fits are achieved, the minimum allowable age is 0.04 Gyr.

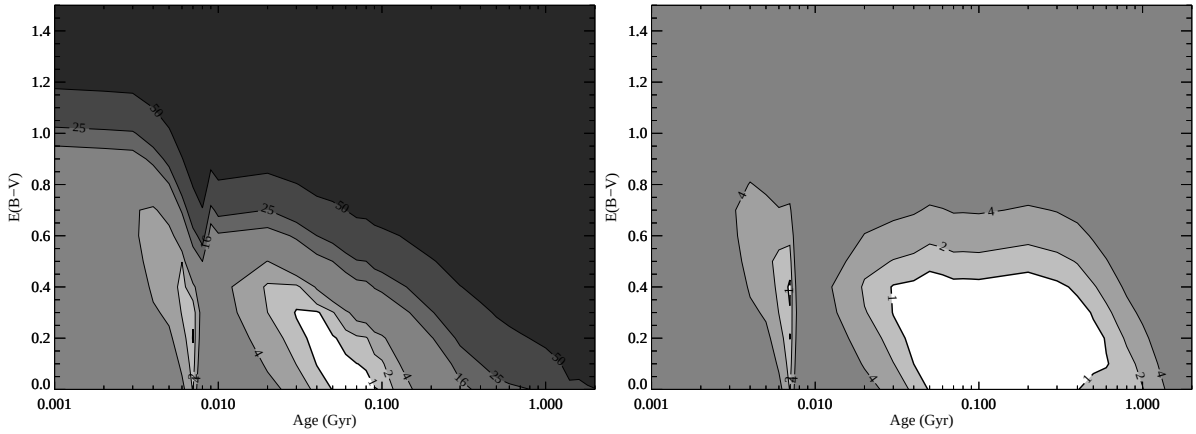

(a) 8 Gyr + Burst

(b) 8 Gyr + Burst + PL

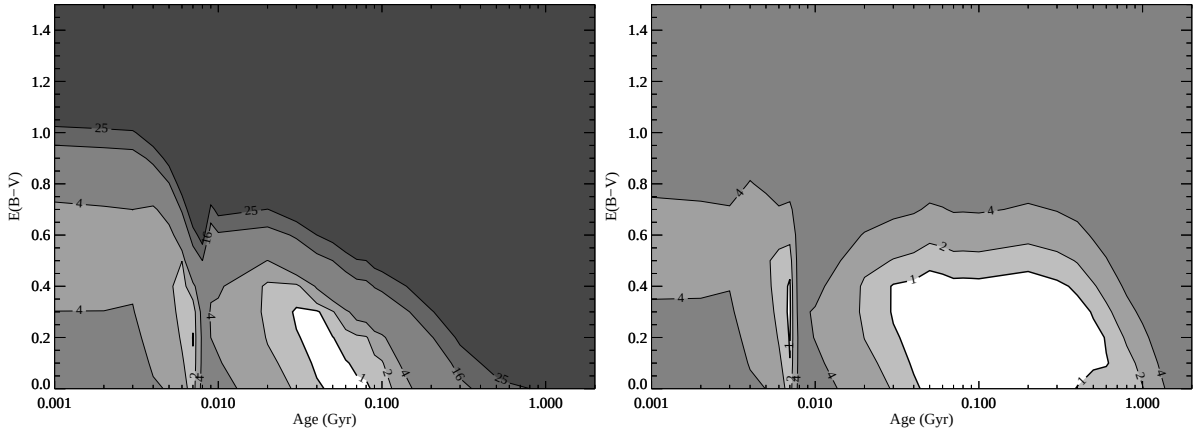

(c) 2 Gyr + Burst

(d) 2 Gyr + Burst + PL

Figure 5.27: Plots showing the contours of χ^2_{red} for the various combination of components that produce an acceptable fit for J0334+00. The particular combination used is given in the sub-caption for the plot. The region in which $\chi^2_{red} < 1$ is shown in white, and the values of χ^2_{red} are given on the contour lines.

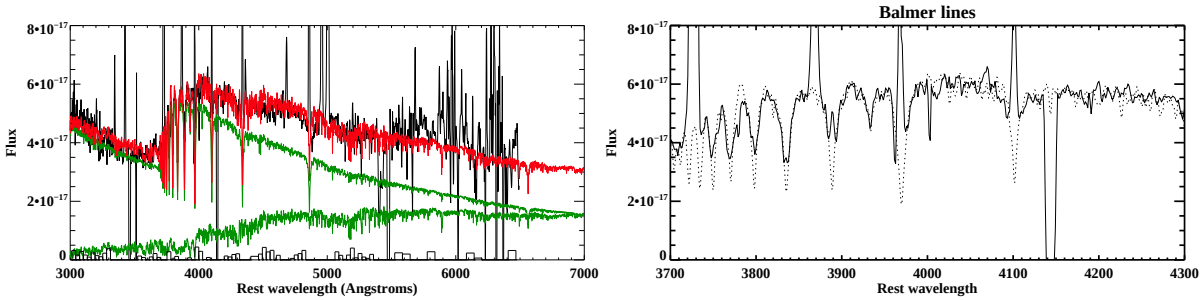

(a) 8 Gyr + Burst - Main fit

(b) 8 Gyr + Burst - Balmer Lines

Figure 5.28: An example of an acceptable fit produced by CONFIT for J0334+00. The fit shown here was produced using combination 2 and includes a YSP with $t_{YSP} = 0.08$ Gyr and E(B-V) = 0.

Figure 5.28 shows an example of an acceptable confit fit produced by combination 2. This particular fit has $t_{YSP} = 0.08$ Gyr and E(B-V) = 0. Further examples of acceptable fits can be found in Appendix A Section A.12.

5.4.13 J0848+01

The initial modelling for J0848+01 was carried out using combination 2, and the resulting best fitting model comprised a YSP $t_{YSP} = 0.05$ with E(B-V) = 0.4 (Table 5.1). The nebular continuum generated for this object contributes $\sim 19\%$ of the flux just below the Balmer edge. J0848+01 has intrinsically low equivalent width Hγ and Hδ emission lines, and therefore it was not possible to make a reliable measurement of the Balmer decrements in order to estimate the reddening. Therefore, an unreddened nebular continuum was subtracted before proceeding with the modelling.

Table 5.17 shows that only models that include a burst component produce successful fits. Figure 5.29(a) shows that for combination 2, there are three regions in which $\chi^2_{red} < 1$. However, it is only the younger and intermediate regions which are successful in terms of the detailed fits around the stellar absorption features.

OSP Age (Gyr)	PL	Model	OSP Flux (%)	YSP Age (Gyr)	YSP Flux (%)	E(B-V)	Power-law (%)
8	No	B	56–66	0.2–0.4	32–43	0.1–0.3	–
		C	–	–	–	–	–
	Yes	B	31–65	0.3–0.5	31–55	0.1–0.3	0–15
		C	–	–	–	–	–
2	No	B	56–72	0.2–0.3	23–38	0.5–0.6	–
		C	–	–	–	–	–
	Yes	B	56–79	0.3	21–42	0.5	0–8
		C	–	–	–	–	–

Table 5.17: The results of the stellar population synthesis modelling for J0848+01. The definitions for each of the columns is the same as that given in the caption for Table 5.3.

For combinations 3 and 7 (Figures 5.29(c) and 5.29(d)), although the region is which $\chi^2_{red} < 1$ is more extended then for combination 2, poor fits to Ca II K allowed all but the youngest and most reddened solutions to be discarded. In the case of combination 6 (Figure 5.29(b)), solutions with $t_{YSP} > 0.5$ Gyr could also be discounted. The resulting range of acceptable fits are shown in Table 5.17.

Figure 5.30 shows an example of an acceptable fit generated by combination 2, which utilises a YSP $t_{YSP} = 0.2$ Gyr and E(B-V) = 0.3. Examples of confit fits for the remaining

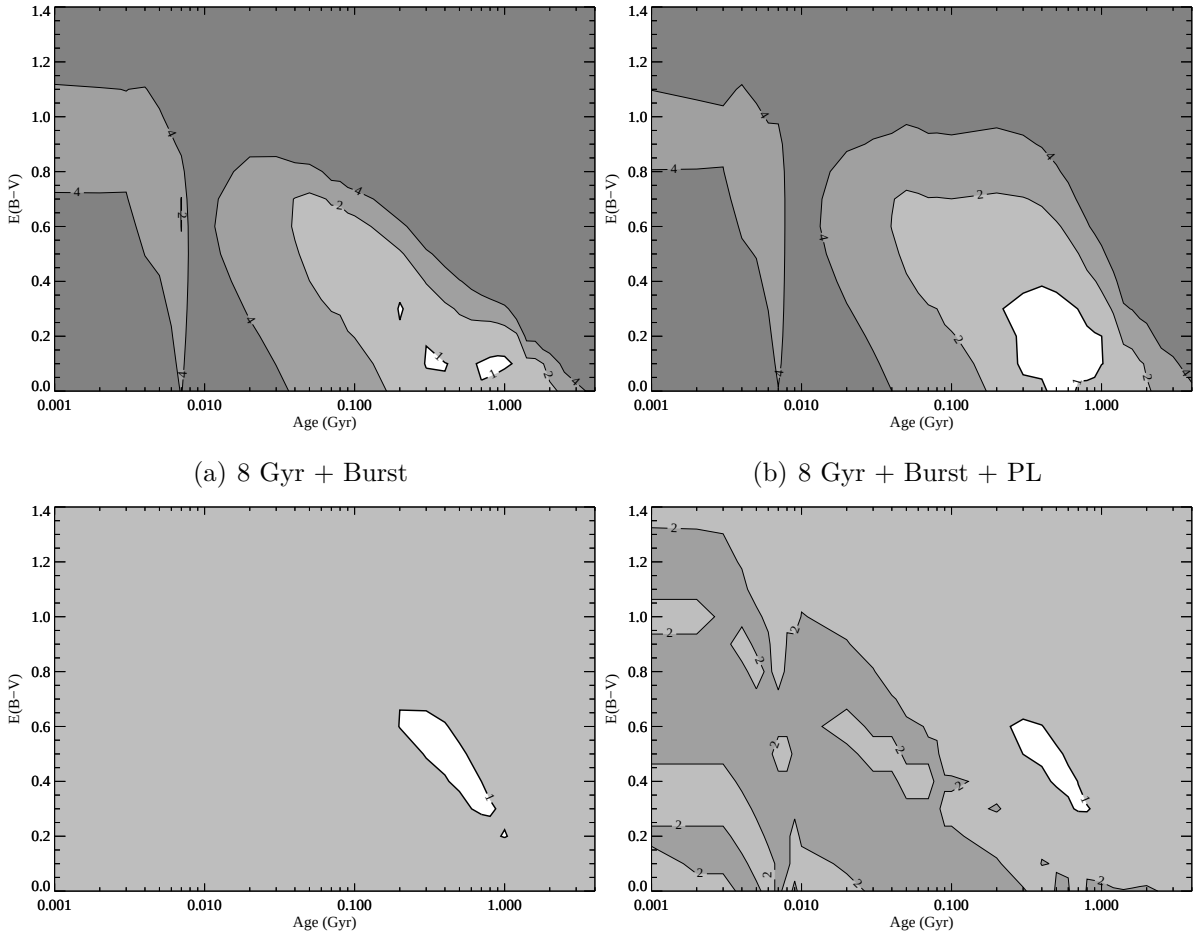

(a) 8 Gyr + Burst

(b) 8 Gyr + Burst + PL

(c) 2 Gyr + Burst

(d) 2 Gyr + Burst + PL

Figure 5.29: Plots showing the contours of χ^2_{red} for the various combination of components that produce an acceptable fit for J0848+01. The particular combination used is given in the sub-caption for the plot. The region in which $\chi^2_{red} < 1$ is shown in white, and the values of χ^2_{red} are given on the contour lines.

successful solutions can be found in Appendix A Section A.13.

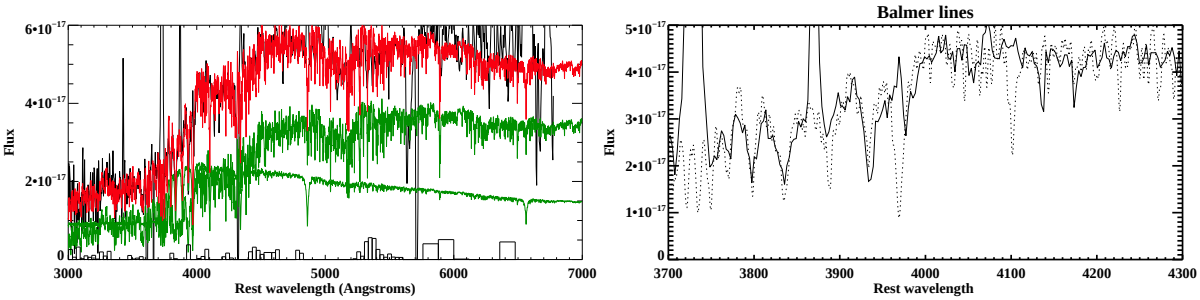

(a) 8 Gyr + Burst - Main fit

(b) 8 Gyr + Burst - Balmer Lines

Figure 5.30: An example of an acceptable fit produced by CONFIT for J0848+01. The fit shown here was generated using combination 2 and include a YSP with t_{YSP} = 0.2 Gyr and E(B-V) = 0.3.

5.4.14 J0904-00

The initial modelling for J0904-00 was carried out using combination 2, which resulted in a best fitting model with t_{YSP}= 0.02 Gyr and E(B-V)=0.3. After subtracting this model, the flux of Hβ was measured from the resulting spectrum in order to construct the nebular model, which contributes $\sim$ 13% to the total flux just below the Balmer edge. No reddening was applied to the nebular continuum before subtraction, because the Hγ/Hβ ratio is consistent with case B recombination (Table 5.2), and thus it was deemed unnecessary to do so.

OSP Age (Gyr)	PL	Model	OSP Flux (%)	YSP Age (Gyr)	YSP Flux (%)	E(B-V)	Power-law (%)
8	No	B	12–32	0.006	72–91	0.3–04	–
			11–31	0.03	73–92	0.2–0.3	–
		C	5–34	0.06–0.2	71–96	0.2–0.4	–
	Yes	B	0–39	0.03–0.3	55–99	0–0.5	0–57
		C	0–34	0.07–0.2	59–100	0.2–0.4	0–22
2	No	B	16–22	0.006	82–87	0.3	–
			26–31	0.02	72–76	0.3	–
		C	8–43	0.06–0.2	64–94	0.2–0.4	
	Yes	B	0-44	0.02–0.4	26–98	0–0.5	0–62
		C	0–43	0.07–0.2	48–100	0.2–0.4	0–22

Table 5.18: The results of the stellar population synthesis modelling for J0904-00. The definitions for each of the columns is the same as that given in the caption for Table 5.3.

Table 5.18 shows the results of the stellar synthesis modelling performed for J0904-00, and shows that all combinations which require two stellar components produce an acceptable fit. However, combination 1 does not produce an adequate result in this case.

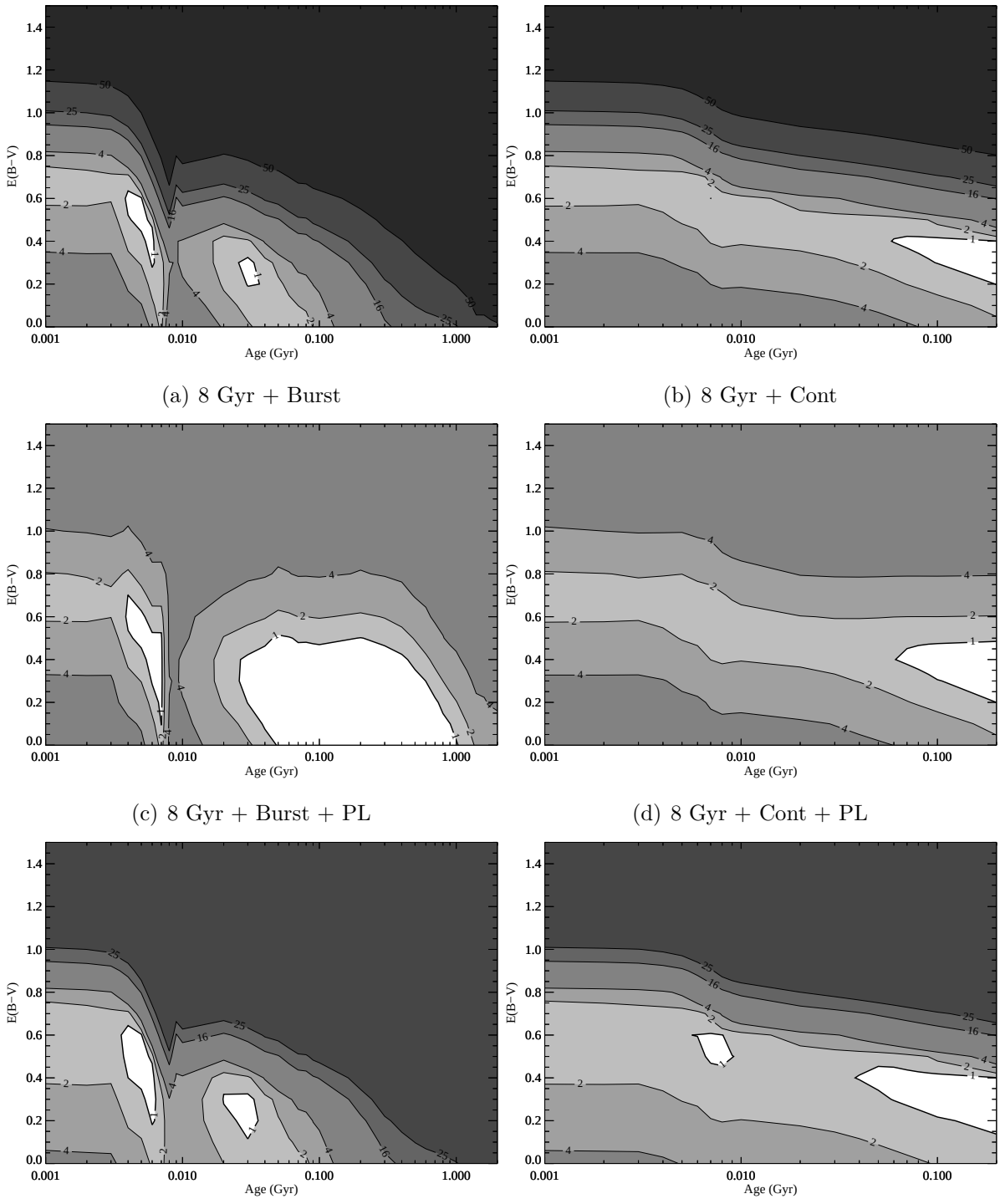

(a) 8 Gyr + Burst

(b) 8 Gyr + Cont

(c) 8 Gyr + Burst + PL

(d) 8 Gyr + Cont + PL

(e) 2 Gyr + Burst

(f) 2 Gyr + Cont

Figure 5.31: Plots showing the contours of χ^2_{red} for the various combination of components that produce an acceptable fit for J0904-00. The particular combination used is given in the sub-caption for the plot. The region in which $\chi^2_{red} < 1$ is shown in white, and the values of χ^2_{red} are given on the contour lines.

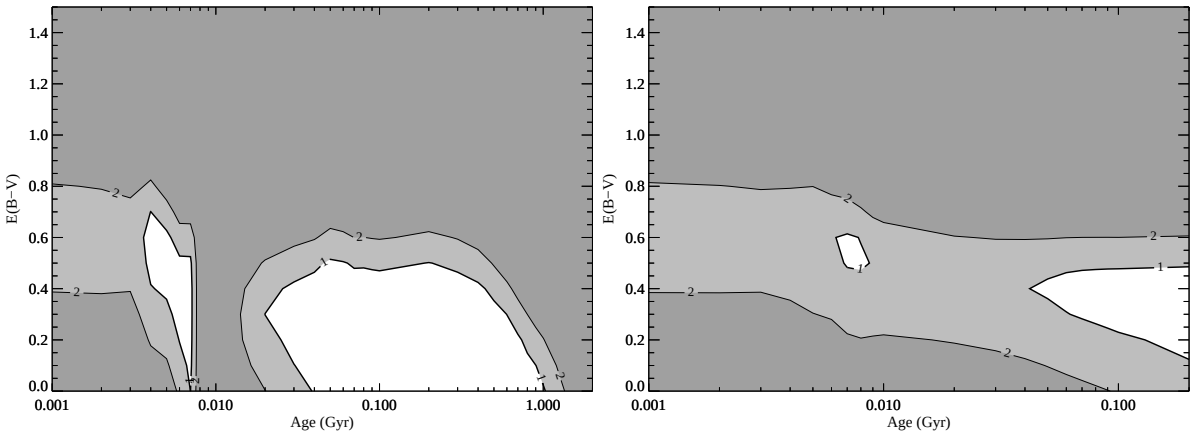

(a) 2 Gyr + Burst + PL

(b) 2 Gyr + Cont + PL

Figure 5.31: [continued]

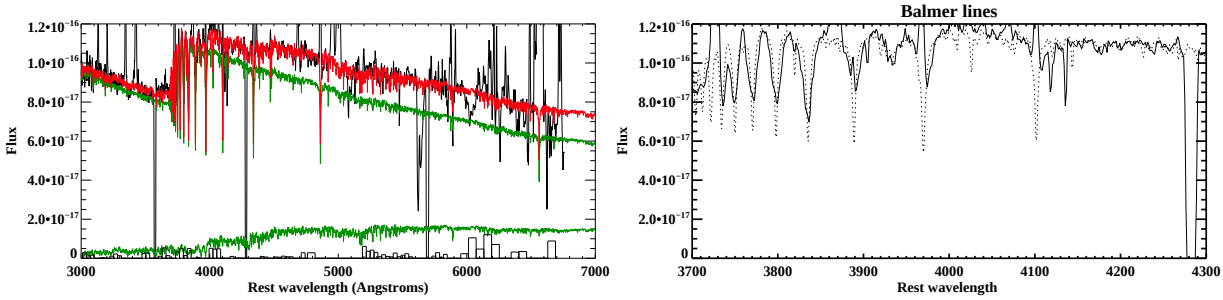

(a) 8 Gyr + Burst - Main fit

(b) 8 Gyr + Burst - Balmer Lines

Figure 5.32: An example of an acceptable fit produced by CONFIT for J0904-00. This fit was produced using combination 2 and includes a YSP with t_{YSP}= 0.006 Gyr and E(B-V)= 0.4.

This is reinforced in Figure 5.32(b) which demonstrates that the Balmer lines are clearly detectable in the spectrum, meaning that a YSP component is *required*.

Figure 5.31 shows the contour plots of χ^2_{red} associated with each of the successful combinations. When considering models with a burst star formation history, there are two regions in which $\chi^2_{red} < 1$ (Figures 5.31(a), 5.31(c), 5.31(e) and 5.31(a)). When no power-law component is included, both these regions produce at least one acceptable fit, however, when a power-law is included, the fits associated with this younger region strongly over predict the Ca II K absorption feature, and were therefore discounted. In all cases where a continuous star formation history was used, it is only at the older ages that the fits produced are acceptable. Table 5.18 shows that the continuous formation models allow for substantially older ages than the burst models.

Figure 5.32 shows an example of an acceptable combination 2 fit for J0904-00, which

includes a YSP with t_{YSP}= 0.006 Gyr and E(B-V)= 0.4. Further examples of acceptable fits can be found in Appendix A, Section A.14.

5.4.15 J0923+01

The initial modelling for J0923+01 was performed using combination 2, which resulted in a best fitting model that included a YSP with t_{YSP}= 0.04 Gyr and E(B-V)= 0.5 (Table 5.1). This model was subtracted from the observed data, and the Hβ flux was then measured from the stellar-subtracted spectrum, which resulted in a nebular continuum model which contributes $\sim$ 14% of the total flux in the 3540–3640 Å range. It was not possible to obtain a reliable estimate of the Balmer decrements in this case because the errors in the ratios of Hδ/Hβ and Hγ/Hβ were larger than the measured value. Therefore, an unreddened nebular continuum was subtracted from the data, which did not result in an unphysical step in the spectrum at the Balmer edge, and was thus considered acceptable.

Table 5.19 shows that, it is only modelling combinations which included a burst component that produce acceptable fits. All the combinations that utilised a continuous star formation model do not produce any results with $\chi^2_{red} < 1$.

Figure 5.33 shows plots of χ^2_{red} for each modelling combination for which acceptable fits have been generated. This figure shows that, in all four cases, there are two regions of interest ($\chi^2_{red} < 1$), however, in all cases, it was possible to reject the youngest region (0.007 Gyr) on the basis of the over prediction of the Ca II K absorption feature.

OSP Age (Gyr)	PL	Model	OSP Flux (%)	YSP Age (Gyr)	YSP Flux (%)	E(B-V)	Power-law (%)
8	No	B	0–19	0.05–0.1	80–100	0.4–0.5	–
		C	–	–	–	–	–
	Yes	B	0–22	0.05–0.4	61–58	0.1–0.6	0–42
		C	–	–	–	–	–
2	No	B	0–26	0.04–0.1	74–100	0.4–0.6	–
		C	–	–	–	–	–
	Yes	B	0–33	0.05–0.3	48–100	0.1–0.6	0–41
		C	–	–	–	–	–

Table 5.19: The results of the stellar population synthesis modelling for J0923+01. The definitions for each of the columns is the same as that given in the caption for Table 5.3.

In the case of combination 2 (Figure 5.33(a)), all solutions produce acceptable fits,

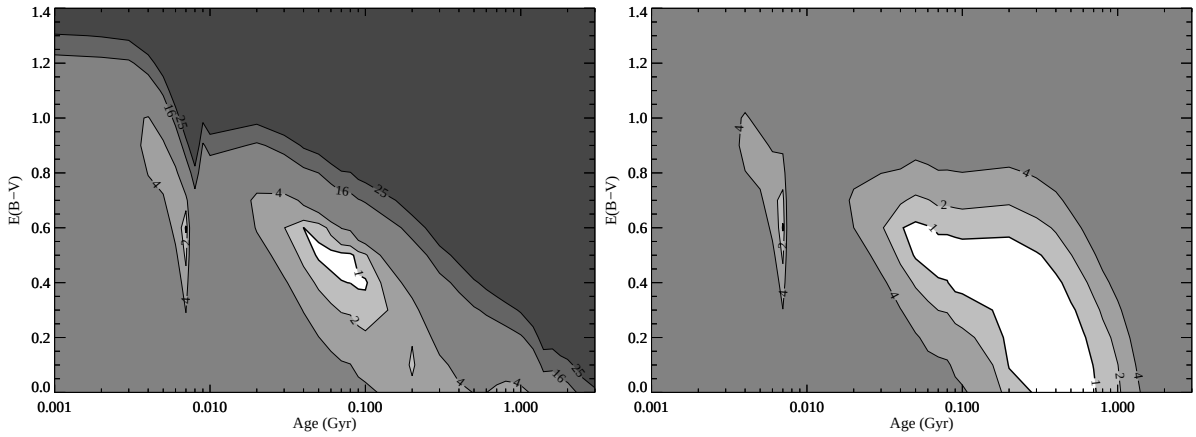

(a) 8 Gyr + Burst

(b) 8 Gyr + Burst + PL

(c) 2 Gyr + Burst

(d) 2 Gyr + Burst + PL

Figure 5.33: Plots showing the contours of χ^2_{red} for the various combination of components that produce an acceptable fit for J0923+01. The particular combination used is given in the sub-caption for the plot. The region in which $\chi^2_{red} < 1$ is shown in white, and the values of χ^2_{red} are given on the contour lines.

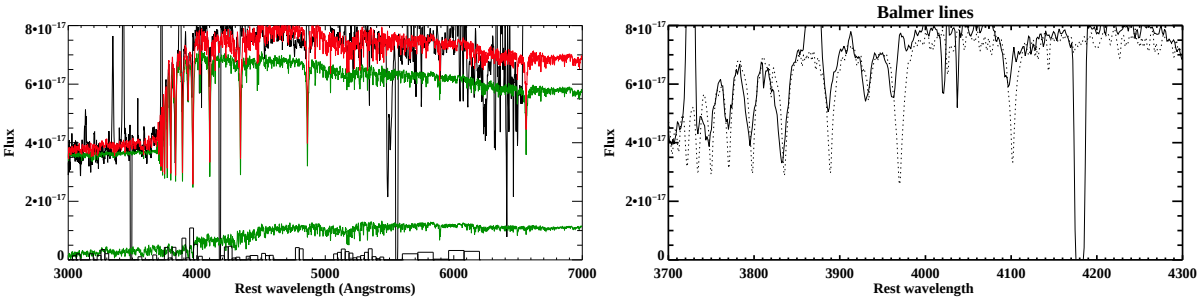

(a) 8 Gyr + Burst - Main fit

(b) 8 Gyr + Burst - Balmer Lines

Figure 5.34: An example of an acceptable fit produced by CONFIT for J0923+01. The fit shown here was generated using combination 2 and incorporates a YSP with t_{YSP}= 0.05 Gyr and E(B-V)= 0.5.

except for at the highest value of reddening (E(B-V)= 0.6). This is because the overall fit to the shape of the spectrum is poor, due to the over-prediction of the flux long wards of 6000 Å. This is a direct result of the fact that it is difficult to constrain the model, due to the strong fringing and residuals from the sky subtraction in this wavelength region. For combination 3, shown in Figure 5.33(c), all solutions in the older region produce acceptable fits.

For combinations 6 and 7, which include a power-law component (Figures 5.33(b) and 5.33(d))), fits with $t_{YSP} > 0.3$ Gyr and $t_{YSP} > 0.4$ Gyr respectively were rejected because, in both cases, the flux at wavelengths above 6000 Å is strongly over predicted. Once again, this is a consequence of the noise in the data at the longest wavelength.

Figure 5.34 shows an example of an acceptable fit generated using combination 2. In this case, the fit includes a YSP with age t_{YSP}= 0.05 Gyr and E(B-V)= 0.5. Examples of acceptable fits for the other successful modelling combinations can be found in Appendix A Section A.14.1.

5.4.16 J0924+01

The initial modelling of J0924+01 was performed using combination 3, which produced a best fitting model with t_{YSP}= 0.003 and E(B-V)= 1.1. After subtracting this model from the spectrum, the Hβ flux was measured in order to generate the nebular continuum model, which contributes $\sim$ 37% of the total flux below the Balmer edge. The Balmer decrements were measured using both the Hγ/Hβ and Hα/Hβ ratios, however, both values produce large errors. Therefore, the nebular continuum was initially reddened using a value of E(B-V)= 0.7, which resulted in an under subtraction of the nebular component. In order to test various values of reddening for the model nebular continuum, reddening beginning with the lowest value determined from the Balmer decrements (E(B-V)=0.2) was applied, and then increased in increments of $\Delta E(B-V) = 0.05$, until the point at which the continuum subtraction no longer resulted in a step in the spectrum at the Balmer edge (E(B-V)= 0.3, Table 5.2). The nebular continuum contributes $\sim$ 14% of the total flux just below the Balmer edge, after the reddening correction has been applied.

J0924+01 was modelled using all nine combinations of components outlined in Section 5.3, and Table 5.20 shows that all combinations which include a YSP/ISP component produce acceptable fits. When considering combinations 2 and 3, the range of acceptable fits is very limited (Figures 5.35(a) and 5.35(e)), with combination 2 producing two solutions with $\chi^2_{red} < 1$, in which the YSP dominates the flux, and combination 3

OSP Age (Gyr)	PL	Model	OSP Flux (%)	YSP Age (Gyr)	YSP Flux (%)	E(B-V)	Power-law (%)
8	No	B	10–20	0.005	77–86	1.0	–
			19–28	0.02	71–78	0.8	–
		C	0–35	0.008–0.1	63–97	0.8–1	–
	Yes	B	6–44	0.004–0.007	27–88	0.4–1.1	0–44
			0–46	0.02–1.2	16–86	0–1.1	0–61
		C	4–42	0.007–0.2	33–90	0.5–1.1	0–34
2	No	B	36–51	0.009	46–59	0.9	–
		C	16–35	0.007	63–80	1.1	–
			15–35	0.02–0.03	62–80	1.0	–
			6–34	0.06–0.1	64–91	0.9	–
	Yes	B	13–68	0.001–0.007	4–81	0–1.5	0–45
			0–67	0.009–1.2	5–88	0–1.4	0–60
		C	0–66	0.001–0.2	6–96	0.2–1.4	0–41

Table 5.20: The results of the stellar population synthesis modelling for J0924+01. The definitions for each of the columns is the same as that given in the caption for Table 5.3.

producing only one solution. When using combination 6 and 7, which both include a power-law component (Figures 5.35(c) and 5.35(c)), a wide range of solutions produce $\chi^2_{red} < 1$, and in both cases all solutions are acceptable, meaning that these combinations do not provide any real constraint on the age and/or reddening of any YSP present.

For combinations 4 and 5 (Figures 5.35(b) and 5.35(a)), which employ a continuous star formation history, the possible range of ages and reddenings in reasonably well constrained by the modelling. In the case of combination 5, where there are three regions in which $\chi^2_{red} < 1$, all the regions produce acceptable fits. The inclusion of a power-law component (Figures 5.35(d) and 5.35(b)) leads to the acceptable range of age and reddening becoming poorly constrained, with the upper age limit being truncated by the upper age of the modelling component.

Figure 5.36 shows an example of an acceptable fit produced by CONFIT , which was generated using combination 2. This fit includes a YSP with t_{YSP}= 0.02 Gyr and E(B-V)= 0.8. Figure 5.36(b) shows that the strength of the Ca II K line is strongly under predicted by the model, which is consistent with the high value of reddening determined here. This is because, the gas and dust which is responsible for the reddening will enhance this feature. In this case, it is relatively easy to search for Ca II K absorption due to the reddening dust column because the YSP dominates the flux, however, when the YSP contributes a lower proportion of the flux, this effect would be more difficult to detect. Examples of CONFIT fits for other successful combinations can be found in

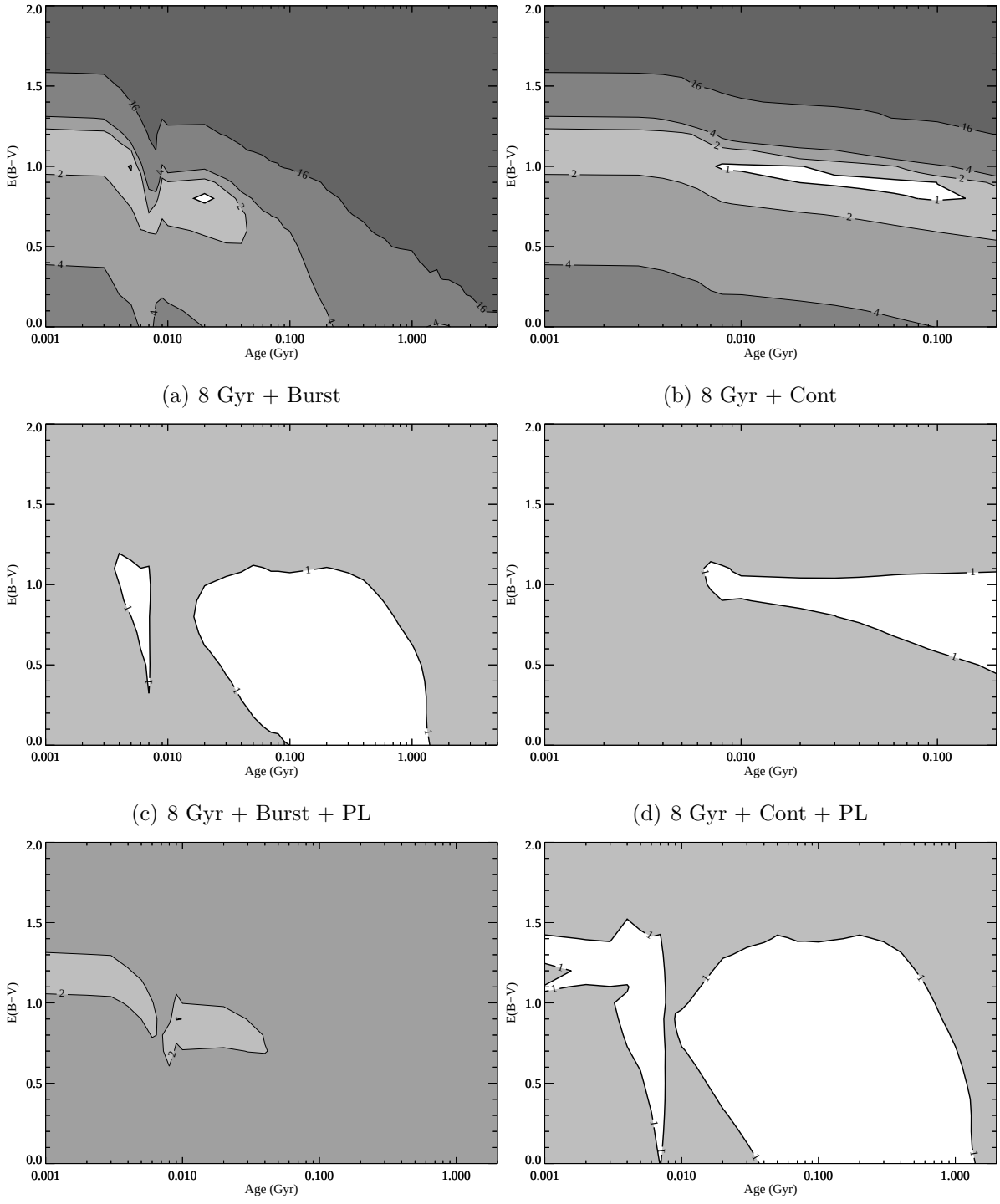

(a) 8 Gyr + Burst

(b) 8 Gyr + Cont

(c) 8 Gyr + Burst + PL

(d) 8 Gyr + Cont + PL

(e) 2 Gyr + Burst

(f) 2 Gyr + Burst + PL

Figure 5.35: Plots showing the contours of χ^2_{red} for the various combination of components that produce an acceptable fit for J0924+01. The particular combination used is given in the sub-caption for the plot. The region in which $\chi^2_{red} < 1$ is shown in white, and the values of χ^2_{red} are given on the contour lines.

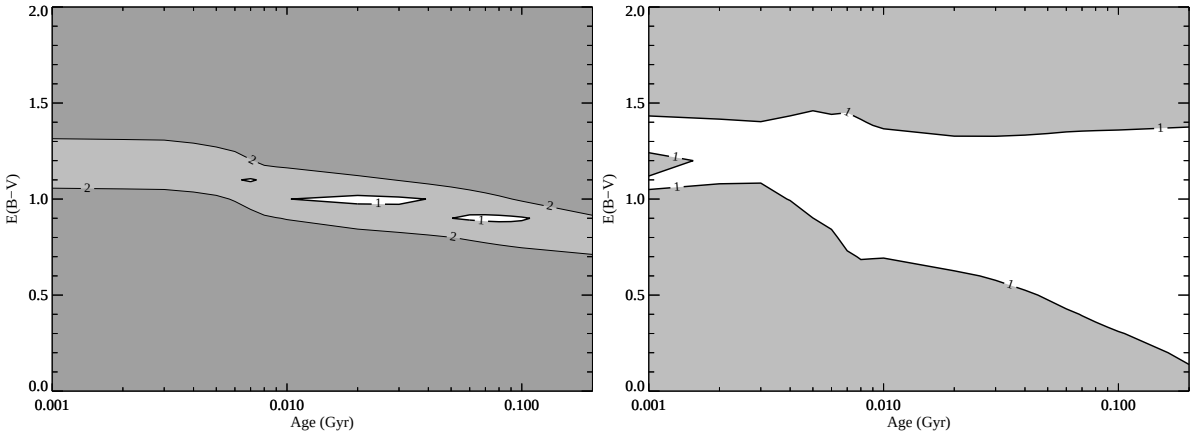

(a) 2 Gyr + Cont (b) 2 Gyr + Cont + PL

Figure 5.35: [continued]

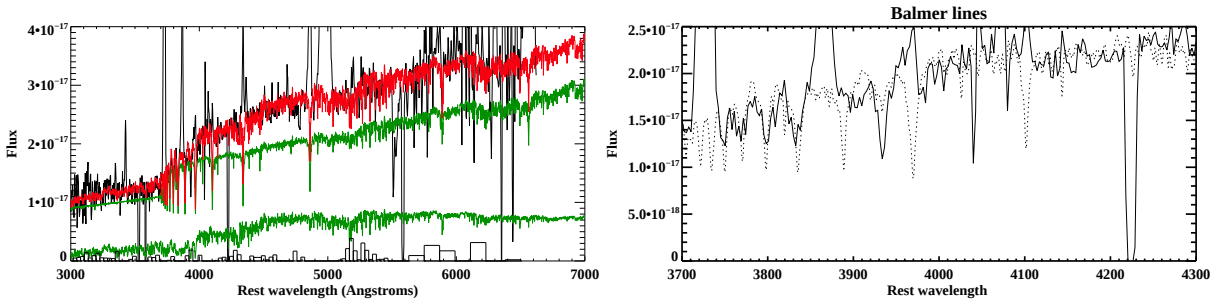

(a) 8 Gyr + Burst - Main fit (b) 8 Gyr + Burst - Balmer Lines

Figure 5.36: An example of an acceptable fit produced by CONFIT for J0924+01. The combination shown here was produced using combination 2 and includes a YSP with t_{YSP}= 0.02 Gyr and E(B-V)= 0.8.

Appendix A Section A.14.2

5.4.17 J0948+00

The initial modelling for J0948+00 was performed using combination 3 and resulted in a best fitting model which included a YSP with t_{YSP}= 0.1 Gyr and E(B-V)=0.3. Having subtracted this model from the spectrum, the nebular continuum model generated from the measured Hβ flux contributes $\sim$ 15% of the total flux below the Balmer edge, and is thus relatively weak. It was not possible to make a reliable measurement of the Balmer decrements because of the low equivalent widths of the Hγ and Hδ lines. Therefore, an unreddened nebular continuum model was subtracted, which did not result in an unphysical step at the Balmer edge.

All nine modelling combinations, which are outlined in Section 5.3, were applied to the spectrum, and the results given in Table 5.21 show that, it is only combinations which include a burst component that produce acceptable fits.

OSP Age (Gyr)	PL	Model	OSP Flux (%)	YSP Age (Gyr)	YSP Flux (%)	E(B-V)	Power-law (%)
8	No	B	30–46	0.2–0.3	53–68	0–0.2	–
		C	–	–	–	–	–
	Yes	B	0–47	0.2–0.4	51–94	0.1–0.5	0–20
		C	–	–	–	–	–
2	No	B	30–40	0.2	58–69	0.3	–
		C	–	–	–	–	–
	Yes	B	0–57	0.2–0.4	41–94	0.1–0.4	0–19
		C	–	–	–	–	–

Table 5.21: The results of the stellar population synthesis modelling for J0948+00. The definitions for each of the columns is the same as that given in the caption for Table 5.3.

Figure 5.37 shows that, for all the modelling combinations that are successful, there is one region in which solutions with $\chi^2_{red} < 1$ can be found. For combinations 2 and 3 (Figures 5.37(a) and 5.37(c)), all the fits associated with these regions are acceptable. In the case of combination 6 (Figure 5.37(b)), which incorporates a power-law component, it was possible to reject solutions with $t_{YSP} \geq 0.3$ Gyr *and* $E(B-V) > 0.4$. For combination 7 (Figure 5.37(d)) it was possible to reject solutions with $t_{YSP} > 0.4$ Gyr and, at younger ages, a number of solutions at the highest and lowest reddenings allowed by the modelling were also rejected. All these solutions were rejected on the basis of poor fits in the region of the age sensitive stellar absorption features. This means that, for all combinations which produce acceptable fits, the range of ages is well constrained to be $0.2 \leq t_{YSP}$ (Gyr) ≤ 0.4, with reddenings in the range $0 \leq E(B-V) \leq 0.5$.

On the basis of the deep r'-band Gemini GMOS-S image (Chapter 3 Figure 3.1(c)), J0948+00 was classified as an undisturbed galaxy, however, the spectrum shows clear evidence of an episode on star formation within the last 0.4 Gyr. This means that like J0142+14 (Section 5.4.3), J0948+00 could also be a candidate E+A galaxy.

Figure 5.38 shows an example of an acceptable fit generated using combination 2, and shows that the OSP and YSP components contribute roughly equal proportions of the total flux in the normalising bin (4520–4580 Å). This fit includes a YSP with t_{YSP}= 0.2 Gyr and E(B-V)= 0.1. Examples of CONFIT fits for the remaining successful combinations can be found in Appendix A Section A.15.

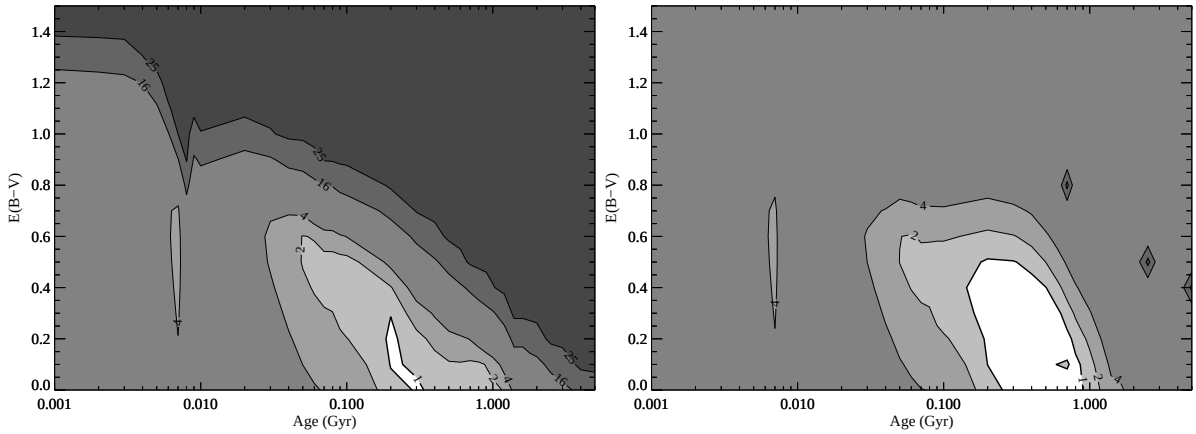

(a) 8 Gyr + Burst

(b) 8 Gyr + Burst + PL

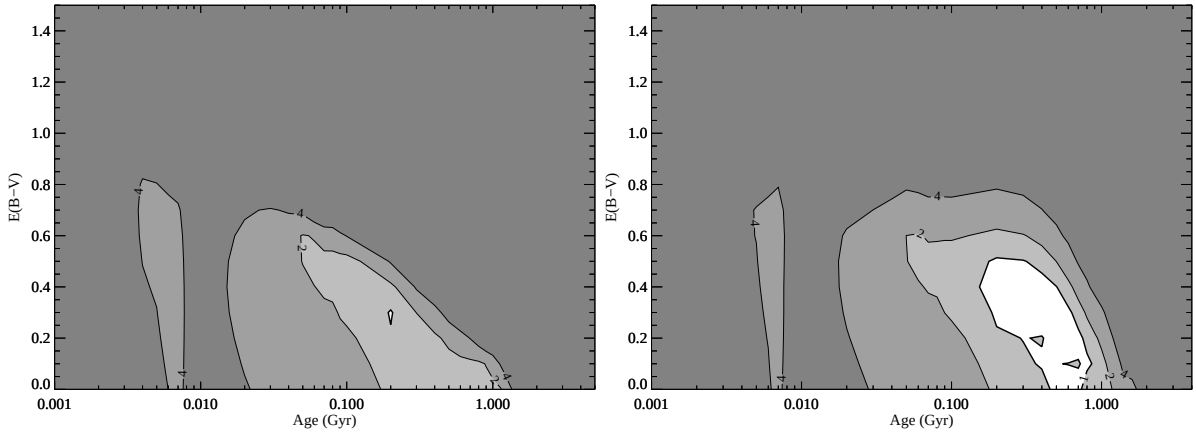

(c) 2 Gyr + Burst

(d) 2 Gyr + Burst + PL

Figure 5.37: Plots showing the contours of χ^2_{red} for the various combination of components that produce an acceptable fit for J0948+00. The particular combination used is given in the sub-caption for the plot. The region in which $\chi^2_{red} < 1$ is shown in white, and the values of χ^2_{red} are given on the contour lines.

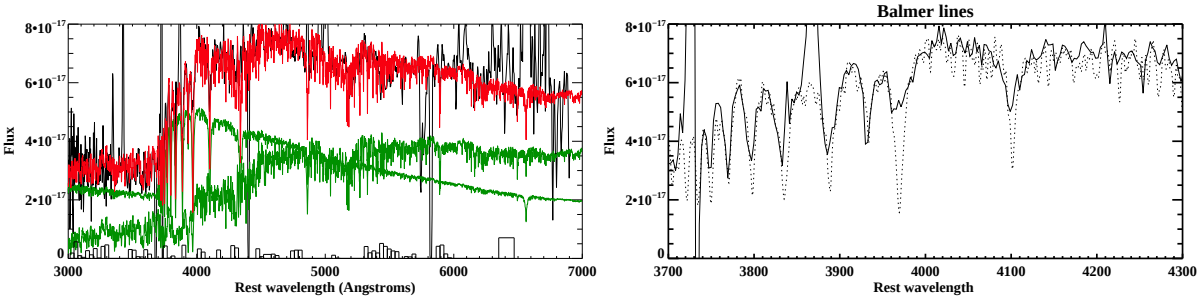

(a) 8 Gyr + Burst - Main fit

(b) 8 Gyr + Burst - Balmer Lines

Figure 5.38: An example of an acceptable fit produced by CONFIT for J0948+00. The fit shown here was generated using combination 2 and includes a YSP with t_{YSP}= 0.2 Gyr and E(B-V)= 0.1.

5.4.18 J2358-00

The initial modelling for J2358-00 was performed using combination 2, and resulted in a best fitting model with t_{YSP}= 0.02 Gyr and E(B-V)= 0.5. The model nebular continuum, generated from the Hβ flux measured from the stellar-subtracted spectrum, contributes $\sim$ 28% of the total flux below the Balmer edge. The reddening derived from the Hγ/Hβ and Hδ/hb ratio is consistent with case B (Table 5.2), and therefore, no reddening has been applied to the model nebular continuum before subtracting it from the spectrum. The resulting spectrum shows no evidence of an unphysical step at the Balmer edge, thus was deemed acceptable.

All nine modelling combinations were utilised in order to perform the stellar synthesis modelling, and the results presented in Table 5.22 show that, it is only models which include a burst component that produce acceptable solutions.

The contour plots of χ^2_{red} for the four successful combinations are presented in Figure 5.39, and show that, for combinations 2 and 3 (Figures 5.39(a) and 5.39(c)), two regions of interest are found. However, in both cases, the younger fits were rejected due to the strong over-prediction of the Ca II K absorption feature. For both these modelling combinations, and those which include a power-law component (Figures 5.39(b) and 5.39(d))), it was also possible to reject a significant number of potential solutions based on the strong over-prediction of Ca II K absorption. In fact, Figure 5.40(b) shows that this feature is unusually weak in the spectrum of J2358-00, although the Balmer lines are clearly detectable. The reason for this is not immediately apparent but is not due to any cosmetic defects in the spectrum at this wavelength. This feature provides a strong constraint on the acceptable ages and reddenings of the YSP when no power-

OSP Age (Gyr)	PL	Model	OSP Flux (%)	YSP Age (Gyr)	YSP Flux (%)	E(B-V)	Power-law (%)
8	No	B	0–19	0.04–0.05	88–95	0.5–0.6	–
		C	–	–	–	–	–
	Yes	B	0–28	0.04–0.2	44–101	0.2–0.6	0–41
		C	–	–	–	–	–
2	No	B	0–13	0.04	89–100	0.6	–
		C	–	–	–	–	–
	Yes	B	20–91	0.04–0.2	54–104	0.4–0.7	0–29
		C	–	–	–	–	–

Table 5.22: The results of the stellar population synthesis modelling for J2358-00. The definitions for each of the columns is the same as that given in the caption for Table 5.3.

law component is included ($0.04 \leq t_{YSP}$ (Gyr) ≤ 0.05, with reddenings in the range $0.5 \leq E(B-V) \leq 0.6$). However, when a power-law component is included, a much wider range of ages and reddenings becomes permissible, although in a majority of cases, the YSP flux is dominant over the OSP.

Figure 5.40 shows an example of an acceptable fit generated using combination 2. In this case, the YSP has t_{YSP}= 0.04 Gyr and E(B-V)= 0.6. Further examples of acceptable fits for other modelling combinations can be found in Appendix A Section A.16.

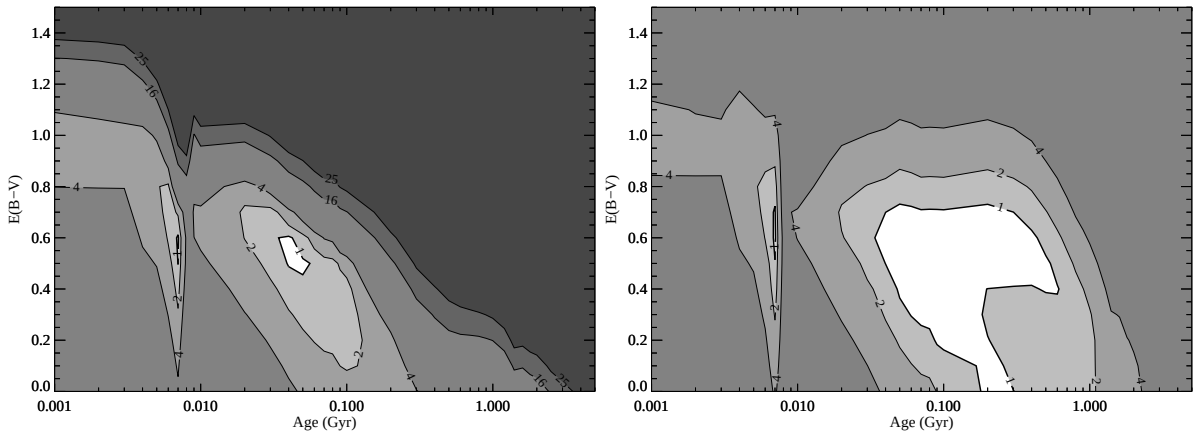

(a) 8 Gyr + Burst

(b) 8 Gyr + Burst + PL

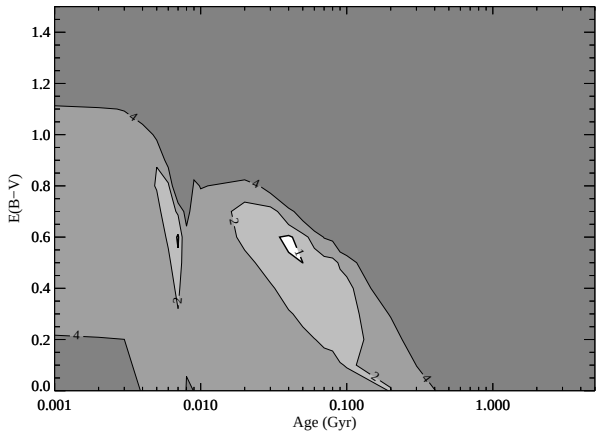

(c) 2 Gyr + Burst

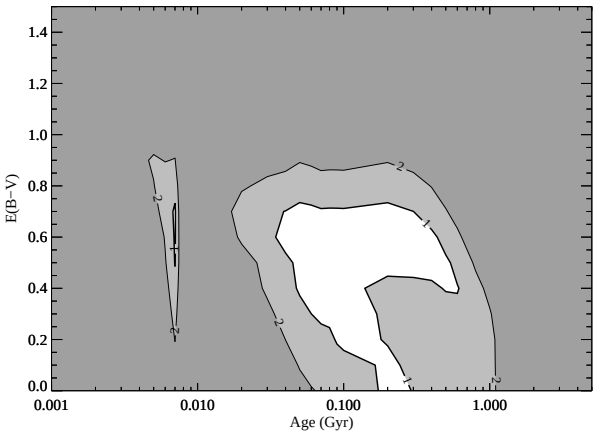

(d) 2 Gyr + Burst + PL

Figure 5.39: Plots showing the contours of χ^2_{red} for the various combination of components that produce an acceptable fit for J2358-00. The particular combination used is given in the sub-caption for the plot. The region in which $\chi^2_{red} < 1$ is shown in white, and the values of χ^2_{red} are given on the contour lines.

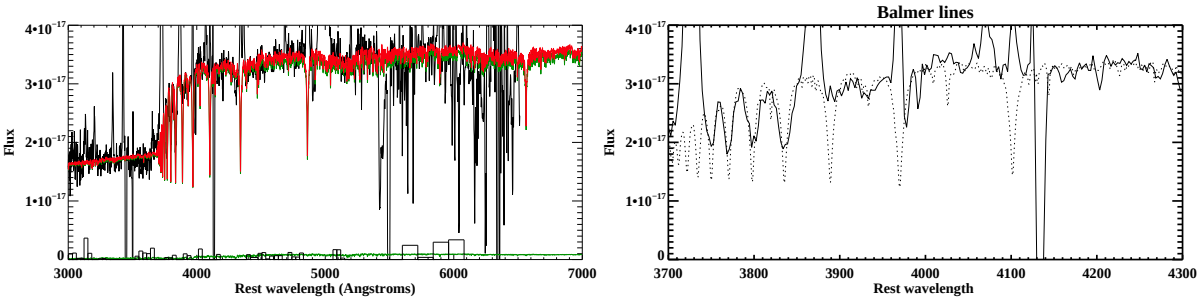

(a) 8 Gyr + Burst - Main fit

(b) 8 Gyr + Burst - Balmer Lines

Figure 5.40: An example of an acceptable fit produced by CONFIT for J2358-00. The fit shown here was produced using combination 2 and includes a YSP with t_{YSP}= 0.04 Gyr and E(B-V)= 0.6.

5.5 The effect of including a power-law component

The significance of the power-law component, particularly in objects which are well fitted by combinations that do not *require* the inclusion of one, remains one of the largest sources of uncertainty in this work. Unfortunately, it is not possible to apply further constrains with the data presented here, but it should be noted that in all but one case (J0332-00), it is possible to fit the Hβ line using the same kinematic components as those used for [OIII]$\lambda\lambda$4959, 5007, which are, or course, produced in the narrow-line region. This strongly suggests that any contamination from scattered quasar light is negligible, because no broad Hβ component (FWHM $>$ 2000 km s^{-1}) is clearly visible in the stellar-subtracted spectrum for any of the objects presented here (except J0332-00). However, it is important to consider the effect that introducing a power-law has on the results of the stellar population modelling. Therefore, an attempt to place an upper limit on the power-law contribution to the total flux for each object, utilising the information yielded by the stellar synthesis modelling, is made.

In the previous section, the results produced by the stellar synthesis modelling were discussed for each object separately. However, one aspect of the modelling that is common between all the objects is that, when a power-law component is included in the fits, the maximum age that produces solution with $\chi^2_{red} < 1$ increases significantly, and the range of reddenings allowed is also extended, a trend clearly illustrated in Figure 5.41. Panel (a) of this figure shows percentage power-law flux in the normalising bin against age for a sub-sample of four of the objects which increase strongly in flux towards the UV (J0218-00, J0320+00, J0334+00 and J0904-00). Each object is plotted using a different symbol and the reddening associated with the YSP is denoted by the colour of

the symbol. Panel (b) shows the same plot, but for a sub-sample of four objects that have the most reddened YSP (J0114+00, J0217-01, J0249+00 and J0924+01).

These figures show that, in both the cases of increasing and decreasing flux towards the UV, the age of the YSP generally increases with increasing power-law flux. The main difference between the two cases is that, when the flux increases strongly towards the UV, the trend is for the reddening of the YSP to increase with power-law flux. In contrast, in the cases where the stellar continuum appears reddened, the reddening of the YSP associated with the fit tends to decrease with increasing power-law contribution.

The reasons for these trends are illustrated in Figure 5.42 which shows examples of combination 6 fits for the minimum and maximum cases of power-law flux in the normalising bin. Panels (a) and (b) show examples of fits for J0924+01, which has one of the most strongly reddened YSPs of the objects in the sample. Panel (a) shows the minimum power-law contribution allowed by combination 6 (0 %), whilst panel (b) shows the maximum contribution (54 %). In both cases, the OSP flux is only a small percentage of the total, and thus, does not have a large effect on the overall shape of the stellar model in either case. However, it is clear that in the maximum case, the power-law mimics the shape of the reddened YSP in the minimum case.

Panels (c) and (d) show the same thing but for J0320+00, which is one of the objects that increases strongly in flux towards the UV. Again panel (c) shows the minimum power-law case produced by combination 6 (0%), and panel (d) shows the maximum power-law case (38%). Once again, it is clear that in the maximum case, the power-law component assumes the general shape of the unreddened YSP in the minimum case. Thus, because the inclusion of a power-law component can mimic the shape of a YSP, this allows for older YSPs to provide acceptable fits, as they are not required to contribute as strongly to the overall shape of the continuum.

The fact that the significance of the power-law component has a dramatic impact on the maximum ages allowed by the modelling means that it is important to be able to constrain the amount of the total flux attributable to it. Unfortunately, it is not possible to do this directly from the results of our stellar synthesis modelling. However, using the technique outlined in Chapter 4, an attempt has been made to place an upper limit on the possible contribution of the power-law to the flux in the normalising bin.

To recap, it was assumed that the percentage contributions, and the values of α, produced by the modelling process are representative of scattered or directly transmitted quasar light. This contribution was then extrapolated from the normalising bin to the wavelength of Hβ (using the appropriate value of α), where Gaussians were constructed

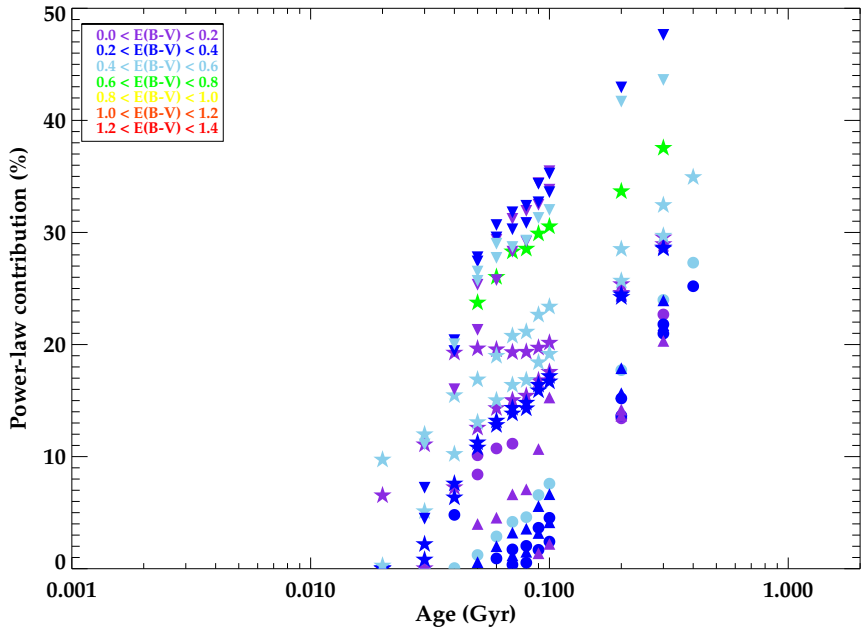

(a) Blue

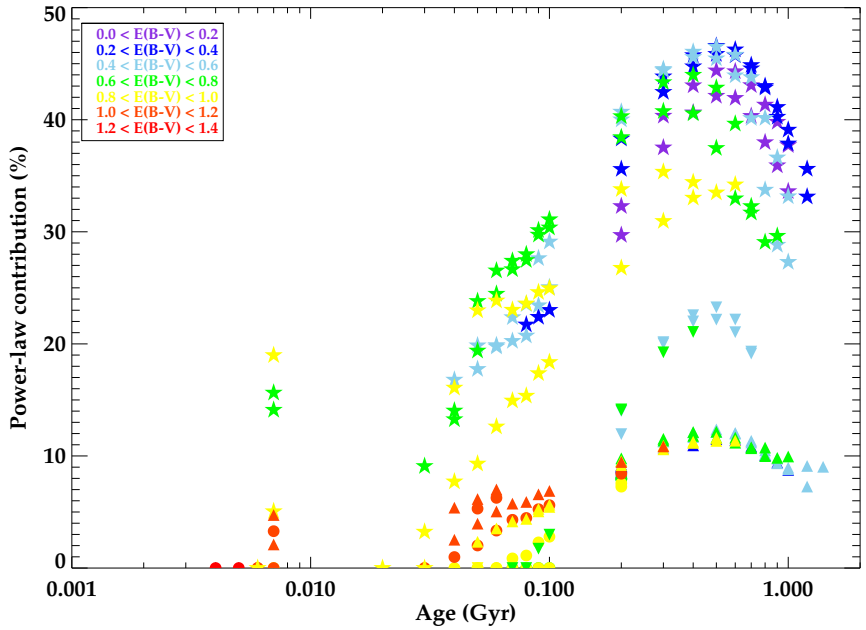

(b) Red

Figure 5.41: A demonstration of the manner in which the age of the YSP varies with an increasing power-law contribution to the flux in the normalising bin. (a) shows four cases in which the flux increases strongly towards the UV. Each object is plotted using a different symbol, and the points show the percentage power-law component in the normalising bin plotted against YSP age, for all the acceptable fits. The colour of the point denotes the reddening associated with the YSP. (b) shows the same but for four objects which have reddened stellar continua.

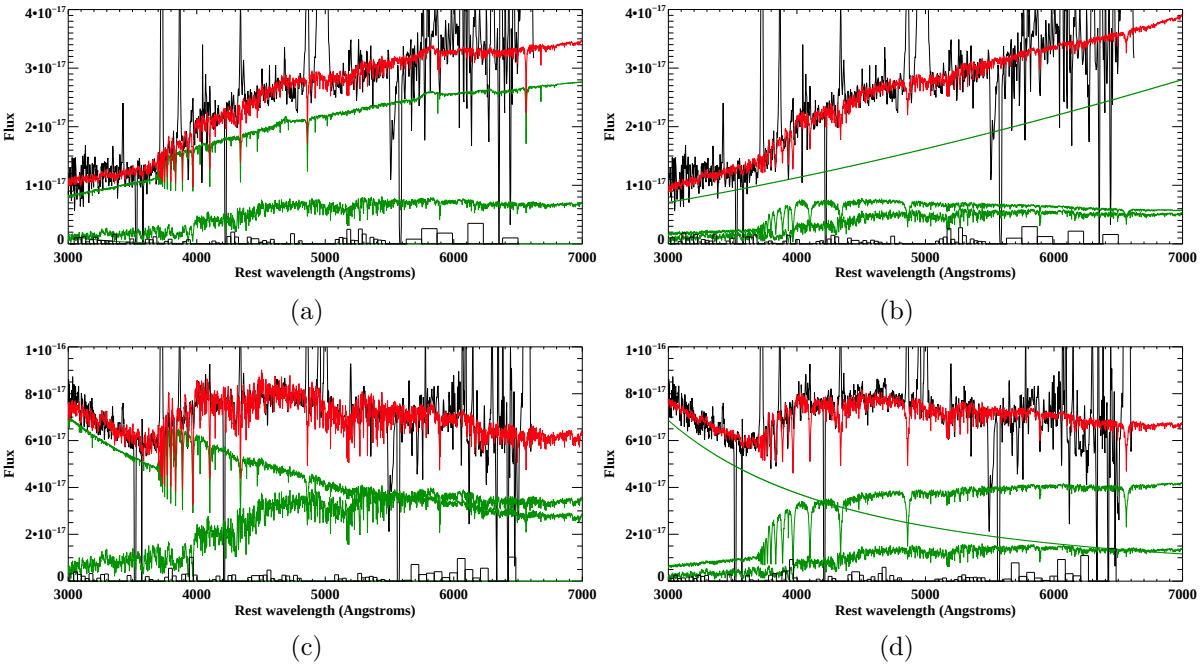

Figure 5.42: Examples of how the power-law contribution is related to the age and reddening of the YSP. (a) shows a fit for J0924+01 which incorporates only and OSP and YSP. (b) shows the same object but with the maximum allowable power-law of $\sim$ 50% included in the fit. (c) and (d) show the same but for J0320+00, which has a maximum allowable power-law component of $\sim$ 40%.

using average values of equivalent width and FWHM (78 Å and 5000 km s^{-1} respectively, see Chapter 4) for the broad Hβ line in quasars of similar luminosity. This produced a model for the Hβ component generated in the broad line region, that would be present as a scattered component at a given level of power-law flux. As the power-law flux increases, this broad Hβ component should, at some point, become detectable. In order to test this, broad Hβ models were constructed assuming different levels of power-law contribution to the total flux, for each object independently (increasing in steps of 5% to the maximum value allowed by the modelling).These were then subtracted in turn, from the stellar-subtracted spectrum, in an attempt to quantify the point at which the over-subtraction of the continuum becomes clearly detectable on visual inspection.

Figure 5.43 shows a zoom of the stellar-subtracted spectrum for each object. In each case, the solid black line shows the data, and the dashed red line denotes the 'just detected' broad Hβ model that was subtracted from the data. The blue dashed line represents the stellar-subtracted data with the with the Hβ model subtracted. In the cases in which the subtraction of the broad Hβ model, associated with the maximum possible contribution to the total flux by the power-law component, does *not* result

in a visible over-subtraction of the continuum when when subtracted from the stellar subtracted spectrum, Figure 5.43 shows this maximum broad Hβ case. In the cases where the over-subtraction of the continuum becomes clearly detectable *below* the maximum value allowed by the modelling, a constraint is placed on the maximum contribution of the power-law to the total flux in the normalising bin. Where this is the case, a plot of the stellar-subtracted spectrum in which it has been determined that the subtraction of the broad Hβ model has just become clearly visible is shown.

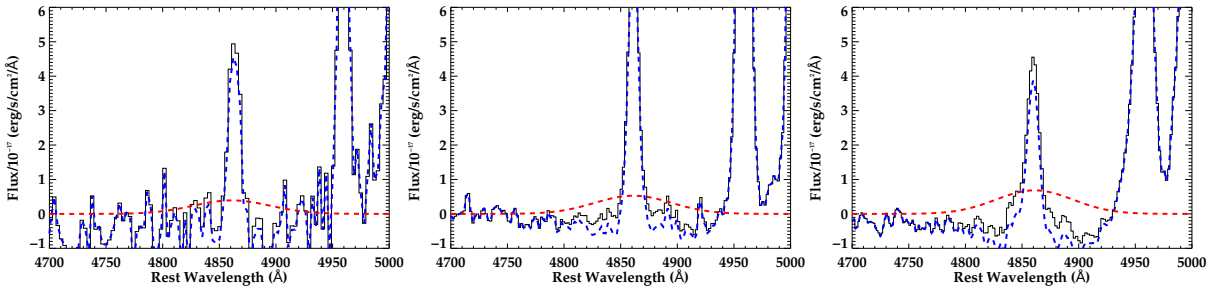

(a) J114+00 5% PL (b) J0123+00 25% PL (c) J0217-00 10% PL

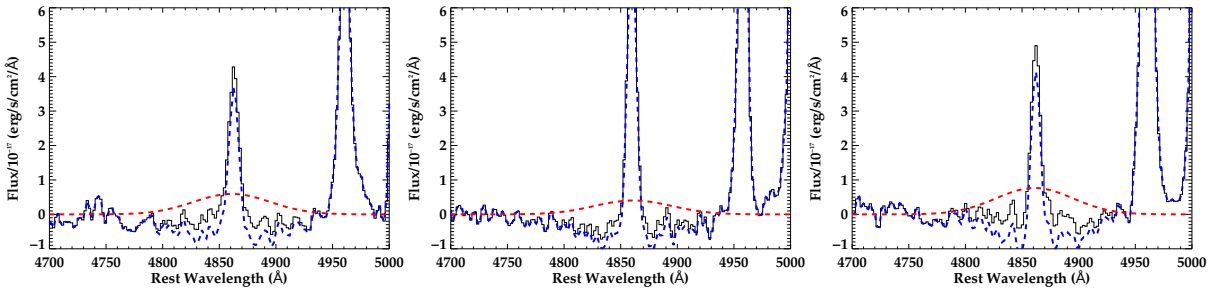

(d) J0217-01 10% PL (e) J0218-00 10% PL (f) J0227+01 15% PL

Figure 5.43: For each object panels (a)-(q) show a zoom of the stellar subtracted spectrum in the region around the Hβ line. The solid black line shows these data, whilst the dashed red line shows the broad Hβ model which has been added to these data. The blue dashed line shows the sum of these two components. Each sub-caption gives the percentage contribution of the power-law to the total flux in the normalising bin from which the broad Hβ model has been constructed.

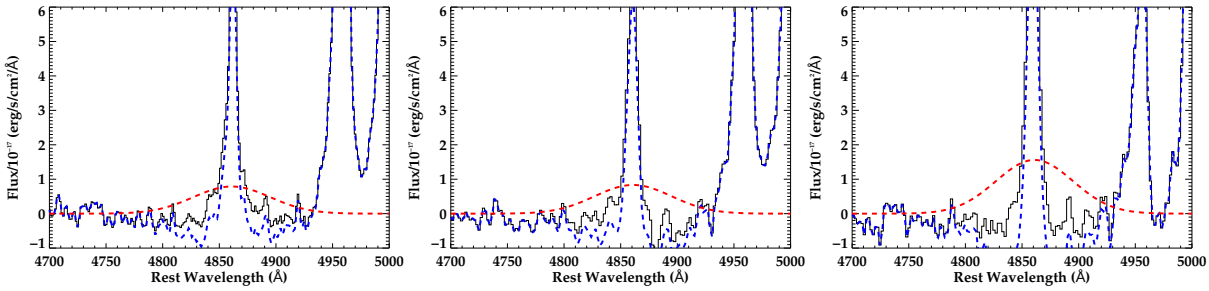

(a) J0234-07 20% PL (b) J0249-00 20% PL (c) J0320+00 20% PL

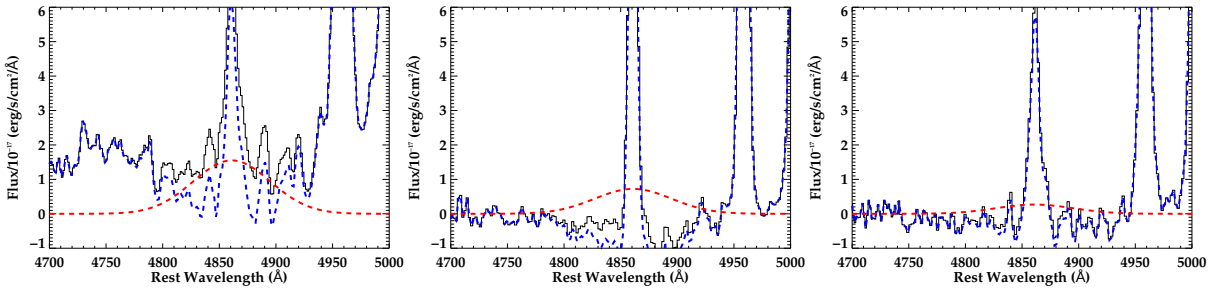

(d) J0332+00 10% PL (e) J0334+00 15% PL (f) J0848+01 5% PL

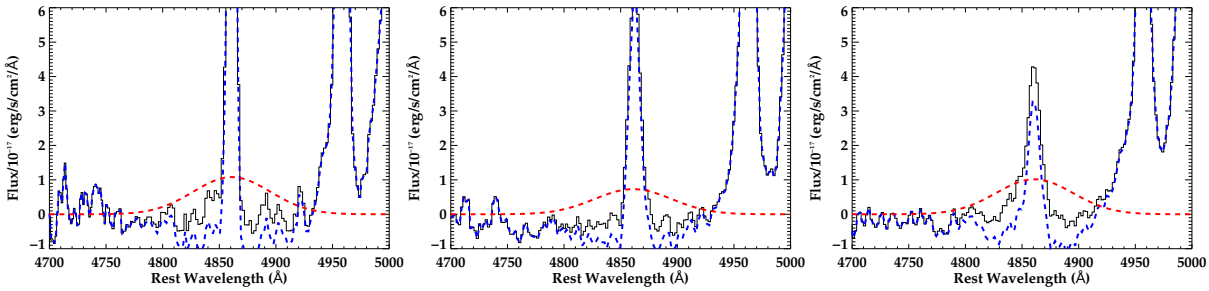

(g) J0904-00 10% PL (h) J0923+01 10% PL (i) J0924+01 45% PL

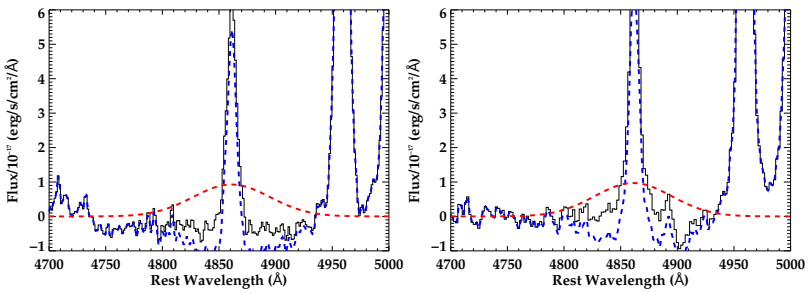

(j) J0948+00 10% PL (k) J2358-00 30% PL

Figure 5.43: [continued]

Although this technique has been applied to J0332-00, the assumption of typical values of EW and FWHM (outlined above) has not been successful in detecting this clear broad component (Figure 5.43(d)). This demonstrates that caution must be exercised when using this method to place constraints on the flux associated with a power-law component. If the broad Hβ component is particularly broad and/or has a double-peaked profile, as is the case for J0332-00, then this method in unlikely to be effective.

The results of this exercise are summarised in Table 5.23 which shows that, for eight of the objects, it has been possible to apply further constraints to the maximum power-law flux in the normalising bin. In all of these instances, this has allowed the further constraint of the maximum possible value for the YSP (t_{max}), with the new values shown

Object	Constrained?	Maximum Power-law (%)	Maximum YSP age (Gyr)
J0114+00	No	5	–
J0123+00	Yes	25	4
J0217-00	Yes	10	0.2
J0217-01	No	10	–
J0218-00	Yes	10	0.2
J0227+01	Yes	15	0.4
J0234-07	No	20	–
J0249-00	No	20	–
J0320-00	Yes	20	0.1
J0332-00	–	10	–
J0334+00	Yes	15	0.2
J0848+01	No	5	–
J0904-00	Yes	10	0.03
J0923+01	Yes	10	0.1
J0924+01	No	45	–
J0948+00	No	10	–
J2358-00	No	30	–

Table 5.23: The table shows whether it has been possible to place any further constraints on the age of the YSP by modelling of the Hβ component. Column 1 gives the name of each object. Column 2 indicates whether the maximum power-law contribution in the normalising bin has been constrained by the broad Hβ component model. Column 3 gives the power-law flux in the normalising bin associated with the broad Hβ model. In the cases where no further constraint can be applied, this will be the maximum flux allowable by the acceptable fits discussed previously. If the power-law flux can be constrained using this technique, column 4 gives the maximum YSP age associated with the constrained power-law if different than discussed in the previous section.

in column 4. In the remaining eight cases to which this technique was applied, even considering the maximum contribution to the flux by the power-law, the subtraction of the associated broad Hβ component is not detectable in the stellar-subtracted spectra. Thus the results of subtracting the broad Hβ component from the stellar-subtracted spectrum do not, in most cases, result in any significant changes to t_{max} allowed by the original modelling.

In order to properly constrain the power-law component in terms of both its contribution to the observed flux and its spectral index, spectopolormetric observations are required. This information will allow more stringent constraints to be placed on the ages, reddenings and contribution to the total flux for any YSP/ISP component present in the host galaxies of these type II quasar. This approach will be discussed in greater detail in Chapter 7.

5.6 Summary of Results

In this section, the results presented thus far are collated, with the aim of determining any common features of the YSPs present in these type II quasar host galaxies. The findings presented here are also compared with those found in studies of PRGs and ULIRGs.

5.6.1 The incidence of YSPs in type II quasars

One of the most obvious features in a spectrum, which can be considered an unambiguous indicator of a strong YSP component, is the detection of the higher-order Balmer absorption lines. These can be found in the approximate wavelength range 3700–3900 Å, and are caused by the absorption of photons by neutral hydrogen in the atmospheres of the stars. In particular, the Balmer absorption series is produced by transitions from the $n = 2$ energy level, and because the number of neutral hydrogen atoms in this state is dependent on temperature, their equivalent widths increase in strength until they reach a maximum in stars that have effective temperatures ~ 9000 K. González Delgado et al. (1999) measured the equivalent widths of the higher-order Balmer lines, using synthetic burst models generated by Starburst99 (Leitherer et al., 1999), and found that they increase with age until 500 Myr, which is the point at which A0-type stars dominate the main sequence turn off. It is well known that the main sequence lifetime of a star is dependent on its temperature and mass, leading to a strong relationship between the presence of Balmer absorption features in the spectrum of a galaxy, and age of its

predominant stellar population.

In light of this information, the higher-order Balmer lines can be used as a clear marker of a substantial YSP. Taking into consideration the potential uncertainties with the subtraction of the higher-order Balmer emission lines, the proportion of type II quasar host galaxies that show Balmer lines in absorption *before* performing the nebular subtraction has first been determined. In this case, it is found that the Balmer absorption lines are detected in 13/19 objects ($\sim$ 68%). Following subtraction of the higher order Balmer lines (in emission) and nebular continuum, the figures presented in Section 5.4, which highlight the region of the fit around the higher order Balmer lines, clearly show that this proportion increases to 14/19 objects ($\sim$ 74%).

In order to more accurately constrain the proportion of type II quasars that contain YSPs, it is also instructive to consider what percentage *require* a YSP component in order to produce an acceptable fit to their SEDs, that is, the proportion that cannot be fitted with a power-law + 8 Gyr model (combination 1) alone. In this sample, only J0234-07 and the type I quasar J0332-00 can be adequately fit using *only* an 8 Gyr OSP combined with a power-law component. Therefore, 17/19 (89%) objects require a YSP in order to fit their overall spectral shape. In all of the remaining cases, this combination of components failed to produce a reasonable fit to the shape of the spectrum around the Balmer break, because a power-law cannot account for the shape in this region. Taking the above information into account allows the unambiguously statement that, YSPs are present in at least 89% of this sample of type II quasars.

5.6.2 The ages of the YSPs in type II quasar host galaxies

The results presented in Tables 5.3 to 5.22 show that the assumptions made in the different modelling combinations can have a profound effect on the results produced. Combinations 6 and 7, both of which utilise a burst model of star formation and include a power-law component, are successful in producing acceptable fits. Combination 6 (t_{OSP} = 8 Gyr) was successful in 20/20 (100 %) of the apertures to which is was applied, whilst combination 7 (t_{ISP} = 2 Gyr) produced successful fits for 17/20 of the apertures (85 %) to which it was applied. However, the success of these combinations is unsurprising considering the increased number of free parameters, and as a consequence, these modelling combinations do not provide any strong constraints on either the ages or the reddenings of the YSP/ISP in the majority of cases (as discussed in Section 5.5).

Combinations 4, 5, 8 and 9, which all include a continuous star formation history, are not as successful at producing acceptable results as those combinations which include a

burst star formation history. In these cases, fits are achieved in 12/22, 7/22, 12/20 and 7/20 cases respectively. Not only is the rate of success low when utilising the continuous formation models, but the results do not provide any true constrains to t_{max}. This is because the age range is truncated by the upper age limit of the model (200 Myr), and it is possible that if these models were allowed to run to older ages, a greater number of successful fits may be achieved. However, it is unlikely that the intense burst of ongoing star-formation, assumed to be occurring in these type II quasar host galaxies, could be sustained over much longer periods of time than allowed for in the models (Springel et al., 2005; Johansson et al., 2009).

In light of the above considerations, the remainder of this chapter will focus on the instantaneous burst models which do not include a power-law component. This is justifiable because it is these combinations of components which give the best constraints on the YSP age, and also allow for direct comparison with other samples of AGN, which have taken a similar modelling approach[1]. Figure 5.44 shows age in Gyr plotted against E(B-V) for combinations 2 and 3 (summarised in section 5.3). For each object, if the modelling for a given combination produced only one region in which $\chi^2_{red} < 1$, that value is plotted in black. In the cases where the modelling for a given combination produced two regions of interest, the values for each region are plotted in the same colour. The apertures that were extracted from companion objects or extended regions, rather than the quasar host galaxy nuclei are plotted as triangles. For each point, the bars show the extent of the acceptable ranges of age and reddening, whilst the points are plotted at the median.

Figure 5.44(a) summarises the results for combination 2, which produced successful results for 20/22 ($\sim 91\%$) of the apertures to which it was applied. Most strikingly, of the 20 apertures that are adequately fit by this combination, 17 *require* the inclusion of a YSP component with $t_{max} \leq 100$ Myr, while the majority of acceptable fits for one object (J0114+00) also include a YSP with $t_{YSP} \leq 100$ Myr. It is only in two cases (J0848+01 and J0948+00) that a YSP $t_{YSP} > 200$ Myr is *required* in order to achieve acceptable results. Figure 5.44(a) also shows that, of the six objects for which more than one region of parameter space generates acceptable fits, five are coincident in age in the older region. The younger regions all have a limited range of ages that are also coincident.

Considering the full sample of objects in Figure 5.44(a), a wide range of reddenings is found, although there does not appear to be any correlation between the YSP age

[1]However, it must be noted that the conclusions drawn would be significantly altered if a power-law component proved to contribute substantially to the total flux.

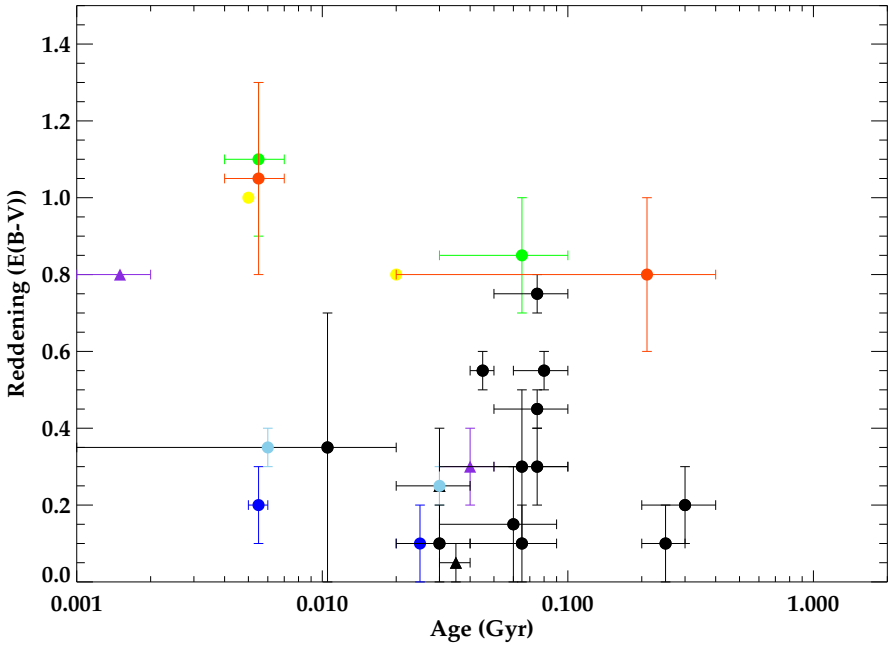

(a) Combination 2 - 8 Gyr + YSP

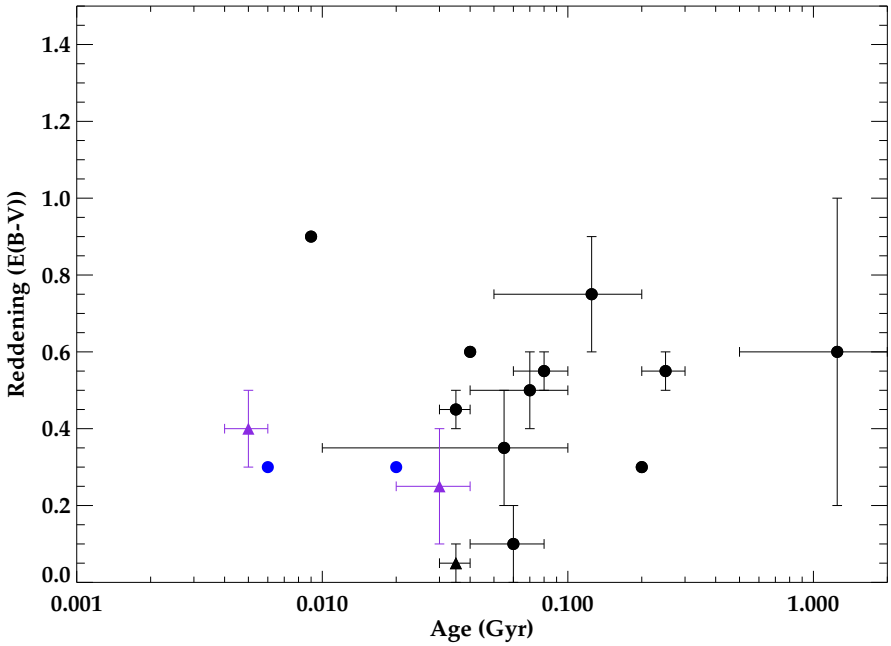

(b) Combination 3 - 2 Gyr + YSP

Figure 5.44: The mean age and reddening found for each of the spectroscopic apertures. Panel (a) shows that results for Combination 2 and panel (b) shows the results for Combination 3. In both panels, the mean reddening of the YSP is plotted against the mean age found for each aperture. In the cases where there is more than one region in which $\chi^2_{red} < 1$, both regions are plotted in the same colour, otherwise each aperture is plotted in black. In the cases that relate to off-nucleus apertures, the point is plotted as a triangle. The bars show the range of values of both age and reddening that provide acceptable fits.

and the reddening associated with the population. If those objects that have stellar populations with reddenings $E(B-V) > 0.4$ are considered to be strongly reddened, then 7/20 (35%) of the apertures fall into this category, whilst 13/20 (65%) are not strongly reddened, of which 36% have mean $E(B-V) \leq 0.1$.

Figure 5.44(b) summarises the results for combinations 3, which produced successful fits for 15/22 ($\sim$ 68%) of the apertures to which it was applied. Comparing Figures 5.44(a) and 5.44(b), shows that when an underlying population of $t_{ISP} = 2$ Gyr is assumed, a higher proportion of the objects for which fits are achieved have $t_{max} >$ 100 Myr (4/15) than in the case where an $t_{OSP} = 8$ Gyr (3/20) is assumed. Once again, if YSPs with $E(B-V) > 0.4$ are categorized as significantly reddened, then 8/14 (57%) of the apertures fall within this definition. This proportion is higher than that found for combination 2, which is not unexpected because a significantly reddened YSP can mimic an unreddened OSP in the overall shape of its spectrum.

5.6.3 A relationship between YSP age and host galaxy morphology?

In Chapter 3, measurements of the surface brightnesses of the tidal features, which were identified as being associated with merger activity (see Table 3.1), were presented. If it is the case that the formation of the YSPs investigated in this chapter are also associated with the same merger event, it is not unreasonable to suppose that there may be some correlation between the tidal features associated with the mergers, and the ages of the YSPs detected in the host galaxies. Therefore, in this section, the possible existence of a correlation between the ages of the YSPs detected in the quasar host galaxies, and the surface brightnesses of these tidal features is investigated.

Figure 5.45 shows the surface brightness of the brightest tidal feature, measured from the Gemini GMOS-S images (for the 15 cases where merger signatures were detected), plotted against the range of acceptable YSP ages for each host galaxy. Figure 5.45(a) shows the results produced by combination 2, and Figure 5.45(b) shows the same for combination 3. In both instances, it can be seen that there is no apparent relationship between these two quantities, however, it must be noted that, due to the small number of data points, and the relatively small spread in YSP ages, no firm conclusions can be drawn from this.

It is also instructive to considered whether there is any relationship between the interaction/merger status of the host galaxy and the age of the detected YSP. The morphological classifications of the type II quasar host galaxies were presented in Chapter

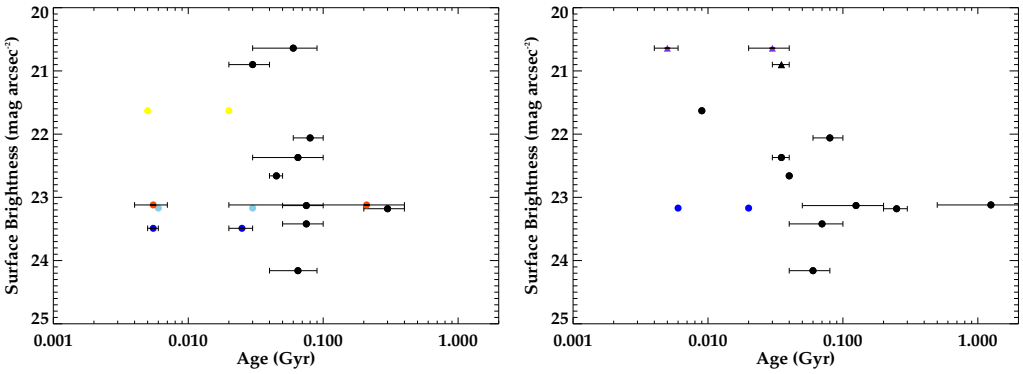

(a) (b)

Figure 5.45: The surface brightness of the brightest feature associated with a merger event plotted against YSP age for each object in which tidal features have been detected. Panel (a) shows the results for combination 2, while panel (b) shows the results derived from combination 3. The colour coding of the points is the same as in Figure 5.44, and once again, the bars show the possible range of YSP age determined for each object. The surface brightnesses have been corrected for Galactic extinction, surface brightness dimming and have also been k-corrected.

3 Table 3.1. In summary, the galaxies were categorised into four groups depending on the nature of the merger signatures detected. Group 1 contains galaxies that are interacting with a companion and are linked by a bridge. Group 2 galaxies are post-coalescence systems with tidal features in the form of tails, shells and fans. Group 3 galaxies have two nuclei within 10 kpc projected separation, and group 4 galaxies are undisturbed.

Table ?? shows the average and median ages of the YSPs, assuming both the youngest and oldest ages allowable by the stellar synthesis modelling, for each of the morphological groups described above. The table shows results only for objects which have been successfully modelled by that combination, so that 17 galaxies are included for combination 2 and 12 galaxies are included for combination 3. Clearly, when considering combination 2, there is no appreciable difference in either the minimum or maximum ages associated with the YSPs in any of the groups. When considering combination 3, the values for group 2 are lower than those found for the other morphological groups, although it must be noted that fewer objects are included in the analysis, because combination 3 is successful in fewer cases than combination 2. Once again, this apparent lack of correlation does not rule out a link between YSP age and morphology because, as discussed previously, the number of data points is too small to enable any relationship to be discounted. Despite this, it is interesting to note that, objects classified as undisturbed (group 4) do not show any difference in the ages of their YSPs compared

Combination	Group	No. in group	Average Minimum Age (Gyr)	Median Minimum Age (Gyr)	Average Maximum Age (Gyr)	Median Maximum Age (Gyr)
2	1,3	5	0.03	0.03	0.14	0.09
	2	8	0.05	0.04	0.12	0.10
	4	4	0.06	0.03	0.13	0.10
3	1,3	3	0.2	0.05	0.75	0.2
	2	7	0.06	0.04	0.09	0.08
	4	2	0.12	–	0.15	–

Table 5.24: The average and median ages of the YSPs detected in the type II quasar host galaxies, broken down by morphological groupings. Column 1 shows the combination of components to which the analysis refers. Column 2 and 3 gives the morphological classification (definitions given in text) and total number of galaxies for which acceptable fits are found that are classified into this group. Columns 4 and 5 give the average and median minimum age of the YSPs of the type II quasars classified into the group, while columns 6 and 7 show the same, but for the maximum ages.

to groups 1, 2 and 3 (combination 2), clearly demonstrating that they are not all simply old, passively evolving elliptical galaxies, but have also experienced a recent episode of star formation. This is particularly evident in the cases of J0142+14 and J0948+00, where the Balmer absorption lines are clearly detectable in the spectrum (Figures 5.6(b) and 5.38(b)).

5.7 Discussion

5.7.1 Comparison with powerful radio galaxies

When considering the age and significance of YSPs in the host galaxies of type II quasars, it is important to consider them in the wider context of active and merging galaxies. Are the ages found here typical of those found in other studies?

In Chapter 3, the 2 Jy sample (Tadhunter et al., 1993, 1998) was introduced, in order to compare the optical morphologies of PRG with the type II quasars presented here. It is also possible to compare the incidence of YSPs in the host galaxies of these two samples, because the same spectral synthesis modelling technique has been applied in both cases.

Tadhunter et al. (2002) present results for an RA limited sub-sample of that discussed in Chapter 3, comprising 23 PRG ($0.15 < z < 0.7$). Using a similar technique to that

adopted here, they modelled the populations of the host galaxies, and found that only $\sim 15\%$ of these PRG play host to clearly detectable, significant YSPs. This finding was based on both stellar synthesis modelling and the clear detection of Balmer absorption features in the spectra. The spectra for the remaining 18 objects modelled by Tadhunter et al. (2002) were adequately fit by an elliptical galaxy template combined with a power-law component.

These results have been further updated (Holt et al., 2006, 2007; Wills et al., 2008), using the same modelling technique as that employed in this work. The availability of improved data has allowed firm detections of YSPs in a further two objects from the original sample, while improving the age estimates for the three sources presented in Tadhunter et al. (2002). This brings the detection rate of YSPs in this sub-set of the 2 Jy sample to 5/22 (23%), with 4/5 of these having $t_{max} \leq 100$ Myr. Therefore, the ages of the YSPs, when detected, are consistent with those found for the type II quasars (Figure 5.46), although the detection rate is significantly lower. These finding are in stark contrast to the results presented here for the type II quasars, where only two object (J0234-07 and J0332-00) can be adequately fit with an OSP + power-law combination of components alone.

Taking into consideration the results of the comparison of optical morphologies presented in Chapter 3, this result could be considered somewhat unexpected. This is because the comparison between the two samples, discussed in Section 3.5.2, imply that these two groups of objects have very similar properties. The absolute magnitudes, rate of interactions, distribution of host galaxies amongst the morphological groups, and the distribution of the surface brightnesses of the tidal features associated with the mergers were shown to be similar. This suggests that both types of AGN reside in similar host galaxies. In contrast, the significant differences in the stellar content of their host galaxies suggests that they are fundamentally different systems. However, it is important to recognise that the quasar luminosity in a number of these PRG is significantly higher than those of many of the type II quasars presented here (Figure 3.7, page 82). This will have the effect of making it more difficult to detect signatures of YSPs in the host galaxies because of the stronger AGN-related continuum components, such as scattered quasar light and nebular continuum. It will also be more difficult to detect the Balmer lines in absorption because there will be stronger Balmer emission filling these in. Therefore, the detection rate of 23% must be taken as a lower limit to the proportion of PRG which host YSPs.

It is also possible that this difference may be enhanced by selection effects associated

with how the SDSS targeted objects for spectroscopic follow up. However, as discussed in Chapter 2, these objects were selected using different algorithms (Quasar, Serendipity and Special) (Zakamska et al., 2003), which all have very different selection criteria. In fact, the majority of the type II quasars discussed here were selected as optical counterparts to FIRST detected objects, which were too faint to be selected for any of the main surveys. Therefore, it is unlikely that this sample will be more biased towards star forming objects that the 2 Jy sample of PRG.

5.7.2 Comparison with ULIRGs

In the context of evolutionary scenarios, such as that proposed by Sanders et al. (1988) (discussed extensively in the previous chapter), it is worthwhile comparing the results derived here with those found for a complete sample of ULIRGs presented by Rodríguez Zaurín et al. (2009, 2010). This sample consists of 36 ULIRGs which includes a complete RA and Dec limited sample of 26 objects with redshifts $z < 0.13$, and also 10 higher redshift objects ($z > 0.18$) characterised by warm infrared colours. The same stellar synthesis modelling technique as that employed here was used, and thus, it is possible to make a direct comparison.

Rodríguez Zaurín et al. (2009) extracted 5 kpc nuclear apertures for all the objects in their complete sample, as well as apertures from extended tidal features. Due to the fact that, in all but three cases, only one aperture centred on the nucleus of each object was extracted, only the apertures centred on the nuclei will be considered. This will allow the comparison between the two groups to be more meaningful.

Rodríguez Zaurín et al. (2009) also model their spectra using a combination of an OSP and YSP, however, they have used an OSP with $t_{YSP} = 12.5$ Gyr. Their use of an older underlying population than assumed for the type II quasars is unlikely to have a significant effect on the YSP ages determined by the modelling. At these old ages, the differences between the stellar templates is minimal, so no significant differences in the spectra of populations comprising of only 8 Gyr or 12.5 Gyr old stars would be expected.

The results presented for the ULIRGs in Rodríguez Zaurín et al. (2010) are very similar in terms of the YSP ages found for the nuclear apertures, the reddenings associated with the YSPs, and the contribution made by the YSP to the total flux in the normalising bin. They find that 91% of the nuclear apertures have $t_{YSP} < 100$ Myr. In comparison, including only the apertures extracted from the quasar host galaxy nuclei, 82%[2] of type

[2]This proportion excludes J0123+00 and J0332-00, which cannot be modelled without the inclusion of a power-law component.

II quasar host galaxies which *require* a YSP component, also have $t_{YSP} < 100$ Myr for the same modelling combination. Figure 5.46 shows that the distribution of ages of the type II quasars and ULIRGs are very similar, with similar detection rates. In terms of the reddenings found for the YSP, Rodríguez Zaurín et al. (2010) derived a median value of E(B-V)= 0.4 for the apertures extracted from the nuclear regions of the ULIRGs. This is also very similar to the median value found for this sample of type II quasars, with E(B-V)= 0.35.

5.8 Timing the quasar activity in galaxy mergers.

Based on the above results, it is clear that in the majority of cases, a YSP with $t_{max} <$ 100 Myr is a significant flux component of the quasar host galaxies studied here. This is consistent with the results presented in Chapter 4 for the detailed analysis of the stellar populations of J0025-10. For the majority (15/17)[3] of objects, when considering fits with no power-law component (combination 2), $\sim 88\%$ have a significant YSP with $t_{max} \leq 100$ Myr.

These findings are interesting in the context of evolutionary scenarios, such as that of Sanders et al. (1988), in which galaxy mergers lead to ULIRGs which then eventually become observable quasars. Such models predict that, at the peak of star formation activity, which is coincident with the coalescence of the two BHs (e.g. di Matteo et al. 2005; Springel et al. 2005; Hopkins et al. 2006), the system should appear as a dust enshrouded system containing a highly reddened YSP (i.e. a ULIRG), in which any quasar activity that may have been triggered is too deeply embedded to be detect directly. It is only with the onset of AGN-related feedback processes, as the AGN begins to dominate, that the gas and dust are removed, resulting in the quenching of star formation activity. Thus, in the Sanders et al. (1988) scenario, when the quasar becomes directly detectable, it should be hosted by a system in which the two nuclei have coalesced and also have an ageing starburst population.

This predicted delay between the merger-induced starburst and visible AGN activity has indeed been detected by some previous stellar population studies (Cid Fernandes et al., 2004; Tadhunter et al., 2005; Davies et al., 2007; Holt et al., 2007; Wills et al., 2008; Wild et al., 2010; Tadhunter et al., 2011; Canalizo & Stockton, 2013; Ramos Almeida et al., 2013) where delays of a few 100 Myr to a few Gyr have been found. This is also true of two of the type II quasar objects presented here, in which delays

[3]J0123-00 and J0332-00 require a power-law component in order to achieve an acceptable fit, and therefore, cannot be directly be compared here.

of up to a few 100 Myr (assuming combination 2) are found. However, this is clearly not the whole story as others (Heckman et al., 1997; Canalizo & Stockton, 2000, 2001; Brotherton et al., 2002; Holt et al., 2007; Wills et al., 2008; Liu et al., 2009; Tadhunter et al., 2011; Villar-Martín et al., 2012) find evidence that the starburst and AGN activity have been triggered quasi-simultaneously.

One of the primary reasons for these apparently discrepant results may be that the triggering mechanisms depends on AGN luminosity. Indeed, Tadhunter et al. (2011) show that the vast majority of the objects in their sample of powerful radio galaxies that have quasar-like luminosities ($L_{[OIII]} > 10^{35}$ W), display clear evidence of a significant contribution to their fluxes from YSPs with ages $t_{YSP} < 0.1$ Gyr. On the other hand, less luminous AGN tend to show evidence for older YSP $0.2 < t_{YSP} < 2$ Gyr (Tadhunter et al., 2005; Emonts et al., 2005; Wild et al., 2010). This is effectively demonstrated in Figure 5.46, where the distribution of YSP ages is shown for various samples of quasars (see caption for details), and Figure 5.47 which shows the same samples but with the inclusion of lower luminosity PRG (as well as the sample of Canalizo & Stockton (2013)).

Taking this luminosity dependence into consideration, if we concentrate on the quasar-like objects with the best spectroscopic data on the stellar populations in the host galaxies (Canalizo & Stockton, 2000; Holt et al., 2007; Wills et al., 2008; Tadhunter et al., 2011; Canalizo & Stockton, 2013; Villar-Martín et al., 2012), in general, ages $t_{ysp} < 0.1$ Gyr are typical in the nuclear regions of the host galaxies. One notable exception to this trend is the study of Canalizo & Stockton (2013), where they find that, although 14/15 quasar host galaxies do have evidence for a significant YSP, they are *all* older ($t_{ISP} \sim 1.2$ Gyr) than those found in the majority of other quasar-like systems.

When comparing the results of such modelling, it is important to note that the dating of stellar populations is, in most cases, complex and has many inherent degeneracies, making it difficult to find unique solutions. In fact, there are very few published cases of quasar-like systems in which the stellar populations have been accurately dated. Some of the few clear cut cases include the powerful radio galaxy 3C459 (Wills et al., 2008), J0025-10 (Bessiere et al., 2014) presented in Chapter 4, and the nearby quasar Mrk 231 (Rodríguez Zaurín et al., 2009; Canalizo & Stockton, 2001) in which the populations are found to have ages $t_{ysp} < 0.1$ Gyr. In the latter case, the findings are supported by the detection of He I absorption features which are associated with B-type stars (González Delgado et al., 1999) which have a lifetime of 20 – 80 Myr. The nearby type II quasar Mrk 447 (Heckman et al., 1997) is clearly identified as having a YSP with an age of $t_{YSP} \sim 6$ Myr, supported by the presence of UV absorption features such as Si IIIλ1417,

which are attributed to the presence of late O and early B super-giants. Figure 5.46 shows how the results of these various studies compares with those found for this sample of type II quasars, and it can be seen that a wide range of ages are found in these different studies. However, it must be noted that the majority of objects which have ages greater than 1 Gyr are taken from the sample of Canalizo & Stockton (2013) (which is the sample of quasars first presented in Dunlop et al. (2003)).

Thanks to the quality and spectral range of these data, the type II quasars presented here are included in an expanding group of objects in which the starburst population can be reliably dated, with the clear detection of the strong Balmer absorption features in a large fraction of the sample ($\sim 75\%$), and a significant contribution to the total flux by the YSP. These findings strongly emphasise that, in the cases in which the stellar populations can be unambiguously fit, it is found that a significant proportion of the flux is attributable to a YSP $t_{ysp} < 0.1$ Gyr.

In light of this, it important to understand why the study of Canalizo & Stockton (2013) find such markedly different results. One possible reason for this discrepancy is that the latter study does not take into account reddening of the YSP. Spectroscopic studies of the YSP in local radio galaxies and ULIRGs emphasise the importance of taking into account reddening, especially for the youngest YSP components (Tadhunter et al., 2005; Rodríguez Zaurín et al., 2009, 2010). Failure to take into account the reddening may lead to the ages of the YSP being over-estimated. Alternatively, the discrepancy may be related to the fact that many of the studies of type II quasar systems concentrate on the near-nuclear bulge regions, whereas the study of Canalizo & Stockton considered apertures that are, by necessity, offset by several kpc from the bright quasar nuclei. However, in this context we note that some of the apertures that give young YSP ages in Mrk231, J0025-10 and J0218-00 are also significantly offset from the AGN nuclei.

One of the goals of the stellar synthesis modelling presented in this chapter is to determine whether a delay between the peak of star formation and the triggering of AGN activity is observed in luminous AGN. Are the stellar populations of their host galaxies significantly older than the expected lifetime of the AGN? The answer to this question is largely dependent of what the lifetime of a typical quasar is (t_{QSO}), which unfortunately is poorly constrained. Estimates, based on a variety of methods, range between $10^6 < t_{QSO}$ yr $< 10^8$ (Martini 2004 and references therein). If the typical lifetime of a quasar is in fact closer to the lower limits (1 Myr), then the results presented in this chapter for both the burst and continuous star formation histories explored, can

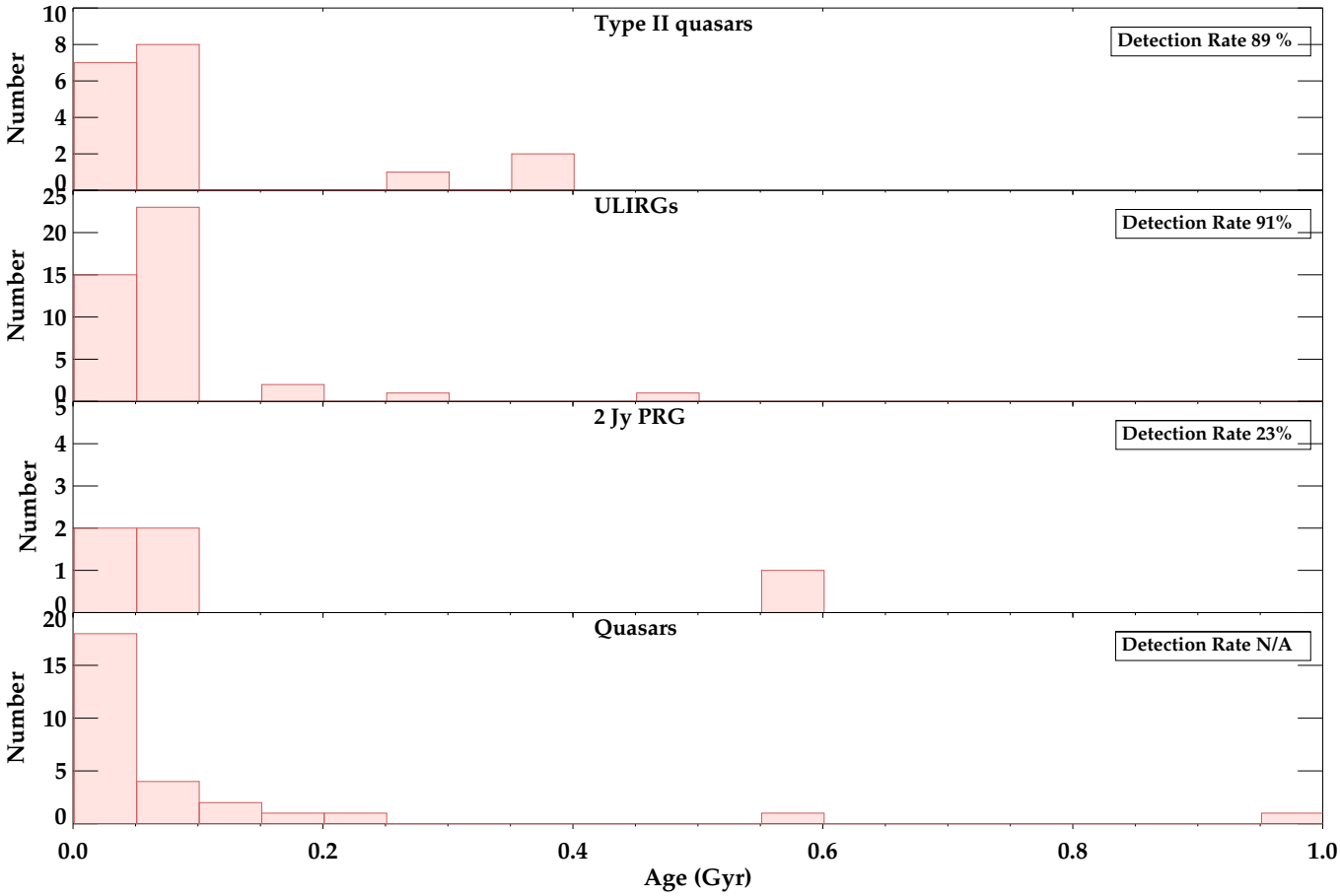

Figure 5.46: Comparison of the YSP ages found for the different samples discussed in this work. The top panel shows the distribution of ages for the type II quasars investigated in this chapter. The following two histograms show the distribution of ages for the ULIRGs and 2 Jy PRGs respectively. The final panel shows the distribution of ages for a compilation of samples taken from the literature and include results from Heckman et al. (1997); Canalizo & Stockton (2000); Tadhunter et al. (2005); Emonts et al. (2006); Holt et al. (2006, 2007); Wills et al. (2008); Liu et al. (2009); Tadhunter et al. (2011); Villar-Martín et al. (2012). Also included are the type II quasars J1309-02 and J1337-01, which were also modelled using CONFIT . The objects shown in this panel include only AGN which have quasar-like luminosities ($L_{[OIII]} > 10^{35}$ W). In each of the panels in which 'complete' samples have been considered, the detection rate of YSPs in the host galaxies is also given.

be interpreted as evidence of a significant delay ($\sim$ 100 Myr) between the peak of star formation and the emergence of the visible quasar activity. On the other hand, if the typical quasar lifetime is closer to the upper limit (50–100 Myr), then it can be concluded that the starburst and AGN activity are concurrent, with the possible exception of two

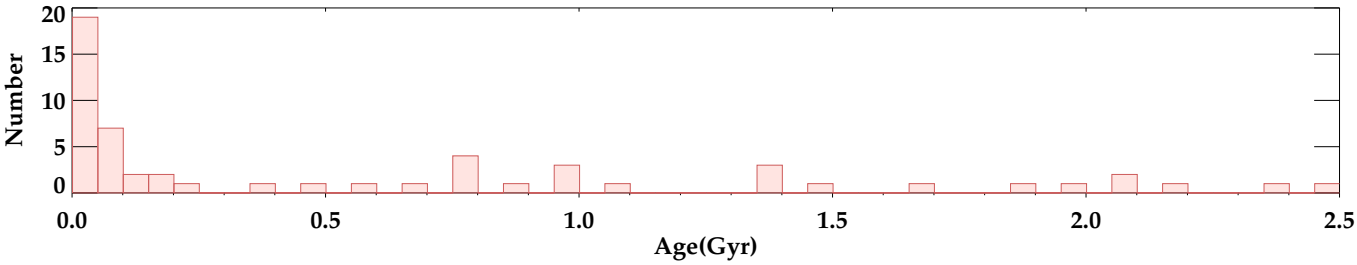

Figure 5.47: The same samples of quasars as shown in the final panel of Figure 5.46 but also including the lower luminosity AGN discussed by Tadhunter et al. (2011) ($L_{[OIII]} < 10^{35}$ W) and also the sample of quasars presented in Canalizo & Stockton (2013).

objects (J0848+01 and J0948+00) that require YSP ages $\sim$ 200 Myr. Only when tighter constraints are placed on quasar lifetimes, will it be possible to answer this question with any degree of certainty.

5.9 Summary

In this chapter, the stellar populations of a volume limited sample of 19 type II quasar host galaxies, selected from the SDSS (Zakamska et al., 2003) have been investigated. The goal of this investigation was to determine if a YSP is present in these host galaxies, and if so, to establish their ages. This has been done using stellar population synthesis modelling, and also by the detection of Balmer absorption lines, which are an unambiguous marker of a YSP. The results of the investigation can be summarised as follows.

- The Balmer absorption lines are clearly detectable in $\sim$ 68% of the objects *before* the nebular continuum and higher order Balmer emission lines are subtracted, and in $\sim$ 75% of the objects after the subtraction.
- $\sim$ 89% of the type II quasars cannot be adequately fit using a combination of an OSP and power-law only. Therefore, they *require* a YSP component in order to produce an adequate fit.
- In the majority of cases, a significant proportion of the flux in the normalising bin is attributable to a YSP component. Values in the range 15–100% have been found for the the objects which can be successfully modelled using combination 2.
- Of the 17 objects which can be fit using combination 2, 15 ($\sim$ 89%) have YSPs with a maximum acceptable age $t_{max} = 100$ Myr.

- Two objects (J0848+01 and J0948) require the inclusion of a YSP component with $t_{YSP} > 0.2$ Gyr.
- The ages found for the YSPs in the type II quasar host galaxies are consistent with those found for the 2 Jy PRG and ULIRGs, although the detection rate is closer to that found for the ULIRGs than for the PRG.

The results presented in this chapter suggest that, in general, type II quasar host galaxies have recently undergone a major burst of merger-induced star formation. Moreover, in the overwhelming majority of cases ($\sim 81\%$) the spectral synthesis modelling results are consistent with the quasar activity being triggered within 100 Myr of the peak of the starburst activity.

In order to continue this investigation of type II quasar host galaxies, in the next chapter the information derived here will be used to calculate their masses and star formation rates. Previous studies, such as those of Dunlop et al. (2003) have concluded that the host galaxies of both radio-loud and radio-quiet quasars are massive ellipticals, therefore, the masses found for this sample will also be compared with those found for the 2 Jy sample of PRG, in order to determine whether this is also found to be the case.

Chapter 6

The stellar masses of type II quasar host galaxies

6.1 Introduction

One of the most fundamental properties of a galaxy is its stellar mass. A tight correlation has been found between the masses of the spheroid component and the masses of the SMBH in the nuclei of galaxies (Magorrian et al., 1998; Marconi et al., 2004; Kormendy & Ho, 2013). This is particularly interesting in the context of AGN and quasars, because knowledge of the SMBH mass allows properties such as the Eddington ratio to be determined.

A number of previous studies of AGN with quasar-like luminosities have mainly focussed on deriving stellar masses from photometry alone (e.g. McLure et al. 1999; Dunlop et al. 2003). Due to the fact that morphological studies have suggested that quasar host galaxies are elliptical, previous works have tended to assume passively evolving stellar populations in which all of the stars were born at high redshift, and thus the current population is an old, slowly evolving one. However, as clearly demonstrated in the previous chapter, this assumption may not hold true in all systems. This has implications for the total stellar mass derived for any particular galaxy, because the mass-to-light (M/L) ratio of a stellar population decreases with decreasing age. Therefore, the assumption of a dominant OSP may result in an overestimation of the true stellar mass.

In this chapter, the total stellar masses of the type II quasar host galaxies are derived using the results of the stellar population modelling presented in the previous chapter. First the masses contained within the spectroscopic apertures are determined. These are then corrected for the flux excluded from the slit. Using the derived stellar masses, the

SMBH masses and Eddington ratios are also calculated, and the results are presented in Section 6.2. The results are then compared with those obtained for other samples of merging and active galaxies in Section 6.3. Finally, the results derived in this Chapter are summarised in Section 6.4.

6.2 Type II quasar host galaxy masses

6.2.1 Stellar Masses within the spectroscopic aperture

Initially, the total stellar mass within the spectroscopic aperture was calculated using the procedure outlined in Chapter 4. Briefly, this involved calculating the stellar mass independently for the OSP and YSP components, considering all combinations (including those with a power-law component) which produced an adequate fit. From these results, the combinations which produced the minimum and maximum total masses were selected, in order to determine the possible range of masses for the system. Not only do these masses depend on the ages and the contribution to the total flux of both the OSP and YSP components, but they also depend on the amount of reddening associated with the YSP. Note that, unlike most previous determinations of AGN host galaxy stellar masses, contamination by AGN continuum components is explicitly accounted for by subtracting a nebular continuum (see Section 4.2.1), and also by considering model combinations that include a power-law component.

Table 6.1 presents the results derived for each of the apertures used for the stellar population modelling. The table gives the minimum allowable mass, the maximum allowable mass, and the masses of the YSPs and OSPs which contribute to these totals. The median and mean masses for each object are calculated from the masses derived for *all* combination of components which produce an acceptable fit for a particular object (except in the cases outlined below). These results show that, in general, it is the mass of the OSP that dominates the total mass of the system, even in the minimum mass case. However, there are several exceptions to this general principle, most notably systems such as J0114+00, J0217-00, J249+00 and J0923+01, which can all be adequately fit without the inclusion of an OSP component. In such cases, the minimum total mass for all possible combinations is generated solely from the mass of the YSP (except in the case of J0217-00 where it is the *maximum* total mass which includes only a YSP/ISP component).

In the cases of J0123+00 and J0332-00, it was not possible to obtain fits without the inclusion of a power-law component. However, in both cases, the inclusion of all possible

Object	Minimum Mass	OSP Mass	YSP Mass	Maximum Mass	OSP Mass	YSP Mass	Median Mass	Mean Mass	Size kpc
J0025-10(Q)	3.2	3.1	0.084	5.4	5.6	0.19	4.7	4.5	5×6.7
J0025-10(G)	0.11	0.032	0.039	0.6	0.57	0.086	0.33	0.34	5×6.7
J0025-10(T)	0.061	0.024	0.020	0.71	0.68	0.037	0.11	0.14	5×6.7
J0114+00	11	0.0	11	64	5.1	58	28	31	$\pi 7.92^2$
(J0114+00)	(21)	(2.0)	(1.3)	(33)	(22)	(11)	(27)	(27)	
J0123+00	4.5	4.5	0.0055	5.7	5.7	0.0	5.1	5.1	8×8
J0142+14	2.1	1.0	1.1	11	10	0.90	3.8	4.6	8×7.9
J0217-00	1.5	0.44	1.0	4.9	0.0	4.9	3.0	3.1	8×7.3
J0217-01	2.1	0.63	1.5	26	14	13	17	14	8×7.7
J0218-00(N)	0.75	0.55	0.19	6.3	6.2	0.089	3.0	3.0	8×7.7
J0218-00(E)	0.48	0.45	0.031	2.3	2.2	0.057	0.72	1.0	5×7.7
J0227+01	1.9	1.5	0.38	9.0	8.9	0.14	5.2	4.8	8×7.6
J0234-07	1.8	1.8	0.0015	44	1.9	42	6.8	6.8	8×6.8
J0249+00	1.2	0.0	1.2	11	1.5	9.8	6.8	6.8	8×8.2
J0320+00	2.3	2.0	0.36	13	13	0.024	8.6	8.0	8×7.8
J0332-00(Q)	4.1	3.8	0.28	22	22	0.0	22	20	8×6.8
J0332-00(C)	2.4	0.0	2.4	4.4	4.4	0.023	4.0	3.9	5×6.8
J0334+00	0.56	0.33	0.23	5.9	5.7	0.15	1.8	2.2	8×8.1
J0848+01	4.1	2.6	1.5	10	9.7	0.29	8.4	8.1	8×7.4
J0904-00	1.5	1.3	0.18	8.2	8.1	0.16	2.2	3.2	8×7.5
J0923+01	1.1	0.0	1.1	6.7	4.9	1.8	3.3	3.4	8×7.9
J0924+01	0.54	0.1	0.44	26	1.1	25	2.4	4.0	8×7.8
J0948+00	1.9	1.1	0.78	8.3	7.9	0.40	4.7	4.9	8×7.1
J2358-00	1.2	0.42	0.77	4.5	0.92	3.6	2.6	2.6	8×8.1

Table 6.1: The masses derived for the spectroscopic apertures used for the stellar population modelling for each of the objects (all masses are given in units of $10^{10}\,M_{\odot}$). Column 1 gives the name of the object, and where appropriate, the region from which the aperture was extracted. Column 2 shows that minimum total mass derived for that aperture, whilst columns 3 and 4 show the component OSP and YSP masses which contribute to that total. Columns 5, 6 and 7 show the same but for the maximum mass derived. Columns 8 and 9 indicate the median and mean masses derived from all acceptable solutions for that aperture, and the final column gives the physical size of the region modelled. See text for full explanation of two sets of values of J0114+00.

solutions when calculating the maximum mass, leads to an unexpectedly large YSP/ISP component ($5.0 \times 10^{12}\,M_{\odot}$ and $1.0 \times 10^{13}\,M_{\odot}$ respectively). This is due to the fact that, in these cases, the models that produce the maximum mass include highly reddened ISPs. Therefore, when converting from flux to mass, the scaling factor is large, producing unrealistically massive ISPs. This is an artefact of the large power-law contribution in both these cases, which means that the ages and reddenings of the YSPs/ISPs are relatively unconstrained. In order to overcome this issue, the maximum mass has been

calculated from an OSP + power-law fit only (combination 1). This is justified by the fact that a highly reddened, massive intermediate age population is unlikely to be a true representation of the host galaxy population, because the highest levels of dust attenuation are likely to be associated with young YSPs still embedded in their natal gas clouds. In the case of J0332-00, combination 1 is an acceptable solution, however, in the case of J0123+00 it is not formerly acceptable (defined as $\chi^2_{red} < 1$). Therefore, a model in which the YSP/ISP contributes a very small fraction of the flux ($\sim$ 2%) was selected, and only the OSP and power-law components were used to determine the total mass of the system. Due to the fact that it is the mass of the OSP that tends to dominate the total mass of the system, the exclusion of the YSP from the calculated mass is unlikely to produce a significant difference in the final result.

6.2.2 Total Stellar Masses

In the previous section, the mass of the stellar components contained within the spectroscopic aperture was derived for each object. However, this is obviously not a true reflection of the total stellar mass of each galaxy, because a substantial proportion of the light of the host galaxy was not contained within the slit. In order to correct for this effect, the Galactic extinction corrected apparent magnitudes of the full sample of quasar host galaxies from Chapter 2 were used (see Table 2.2). These values account for all the light captured within a 30 kpc diameter aperture, centred on the quasar host galaxy. In order to calculate the stellar mass associated with the light excluded from the aperture, two extreme assumptions were made.

1. The stellar population associated with the flux outside the slit is made up of the same combination of components as those that produce the minimum mass within the spectroscopic aperture.

2. The stellar population associated with the flux outside the slit is made up of the same combination of components as those that produce the maximum mass within the spectroscopic aperture.

In order to obtain a minimum possible mass, the results produced by assumption 1 were summed with the minimum mass derived for the spectroscopic aperture; and to calculate the maximum values, the results of assumption 2 were summed with the maximum mass derived from the aperture modelling. In the three cases in which more than one aperture had been extracted, the minimum masses and maximum masses were summed

Object	% of Flux in Aperture	Minimum Mass	OSP Mass	YSP Mass	Maximum Mass	OSP Mass	YSP Mass
J0025-10	59	3.6	3.5	0.18	13	12	0.40
J0114+00	65	18	0.00	18	98	7.9	90
(J0114+00)	65	(33)	(31)	(2.0)	(51)	(34)	(17)
J0123+00	22	26	22	3.7	26	26	0.00
J0142+14	54	3.9	1.9	2.0	21	19	1.7
J0217-00	30	4.9	1.5	3.5	17	0.00	17
J0217-01	88	2.4	0.72	1.7	30	16	14
J0218-00	33	3.4	2.6	0.78	27	26	0.40
J0227+01	37	5.1	4.1	1.0	24	24	0.38
J0234-07	52	3.5	3.5	0.0028	85	3.6	82
J0249+00	68	1.8	0.00	1.8	17	2.3	15
J0320+00	48	4.9	4.2	0.76	28	28	0.051
J0332-00	80	7.7	5.0	2.7	34	34	0.060
J0334+00	76	0.73	0.43	0.30	7.7	7.5	0.19
J0848+01	38	11	6.8	4.1	27	26	0.77
J0904-00	49	3.0	2.7	0.38	17	16	0.33
J0923+01	49	2.2	0.00	2.2	14	9.9	3.6
J0924+01	38	1.4	0.27	1.1	68	2.8	65
J0948+00	68	2.8	1.6	1.2	12	12	0.60
J2358-00	19	6.2	2.2	4.0	23	4.8	18

Table 6.2: The masses derived for each object after correcting to the total flux. Column 1 gives the name, column 2 shows the percentage of the flux that was contained within the spectroscopic aperture used for the population modelling. Column 3 denotes the total minimum allowed mass, whilst columns 4 and 5 give the OSP and YSP contribution respectively. Columns 6, 7 and 8 are the same except relate to the maximum possible mass. In all columns, masses are given in units of $10^{10}\,M_{\odot}$.

independently for each aperture, and then the different possible minimum and maximum aperture masses were examined to determine the total minimum and maximum values. The results of this exercise are presented in Table 6.2, where the percentages of the flux captured within the spectroscopic apertures are also given.

However, when considering these results, the masses derived for J0114+00 are likely to be anomalous. This is due to the poorly constrained results of the stellar population modelling, which allow for a highly reddened YSP/ISP component that contributes up to 98% of the total flux of the system (for combinations 3 and 7, see Table 5.3). Therefore, in the case of the maximum mass, the system is predominately made up of a YSP/ISP component (92 %). If instead, masses derived only from acceptable fits produced by combination 2 (8 Gyr OSP +YSP) are considered, a total maximum mass of $5.1 \times 10^{11}\,M_{\odot}$ is found. In this case, the YSP contributes $\sim 33\%$ of the total mass of

the system. These values are included in brackets in Tables 6.1 and 6.2 for reference.

The results presented above show that these type II quasars are hosted almost exclusively by galaxies with total stellar masses $M_{tot} > 10^{10}\,\mathrm{M}_{\odot}$ (with only J0334+00 having a minimum possible mass below this threshold). The range of masses found is $7.3 \times 10^{9}\,\mathrm{M}_{\odot} \leq M_{tot} \leq 9.8 \times 10^{11}\,\mathrm{M}_{\odot}$. When considering the minimum mass case, the median mass of the sample is $3.6 \times 10^{10}\,\mathrm{M}_{\odot}$ and in the maximum mass case, the median is $2.4 \times 10^{11}\,\mathrm{M}_{\odot}$. The median mass for each object has also been calculated by considering all possible solutions for each object, and produces masses in the range $2.3 \times 10^{10}\,\mathrm{M}_{\odot} \leq M_{tot} \leq 4.3 \times 10^{11}\,\mathrm{M}_{\odot}$, with a median mass of $1.2 \times 10^{11}\,\mathrm{M}_{\odot}$. Once again, adopting the characteristic mass derived from the mass function of Cole et al. (2001) ($m_{*} = 1.4 \times 10^{11}\,\mathrm{M}_{\odot}$), the type II quasar host galaxy median masses are $0.3m_{*}$ and $1.7m_{*}$, for the minimum and maximum mass cases respectively, and $0.9m_{*}$ for the median mass case.

Having determined the range of masses which are allowed by the stellar population modelling results presented in the previous chapter, it is also necessary to compare the masses of the type II quasars with those found for comparable samples in the literature. However, surprisingly few systematic studies of the properties of type II quasar host galaxies at low to intermediate redshift are available. Although there are a number of other works that consider the masses of AGN host galaxies, they are mostly focussed on higher redshift samples ($z > 1$) (Jahnke et al., 2009; Decarli et al., 2010; Merloni et al., 2010; Mainieri et al., 2011; Floyd et al., 2013; Bongiorno et al., 2014), and in the vast majority of cases, concentrate on type I objects.

Both of these issues make it difficult to draw direct comparisons, because of factors such as the possible effects of the evolution with redshift of quasar host galaxies, differences in the morphology of AGN host galaxies with luminosity (spirals vs. ellipticals for low and high power AGN respectively), and the difficulty of deriving the stellar properties of type I AGN. This last point is particularly important for quasars, because the stellar continuum and features are 'washed out' by the point source of the quasar, which outshines the entire galaxy. To adequately overcome this issue requires the use of high-resolution imaging, such as that provided by *HST*, or ground based imaging assisted by adaptive optics. By these means, it is possible to disentangle the quasar light from that of its underlying galaxy. The use of type II quasars in this work largely negates this issue because the quasar is not, by definition, directly visible, and thus removes the need to perform an a PSF subtraction before investigating the properties of the underlying galaxy. Another source of difficulty when making direct comparisons between different

works is the use of different assumptions about the IMF, which are not always explicitly stated, and the use of different stellar models, which potentially can have a significant effect on the stellar masses obtained (see Chapter 4).

Taking the above issues into consideration, the study most comparable with the type II quasars presented in this thesis is that of Dunlop et al. (2003), who used high resolution *HST* imaging in order to study the host galaxies of AGN with quasar-like luminosities, ($M_V < -23$, consistent with the luminosity criterion imposed for the type II quasars). The sample also covers comparable redshifts ($0.1 < z < 0.25$) to those of the type II quasars, although Dunlop et al. (2003) do use type I quasars. However, if unified models hold true, this should not make a difference to the results based on the intrinsic properties of the host galaxies.

Considering only the radio-quiet portion of the Dunlop et al. (2003) sample (13 objects), they find masses ranging from $1.9 \times 10^{10}\,\mathrm{M}_\odot$ to $6.2 \times 10^{11}\,\mathrm{M}_\odot$, with a median mass of $1.3 \times 10^{11}\,\mathrm{M}_\odot$[1]. These masses are in good agreement with those found for the type II quasars. Performing a K-S test in order to ascertain whether the two samples are drawn from the same underlying population produces a probability P = 0.871, which means that there is no statistical difference between the masses of the two samples.

Dunlop et al. (2003) used single filter R-band photometry of the deconvolved host galaxy, and assumed an old passively evolving population with a fixed M/L ratio at a given luminosity ($M_{bulge} = 0.0123 L_R^{1.31}$). However, as was unambiguously shown in the previous chapter, in the case of the type II quasars, a YSP can make a major contribution to the total flux in the optical. Because the implicit assumption made by Dunlop et al. is that the galaxy contains a single, old stellar population, it is then difficult to reconcile the fact that the mass distributions of the type II quasars and the Dunlop et al. radio-quiet sample are so similar. One explanation is related to the fact that the M/L_R ratio used by Dunlop et al. is ~ 3.4, which is significantly lower than the $M/L_R \sim 5$ estimated for the 8 Gyr *Starburst99* templates used for the type II quasars. Moreover, Canalizo & Stockton (2013) used optical spectra to model the stellar populations of a number of RLQ and RQQ quasars from the Dunlop et al. sample, and assuming an OSP of 10 Gyr, find that, for an average spectrum, a ~ 2 Gyr population is also required in order to achieve an acceptable fit. This suggests that the stellar populations of the Dunlop et al. sample are older on average than those of the type II quasars (but see discussion in Chapter 5). Therefore, the combination of the lower assumed M/L ratio and the older

[1]The masses presented here have been recalculated for the cosmology assumed in this thesis ($H_0 = 70\,\mathrm{km\ s^{-1}\ Mpc^{-1}}$, $\Omega_m = 0.27$, $\Omega_\Lambda = 0.73$) using the same mass-to-light conversion factor as assumed by (Dunlop et al., 2003).

average stellar population ages of the Dunlop et al. sample could help to explain why the stellar mass distribution of that sample and the type II quasars are so similar, despite the markedly different assumptions made about the stellar populations.

6.2.3 SMBH masses and Eddington Ratios

As stated in the introduction, deriving the stellar mass of a galaxy makes it possible to calculate the mass of the SMBH at its heart. This is because, as discussed in Chapter 1, there is a strong correlation between the mass of the bulge of the galaxy and the mass of the central SMBH (e.g. Kormendy & Ho 2013). When that galaxy also hosts an AGN, it is possible to determine the Eddington luminosity (L_{edd}). Therefore, if the bolometric luminosity of the quasar is known (L_{bol}), the Eddington ratio (L_{bol}/L_{edd}) can be determined.

To calculate the SMBH masses and thus the Eddington ratios for the sample of type II quasars, the $M_* - \mathrm{M}_{BH}$ relationship presented by Häring & Rix (2004) was used. This relationship is given as

$$log(\,\mathrm{M}_{BH}\,/\,\mathrm{M}_{\odot}) = (8.20 \pm 0.10) + (1.12 \pm 0.06) \times log(M_{bulge}/10^{11}\,\mathrm{M}_{\odot}).$$

For the type II quasars presented in this thesis, it was assumed that the total mass of the system can be considered equivalent to the bulge mass, because quasars are predominantly found in elliptical host galaxies (Dunlop et al. 2003; Bennert et al. 2008, also the results presented in Chapter 3). Four different assumptions were made in order to determine the possible range of SMBH masses, and thus Eddington ratios. In all cases, the total stellar mass refers to the mass of the system once the light outside the slit has been accounted for (i.e. the values presented in Table 6.2).

1. M_{bulge} was considered to be the minimum total stellar mass found for the galaxy.
2. M_{bulge} was considered to be the maximum total stellar mass found for the galaxy.
3. M_{bulge} was considered to be the minimum total OSP mass found for the galaxy.
4. M_{bulge} was considered to be the maximum total OSP mass found for the galaxy.

The reason for testing assumptions 3 and 4 is that it is possible that there is a lag between the increase in stellar mass, brought about by the merger, and the corresponding increase in M_{BH} due to accretion, which will bring the relationship back to that observed in quiescent galaxies (for which Häring & Rix 2004 derived the above relationship).

Table 6.3: The masses of the super massive black holes in the quasar host galaxies, and their associated Eddington ratios. Column 1 gives the name of the object. Columns 2–9 show the black hole mass (M_{BH}), and associated Eddington ratio (L/L_{edd}) for each of the objects, making assumptions 1, 2, 3 and 4 respectively. Columns 10 and 11, give the mean M_{BH} and L/L_{edd} for each object, derived from the all the results presented in the proceeding columns. The median value found for each assumption and for the mean values is given at the bottom of each column. All the black hole masses are given as $log(M_{BH}/M_{\odot})$, and all Eddington ratios are given as $log(L/L_{edd})$.

	Total Mass				OSP Mass only				All	
Object	Min M_{BH}	L/L_{edd}	Max M_{BH}	L/L_{edd}	Min M_{BH}	L/L_{edd}	Max M_{BH}	L/L_{edd}	Mean M_{BH}	Mean L/L_{edd}
J0025-10	7.7	0.054	8.3	-0.57	7.7	0.068	8.3	-0.53	8.1	-0.14
J0114+00	8.5	-0.79	9.3	-1.62	0	–	8.1	-0.4	8.8	-0.84
J0123+00	8.7	-0.5	8.7	-0.5	8.6	-0.43	8.7	-0.5	8.7	-0.48
J0142+14	7.7	0.041	8.6	-0.77	7.4	0.4	8.5	-0.73	8.3	0.00
J0217-00	7.9	-0.08	8.4	-0.67	0	–	7.3	0.51	7.9	0.03
J0217-01	7.5	0.068	8.7	-1.16	6.9	0.66	8.4	-0.84	8.3	0.17
J0218-00	7.7	0.2	8.7	-0.8	7.5	0.33	8.7	-0.79	8.4	0.00
J0227+01	7.9	0.052	8.6	-0.71	7.8	0.16	8.6	-0.7	8.4	-0.13
J0234-07	7.7	0.11	9.2	-1.45	7.7	0.11	7.7	0.093	8.6	-0.02
J0249+00	7.4	0.3	8.5	-0.8	0	–	7.5	0.18	8.0	-0.04
J0320+00	7.9	-0.31	8.7	-1.16	7.8	-0.23	8.7	-1.15	8.5	-0.52
J0332-00	8.1	-0.55	8.8	-1.26	7.9	-0.33	8.8	-1.26	8.6	-0.67
J0334+00	6.9	0.71	8.1	-0.43	6.7	0.96	8.1	-0.42	7.8	0.57
J0848+01	8.2	-0.65	8.7	-1.09	8	-0.43	8.7	-1.08	8.5	-0.72
J0904-00	7.6	0.34	8.5	-0.49	7.6	0.4	8.4	-0.48	8.2	0.13
J0923+01	7.5	0.5	8.3	-0.38	0	–	8.2	-0.23	8.0	0.02
J0924+01	7.2	0.37	9.1	-1.51	6.4	1.2	7.6	0.035	8.5	0.68
J0948+00	7.6	-0.03	8.3	-0.75	7.3	0.23	8.3	-0.73	8.1	-0.13
J2358-00	8	0.38	8.6	-0.26	7.5	0.88	7.8	0.51	8.2	0.54
Median	7.7	0.054	8.6	-0.77	7.6	0.23	8.3	-0.5	8.3	-0.017

In order to calculate the intrinsic bolometric luminosities of the quasars, the $L_{[OIII]}$ values presented by Zakamska et al. (2003) (see Table 2.1) were used, along with the relationship between $L_{[OIII]}$ and bolometric luminosity derived by Heckman et al. (2004) ($L_{bol}/L_{[OIII]} = 3500$).

The results associated with each of the four assumptions outlined above are presented in Table 6.3. These results suggest that these quasar host galaxies harbour moderately massive black holes. The median SMBH mass and Eddington ratio derived for each assumption are shown in the final row of Table 6.3. Using these results, the medians of the SMBH masses range from $4.0\times10^7\,M_\odot$ to $4.0\times10^8\,M_\odot$, depending on the assumptions made. When considering the mean values derived from all four assumptions, the median mass is $2.0\times10^8\,M_\odot$. The associated median Eddington accretion rates are in the range $0.17 \leq L/L_{edd} \leq 1.7$ with the median derived from the mean SMBH masses being 0.96. However, if the results associated with assumptions 1 and 3, which produce the minimum SMBH masses and thus maximum Eddington ratios are discounted, this range becomes $0.17 \leq L/L_{edd} \leq 0.32$. Taking the mean of the Eddington ratios produced by assumptions 2 and 4 for each object, the median value for the whole sample is $L/L_{edd} = 0.28$

These masses can be compared with those found by McLure & Dunlop (2004), who constructed a sample of 12698 type I quasars, selected to have absolute magnitudes $M_i(AB) < -22$ (equivalent to $M_B < -22.65$ for a typical quasar SED; Schneider et al. 2003) from the SDSS DR1, in the redshift range $0.1 \leq z \leq 2$. They used this sample to determine the virial masses of the central SMBH based on the Mg II line. They found that, in the redshift range of these type II quasars ($0.3 < z < 0.41$), the mean SMBH mass is $\sim 10^{8.1}\,M_\odot$. However, there is a very large scatter around this value, with masses ranging from few $\times\,10^7\,M_\odot$ to $\sim 10^9\,M_\odot$. They also calculated Eddington ratios, and in the same redshift range, they found a mean value of $L/L_{edd} \sim 0.2$, again with a very large spread ($0.01 \leq L/L_{edd} \leq 1.25$). The values for the SMBH masses and Eddington ratios found for the type II quasars are entirely consistent with the upper envelope of values found by McLure & Dunlop (2004) for type I quasars. This demonstrates that the type II quasars are typical of the whole quasar population in terms of their black hole masses and Eddington ratios.

6.3 Discussion

6.3.1 The mass contribution of the YSP

In the previous chapter it was shown that, for the majority of acceptable fits, it is the YSP that dominate the *fluxes* of the systems. In contrast, in this chapter it has been demonstrated that it is the OSP that dominate the *masses* of the systems. This point is illustrated in Figure 6.1 which shows the median YSP masses plotted against the median OSP masses derived from the spectroscopic apertures. The black circles represent the apertures extracted from the quasar host galaxies, while the green circles represent the data extracted from extended regions. This plot shows that, even though it is the OSP that constitutes most of the mass of each system, there are a significant number of cases in which the mass of the YSP is comparable with, or exceeds that of the OSP. This is clearly demonstrated by Figure 6.1, which shows that the proportion of the total mass that is attributable to the YSP ranges from $< 1\%$ for J0123+00, J0237-07 and J0332-00(Q), to 96 % for J0923+01. These, however are the most extreme cases, and a more typical value for the proportion of the total mass which is made up by the YSP component is $\sim 23\%$ (median YSP mass). These findings make it clear that, for these type II quasar host galaxies, the manner in which the mass is distributed between the stellar populations varies significantly between individual objects.

The information provided by this analysis of the OSP and YSP stellar masses provides interesting information on the nature of the mergers taking place in at least 79% of the type II quasar host galaxies discussed in this chapter. This is because, in 57% of cases, the median YSP mass contributes $> 20\%$ of the mass of the system, and in 30% of apertures, the median YSP contribution to the total stellar mass is $> 50\%$ of the total. Therefore, a large amount of cold gas was required in order to form many of these YSPs.

The median of the possible YSP masses (including the correction for the flux outside of the modelling aperture) for each object is $\sim 2.1\times10^{10}\,M_{\odot}$ (the medians of the minimum and maximum YSP masses are $3.1 \times 10^{9}\,M_{\odot}$ and $1.4 \times 10^{11}\,M_{\odot}$ respectively), therefore, *at least* this amount of cold gas is required to trigger the star formation, which equates to $\sim 5\times$ the cold gas content of the Milky Way (Draine, 2011). Following the argument presented by Rodríguez Zaurín et al. (2010), the typical hydrogen gas mass associated with Sc type spirals (i.e. the most gas rich galaxies) is $\sim 1.4\times10^{10}\,M_{\odot}$ (considering both H_2 and HI). Therefore, accounting for the fact that star formation is a fairly inefficient process ($\sim 50\%$), 26% of the systems would require mergers between two such objects in order to account for the *minimum* YSP masses. When considering the maximum

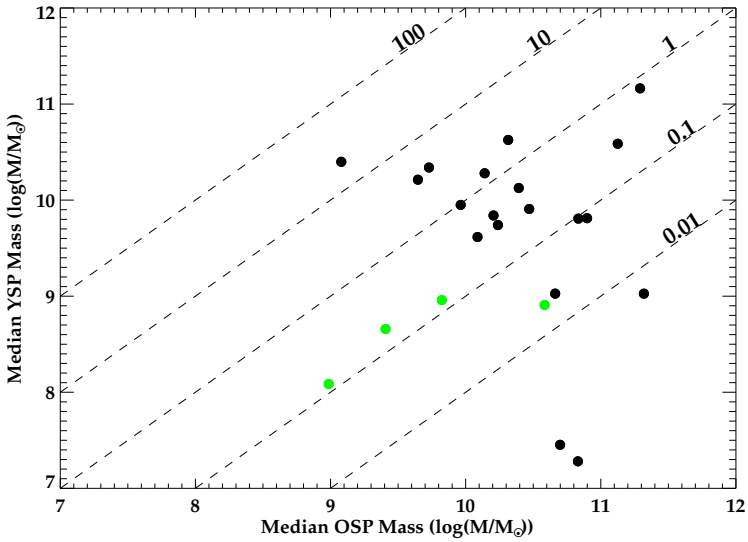

Figure 6.1: The median stellar mass allowable for the YSP component plotted against the median stellar mass allowable for the OSP component for each aperture modelled. The black points are the apertures that were extracted from the quasar host galaxies, whilst the green points denote the apertures that were extracted from the extended regions. The dashed lines show the mass of the YSP as a proportion of the mass of the OSP, and each line is labelled in the plot.

mass YSPs for each system, this proportion increases to 85 % of the type II quasar host galaxies, and when considering the median YSP masses, this figure is 68 %. For the median YSP masses, 26% of the objects require $> 10^{10}\,M_{\odot}$ of cold gas in order to provide sufficient fuel to feed the star formation. Therefore, when considering the median masses, a large proportion of the objects (47%) would require mergers between two *typical* late type spirals in order to provide the required amount of gas to fuel the starburst. This, of course, assumes that a significant proportion of the gas will not be lost in outflows powered by the quasar/starburst before it can be converted into stars. However, in 26% of cases, it would be necessary for the progenitor galaxies to be drawn from the more massive end of the Sc galaxy population, in order to provide the required fuel. These YSP masses are similar to the gas masses found for ULIRGs and are up to 10× the ISM mass found for the 2 Jy sample of PRG (Tadhunter el al., submitted)

The results presented above, show that in a substantial proportion of the sample, both the proportional contributions of the YSP to the total masses and the absolute YSP masses are consistent with the quasars being triggered in major, gas-rich mergers.

6.3.2 Comparison with starburst radio galaxies and ULIRGs

In order to provide some further context to the masses derived in this work for type II quasar host galaxies, these results can be compared with those obtained for other types of active and merging galaxies with evidence for star formation, such as the results presented in Tadhunter et al. (2011) for a sample of starburst radio galaxies. The latter work only included objects in which star formation had been detected, which is a sub-population of PRG comprising $\sim 15-25\%$ of the total. This sample is highly suitable for the purpose of comparison, because $\sim 75\%$ of type II quasar host galaxies also show strong evidence for star formation, thus considering only this sub-population compares like with like. Another factor that makes this particular sample ideal for comparison is that the masses were derived using the same technique as that used in this study of type II quasars.

In the context of evolutionary scenarios (discussed extensively in previous chapters), it is also instructive to compare the masses of type II quasar host galaxies with those found for ULIRGs. For this purpose, the complete sample of local ULIRGs presented in Rodríguez Zaurín et al. (2009, 2010) is once again used. The masses calculated for the ULIRGs were also derived using the same technique as adopted in this thesis.

Tadhunter et al. (2011) derived total masses for both the starburst PRG and ULIRG samples, including a correction for the flux which lies outside of the slit, based on a best-fitting model. Therefore, in order to make a valid comparison, the median total stellar masses derived for the type II quasar host galaxies was used. Both the starburst PRG and the ULIRG samples were modelled using the Bruzual & Charlot (2003) templates, assuming a Salpeter IMF, therefore the scaling factor of 1.36, derived in Chapter 4, was applied to both these datasets before making the comparison.

Figure 6.2 shows the distributions of total stellar masses for all three populations. Panel (a) shows the distribution for the type II quasars, which have a median stellar mass $M_* = 1.2\times10^{11}$ $M_\odot$. Comparing this with the starburst radio galaxies in panel (b) shows that there is a large range of overlap in the masses between the two samples, although the radio galaxies are distributed around higher masses than the type II quasars host galaxies, with a median mass $M_* = 3.6\times10^{11}$ $M_\odot$. It is also notable that the distribution reaches to lower values for the type II quasars than for PRG. Interestingly, the highest mass type II quasar host galaxy is, in fact, the only true radio-loud object in the sample (J0114-00). Performing a K-S test in order to compare the distribution of stellar masses of the type II quasars and starburst PRG produces a probability P=0.002, and therefore, it is possible to reject the null hypothesis that the two samples are drawn from the same

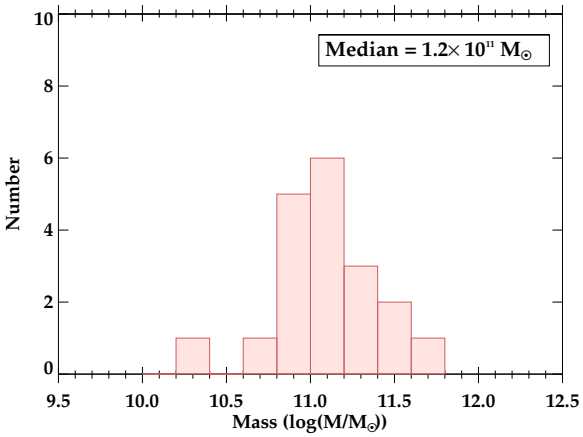

(a) Type II quasars

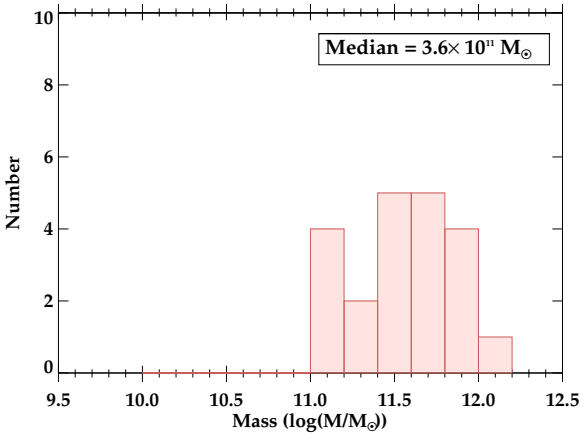

(b) Starburst RG

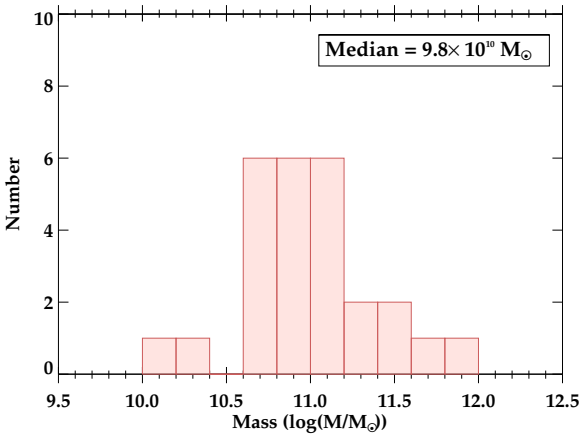

(c) ULIRGs

Figure 6.2: The total masses of the different types of quasar host galaxies. (a) shows the distribution of masses for the type II quasars, (b) displays the distribution of masses for the starburst radio galaxies and (c) shows the range of masses found for the ULIRGs.

underlying population at better than a 3σ confidence level.

These results are consistent with those found for the RLQ and RQQ within the Dunlop et al. (2003) sample, which are matched in absolute R-band magnitude, facilitating a direct comparison between the properties of their host galaxies. They also find that there is evidence for a difference between the stellar masses of radio-loud and radio-quiet hosts, with RQQ and RLQ having median masses of $1.3 \times 10^{11}\,\mathrm{M}_{\odot}$ and $2.3 \times 10^{11}\,\mathrm{M}_{\odot}$ respectively. Performing a K-S test for these two samples shows that they are drawn from different underlying populations at the 99.6%, $\simeq 3\sigma$ confidence level.

Floyd et al. (2013) also study a sample of radio-loud and radio-quiet quasars, in order to compare the properties of their host galaxies. They define sub-samples of 10 radio-loud and 10 radio-quiet quasars, split into two redshift ranges ($0.83 \leq z \leq 1.0$ and $1.67 \leq z \leq 2.01$), matched in terms of their optical luminosity and redshift distributions. They also select the quasar luminosities of both samples to fall in the range $-24 \leq M_V \leq -25$ in order to facilitate comparisons at different redshifts within their sample. At both $z \sim 1$ and $z \sim 2$ they find a significant difference between the masses of the radio-loud and radio-quiet samples[2]. At $z \sim 1$ they find that for RQQ $2 \times 10^{11} \leq M_*/\,\mathrm{M}_{\odot} \leq 6 \times 10^{11}$, but for RLQ $4 \times 10^{11} \leq M_*/\,\mathrm{M}_{\odot} \leq 1.3 \times 10^{12}$. At $z \sim 2$ they find that for RQQ $3 \times 10^{10} \leq M_*/\,\mathrm{M}_{\odot} \leq 3 \times 10^{11}$, but for RLQ $1 \times 10^{11} \leq M_*/\,\mathrm{M}_{\odot} \leq 1.3 \times 10^{12}$.

Although these two studies use different methods to determine the masses of the host galaxies, with Dunlop et al. (2003) assuming a passively evolving population, and Floyd et al. (2013) using crude spectral synthesis modelling of multi-wavelength photometric data[3], they both apply their chosen technique consistently within their samples. In the previous chapter, it was shown that type II (predominately radio-quiet) quasars have a much higher incidence of star-formation than do PRG, therefore, the largest uncertainty in the masses derived by these two studies is the failure to fully account for any differences in the composition of the stellar populations in the two different groups.

Panel (c) presents the distribution of masses found for the ULIRG sample, and once again this figure shows that there is a large region of overlap between the mass distributions of the type II quasars (panel (a)) and the ULIRGs. In this case, the masses are distributed around the lower median value of $M_* = 9.9 \times 10^{10}\ \mathrm{M}_{\odot}$. A K-S test was again performed in order to determine whether the type II quasar and ULIRG samples are drawn from the same underlying population, and it was found that there is no sta-

[2]Floyd et al. (2013) do not present individual masses for their samples, only the values stated in the text. Therefore, it is not possible to carry out a K-S test to determine the significance of the difference in masses they find between their radio-loud and radio-quiet samples.

[3]Floyd et al. (2013) assumed a model comprising an OSP and an unreddened YSP of fixed age (100 Myr).

tistically significant difference between the stellar mass distributions of the two samples (P=0.483).

These comparisons strongly suggest that these two distinct types of objects (type II quasars and ULIRGs) are drawn from similar underlying populations, while the host galaxies of PRG are distinctly different. This is consistent with the findings presented in the previous chapter, which showed that the type II quasars have a high incidence of recent star formation ($\sim 75\%$), a trait strongly associated with ULIRGs. This finding not only has implications for evolutionary scenarios in which ULIRGs evolve into optical quasars, but also for models which suggest that quasars cycle through both radio-loud and radio-quiet phases. In particular, based on the type II quasar results, the Nipoti et al. (2005) scenario appears highly unlikely.

The evolutionary scenario of Sanders et al. (1988), discussed previously, proposes that merging gas-rich galaxies become ULIRGs in which AGN are triggered due to the copious gas supply, and favourable conditions for funnelling the gas into the central region, where it can be accreted by the SMBH. Such systems later develop into optical quasars, after the obscuring dust has been expelled via outflow processes (either stellar or AGN driven). If this is true, the stellar masses of ULIRGs and quasar host galaxies should be similar, as observed here.

In Chapter 3, it was shown that the optical morphologies of this sample of type II quasars and those of a sub-sample of the 2 Jy PRG ($z > 0.2$, and classified as strong line radio galaxies) have very similar characteristics in terms of the rate of detection of merger and interactions signatures, the surface brightnesses of those features, and the absolute r'-band magnitudes of their host galaxies. However, the results presented both in the previous chapter, and the comparison of the distribution of masses of the type II quasars and PRG presented here, suggest that fundamental differences exist between the two classes of objects. The difference in the stellar masses between the two populations is also consistent with the idea that one of the main factors that influences whether an AGN is radio-loud is the mass of its SMBH (e.g Laor 2000; McLure & Dunlop 2004; Best et al. 2005).

6.4 Summary

In this chapter, the results of the stellar population modelling have been used to derive the masses of the stellar components of the type II quasar host galaxies. The stellar masses have also been compared with those estimated in a similar manner for samples of

starburst PRG and ULIRG. The results highlight the importance of taking into account the ages and reddenings of the stellar populations when calculating the stellar masses of AGN host galaxies. The main findings of this chapter are as follows.

- The medians of stellar masses of the type II quasar host galaxies in the minimum and maximum mass cases are $3.6 \times 10^{10}\,\mathrm{M}_{\odot}$ and 2.4×10^{11} respectively. In the minimum mass case, the range of masses is $7.3 \times 10^{9}\,\mathrm{M}_{\odot} \leq M_{tot} \leq 2.6 \times 10^{11}\,\mathrm{M}_{\odot}$, and in the maximum mass case, the range is $7.7 \times 10^{10}\,\mathrm{M}_{\odot} \leq M_{tot} \leq 9.8 \times 10^{11}\,\mathrm{M}_{\odot}$.

- The YSP/ISP component can contribute a significant proportion of the total mass of the host galaxy ($> 50\%$). Therefore, when deriving the stellar masses of quasar host galaxies, it is essential to account for the contribution of the YSP component.

- Considering the median mass for each object, the median mass of the YSP/ISP component is $2.1 \times 10^{10}\,\mathrm{M}_{\odot}$, with a range $3.7 \times 10^{7}\,\mathrm{M}_{\odot} \leq M_{gas} \leq 2.3 \times 10^{11}\,\mathrm{M}_{\odot}$. This suggests that for the majority of the systems ($\sim 70\%$), the progenitor galaxies must be drawn from typical mass, or larger, gas-rich, late-type galaxies, and is consistent with the idea that a significant fraction of quasars are triggered in major gas-rich mergers.

- The stellar masses of type II quasar host galaxies are significantly lower than those of starburst PRG, but statistically indistinguishable from those of ULIRGs.

- Type II quasar host galaxies harbour massive SMBH with median masses in the range $4.0 \times 10^{7}\,\mathrm{M}_{\odot}$ to $4 \times 10^{8}\,\mathrm{M}_{\odot}$, depending on the assumptions made. The associated Eddington ratios range between 0.17 and 1.70. These results are consistent with those found for type I quasars of similar luminosity and redshift.

Chapter 7

Conclusions and Future Work

In Chapter 1, the three main questions tackled in this thesis were outlined. These questions are as follows.

- How are quasars triggered?
- When are quasars triggered?
- Are quasars only hosted by the most massive early-type galaxies?

In the previous four chapters, these themes have been explored through an investigation of the characteristics of a volume limited sample of 20 type II quasars ($0.3 \leq z \leq 0.41$), selected to have emission line luminosities $L_{[OIII]} > 10^{35}$ W. Drawing together all the strands of evidence presented in these chapters, an attempt can be made to answer the questions listed above.

The results provide strong evidence that, in a substantial number of cases, the type II quasars presented in this thesis have been triggered in galaxy mergers. This is demonstrated by the results of the morphological study, presented in Chapter 3, which shows that 75% of the host galaxies have been involved in mergers or interactions. Although it was also shown that this rate of interaction is similar to that found for a sample of control galaxies, matched in absolute magnitude and redshift, the surface brightnesses of the tidal features associated with the type II quasars is up to two magnitudes brighter than those found for the quiescent galaxies. This may suggest that the progenitor galaxies of the type II quasar hosts were more gas-rich than those of the quiescent sample. A gas-rich merger triggering mechanism is also supported by results presented in Chapter 6, which demonstrate that the YSP components can contribute a substantial proportion

of the total masses of the systems, with the total YSP masses often implying starbursts driven by major, gas-rich mergers.

In terms of the timing of the triggering of the quasar activity in relation to the main merger event, the results presented in Chapters 4 and 5 demonstrate that, in a large fraction of cases, the quasar activity is triggered quasi-simultaneously with the starburst. This is illustrated by the fact that, for the 19 objects for which optical spectroscopy is available, 75% *require* the inclusion of a YSP with $t_{YSP} < 100$ Myr, in order to adequately model their optical spectra (for an OSP + YSP combination). It was also shown that the YSP can contribute a significant proportion of the total flux of the system in the normalising bin.

Finally, the results presented in Chapter 6 show that the host galaxies of the type II quasars are almost exclusively massive ($M_* > 10^{10}\,\mathrm{M}_\odot$), with masses that are comparable to those found for ULIRGs, but are substantially lower than those found for PRG. This supports the idea that ULIRGs and quasars, form part of an evolutionary sequence, whereas PRG represent a separate population.

However, although the results presented in this thesis represent a step forward in understanding how, when and where quasars are triggered, there remain a number of unresolved issues. Some ideas for future projects are presented below.

7.0.1 Spectropolarimetry

It was made clear in Chapter 5 that one of the major uncertainties in the stellar synthesis modelling (and therefore, mass determinations) is to what extent scattered or directly transmitted quasar light contaminates the spectrum of the quasar host galaxy. Employing type II quasars mitigates the issue of directly transmitted light to a large degree, however, as shown in Chapter 5, when attempting to employ a power-law component in order to account for this possible contamination, it becomes more difficult to constrain the properties of the stellar populations.

In order to overcome this issue, it is essential to determine the importance of any scattered AGN component, and thereby discount solutions which wrongly predict the power-law contribution. This can be achieved through the use of spectropolarimetry, which involves measuring the polarisation of the host galaxy light in a number of different wavelength bins (~ 500 Å width), across the optical wavelength range. This will allow any quasar scattered light to be accounted for because the scattering event itself will cause the light to become polarised, thereby disentangling it from the directly transmitted host galaxy light. By measuring this effect over an extended wavelength range, it

would be possible to determine the slope of the power-law component, which is assumed to represent the scattered quasar light, and also, the percentage it contributes to the total flux. This will allow the age of the YSP to be much better constrained.

Therefore, as part of an ongoing campaign to fully characterise these type II quasar host galaxy, and thus, gain insights into the triggering mechanism for the quasar itself, it is imperative to acquire this information in order to properly constrain the possible ranges of ages and reddenings of the significant YSP components. However, because the targets are faint, it will be technically challenging to acquire this information so to this end, applications have been made to use FORS2, mounted on the VLT at Paranal, Chile, to complete these observations. Use of such advanced facilities in essential in order to be able to obtain the necessary data with adequate signal-to-noise in a reasonable amount of time.

7.0.2 Stellar Masses

In Chapter 6, the stellar masses of the type II quasar host galaxies were derived using the results of the spectral synthesis modelling presented in Chapters 4 and 5. However, due to the fact that in a number of cases, it was difficult to properly constrain the ages, reddenings and flux contributions of the components, some mass estimates where poorly constrained. In order to overcome this problem, it is possible to use near infrared K-band photometry in order to make an independent assessment of the total mass of the OSP component (e.g. McLure et al. 2006). This is because, the near infrared is likely to be dominated by the flux of the OSP component of the galaxy, therefore, by determining the K-band luminosities of the quasar host galaxies, and using an assumed mass-to-light ratio (e.g. Bell et al. (2003)), it will be possible to calculate the OSP stellar masses.

The ability to determine the OSP masses independently will make it possible to apply further constraints on the mass of the YSP by limiting the number of potential solutions from the stellar population modelling. As an example, a possible solution for J0114+00 is that nearly 100 % of the mass is contributed by a highly reddened ISP. This is unlikely to be a true reflection of the stellar population of the host galaxy, however, there is no objective reason to reject this solution based on the fit of the stellar population model to the spectroscopic data. However, it is likely that a model comprising of a highly reddened ISP will over-predict the K-band flux, thereby allowing such models to be rejected as possible solutions.

In order to take advantage of this possibility, deep, K_s-band data has already been obtained for the majority of the objects in the sample of type II quasars (PI: Bessiere,

Program: W/2013B/19). The data was collected using the LIRIS instrument, mounted on the 4.2 m William Herschel Telescope in La Palma, Spain. The imaging strategy was to use a 9 point dither pattern, exposing for 15 seconds at each point in the dither. A random jitter at each position was also applied, and the cycle repeated three times. The purpose of the dithering and jittering is to allow for a good sky subtraction, because the sky dominates the exposure at these wavelengths. The data has been full reduced, using a dedicated pipeline tool within the IRAF environment. The analysis of these data will begin shortly.

7.0.3 Testing different star formation histories

In Chapters 4 and 5, two contrasting assumptions about the star formation history of the YSP components were made. The assumptions were that, on the one hand, all the stars were formed in one instantaneous burst, and on the other, that the galaxy has been forming stars at a continuous rate over the entire period since star formation was initiated. These two models represent extreme scenarios and are possibly not a true reflection of the star forming history of the galaxies. Therefore, it will be instructive to extend the suite of models to include a burst of star formation induced by the merger, but instead of assuming an instantaneous burst, to instead assume an exponentially decaying star formation rate (e.g. Wild et al. 2010), with various e-folding times (e.g. τ = 10 Myr, 50 Myr, 100 Myr). This may represent a more realistic mode of star formation due to the fact that it is likely that the rate will decay as the gas involved in forming the stars is slowly exhausted, either through consumption by the star formation process itself, or by being removed by negative feedback from the quasar.

7.0.4 Expanding the sample

The original selection of this sample of type II quasars was based on the catalogue of candidate objects presented by Zakamska et al. (2003). Their work exploited SDSS data release 1, which covered a limited portion of the sky. Although the results presented in this thesis strongly suggest that luminous quasars are often triggered in major gas rich mergers, the small sample size of 20 objects (19 with spectroscopic data), which fulfilled the selection criteria, limits the robustness of the statistical analysis of the results.

However, the Zakamska et al. (2003) catalogue was further updated by Reyes et al. (2008), using the information provided by the SDSS data release 7, which covered the entire intended footprint of the spectroscopic survey. This means that Reyes et al.

(2008) were able to include a substantially increased number of candidate objects in their catalogue, as well as capitalising on the improved flux calibration of the spectroscopic data. Applying the same selection criteria to the objects presented in this catalogue selects another 22 objects, which would increase the total sample size to 42 and make it more complete, while at the same time keeping the sample homogeneous.

Therefore, in the future, it will be interesting to obtain optical imaging and long-slit spectroscopy of these objects, of the same quality as that obtained for the original members of the sample. In this way, a comparable analysis can be carried out.

7.0.5 Looking for quasar feedback

As has been previously discussed, AGN are now considered to play a fundamental role in the evolution of galaxies, by acting as the mediating force in bringing the M_{BH} -σ_* relation into line, through feedback processes and quenching of star formation. If this is true, then this sample of type II quasars are ideal candidates for testing this theory. This is because the results of the stellar population modelling strongly suggests that these are objects in which merger induced star formation is/was significant, while at the same time, they host luminous quasars. Therefore, it is reasonable to expect that it is exactly these kinds of objects in which feedback processes would be evident.

In order to take advantage of this potential mine of information, it is necessary to take full advantage of new, advanced instruments that are currently coming online. In this case, the recently commissioned optical integral field unit (IFU) MUSE, which has been installed on the VLT, with its potential for the use of adaptive optics, will allow the acquisition of spatially resolved information about the gas kinematics on scales of $\sim$ 0.2 kpc (0.03 – 0.05 arcsec spatial resolution (FWHM)[1]) at the typical redshift of these galaxies. Thus it will be possible to map bulk motions of the ionised gas and thus detect signatures of out flowing material.

This exploration of the properties of the host galaxies of type II quasars has shown that, contrary to studies such as those of Dunlop et al. (2003), that they are *not* 'red and dead' objects, but are instead dynamic, evolving objects. Therefore, an understanding of the processes that are driving this evolution are essential to understanding galaxies in the modern day Universe.

[1] http://www.eso.org/sci/facilities/develop/instruments/muse.html

Bibliography

Adams T. F., 1977, ApJS, 33, 19

Alexander D. M., Bauer F. E., Brandt W. N., Hornschemeier A. E., Vignali C., Garmire G. P., Schneider D. P., Chartas G., Gallagher S. C., 2003, AJ, 125, 383

Alexander D. M., Swinbank A. M., Smail I., McDermid R., Nesvadba N. P. H., 2010, MNRAS, 402, 2211

Antonucci R., 1993, ARA&A, 31, 473

Bahcall J. N., Kirhakos S., Saxe D. H., Schneider D. P., 1997, ApJ, 479, 642

Baldwin J. A., Phillips M. M., Terlevich R., 1981, PASP, 93, 5

Barro G., Gallego J., Pérez-González P. G., Eliche-Moral C., Balcells M., Villar V., Cardiel N., Cristobal-Hornillos D., Gil de Paz A., Guzmán R., Pelló R., Prieto M., Zamorano J., 2009, A&A, 494, 63

Barro G., Pérez-González P. G., Gallego J., Ashby M. L. N., Kajisawa M., Miyazaki S., Villar V., Yamada T., Zamorano J., 2011, ApJS, 193, 13

Barth A. J., Voevodkin A., Carson D. J., Woźniak P., 2014, AJ, 147, 12

Barthel P. D., 1989, ApJ, 336, 606

Bauer F. E., Alexander D. M., Brandt W. N., Schneider D. P., Treister E., Hornschemeier A. E., Garmire G. P., 2004, AJ, 128, 2048

Baum S. A., Heckman T., 1989, ApJ, 336, 702

Baum S. A., Zirbel E. L., O'Dea C. P., 1995, ApJ, 451, 88

Becker R. H., White R. L., Helfand D. J., 1995, ApJ, 450, 559

Bell E. F., McIntosh D. H., Katz N., Weinberg M. D., 2003, ApJs, 149, 289

Bell E. F., Naab T., McIntosh D. H., Somerville R. S., Caldwell J. A. R., Barden M., Wolf C., Rix H.-W., Beckwith S. V., Borch A., Häussler B., Heymans C., Jahnke K., Jogee S., Koposov S., Meisenheimer K., Peng C. Y., Sanchez S. F., Wisotzki L., 2006, ApJ, 640, 241

Bennert N., Canalizo G., Jungwiert B., Stockton A., Schweizer F., Peng C. Y., Lacy M., 2008, ApJ, 677, 846

Bennert N., Falcke H., Schulz H., Wilson A. S., Wills B. J., 2002, ApJL, 574, L105

Bennert V. N., Auger M. W., Treu T., Woo J.-H., Malkan M. A., 2011, ApJ, 742, 107

Bessiere P. S., Tadhunter C. N., Ramos Almeida C., Villar Martín M., 2012, MNRAS, 426, 276

Bessiere P. S., Tadhunter C. N., Ramos Almeida C., Villar Martín M., 2014, MNRAS, 438, 1839

Best P. N., Kauffmann G., Heckman T. M., Brinchmann J., Charlot S., Ivezić Ž., White S. D. M., 2005, MNRAS, 362, 25

Bian W., Gu Q., Zhao Y., Chao L., Cui Q., 2006, MNRAS, 372, 876

Blanton M. R., 2006, ApJ, 648, 268

Blundell K. M., Rawlings S., Willott C. J., 1999, AJ, 117, 677

Boehringer H., Voges W., Fabian A. C., Edge A. C., Neumann D. M., 1993, MNRAS, 264, L25

Böker T., Falcón-Barroso J., Schinnerer E., Knapen J. H., Ryder S., 2008, AJ, 135, 479

Bongiorno A., Maiolino R., Brusa M., Marconi A., Piconcelli E., Lamastra A., Cano-Díaz M., Schulze A., Magnelli B., Vignali C., Fiore F., Menci N., Cresci G., La Franca F., Merloni A., 2014, Monthly Notices of the Royal Astronomical Society, 443, 2077

Bongiorno A., Mignoli M., Zamorani G., Lamareille F., Lanzuisi G., Miyaji T., Bolzonella M., Carollo C. M., Contini T., Kneib J. P., Le Fèvre O., 2010, A&A, 510, A56+

Bournaud F., Combes F., Semelin B., 2005, MNRAS, 364, L18

Bower R. G., Benson A. J., Malbon R., Helly J. C., Frenk C. S., Baugh C. M., Cole S., Lacey C. G., 2006, MNRAS, 370, 645

Bressan A., Fagotto F., Bertelli G., Chiosi C., 1993, A&AS, 100, 647

Bridle A. H., Perley R. A., 1984, Annual Review of Astronomy and Astrophysics, 22, 319

Brotherton M. S., Grabelsky M., Canalizo G., van Breugel W., Filippenko A. V., Croom S., Boyle B., Shanks T., 2002, PASP, 114, 593

Bruzual G., Charlot S., 2003, MNRAS, 344, 1000

Calzetti D., Armus L., Bohlin R. C., Kinney A. L., Koornneef J., Storchi-Bergmann T., 2000, ApJ, 533, 682

Canalizo G., Stockton A., 2000, ApJ, 528, 201

Canalizo G., Stockton A., 2001, ApJ, 555, 719

Canalizo G., Stockton A., 2013, ApJ, 772, 132

Cappellari M., McDermid R. M., Alatalo K., Blitz L., Bois M., Bournaud F., Bureau M., Crocker A. F., Davies R. L., Davis T. A., de Zeeuw P. T., Duc P.-A., Emsellem E., Khochfar S., 2013, MNRAS, 432, 1862

Cardelli J. A., Clayton G. C., Mathis J. S., 1989, ApJ, 345, 245

Cattaneo A., Combes F., Colombi S., Bertin E., Melchior A.-L., 2005, MNRAS, 359, 1237

Cid Fernandes R., González Delgado R. M., Schmitt H., Storchi-Bergmann T., Martins L. P., Pérez E., Heckman T., Leitherer C., Schaerer D., 2004, ApJ, 605, 105

Cisternas M., Gadotti D. A., Knapen J. H., Kim T., Díaz-García S., Laurikainen E., Salo H., González-Martín O., Ho L. C., Elmegreen B. G., Zaritsky D., Sheth K., Athanassoula E., Bosma A., 2013, ApJ, 776, 50

Cisternas M., Jahnke K., Inskip K. J., Kartaltepe J., Koekemoer A. M., Lisker T., Robaina A. R., Scodeggio M., Sheth K., Trump J. R., Andrae R., Miyaji T., Lusso E., Brusa M., Capak P., Cappelluti N., Civano F., 2011, ApJ, 726, 57

Coelho P., Gadotti D. A., 2011, ApJL, 743, L13

Cole S., Norberg P., Baugh C. M., Frenk C. S., Bland-Hawthorn J., Bridges T., Cannon R., Colless M., Collins C., Couch W., Cross N., Dalton G., De Propris R., Driver S. P., Efstathiou G., 2001, MNRAS, 326, 255

Combes F., 2001, in I. Aretxaga, D. Kunth, & R. Mújica ed., Advanced Lectures on the Starburst-AGN Fueling the AGN. p. 223

Comerón S., Knapen J. H., Beckman J. E., Laurikainen E., Salo H., Martínez-Valpuesta I., Buta R. J., 2010, MNRAS, 402, 2462

Condon J. J., Cotton W. D., Greisen E. W., Yin Q. F., Perley R. A., Taylor G. B., Broderick J. J., 1998, AJ, 115, 1693

Condon J. J., Kellermann K. I., Kimball A. E., Ivezić Ž., Perley R. A., 2013, ApJ, 768, 37

Croton D. J., Springel V., White S. D. M., De Lucia G., Frenk C. S., Gao L., Jenkins A., Kauffmann G., Navarro J. F., Yoshida N., 2006, MNRAS, 365, 11

Dahari O., 1984, AJ, 89, 966

Davies R. I., Müller Sánchez F., Genzel R., Tacconi L. J., Hicks E. K. S., Friedrich S., Sternberg A., 2007, ApJ, 671, 1388

Decarli R., Falomo R., Treves A., Labita M., Kotilainen J. K., Scarpa R., 2010, MNRAS, 402, 2453

di Matteo T., Springel V., Hernquist L., 2005, Nat, 433, 604

Dicken D., Tadhunter C., Axon D., Morganti R., Inskip K. J., Holt J., González Delgado R., Groves B., 2009, ApJ, 694, 268

Dicken D., Tadhunter C., Morganti R., Axon D., Robinson A., Magagnoli M., Kharb P., Ramos Almeida C., Mingo B., Hardcastle M., Nesvadba N. P. H., Singh V., Kouwenhoven M. B. N., Rose M., Spoon H., Inskip K. J., Holt J., 2014, ApJ, 788, 98

Dickinson M., Giavalisco M., GOODS Team 2003, in Bender R., Renzini A., eds, The Mass of Galaxies at Low and High Redshift The Great Observatories Origins Deep Survey. p. 324

Dickson R., Tadhunter C., Shaw M., Clark N., Morganti R., 1995, MNRAS, 273, L29

Donnelly R. H., Partridge R. B., Windhorst R. A., 1987, ApJ, 321, 94

Draine B. T., 2011, Physics of the Interstellar and Intergalactic Medium, Princeton University Press, USA

Dressler A., 1989, in Osterbrock D. E., Miller J. S., eds, Active Galactic Nuclei Vol. 134 of IAU Symposium, Observational Evidence for Supermassive Black Holes. p. 217

Dunlop J. S., McLure R. J., Kukula M. J., Baum S. A., O'Dea C. P., Hughes D. H., 2003, MNRAS, 340, 1095

Eckart M. E., McGreer I. D., Stern D., Harrison F. A., Helfand D. J., 2010, ApJ, 708, 584

Edge D. O., Shakeshaft J. R., McAdam W. B., Baldwin J. E., Archer S., 1959, MEMRAS, 68, 37

Eisenstein D. J., Annis J., Gunn J. E., Szalay A. S., Connolly A. J., Nichol R. C., Bahcall N. A., Bernardi M., Burles S., Castander F. J., Fukugita M., 2001, AJ, 122, 2267

Ellison S. L., Patton D. R., Mendel J. T., Scudder J. M., 2011, MNRAS, 418, 2043

Emonts B. H. C., Morganti R., Tadhunter C. N., Holt J., Oosterloo T. A., van der Hulst J. M., Wills K. A., 2006, A & A, 454, 125

Emonts B. H. C., Morganti R., Tadhunter C. N., Oosterloo T. A., Holt J., van der Hulst J. M., 2005, MNRAS, 362, 931

Faber S. M., Willmer C. N. A., Wolf C., Koo D. C., Weiner B. J., Newman J. A., Im M., Coil A. L., Conroy C., Cooper M. C., Davis M., Finkbeiner D. P., Gerke B. F., Gebhardt K., Groth E. J., Guhathakurta P., 2007, ApJ, 665, 265

Fabian A. C., Sanders J. S., Ettori S., Taylor G. B., Allen S. W., Crawford C. S., Iwasawa K., Johnstone R. M., Ogle P. M., 2000, MNRAS, 318, L65

Fagotto F., Bressan A., Bertelli G., Chiosi C., 1994a, A&AS, 104, 365

Fagotto F., Bressan A., Bertelli G., Chiosi C., 1994b, A&AS, 105, 29

Fanaroff B. L., Riley J. M., 1974, MNRAS, 167, 31P

Farrah D., Urrutia T., Lacy M., Efstathiou A., Afonso J., Coppin K., Hall P. B., Lonsdale C., Jarrett T., Bridge C., Borys C., Petty S., 2012, ApJ, 745, 178

Feldmann R., Mayer L., Carollo C. M., 2008, ApJ, 684, 1062

Ferrarese L., Merritt D., 2000, ApJL, 539, L9

Floyd D. J. E., Dunlop J. S., Kukula M. J., Brown M. J. I., McLure R. J., Baum S. A., O'Dea C. P., 2013, MNRAS, 429, 2

Floyd D. J. E., Kukula M. J., Dunlop J. S., McLure R. J., Miller L., Percival W. J., Baum S. A., O'Dea C. P., 2004, MNRAS, 355, 196

Frei Z., Gunn J. E., 1994, AJ, 108, 1476

Friedli D., Benz W., 1993, A&A, 268, 65

Fuentes-Williams T., Stocke J. T., 1988, AJ, 96, 1235

Fukugita M., Shimasaku K., Ichikawa T., 1995, PASP, 107, 945

Gebhardt K., Bender R., Bower G., Dressler A., Faber S. M., Filippenko A. V., Green R., Grillmair C., Ho L. C., Kormendy J., Lauer T. R., Magorrian J., Pinkney J., Richstone D., Tremaine S., 2000, ApJL, 539, L13

Gehren T., Fried J., Wehinger P. A., Wyckoff S., 1984, ApJ, 278, 11

Giacconi R., Zirm A., Wang J., Rosati P., Nonino M., Tozzi P., Gilli R., Mainieri V., Hasinger G., Kewley L., Bergeron J., Borgani S., Gilmozzi R., Grogin N., Koekemoer A., Schreier E., Zheng W., Norman C., 2002, ApJs, 139, 369

Girardi L., Bressan A., Bertelli G., Chiosi C., 2000, A&AS, 141, 371

González Delgado R. M., Leitherer C., Heckman T. M., 1999, ApJs, 125, 489

Greene J. E., Ho L. C., 2007, ApJ, 667, 131

Greene J. E., Peng C. Y., Kim M., Kuo C.-Y., Braatz J. A., Impellizzeri C. M. V., Condon J. J., Lo K. Y., Henkel C., Reid M. J., 2010, ApJ, 721, 26

Greene J. E., Zakamska N. L., Liu X., Barth A. J., Ho L. C., 2009, ApJ, 702, 441

Greene J. E., Zakamska N. L., Smith P. S., 2012, ApJ, 746, 86

Grogin N. A., Koekemoer A. M., Schreier E. J., Bergeron J., Giacconi R., Hasinger G., Kewley L., Norman C., Rosati P., Tozzi P., Zirm A., 2003, ApJ, 595, 685

Gültekin K., Richstone D. O., Gebhardt K., Lauer T. R., Tremaine S., Aller M. C., Bender R., Dressler A., Faber S. M., Filippenko A. V., Green R., Ho L. C., Kormendy J., Magorrian J., Pinkney J., Siopis C., 2009, ApJ, 698, 198

Häring N., Rix H.-W., 2004, ApJL, 604, L89

Hasinger G., 2004, Nuc. Phys. B, 132, 86

Heckman T. M., 1980, A&A, 87, 152

Heckman T. M., Gonzalez-Delgado R., Leitherer C., Meurer G. R., Krolik J., Wilson A. S., Koratkar A., Kinney A., 1997, ApJ, 482, 114

Heckman T. M., Kauffmann G., Brinchmann J., Charlot S., Tremonti C., White S. D. M., 2004, ApJ, 613, 109

Heckman T. M., Ptak A., Hornschemeier A., Kauffmann G., 2005, ApJ, 634, 161

Heckman T. M., Smith E. P., Baum S. A., van Breugel W. J. M., Miley G. K., Illingworth G. D., Bothun G. D., Balick B., 1986, ApJ, 311, 526

Heller C. H., Shlosman I., 1994, ApJ, 424, 84

Hernquist L., Spergel D. N., 1992, ApJL, 399, L117

Ho L. C., Filippenko A. V., Sargent W. L. W., 1997a, ApJS, 112, 315

Ho L. C., Filippenko A. V., Sargent W. L. W., 1997b, ApJ, 487, 591

Holt J., Tadhunter C., Morganti R., Bellamy M., González Delgado R. M., Tzioumis A., Inskip K. J., 2006, MNRAS, 370, 1633

Holt J., Tadhunter C. N., González Delgado R. M., Inskip K. J., Rodriguez Zaurin J., Emonts B. H. C., Morganti R., Wills K. A., 2007, MNRAS, 381, 611

Holt J., Tadhunter C. N., Morganti R., 2003, MNRAS, 342, 227

Hook I. M., Jørgensen I., Allington-Smith J. R., Davies R. L., Metcalfe N., Murowinski R. G., Crampton D., 2004, PASP, 116, 425

Hopkins P. F., Hernquist L., Cox T. J., Di Matteo T., Robertson B., Springel V., 2006, ApJS, 163, 1

Hopkins P. F., Hernquist L., Cox T. J., Kereš D., 2008, ApJs, 175, 356

Hunt L. K., Malkan M. A., 1999, ApJ, 516, 660

Hyvönen T., Kotilainen J. K., Örndahl E., Falomo R., Uslenghi M., 2007, A& A, 462, 525

Inskip K. J., Tadhunter C. N., Morganti R., Holt J., Ramos Almeida C., Dicken D., 2010, MNRAS, 407, 1739

Jahnke K., Bongiorno A., Brusa M., Capak P., Cappelluti N., Cisternas M., Civano F., Colbert J., Comastri A., Elvis M., Hasinger G., Ilbert O., Impey C., Inskip K., Koekemoer A. M., Lilly S., 2009, ApJL, 706, L215

Jogee S., 2006, in D. Alloin ed., Physics of Active Galactic Nuclei at all Scales Vol. 693 of Lecture Notes in Physics, Berlin Springer Verlag, The Fueling and Evolution of AGN: Internal and External Triggers. pp 143–+

Johansson P. H., Naab T., Burkert A., 2009, ApJ, 690, 802

Kauffmann G., Haehnelt M., 2000, MNRAS, 311, 576

Keel W. C., 1996, AJ, 111, 696

Kelly B. C., Vestergaard M., Fan X., Hopkins P., Hernquist L., Siemiginowska A., 2010, ApJ, 719, 1315

Kewley L. J., Groves B., Kauffmann G., Heckman T., 2006, MNRAS, 372, 961

Kirhakos S., Bahcall J. N., Schneider D. P., Kristian J., 1999, ApJ, 520, 67

Knapen J. H., Beckman J. E., Heller C. H., Shlosman I., de Jong R. S., 1995, ApJ, 454, 623

Knapen J. H., Shlosman I., Peletier R. F., 2000, ApJ, 529, 93

Kormendy J., 1993, in Beckman J., Colina L., Netzer H., eds, The Nearest Active Galaxies A critical review of stellar-dynamical evidence for black holes in galaxy nuclei. pp 197–218

Kormendy J., Bender R., Cornell M. E., 2011, Nature, 469, 374

Kormendy J., Ho L. C., 2013, ARA & A, 51, 511

Kormendy J., Richstone D., 1995, ARA&A, 33, 581

Kroupa P., 2001, MNRAS, 322, 231

Laine S., Shlosman I., Knapen J. H., Peletier R. F., 2002, ApJ, 567, 97

LaMassa S. M., Heckman T. M., Ptak A., Hornschemeier A., Martins L., Sonnentrucker P., Tremonti C., 2009, Astrophysical Journal, 705, 568

Laor A., 2000, ApJL, 543, L111

Laurikainen E., Salo H., Buta R., 2004, ApJ, 607, 103

Leitherer C., Ortiz Otálvaro P. A., Bresolin F., Kudritzki R.-P., Lo Faro B., Pauldrach A. W. A., Pettini M., Rix S. A., 2010, ApJS, 189, 309

Leitherer C., Schaerer D., Goldader J. D., González Delgado R. M., Robert C., Kune D. F., de Mello D. F., Devost D., Heckman T. M., 1999, ApJS, 123, 3

Li C., Kauffmann G., Heckman T. M., Jing Y. P., White S. D. M., 2008, MNRAS, 385, 1903

Li C., Kauffmann G., Wang L., White S. D. M., Heckman T. M., Jing Y. P., 2006, MNRAS, 373, 457

Liu X., Zakamska N. L., Greene J. E., Strauss M. A., Krolik J. H., Heckman T. M., 2009, ApJ, 702, 1098

Lotz J. M., Jonsson P., Cox T. J., Primack J. R., 2008, MNRAS, 391, 1137

Lynden-Bell D., 1969, Nat, 223, 690

Madau P., Ferguson H. C., Dickinson M. E., Giavalisco M., Steidel C. C., Fruchter A., 1996, MNRAS, 283, 1388

Magorrian J., Tremaine S., Richstone D., Bender R., Bower G., Dressler A., Faber S. M., Gebhardt K., Green R., Grillmair C., Kormendy J., Lauer T., 1998, AJ, 115, 2285

Maia M. A. G., Machado R. S., Willmer C. N. A., 2003, AJ, 126, 1750

Mainieri V., Bongiorno A., Merloni A., Aller M., Carollo M., Iwasawa K., Koekemoer A. M., Mignoli M., 2011, A&A, 535, A80

Maiolino R., Gallerani S., Neri R., Cicone C., Ferrara A., Genzel R., Lutz D., Sturm E., Tacconi L. J., Walter F., Feruglio C., Fiore F., Piconcelli E., 2012, MNRAS, 425, L66

Malkan M. A., Margon B., Chanan G. A., 1984, ApJ, 280, 66

Maraston C., Daddi E., Renzini A., Cimatti A., Dickinson M., Papovich C., Pasquali A., Pirzkal N., 2006, ApJ, 652, 85

Marconi A., Hunt L. K., 2003, ApJL, 589, L21

Marconi A., Risaliti G., Gilli R., Hunt L. K., Maiolino R., Salvati M., 2004, MNRAS, 351, 169

Martini P., 2004, Coevolution of Black Holes and Galaxies. Cambridge University Press, UK

Martini P., Weinberg D. H., 2001, ApJ, 547, 12

McConnell N. J., Ma C.-P., 2013, ApJ, 764, 184

McIntosh D. H., Guo Y., Hertzberg J., Katz N., Mo H. J., van den Bosch F. C., Yang X., 2008, MNRAS, 388, 1537

McLure R. J., Dunlop J. S., 2002, MNRAS, 331, 795

McLure R. J., Dunlop J. S., 2004, MNRAS, 352, 1390

McLure R. J., Jarvis M. J., Targett T. A., Dunlop J. S., Best P. N., 2006, MNRAS, 368, 1395

McLure R. J., Kukula M. J., Dunlop J. S., Baum S. A., O'Dea C. P., Hughes D. H., 1999, MNRAS, 308, 377

McNamara B. R., Wise M., Nulsen P. E. J., David L. P., Sarazin C. L., Bautz M., Markevitch M., Vikhlinin A., Forman W. R., Jones C., Harris D. E., 2000, ApJL, 534, L135

Merloni A., 2004, MNRAS, 353, 1035

Merloni A., Bongiorno A., Bolzonella M., Brusa M., Civano F., Comastri A., Elvis M., Fiore F., Gilli R., Hao H., Jahnke K., Koekemoer A. M., Lusso E., Mainieri V., Mignoli M., 2010, ApJ, 708, 137

Merritt D., Ferrarese L., 2001, MNRAS, 320, L30

Mortlock D. J., Warren S. J., Venemans B. P., Patel M., Hewett P. C., McMahon R. G., Simpson C., Theuns T., Gonzáles-Solares E. A., Adamson A., Dye S., Hambly N. C., Hirst P., Irwin M. J., Kuiper E., Lawrence A., Röttgering H. J. A., 2011, Nature, 474, 616

Mulchaey J. S., Regan M. W., 1997, ApJL, 482, L135

Naab T., Khochfar S., Burkert A., 2006, ApJL, 636, L81

Nenkova M., Sirocky M. M., Nikutta R., Ivezić Ž., Elitzur M., 2008, ApJ, 685, 160

Nipoti C., Blundell K. M., Binney J., 2005, MNRAS, 361, 633

Norman C., Scoville N., 1988, ApJ, 332, 124

Oh S., Oh K., Yi S. K., 2012, ApJS, 198, 4

Osterbrock D. E., Ferland G. J., 2006, Astrophysics of gaseous nebulae and active galactic nuclei, 2nd. ed. University Science Book

Padovani P., Mainieri V., Tozzi P., Kellermann K. I., Fomalont E. B., Miller N., Rosati P., Shaver P., 2009, ApJ, 694, 235

Pérez-González P. G., Trujillo I., Barro G., Gallego J., Zamorano J., Conselice C. J., 2008, ApJ, 687, 50

Pier E. A., Krolik J. H., 1992, ApJ, 401, 99

Quinn P. J., 1984, ApJ, 279, 596

Ramos Almeida C., Bessiere P. S., Tadhunter C. N., Inskip K. J., Morganti R., Dicken D., González-Serrano J. I., Holt J., 2013, MNRAS, 436, 997

Ramos Almeida C., Bessiere P. S., Tadhunter C. N., Pérez-González P. G., Barro G., Inskip K. J., Morganti R., Holt J., Dicken D., 2012, MNRAS, 419, 687

Ramos Almeida C., Rodríguez Espinosa J. M., Acosta-Pulido J. A., Alonso-Herrero A., Pérez García A. M., Rodríguez-Eugenio N., 2013, MNRAS, 429, 3449

Ramos Almeida C., Tadhunter C. N., Inskip K. J., Morganti R., Holt J., Dicken D., 2011, MNRAS, 410, 1550

Rawlings S., Saunders R., Miller P., Jones M. E., Eales S. A., 1990, MNRAS, 246, 21P

Reichard T. A., Heckman T. M., Rudnick G., Brinchmann J., Kauffmann G., Wild V., 2009, ApJ, 691, 1005

Reid R. I., Kronberg P. P., Perley R. A., 1999, ApJS, 124, 285

Reyes R., Zakamska N. L., Strauss M. A., Green J., Krolik J. H., Shen Y., Richards G. T., Anderson S. F., Schneider D. P., 2008, AJ, 136, 2373

Richards G. T., Fan X., Newberg H. J., Strauss M. A., Vanden Berk D. E., Schneider D. P., Yanny B., Boucher A., Burles S., Frieman J. A., Gunn J. E., Hall P. B., Ivezić Ž., Kent S., Loveday J., Lupton R. H., Rockosi C. M., Schlegel D. J., 2002, AJ, 123, 2945

Robinson T., 2001, PhD thesis, Univ. Sheffield

Robinson T. G., Tadhunter C. N., Axon D. J., Robinson A., 2000, MNRAS, 317, 922

Rodríguez Zaurín J., Tadhunter C. N., González Delgado R. M., 2009, MNRAS, 400, 1139

Rodríguez Zaurín J., Tadhunter C. N., González Delgado R. M., 2010, MNRAS, 403, 1317

Rupke D. S. N., Veilleux S., 2011, ApJL, 729, L27

Sakamoto K., Okumura S. K., Ishizuki S., Scoville N. Z., 1999, ApJ, 525, 691

Sanders D. B., Soifer B. T., Elias J. H., Madore B. F., Matthews K., Neugebauer G., Scoville N. Z., 1988, ApJ, 325, 74

Schawinski K., Urry C. M., Simmons B. D., Fortson L., Kaviraj S., Keel W. C., Lintott C. J., Masters K. L., Nichol R. C., Sarzi M., Skibba R., Treister E., Willett K. W., Wong O. I., Yi S. K., 2014, MNRAS, 440, 889

Schlegel D. J., Finkbeiner D. P., Davis M., 1998, ApJ, 500, 525

Schmidt M., 1963, Nature, 197, 1040

Schmidt M., Green R. F., 1983, ApJ, 269, 352

Schmitt H. R., 2001, AJ, 122, 2243

Schneider D. P., Fan X., Hall P. B., Jester S., Richards G. T., Stoughton C., Strauss M. A., SubbaRao M., Vanden Berk D. E., Anderson S. F., Brandt W. N., Gunn J. E., Gray J., Trump J. R., Voges W., Yanny B., Bahcall N. A., Blanton M. R., Boroski W. N., 2003, AJ, 126, 2579

Schneider D. P., Richards G. T., Hall P. B., Strauss M. A., Anderson S. F., Boroson T. A., Ross N. P., Shen Y., Brandt W. N., Fan X., Inada N., Jester S., Knapp G. R., Krawczyk C. M., Thakar A. R., Vanden Berk D. E., Voges W., Yanny B., York D. G., 2010, AJ, 139, 2360

Serber W., Bahcall N., Ménard B., Richards G., 2006, ApJ, 643, 68

Seyfert C. K., 1943, ApJ, 97, 28

Shabala S. S., Ash S., Alexander P., Riley J. M., 2008, MNRAS, 388, 625

Shen Y., Richards G. T., Strauss M. A., Hall P. B., Schneider D. P., Snedden S., Bizyaev D., Brewington H., Malanushenko V., Malanushenko E., Oravetz D., Pan K., Simmons A., 2011, ApJS, 194, 45

Shlosman I., Frank J., Begelman M. C., 1989, Nature, 338, 45

Sikora M., Stawarz Ł., Lasota J.-P., 2007, ApJ, 658, 815

Silk J., Rees M. J., 1998, A&A, 331, L1

Silverman J. D., Kampczyk P., Jahnke K., Andrae R., Lilly S. J., Elvis M., Civano F., Mainieri V., Vignali C., Zamorani G., Nair P., Le Fèvre O., de Ravel L., Bardelli S., Bongiorno A., 2011, ApJ, 743, 2

Simkin S. M., Su H. J., Schwarz M. P., 1980, ApJ, 237, 404

Slavcheva-Mihova L., Mihov B., 2011, A&A, 526, A43+

Smith E. P., Heckman T. M., 1989, ApJ, 341, 658

Springel V., Di Matteo T., Hernquist L., 2005, MNRAS, 361, 776

Stern D., Eisenhardt P., Gorjian V., Kochanek C. S., Caldwell N., Eisenstein D., Brodwin M., Brown M. J. I., Cool R., Dey A., Green P., Jannuzi B. T., Murray S. S., Pahre M. A., Willner S. P., 2005, ApJ, 631, 163

Strauss M. A., Weinberg D. H., Lupton R. H., Narayanan V. K., Annis J., Bernardi M., Blanton M., Burles S., Connolly A. J., Dalcanton J., Doi M., Eisenstein D., Frieman J. A., Fukugita M., Gunn J. E., Ivezić Ž., Kent S., Kim R. S. J., 2002, AJ, 124, 1810

Sturm E. e., 2011, ApJL, 733, L16

Swinbank A. M., Balogh M. L., Bower R. G., Zabludoff A. I., Lucey J. R., McGee S. L., Miller C. J., Nichol R. C., 2012, MNRAS, 420, 672

Tadhunter C., Dickson R., Morganti R., Robinson T. G., Wills K., Villar-Martin M., Hughes M., 2002, MNRAS, 330, 977

Tadhunter C., Holt J., González Delgado R., Rodríguez Zaurín J., Villar-Martín M., Morganti R., Emonts B., Ramos Almeida C., Inskip K., 2011, MNRAS, 412, 960

Tadhunter C., Robinson T. G., González Delgado R. M., Wills K., Morganti R., 2005, MNRAS, 356, 480

Tadhunter C. N., Morganti R., di Serego-Alighieri S., Fosbury R. A. E., Danziger I. J., 1993, MNRAS, 263, 999

Tadhunter C. N., Morganti R., Robinson A., Dickson R., Villar-Martin M., Fosbury R. A. E., 1998, MNRAS, 298, 1035

Toomre A., Toomre J., 1972, ApJ, 178, 623

Tran K.-V. H., Franx M., Illingworth G., Kelson D. D., van Dokkum P., 2003, ApJ, 599, 865

Tran K.-V. H., Franx M., Illingworth G. D., van Dokkum P., Kelson D. D., Magee D., 2004, ApJ, 609, 683

Tremaine S., Gebhardt K., Bender R., Bower G., Dressler A., Faber S. M., Filippenko A. V., Green R., Grillmair C., Ho L. C., Kormendy J., Lauer T. R., Magorrian J., Pinkney J., Richstone D., 2002, ApJ, 574, 740

Tremonti C. A., Moustakas J., Diamond-Stanic A. M., 2007, ApJL, 663, L77

Ueda Y., Akiyama M., Ohta K., Miyaji T., 2003, ApJ, 598, 886

van Dokkum P. G., Conroy C., 2010, Nature, 468, 940

Vázquez G. A., Leitherer C., 2005, ApJ, 621, 695

Villar-Martín M., Cabrera Lavers A., Bessiere P., Tadhunter C., Rose M., de Breuck C., 2012, MNRAS, 423, 80

Villar-Martín M., Emonts B., Rodríguez M., Torres M. P., Drouart G., 2013, MNRAS, 432, 2104

Villar-Martín M., Tadhunter C., Humphrey A., Encina R. F., Delgado R. G., Torres M. P., Martínez-Sansigre A., 2011, MNRAS, 416, 262

Villar-Martín M., Tadhunter C., Pérez E., Humphrey A., Martínez-Sansigre A., Delgado R. G., Pérez-Torres M., 2010, MNRAS, 407, L6

Voges W., Aschenbach B., Boller T., Bräuninger H., Briel U., Burkert W., Dennerl K., Englhauser J., Gruber R., Haberl F., Hartner G., Hasinger G., Kürster M., Pfeffermann E., Pietsch W., 1999, A & A, 349, 389

Walker I. R., Mihos J. C., Hernquist L., 1996, ApJ, 460, 121

Wandel A., Peterson B. M., Malkan M. A., 1999, ApJ, 526, 579

Wild V., Heckman T., Charlot S., 2010, MNRAS, 405, 933

Willott C. J., Rawlings S., Blundell K. M., Lacy M., Eales S. A., 2001, MNRAS, 322, 536

Wills K. A., Tadhunter C., Holt J., González Delgado R., Inskip K. J., Rodríguez Zaurín J., Morganti R., 2008, MNRAS, 385, 136

Xu C., Livio M., Baum S., 1999, AJ, 118, 1169

York D. G., Adelman J., Anderson Jr. J. E., Anderson S. F., Annis J., Bahcall N. A., Bakken J. A., Barkhouser R., Bastian S., Berman E., Boroski W. N., Bracker S., Briegel C., Briggs J. W., Brinkmann 2000, AJ, 120, 1579

Zakamska N. L., Strauss M. A., Heckman T. M., Ivezić Ž., Krolik J. H., 2004, AJ, 128, 1002

Zakamska N. L., Strauss M. A., Krolik J. H., Collinge M. J., Hall P. B., Hao L., Heckman T. M., Ivezić Ž., Richards G. T., Schlegel D. J., Schneider D. P., Strateva I., Vanden Berk D. E., Anderson S. F., Brinkmann J., 2003, AJ, 126, 2125

Zakamska N. L., Strauss M. A., Krolik J. H., Ridgway S. E., Schmidt G. D., Smith P. S., Heckman T. M., Schneider D. P., Hao L., Brinkmann J., 2006, AJ, 132, 1496

Zel'dovich Y. B., Novikov I. D., 1965, Soviet Physics Doklady, 9, 834

Appendix A

Confit fits

A.1 Examples of CONFIT fits for J0025-00

Quasar Host Nucleus

The plots shown in Figure A.1 show examples of acceptable CONFIT fits for the different assumed combinations. The OSP ages and whether a power-law compoent was included are shown in the sub-caption for each figure. The YSP ages and reddenings for each of the sub figures are A.1(a) & A.1(b) $t_{YSP} = 0.2$ Gyr and $E(B-V) = 0.2$, A.1(c) & A.1(d) $t_{YSP} = 0.09$ Gyr and $E(B-V) = 0.3$, A.1(e) & A.1(f) $t_{YSP} = 0.04$ Gyr and $E(B-V) = 0.3$, A.1(g) & A.1(h) $t_{YSP} = 0.04$ Gyr and $E(B-V) = 0.3$.

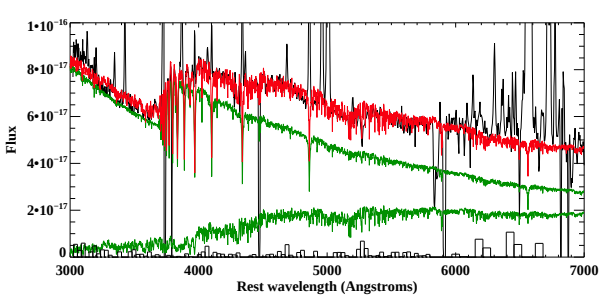

(a) 8 Gyr + Cont - Main Fit

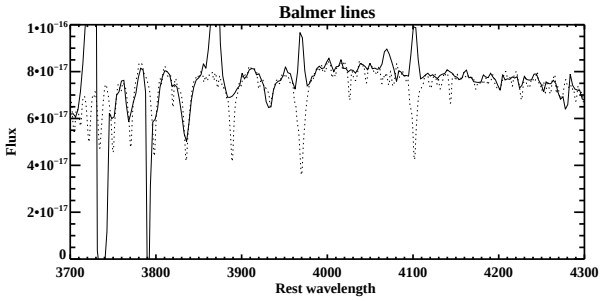

(b) 8 Gyr + Cont - Balmer Lines

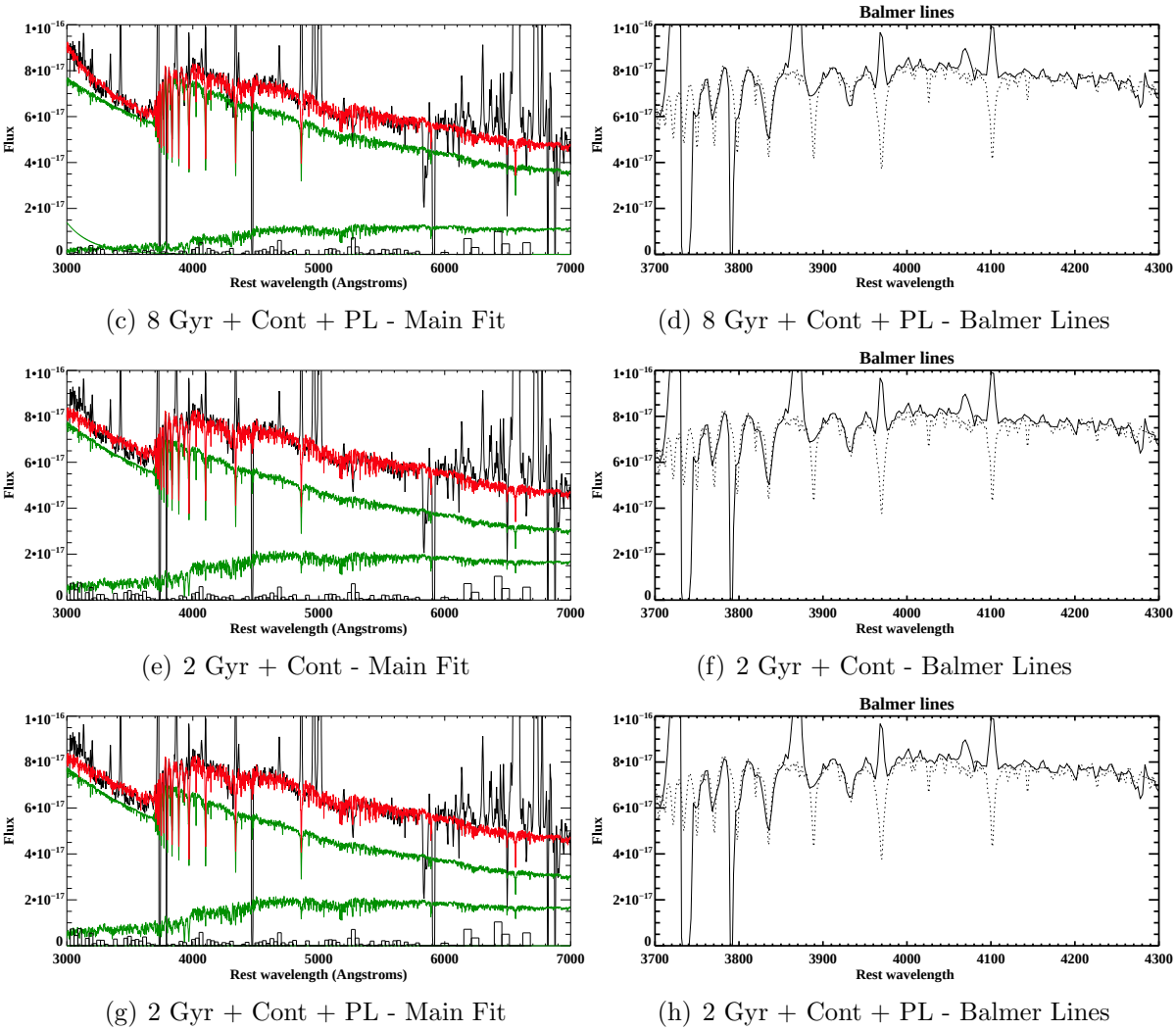

(c) 8 Gyr + Cont + PL - Main Fit

(d) 8 Gyr + Cont + PL - Balmer Lines

(e) 2 Gyr + Cont - Main Fit

(f) 2 Gyr + Cont - Balmer Lines

(g) 2 Gyr + Cont + PL - Main Fit

(h) 2 Gyr + Cont + PL - Balmer Lines

Figure A.1: The best fitting CONFIT models for each combination of components that provided an acceptable fit for the aperture extracted from J0025-00 Quasar Host

Galaxy

The plots shown in Figure A.2 show examples of acceptable CONFIT fits for the different assumed combinations. The OSP ages and whether a power-law compoent was included are shown in the sub-caption for each figure. The YSP ages and reddenings for each of the sub figures are A.2(a) & A.2(b) $t_{YSP} = 0.06$ Gyr and $E(B-V) = 0.1$.

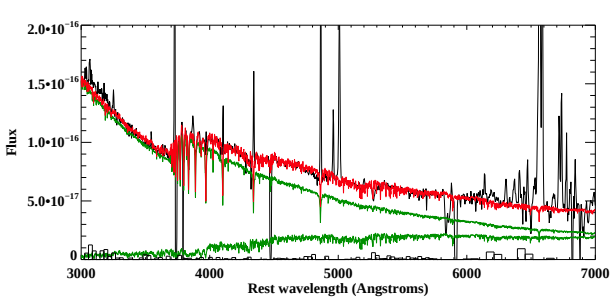

(a) 8 Gyr + Cont - Main Fit

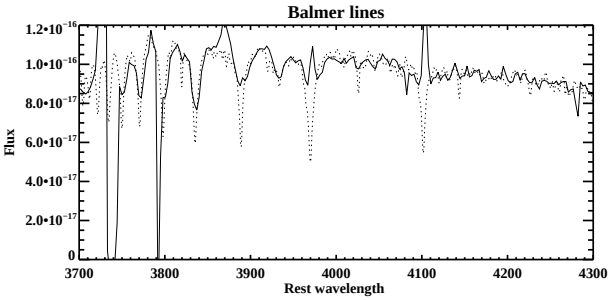

(b) 8 Gyr + Cont - Balmer Lines

Figure A.2: An example of an acceptable fit produced by CONFIT for J0025-10 - Companion Nucleus.

Tidal Tail

The plots shown in Figure A.3 show examples of acceptable CONFIT fits for the different assumed combinations. The OSP ages and whether a power-law compoent was included are shown in the sub-caption for each figure. The YSP ages and reddenings for each of the sub figures are A.3(a) & A.3(b) $t_{YSP} = 0.2$ Gyr and $E(B-V) = 0.1$, A.3(c) & A.3(d) $t_{YSP} = 0.2$ Gyr and $E(B-V) = 0.0$.

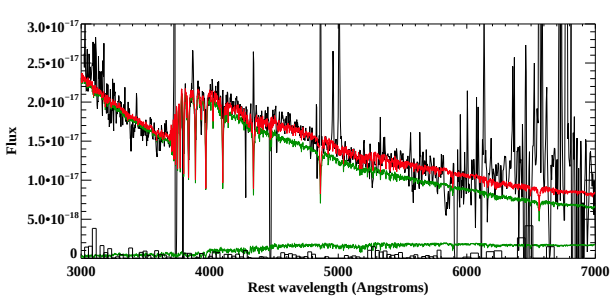

(a) 8 Gyr + Cont - Main Fit

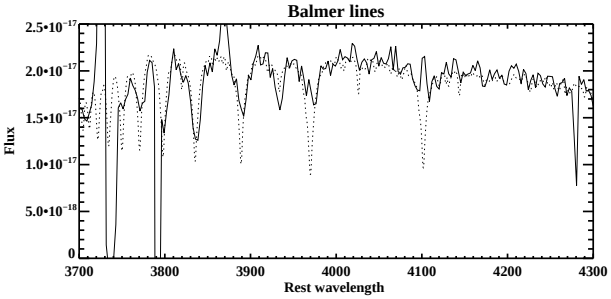

(b) 8 Gyr + Cont - Balmer Lines

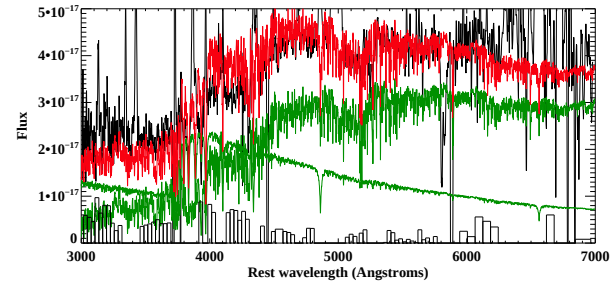

(c) 2 Gyr + Cont - Main Fit

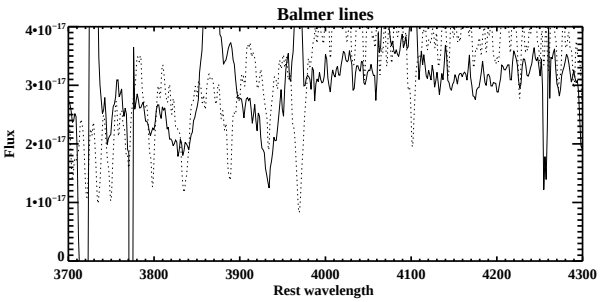

(d) 2 Gyr + Cont - Balmer Lines

Figure A.3: The best fitting CONFIT models for each combination of components that provided an acceptable fit for the aperture extracted from J0025-00 Tidal Tail.

A.2 Examples of CONFIT fits for J0114+00

The plots shown in Figure A.4 show examples of acceptable CONFIT fits for the different assumed combinations. The OSP ages and whether a power-law compoent was included are shown in the sub-caption for each figure. The YSP ages and reddenings for each of the sub figures are A.4(a) & A.4(b) $t_{YSP} = 0.2$ Gyr and $E(B-V) = 1.0$, A.4(c) & A.4(d) $t_{YSP} = 0.2$ Gyr and $E(B-V) = 0.3$, A.4(e) & A.4(f) $t_{YSP} = 0.2$ Gyr and $E(B-V) = 1.0$, A.4(g) & A.4(h) $t_{YSP} = 1.4$ Gyr and $E(B-V) = 0.3$, A.4(i) & A.4(j) $t_{YSP} = 1.4$ Gyr and $E(B-V) = 0.3$.

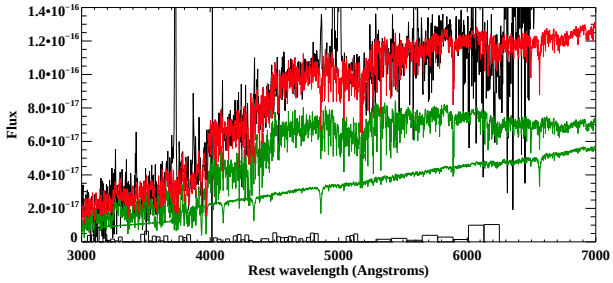

(a) 8 Gyr + Cont - Main Fit

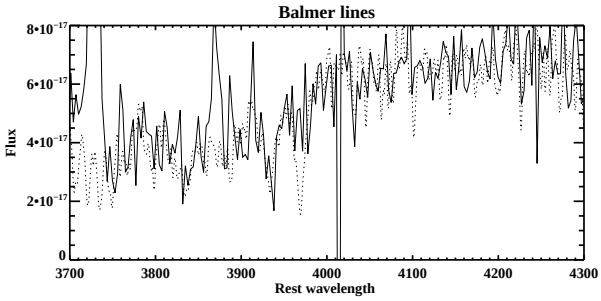

(b) 8 Gyr + Cont - Balmer Lines

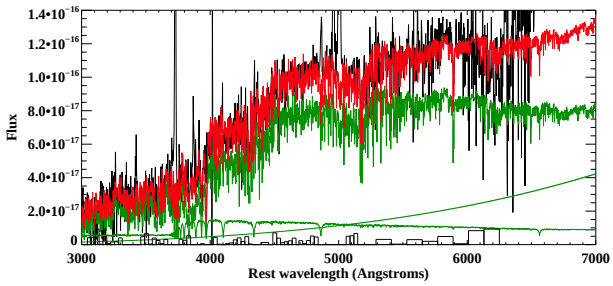

(c) 8 Gyr + Burst + Pl - Main Fit

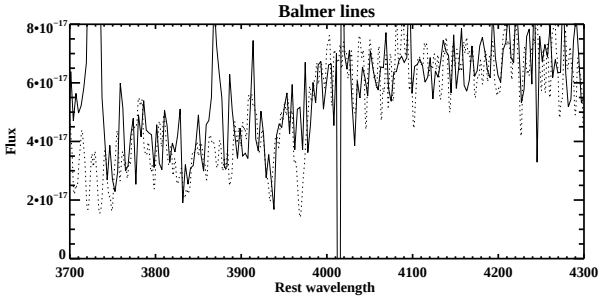

(d) 8 Gyr + Burst + PL - Balmer Lines

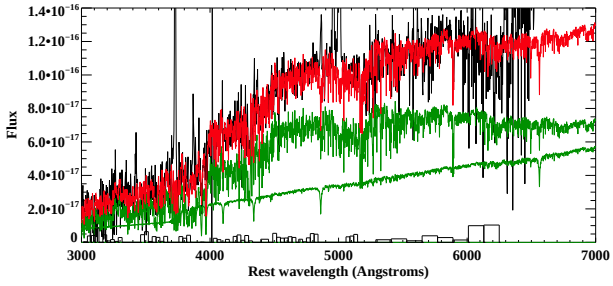

(e) 8 Gyr + Cont + PL - Main Fit

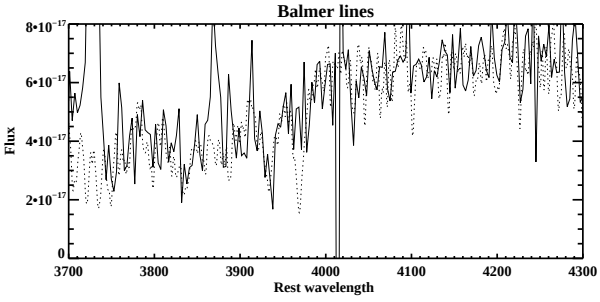

(f) 8 Gyr + Cont + PL - Balmer Lines

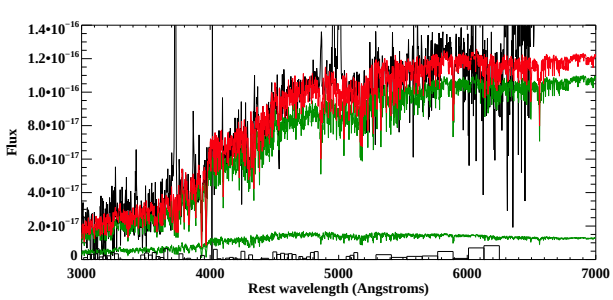

(g) 2 Gyr + Burst - Main Fit

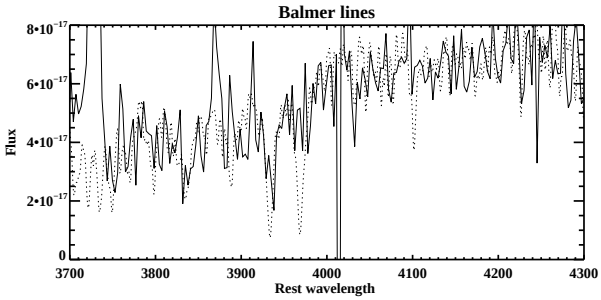

(h) 2 Gyr + Burst - Balmer Lines

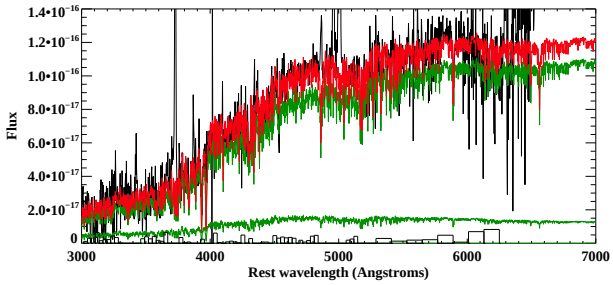

(i) 2 Gyr + Burst + PL - Main Fit

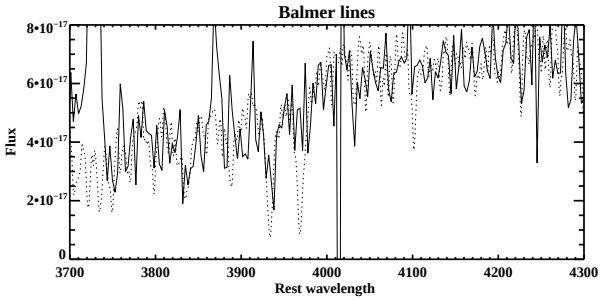

(j) 2 Gyr + Burst + PL - Balmer Lines

Figure A.4: The best fitting CONFIT models for each combination of components that provided an acceptable fit for the aperture extracted from J0114+00

A.3 Examples of CONFIT fits for J0123+00

The plots shown in Figure A.5 show examples of acceptable CONFIT fits for the different assumed combinations. The OSP ages and whether a power-law compoent was included are shown in the sub-caption for each figure. The YSP ages and reddenings for each of the sub figures are A.5(a) & A.5(b) $t_{YSP} = 0.005$ Gyr and $E(B-V) = 1.7$.

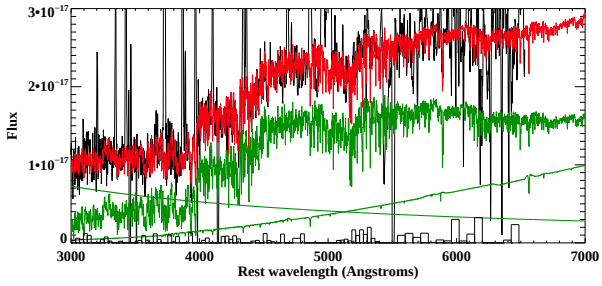

(a) 8 Gyr + Cont + PL - Main Fit

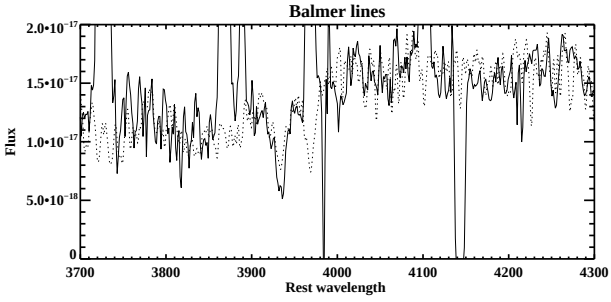

(b) 8 Gyr + Cont + PL - Balmer Lines

Figure A.5: The best fitting CONFIT models for each combination of components that provided an acceptable fit for the aperture extracted from J0123+00

A.4 Examples of CONFIT fits for J0142+14

The plots shown in Figure A.6 show examples of acceptable CONFIT fits for the different assumed combinations. The OSP ages and whether a power-law compoent was included are shown in the sub-caption for each figure. The YSP ages and reddenings for each of the sub figures are A.6(c) & A.6(d) $t_{YSP} = 0.05$ Gyr and $E(B-V) = 0.4$, A.6(a) & A.6(b) $t_{YSP} = 0.05$ Gyr and $E(B-V) = 0.4$, A.6(e) & A.6(f) $t_{YSP} = 0.05$ Gyr and $E(B-V) = 0.4$.

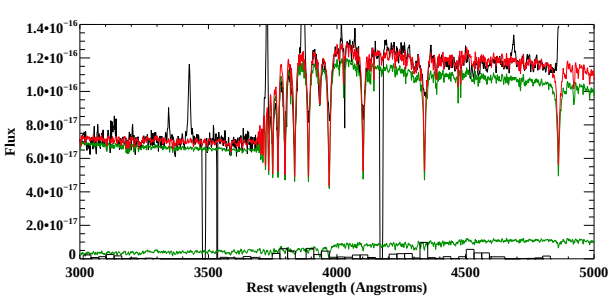

(a) 2 Gyr + Burst - Main Fit

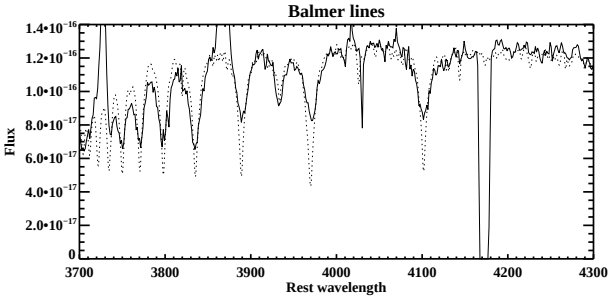

(b) 2 Gyr + Burst - Balmer Lines

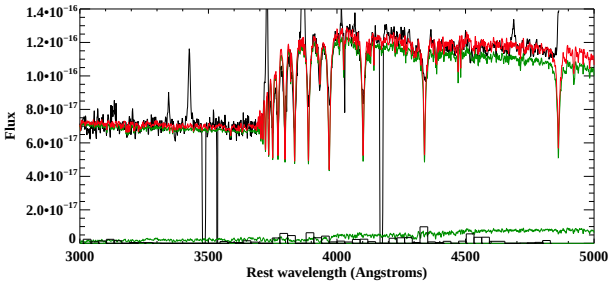

(c) 8 Gyr + Burst + PL - Main Fit

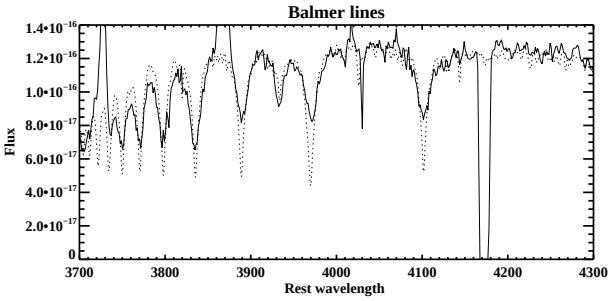

(d) 8 Gyr + Burst + PL - Balmer Lines

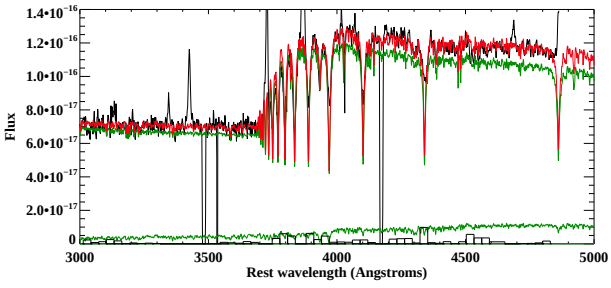

(e) 2 Gyr + Burst + PL - Main Fit

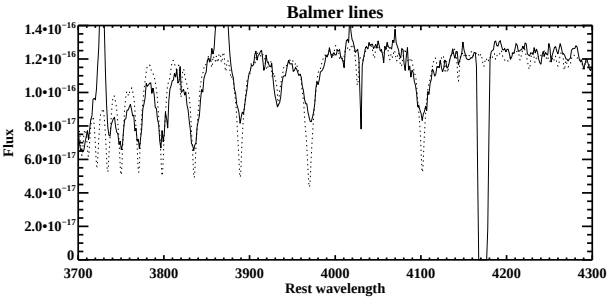

(f) 2 Gyr + Burst + PL - Balmer Lines

Figure A.6: The best fitting CONFIT models for each combination of components that provided an acceptable fit for the aperture extracted from J0142+14.

A.5 Examples of CONFIT fits for J0217-00

The plots shown in Figure A.7 show examples of acceptable CONFIT fits for the different assumed combinations. The OSP ages and whether a power-law compoent was included are shown in the sub-caption for each figure. The YSP ages and reddenings for each of the sub figures are A.7(a) & A.7(b) $t_{YSP} = 0.3$ Gyr and $E(B-V) = 0.4$, A.7(c) & A.7(d) $t_{YSP} = 0.09$ Gyr and $E(B-V) = 0.5$, A.7(e) & A.7(f) $t_{YSP} = 0.3$ Gyr and $E(B-V) = 0.3$.

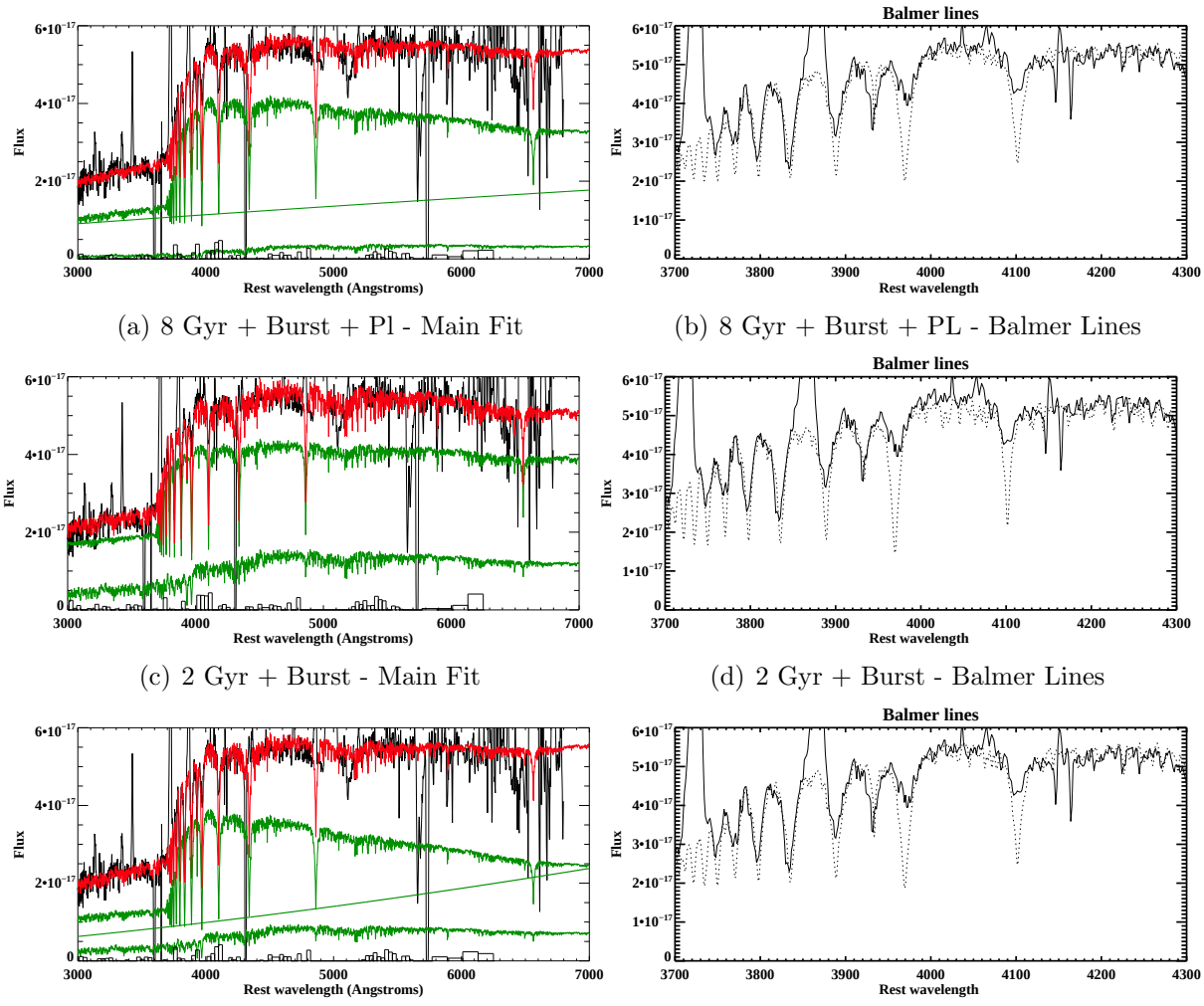

(a) 8 Gyr + Burst + Pl - Main Fit

(b) 8 Gyr + Burst + PL - Balmer Lines

(c) 2 Gyr + Burst - Main Fit

(d) 2 Gyr + Burst - Balmer Lines

(e) 2 Gyr + Burst + PL - Main Fit

(f) 2 Gyr + Burst + PL - Balmer Lines

Figure A.7: The best fitting CONFIT models for each combination of components that provided an acceptable fit for the aperture extracted from J0217-00

A.5.1 Example CONFIT fits for J0217-01

The plots shown in Figure A.8 show examples of acceptable CONFIT fits for the different assumed combinations. The OSP ages and whether a power-law compoent was included are shown in the sub-caption for each figure. The YSP ages and reddenings for each of the sub figures are A.8(a) & A.8(b) $t_{YSP} = 0.08$ Gyr and $E(B-V) = 1.1$, A.8(c) & A.8(d) $t_{YSP} = 0.2$ Gyr and $E(B-V) = 0.6$, A.8(e) & A.8(f) $t_{YSP} = 0.2$ Gyr and $E(B-V) = 0.1$.

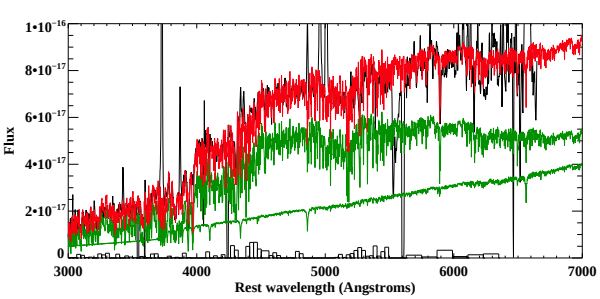

(a) 8 Gyr + Cont - Main Fit

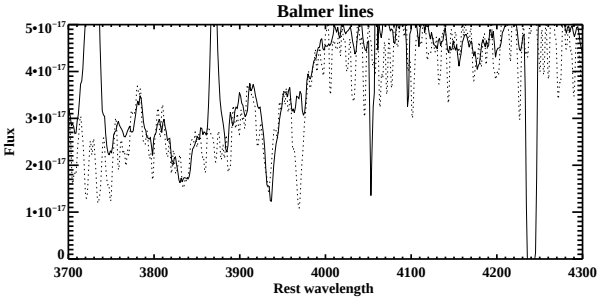

(b) 8 Gyr + Cont - Balmer Lines

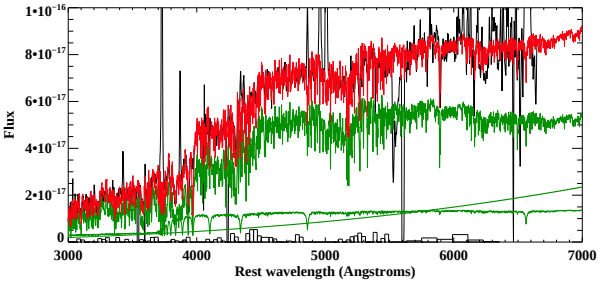

(c) 8 Gyr + Burst + Pl - Main Fit

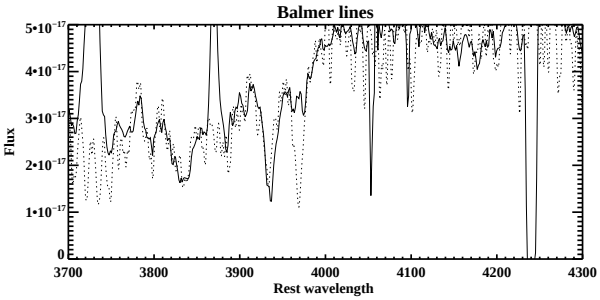

(d) 8 Gyr + Burst + PL - Balmer Lines

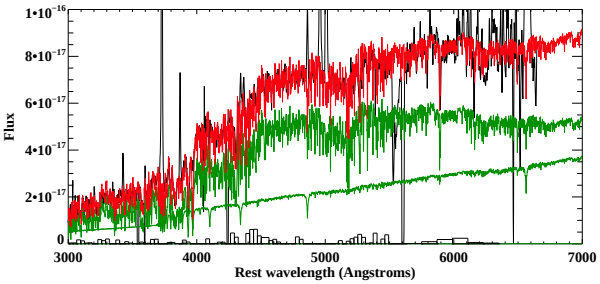

(e) 8 Gyr + Cont + PL - Main Fit

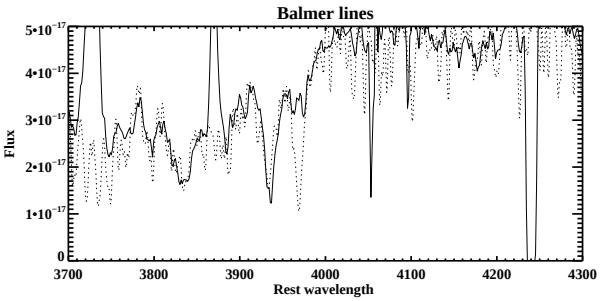

(f) 8 Gyr + Cont + PL - Balmer Lines

Figure A.8: The best fitting CONFIT models for each combination of components that provided an acceptable fit for the aperture extracted from J0217-01

A.6 Examples of CONFIT fits for J0218-00

A.6.1 Aperture N

The plots shown in Figure A.9 show examples of acceptable CONFIT fits for the different assumed combinations. The OSP ages and whether a power-law compoent was included are shown in the sub-caption for each figure. The YSP ages and reddenings for each of the sub figures are A.9(a) & A.9(b) $t_{YSP} = 0.2$ Gyr and $E(B-V) = 0.4$, A.9(e) & A.9(f) $t_{YSP} = 0.2$ Gyr and $E(B-V) = 0.5$, A.9(c) & A.9(d) $t_{YSP} = 0.2$ Gyr and $E(B-V) = 0.4$, A.9(g) & A.9(h) $t_{YSP} = 0.2$ Gyr and $E(B-V) = 0.5$.

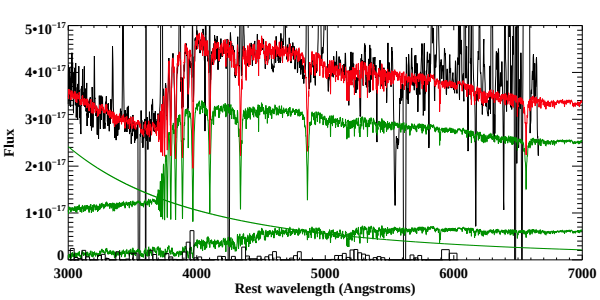

(a) 8 Gyr + Burst + PL - Main Fit

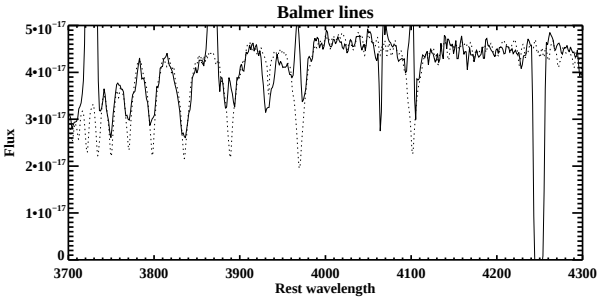

(b) 8 Gyr + Burst + PL - Balmer Lines

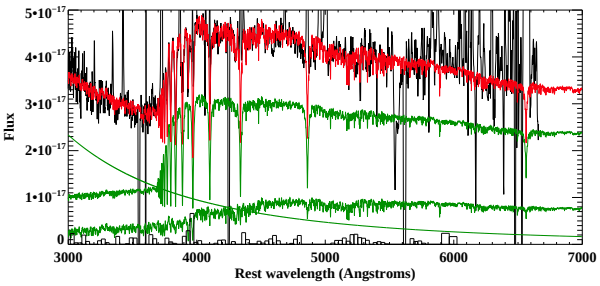

(c) 2 Gyr + Burst + PL - Main Fit

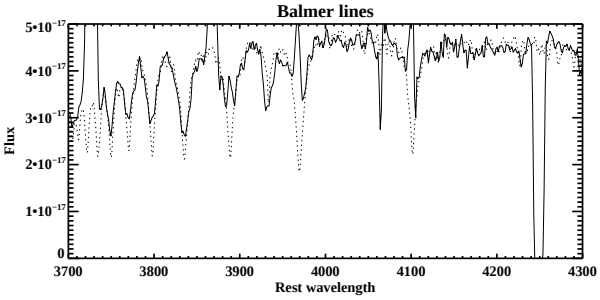

(d) 2 Gyr + Burst + PL - Balmer Lines

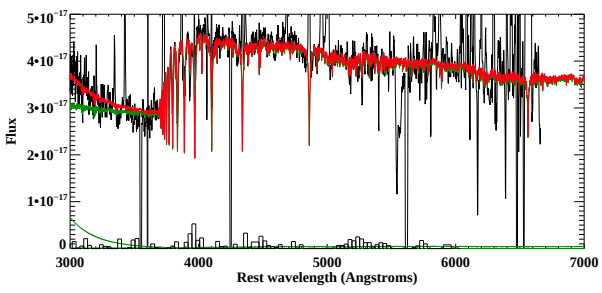

(e) 8 Gyr + Cont + PL - Main Fit

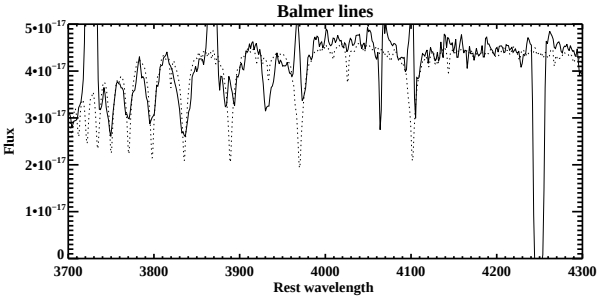

(f) 8 Gyr + Cont + PL - Balmer Lines

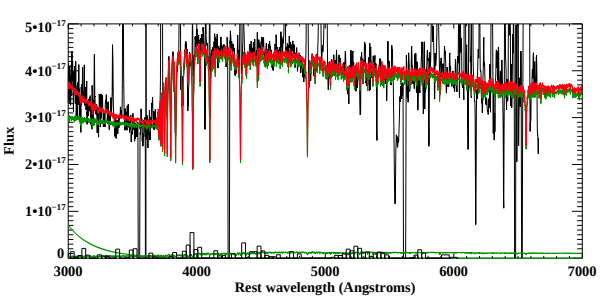

(g) 2 Gyr + Cont + PL - Main Fit

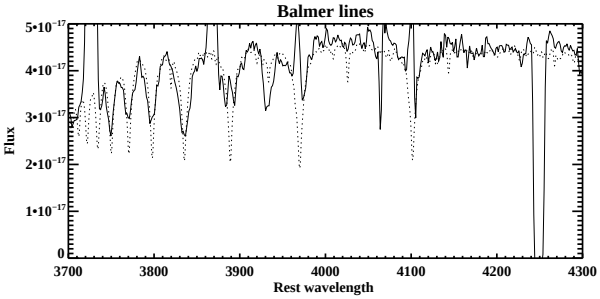

(h) 2 Gyr + Cont + PL - Balmer Lines

Figure A.9: The best fitting CONFIT models for each combination of components that provided an acceptable fit for the nuclear aperture extracted from J0218-00.

A.6.2 Aperture E

The plots shown in Figure A.10 show examples of acceptable CONFIT fits for the different assumed combinations. The OSP ages and whether a power-law compoent was included are shown in the sub-caption for each figure. The YSP ages and reddenings for each of the sub figures are A.10(a) & A.10(b) $t_{YSP} = 0.09$ Gyr and $E(B-V) = 0.3$, A.10(c) & A.10(d) $t_{YSP} = 0.2$ Gyr and $E(B-V) = 0.3$, A.10(e) & A.10(e) $t_{YSP} = 0.07$ Gyr and $E(B-V) = 0.4$.

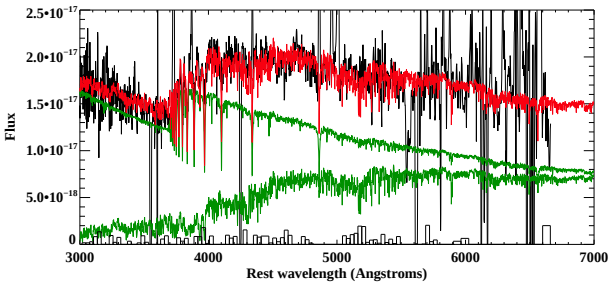

(a) 8 Gyr + Cont - Main Fit

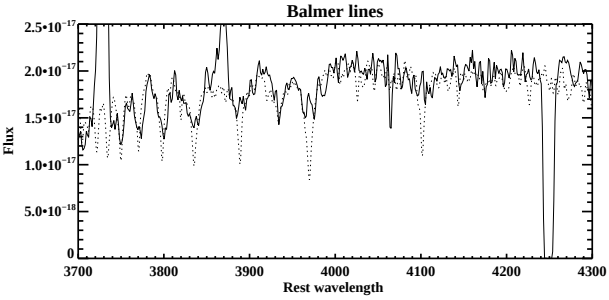

(b) 8 Gyr + Cont - Balmer Lines

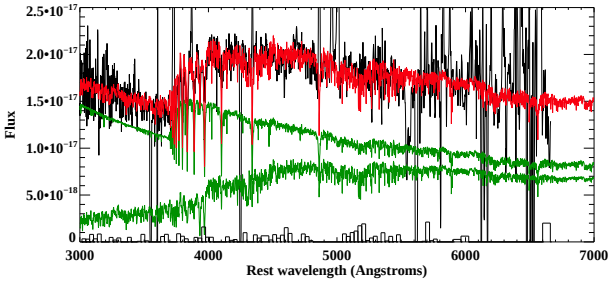

(c) 2 Gyr + Burst - Main Fit

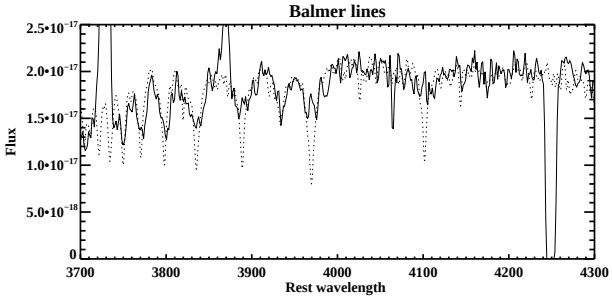

(d) 2 Gyr + Burst - Balmer Lines

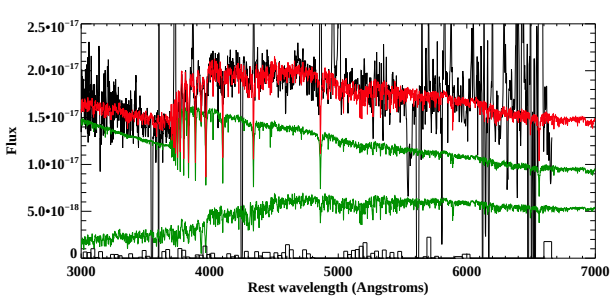

(e) 2 Gyr + Cont - Main Fit

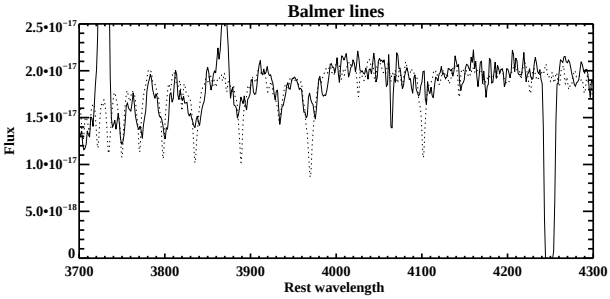

(f) 8 Gyr + Cont - Balmer Lines

Figure A.10: Example of acceptable CONFIT fits for each of the combinations that produced an acceptable fit for the extended aperture extracted from J0218-00.

A.7 Examples of Confit plots for J0227+01

The plots shown in Figure A.11 show examples of acceptable CONFIT fits for the different assumed combinations. The OSP ages and whether a power-law compoent was included are shown in the sub-caption for each figure. The YSP ages and reddenings for each of the sub figures are A.11(a) & A.11(b) $t_{YSP} = 0.2$ Gyr and $E(B-V) = 0.5$, A.11(c) & A.11(d) $t_{YSP} = 0.05$ Gyr and $E(B-V) = 0.5$, A.11(e) & A.11(f) $t_{YSP} = 0.2$ Gyr and $E(B-V) = 0.5$, A.11(g) & A.11(h) $t_{YSP} = 0.03$ Gyr and $E(B-V) = 0.5$, A.11(i) & A.11(j) $t_{YSP} = 0.2$ Gyr and $E(B-V) = 0.5$, A.11(k) & A.11(l) $t_{YSP} = 0.04$ Gyr and $E(B-V) = 0.5$, A.11(m) & A.11(n) $t_{YSP} = 0.2$ Gyr and $E(B-V) = 0.5$.

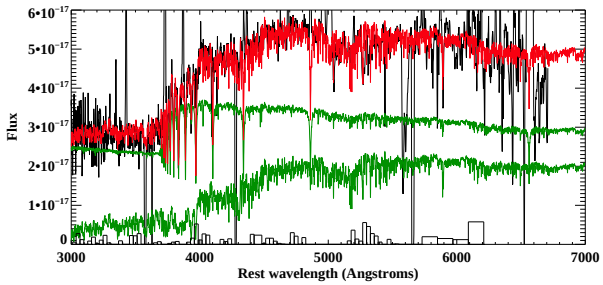

(a) 8 Gyr + Cont - Main Fit

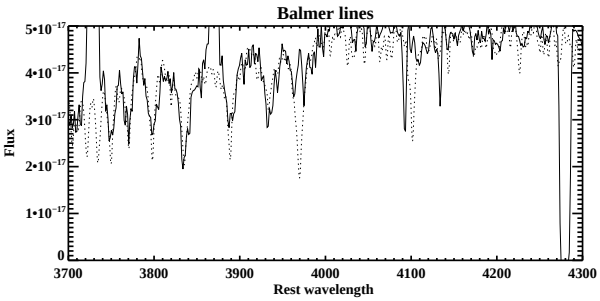

(b) 8 Gyr + Cont - Balmer Lines

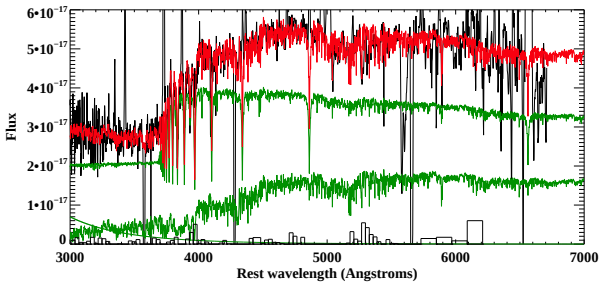

(c) 8 Gyr + Burst + Pl - Main Fit

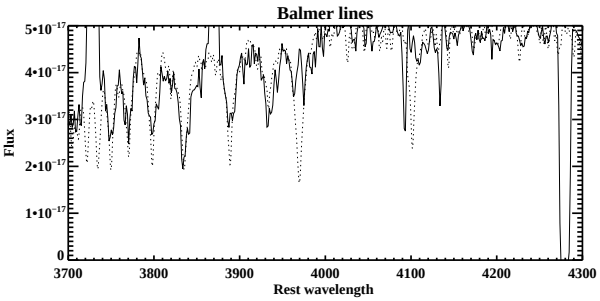

(d) 8 Gyr + Burst + PL - Balmer Lines

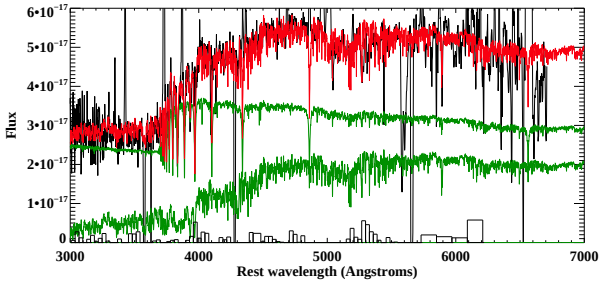

(e) 8 Gyr + Cont + PL - Main Fit

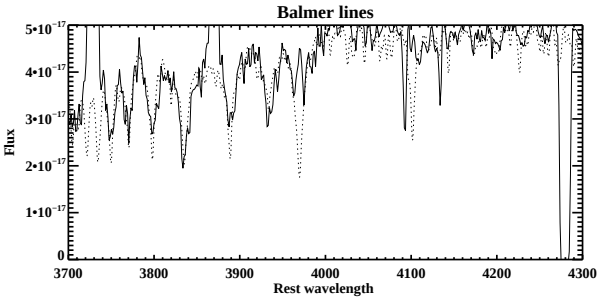

(f) 8 Gyr + Cont + PL - Balmer Lines

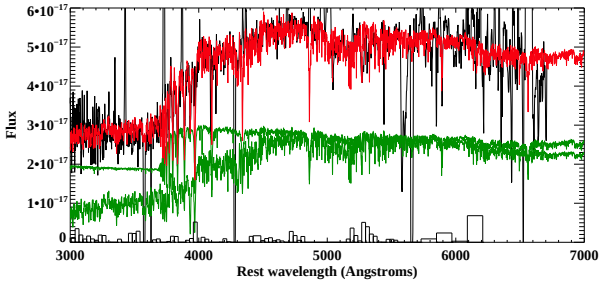

(g) 2 Gyr + Burst - Main Fit

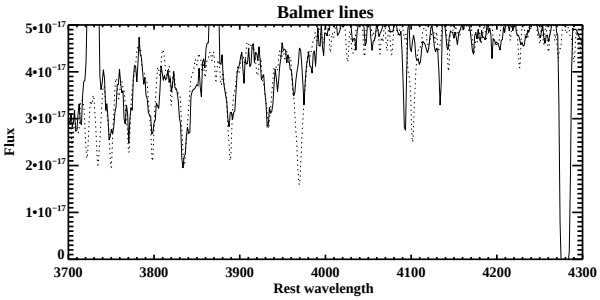

(h) 2 Gyr + Burst - Balmer Lines

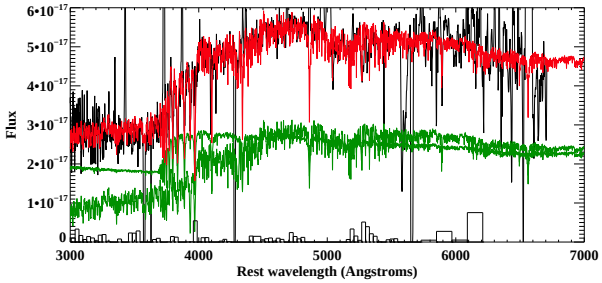

(i) 2 Gyr + Cont - Main Fit

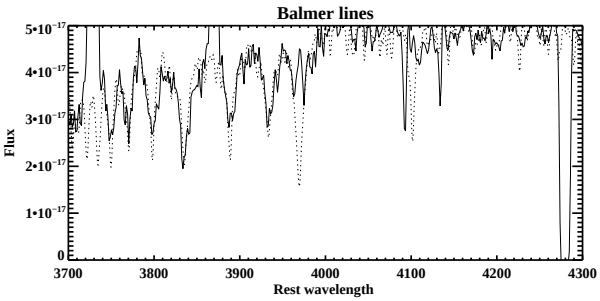

(j) 2 Gyr + Cont - Balmer Lines

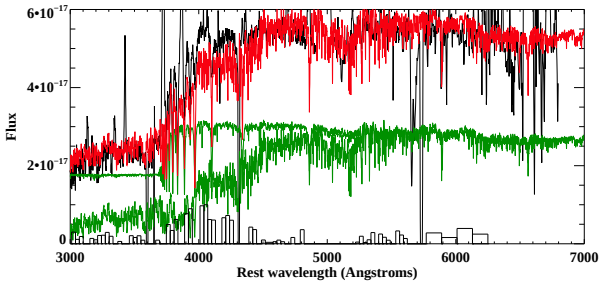

(k) 2 Gyr + Burst + PL - Main Fit

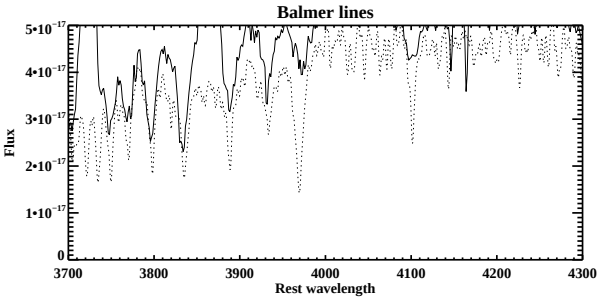

(l) 2 Gyr + Burst + PL - Balmer Lines

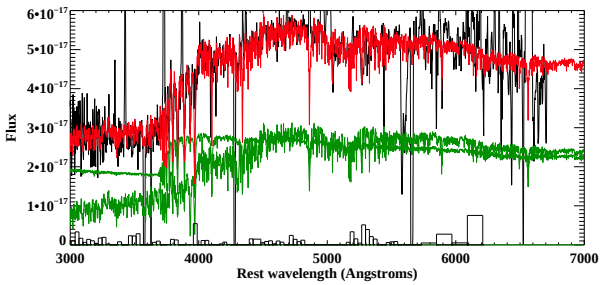

(m) 2 Gyr + Cont + PL - Main Fit

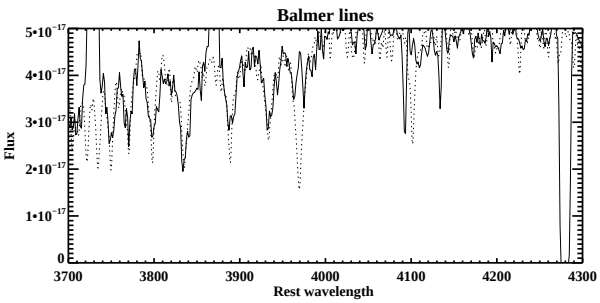

(n) 2 Gyr + Cont + PL - Balmer Lines

Figure A.11: The best fitting CONFIT models for each combination of components that provided an acceptable fit for the aperture extracted from J0227+01

A.8 Examples of CONFIT plots for J0234-07

The plots shown in Figure A.12 show examples of acceptable CONFIT fits for the different assumed combinations. The OSP ages and whether a power-law compoent was included are shown in the sub-caption for each figure. The YSP ages and reddenings for each of the sub figures are A.12(a) & A.12(b) $t_{YSP} = 0.003$ Gyr and $E(B-V) = 0.4$, A.12(c) & A.12(d) $t_{YSP} = 0.005$ Gyr and $E(B-V) = 0$, A.12(g) & A.12(h) $t_{YSP} = 0.006$ Gyr and $E(B-V) = 1.4$, A.12(e) & A.12(f) $t_{YSP} = 0.005$ Gyr and $E(B-V) = 1.0$, A.12(i) & A.12(j) $t_{YSP} = 0.004$ Gyr and $E(B-V) = 1.1$.

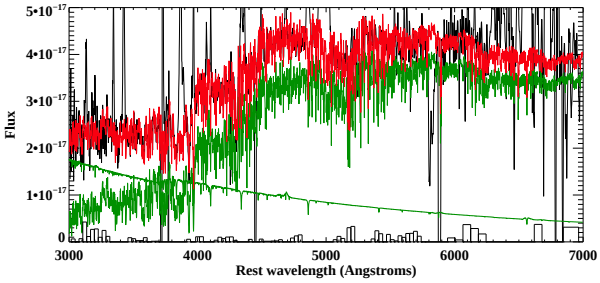

(a) 8 Gyr + Cont - Main Fit

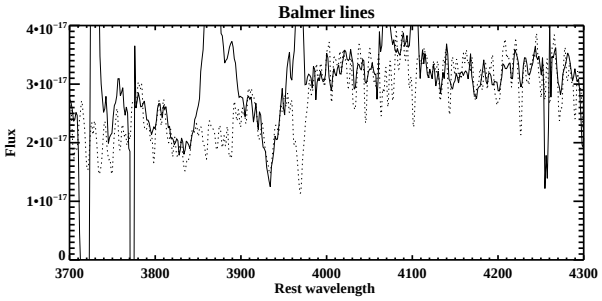

(b) 8 Gyr + Cont - Balmer Lines

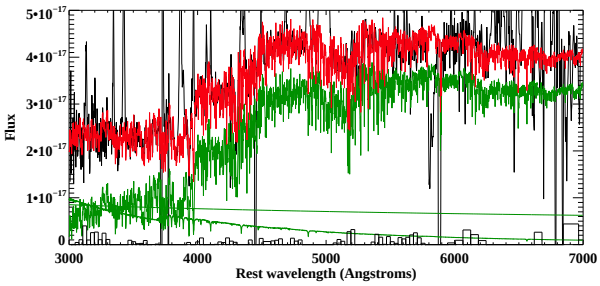

(c) 8 Gyr + Burst + Pl - Main Fit

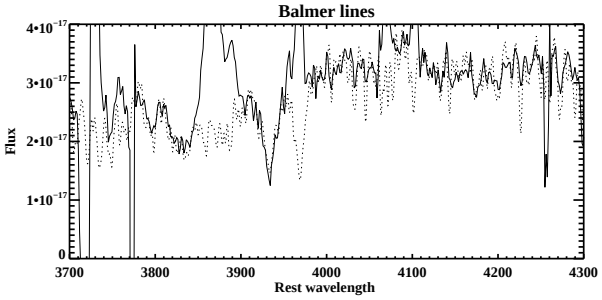

(d) 8 Gyr + Burst + PL - Balmer Lines

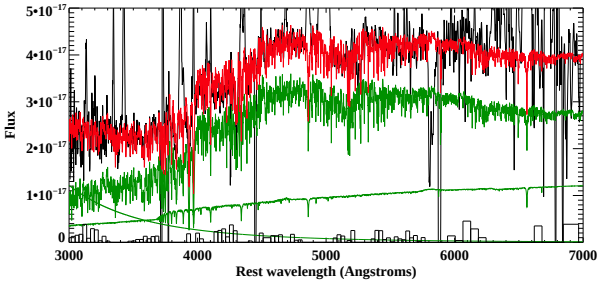

(e) 2 Gyr + Burst + PL - Main Fit

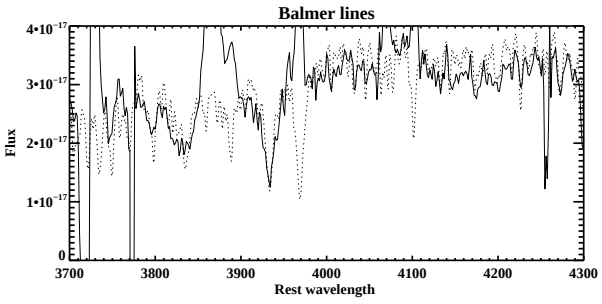

(f) 2 Gyr + Burst + PL - Balmer Lines

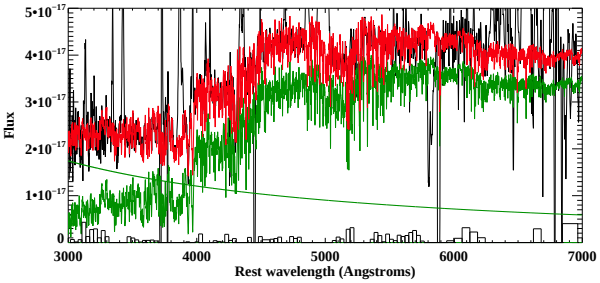

(g) 8 Gyr + Cont + PL - Main Fit

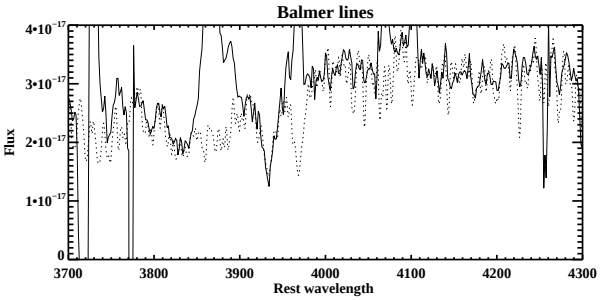

(h) 8 Gyr + Cont + PL - Balmer Lines

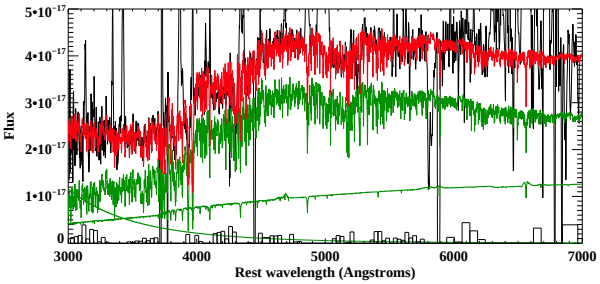

(i) 2 Gyr + Cont + PL - Main Fit

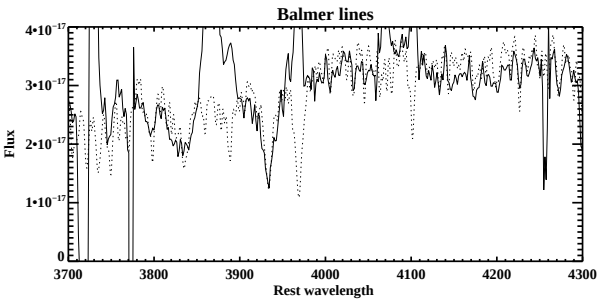

(j) 2 Gyr + Cont + PL - Balmer Lines

Figure A.12: The best fitting CONFIT models for each combination of components that provided an acceptable fit for the aperture extracted from J0234-07.

A.9 Examples of CONFIT plots for J0249-00

The plots shown in Figure A.13 show examples of acceptable CONFIT fits for the different assumed combinations. The OSP ages and whether a power-law compoent was included are shown in the sub-caption for each figure. The YSP ages and reddenings for each of the sub figures are A.13(a) & A.13(b) $t_{YSP} = 0.6$ Gyr and $E(B-V) = 0.5$, A.13(c) & A.13(d) $t_{YSP} = 0.09$ Gyr and $E(B-V) = 0.8$, A.13(e) & A.13(f) $t_{YSP} = 0.2$ Gyr and $E(B-V) = 0.8$.

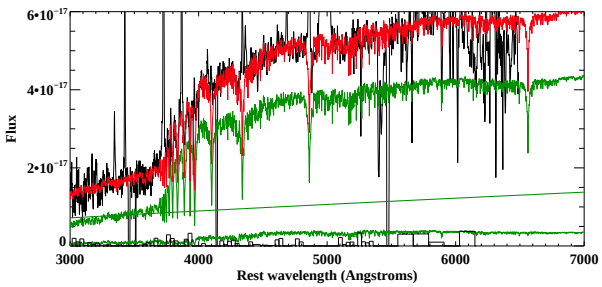

(a) 8 Gyr + Burst + Pl - Main Fit

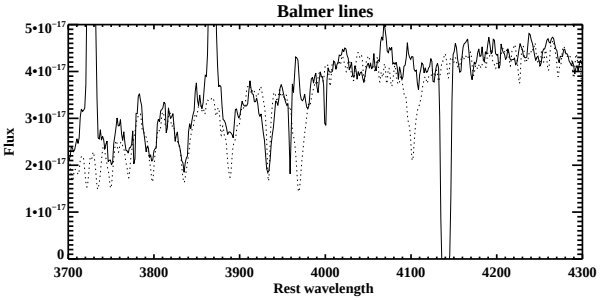

(b) 8 Gyr + Burst + PL - Balmer Lines

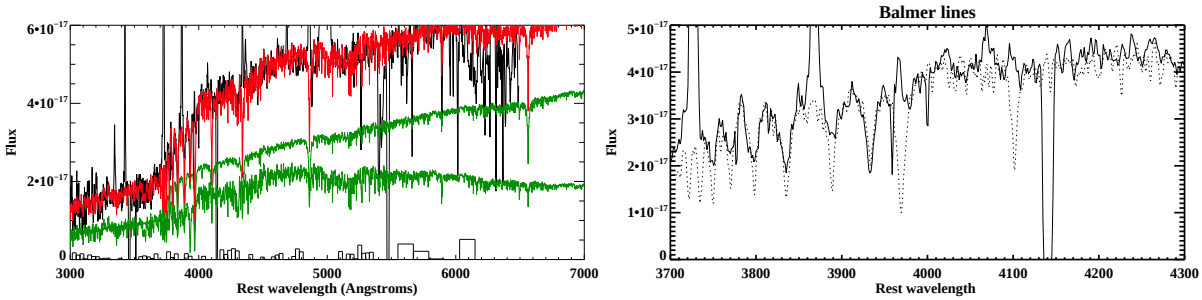

(c) 2 Gyr + Burst - Main Fit

(d) 2 Gyr + Burst - Balmer Lines

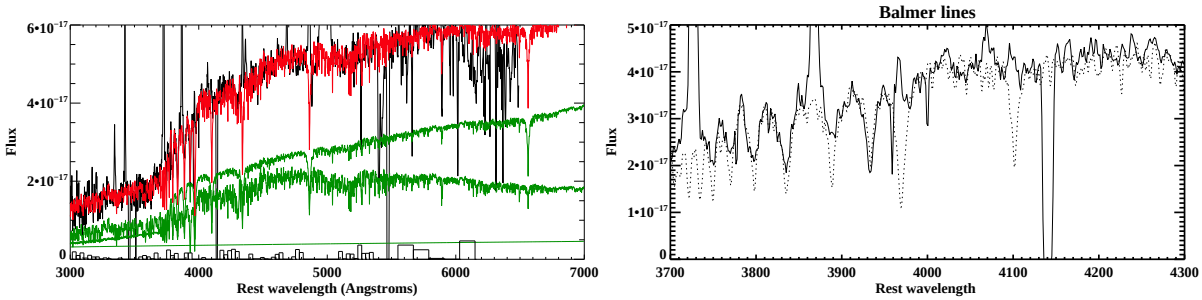

(e) 2 Gyr + Burst + PL - Main Fit

(f) 2 Gyr + Burst + PL - Balmer Lines

Figure A.13: The best fitting CONFIT models for each combination of components that provided an acceptable fit for the aperture extracted from J0249-00

A.10 Examples of CONFIT plots for J0320-00

The plots shown in Figure A.14 show examples of acceptable CONFIT fits for the different assumed combinations. The OSP ages and whether a power-law compoent was included are shown in the sub-caption for each figure. The YSP ages and reddenings for each of the sub figures are A.14(a) & A.14(b) $t_{YSP} = 0.08$ Gyr and $E(B-V) = 0.2$, A.14(c) & A.14(d) $t_{YSP} = 0.02$ Gyr and $E(B-V) = 0.3$, A.14(e) & A.14(f) $t_{YSP} = 0.06$ Gyr and $E(B-V) = 0.4$, A.14(g) & A.14(h) $t_{YSP} = 0.02$ Gyr and $E(B-V) = 0.4$, A.14(i) & A.14(j) $t_{YSP} = 0.03$ Gyr and $E(B-V) = 0.5$.

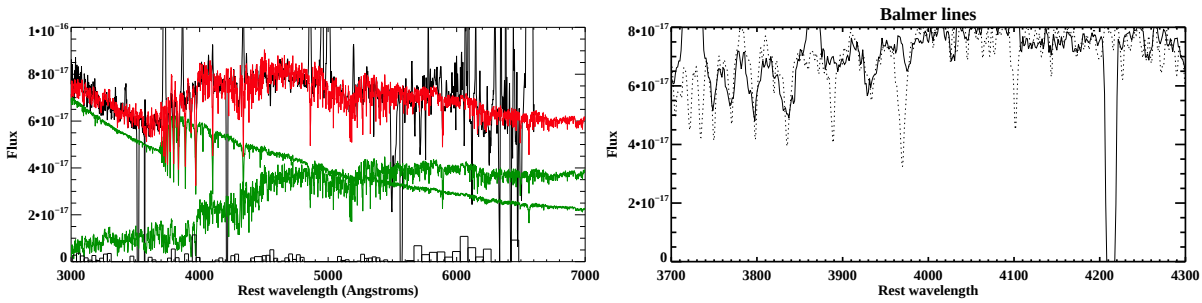

(a) 8 Gyr + Cont - Main Fit

(b) 8 Gyr + Cont - Balmer Lines

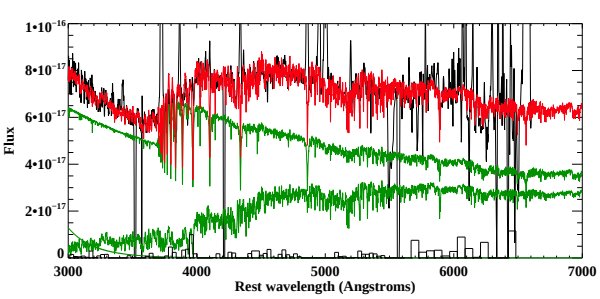

(c) 8 Gyr + Burst + Pl - Main Fit

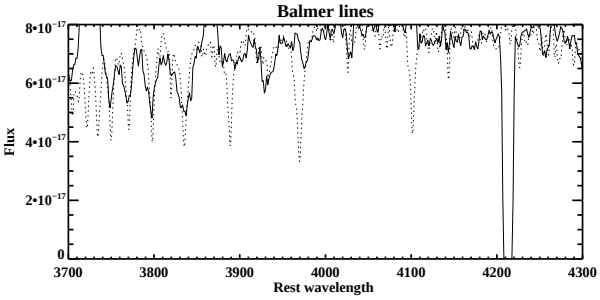

(d) 8 Gyr + Burst + PL - Balmer Lines

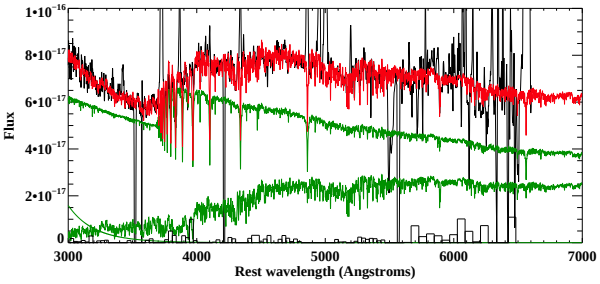

(e) 8 Gyr + Cont + PL - Main Fit

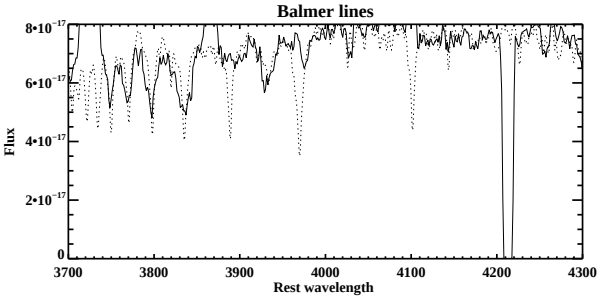

(f) 8 Gyr + Cont + PL - Balmer Lines

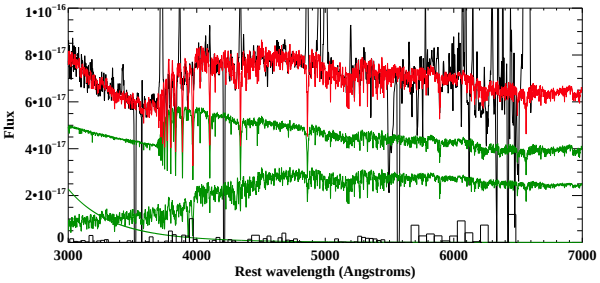

(g) 2 Gyr + Burst + PL - Main Fit

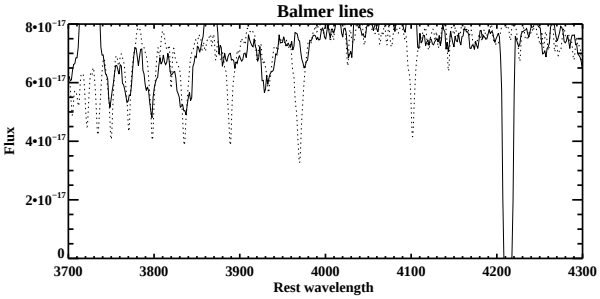

(h) 2 Gyr + Burst + PL - Balmer Lines

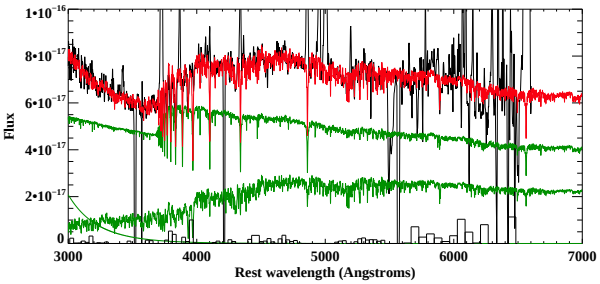

(i) 2 Gyr + Cont + PL - Main Fit

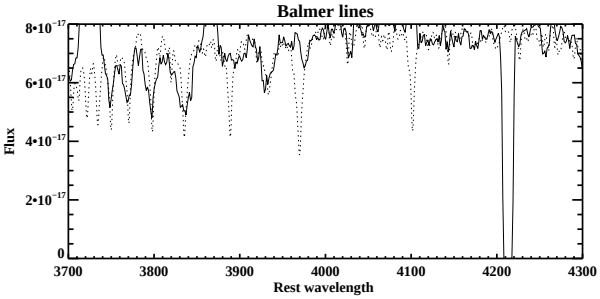

(j) 2 Gyr + Cont + PL - Balmer Lines

Figure A.14: The best fitting CONFIT models for each combination of components that provided an acceptable fit for the aperture extracted from J0320-00

A.11 Examples of CONFIT plots for J0332-00

A.11.1 Quasar host galaxy

The plots shown in Figure A.15 show examples of acceptable CONFIT fits for the different assumed combinations. The OSP ages and whether a power-law compoent was included are shown in the sub-caption for each figure. The YSP ages and reddenings for each of the sub figures are A.15(a) & A.15(b) $t_{YSP} = 0.005$ Gyr and $E(B-V) = 1.4$, A.15(c) & A.15(d) $t_{YSP} = 0.008$ Gyr and $E(B-V) = 0.5$.

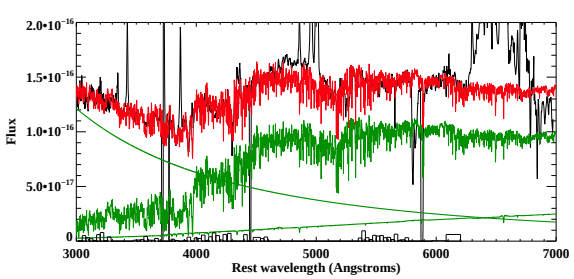

(a) 8 Gyr + Cont + PL - Main Fit

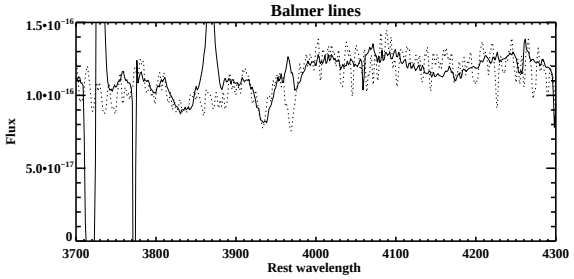

(b) 8 Gyr + Cont + PL - Balmer Lines

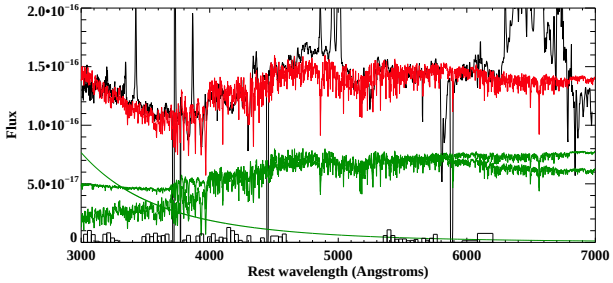

(c) 2 Gyr + Burst + PL - Main Fit

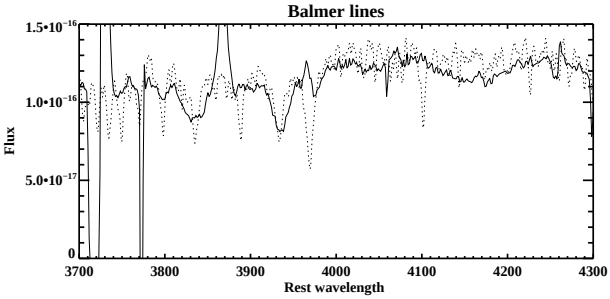

(d) 2 Gyr + Burst + PL - Balmer Lines

Figure A.15: The best fitting CONFIT models for each combination of components that provided an acceptable fit for the J0332-00 - Quasar host aperture.

A.11.2 Companion Galaxy

The plots shown in Figure A.16 show examples of acceptable CONFIT fits for the different assumed combinations. The OSP ages and whether a power-law compoent was included are shown in the sub-caption for each figure. The YSP ages and reddenings for each of the sub figures are A.16(a) & A.16(b) $t_{YSP} = 0.007$ Gyr and $E(B-V) = 0.7$, A.16(c) & A.16(d) $t_{YSP} = 0.08$ Gyr and $E(B-V) = 0.3$, A.16(e) & A.16(f) $t_{YSP} = 0.2$ Gyr and $E(B-V) = 0.5$.

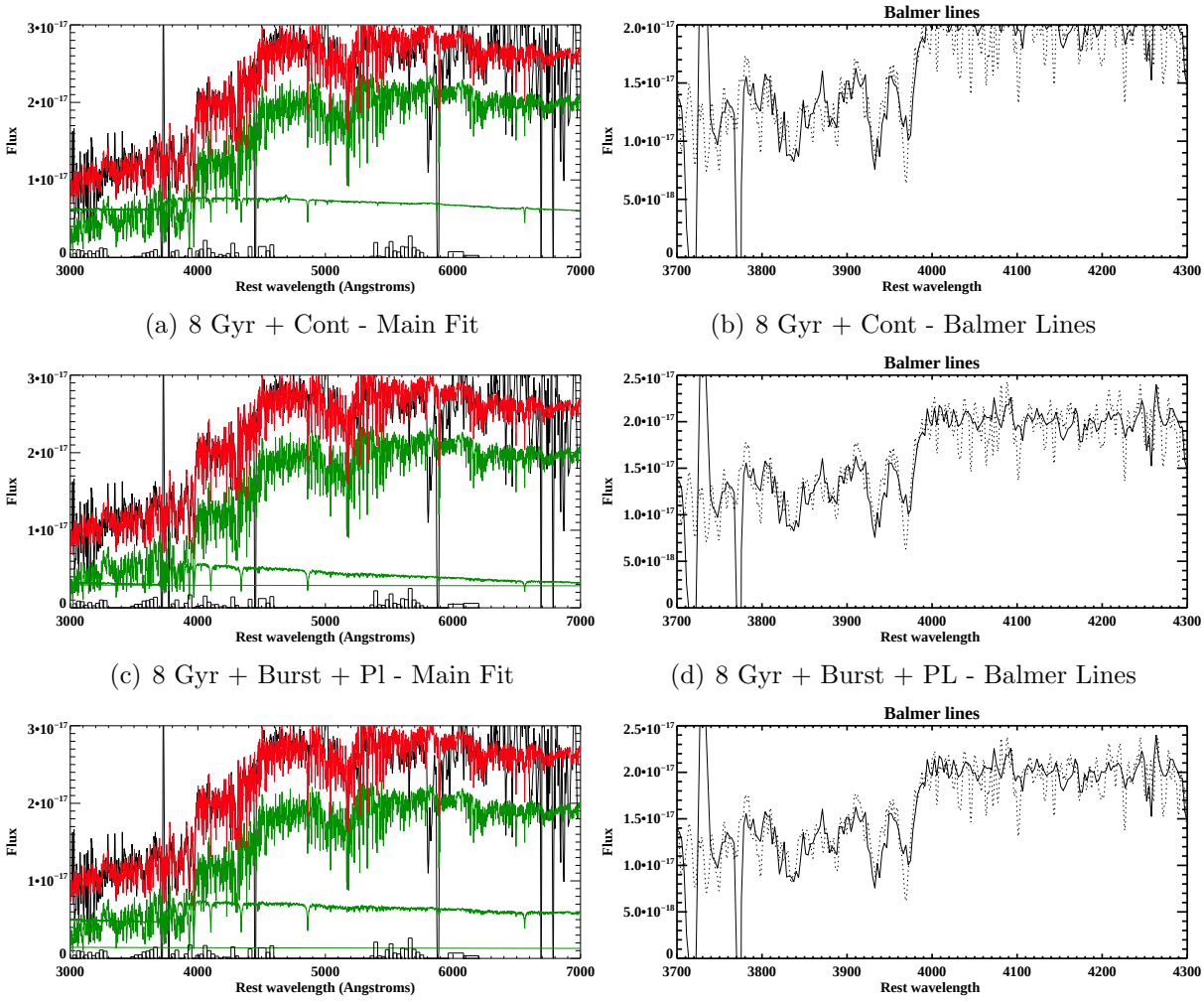

(a) 8 Gyr + Cont - Main Fit

(b) 8 Gyr + Cont - Balmer Lines

(c) 8 Gyr + Burst + Pl - Main Fit

(d) 8 Gyr + Burst + PL - Balmer Lines

(e) 8 Gyr + Cont + PL - Main Fit

(f) 8 Gyr + Cont + PL - Balmer Lines

Figure A.16: The best fitting CONFIT models for each combination of components that provided an acceptable fit for the J0332-00 - Companion Nucleus aperture.

A.12 Examples of CONFIT plots for J0334-00

The plots shown in Figure A.17 show examples of acceptable CONFIT fits for the different assumed combinations. The OSP ages and whether a power-law compoent was included are shown in the sub-caption for each figure. The YSP ages and reddenings for each of the sub figures are A.17(a) & A.17(b) $t_{YSP} = 0.05$ Gyr and $E(B-V) = 0.3$, A.17(c) & A.17(d) $t_{YSP} = 0.04$ Gyr and $E(B-V) = 0.2$, A.17(e) & A.17(f) $t_{YSP} = 0.05$ Gyr and $E(B-V) = 0.3$.

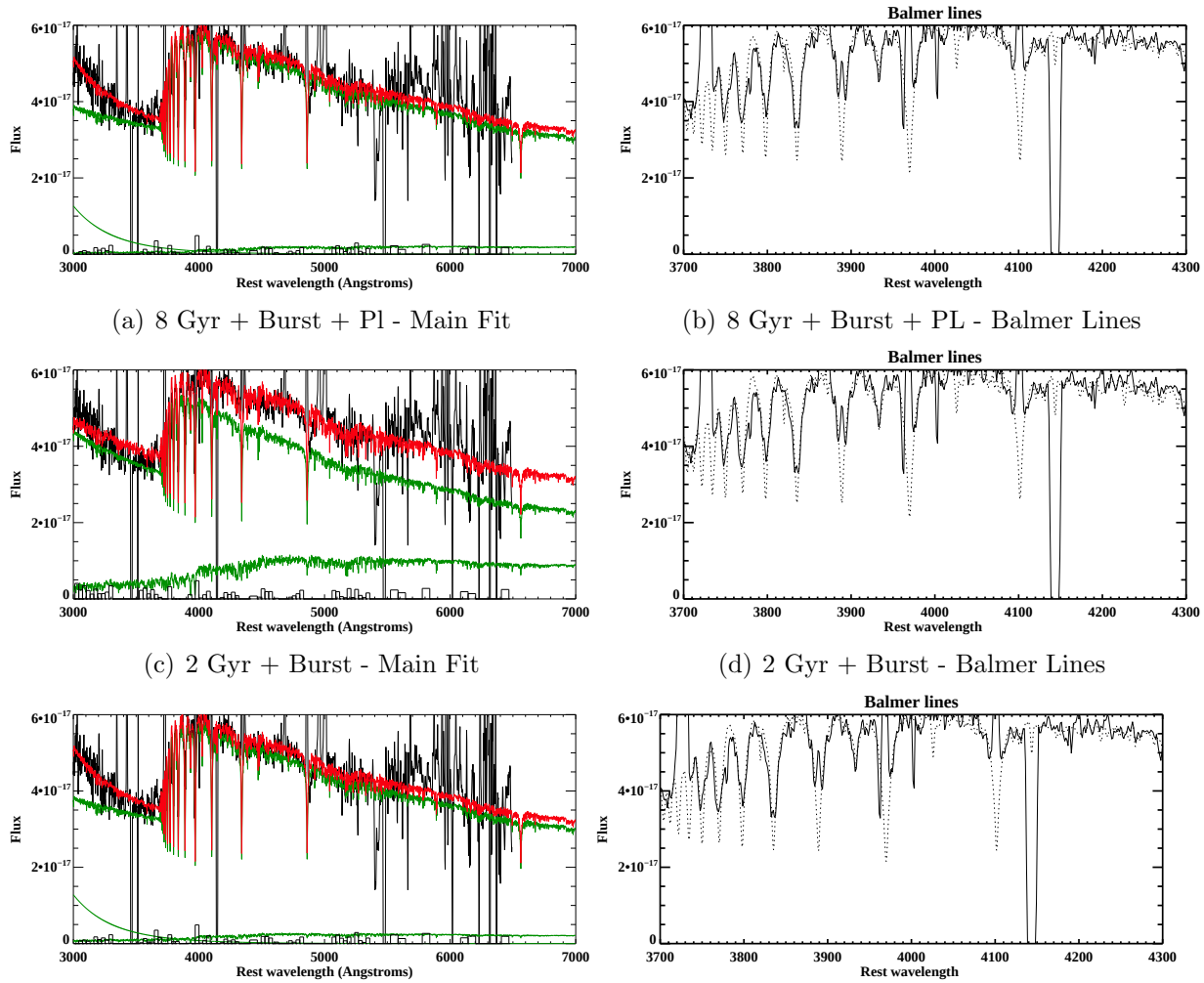

(a) 8 Gyr + Burst + Pl - Main Fit

(b) 8 Gyr + Burst + PL - Balmer Lines

(c) 2 Gyr + Burst - Main Fit

(d) 2 Gyr + Burst - Balmer Lines

(e) 2 Gyr + Burst + PL - Main Fit

(f) 2 Gyr + Burst + PL - Balmer Lines

Figure A.17: The best fitting CONFIT models for each combination of components that provided an acceptable fit for the aperture extracted from J0334-00

A.13 Examples of CONFIT plots for J0848+01

The plots shown in Figure A.18 show examples of acceptable CONFIT fits for the different assumed combinations. The OSP ages and whether a power-law compoent was included are shown in the sub-caption for each figure. The YSP ages and reddenings for each of the sub figures are A.18(a) & A.18(b) $t_{YSP} = 0.4$ Gyr and $E(B-V) = 0.2$, A.18(c) & A.18(d) $t_{YSP} = 0.2$ Gyr and $E(B-V) = 0.6$, A.18(e) & A.18(f) $t_{YSP} = 0.3$ Gyr and $E(B-V) = 0.5$.

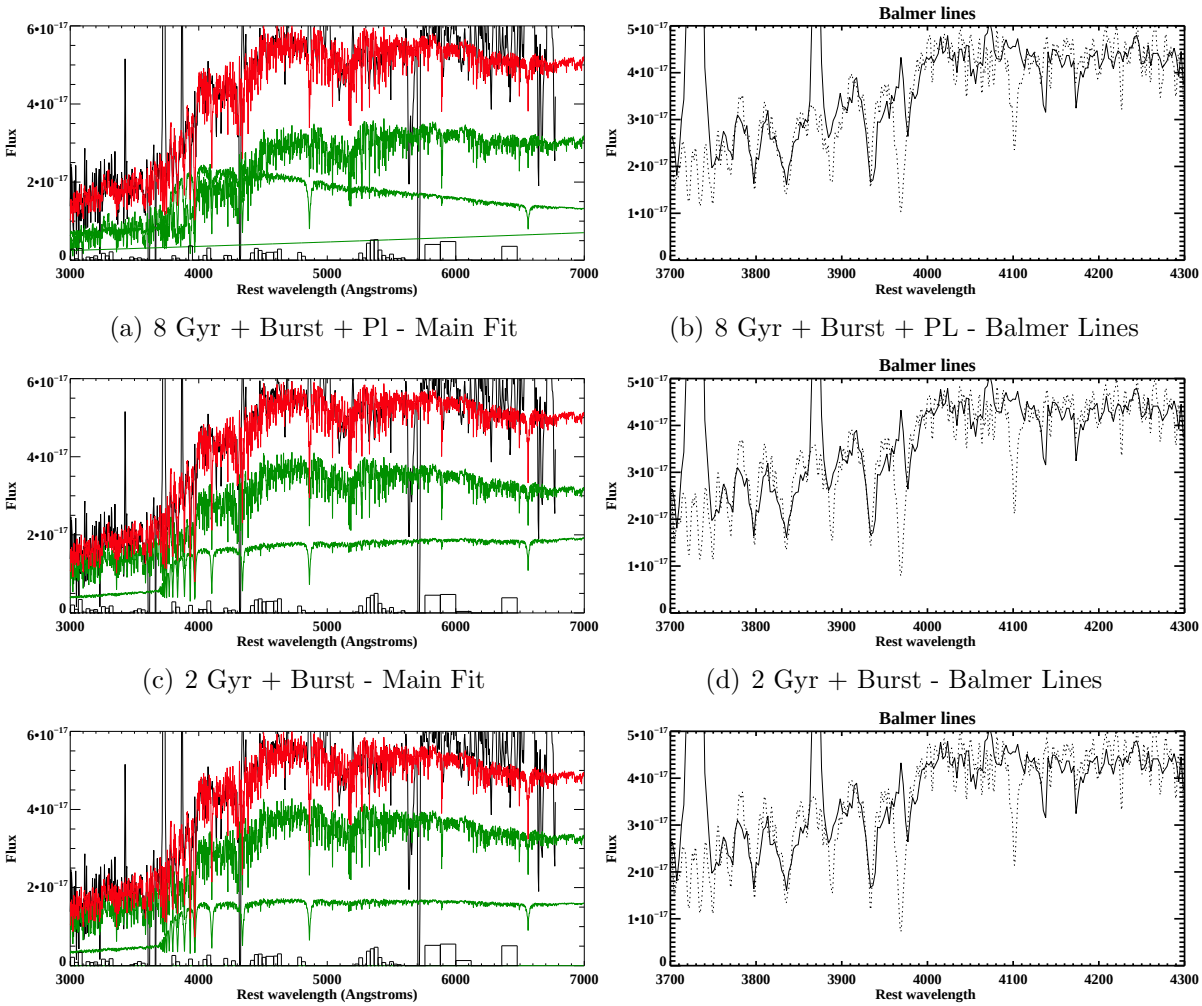

(a) 8 Gyr + Burst + Pl - Main Fit

(b) 8 Gyr + Burst + PL - Balmer Lines

(c) 2 Gyr + Burst - Main Fit

(d) 2 Gyr + Burst - Balmer Lines

(e) 2 Gyr + Burst + PL - Main Fit

(f) 2 Gyr + Burst + PL - Balmer Lines

Figure A.18: The best fitting CONFIT models for each combination of components that provided an acceptable fit for the aperture extracted from J0848+01

A.14 Examples of CONFIT plots for J0904-00

The plots shown in Figure A.19 show examples of acceptable CONFIT fits for the different assumed combinations. The OSP ages and whether a power-law compoent was included are shown in the sub-caption for each figure. The YSP ages and reddenings for each of the sub figures are A.19(a) & A.19(b) $t_{YSP} = 0.2$ Gyr and $E(B-V) = 0.3$, A.19(c) & A.19(d) $t_{YSP} = 0.2$ Gyr and $E(B-V) = 0.3$, A.19(e) & A.19(f) $t_{YSP} = 0.2$ Gyr and $E(B-V) = 0.4$, A.19(g) & A.19(h) $t_{YSP} = 0.006$ Gyr and $E(B-V) = 0.4$, A.19(i) & A.19(j) $t_{YSP} = 0.1$ Gyr and $E(B-V) = 0.4$, A.19(k) & A.19(l) $t_{YSP} = 0.1$ Gyr and $E(B-V) = 0.2$, A.19(m) & A.19(n) $t_{YSP} = 0.2$ Gyr and $E(B-V) = 0.4$.

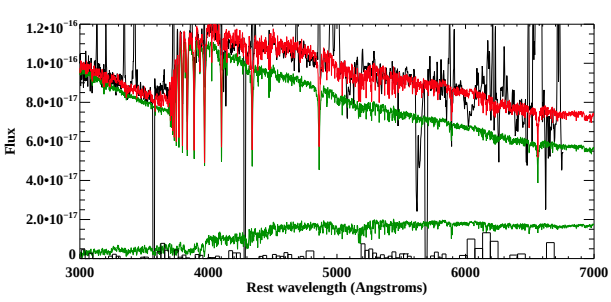

(a) 8 Gyr + Cont - Main Fit

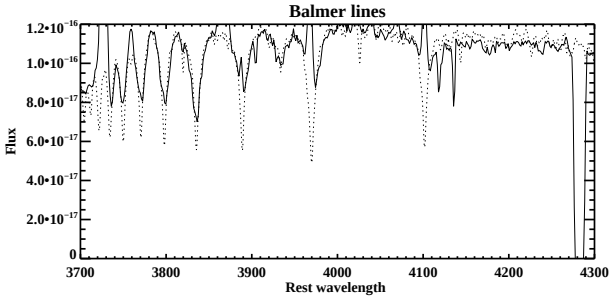

(b) 8 Gyr + Cont - Balmer Lines

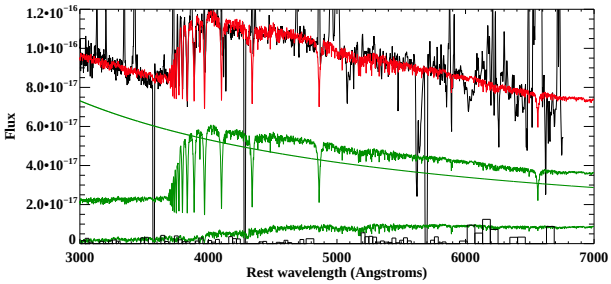

(c) 8 Gyr + Burst + Pl - Main Fit

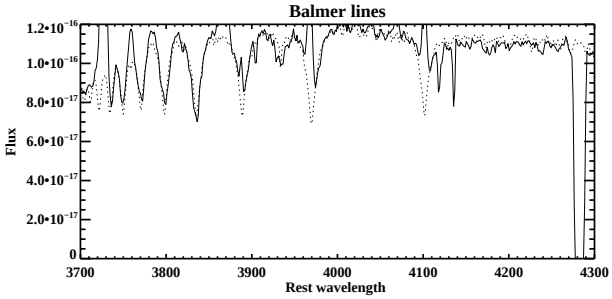

(d) 8 Gyr + Burst + PL - Balmer Lines

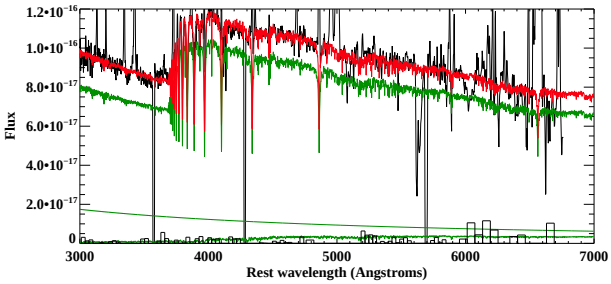

(e) 8 Gyr + Cont + PL - Main Fit

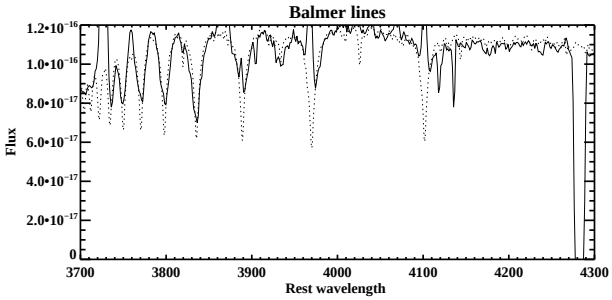

(f) 8 Gyr + Cont + PL - Balmer Lines

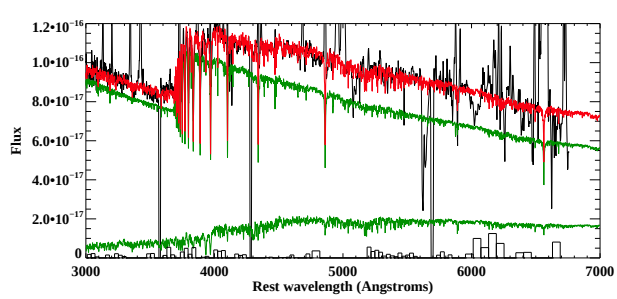

(g) 2 Gyr + Burst - Main Fit

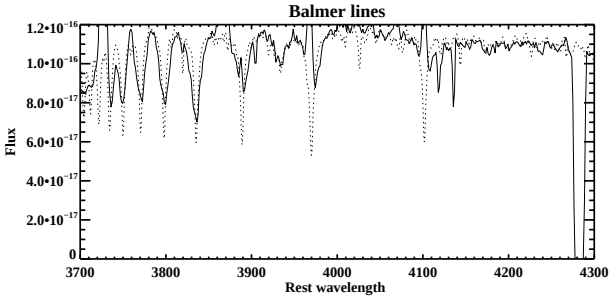

(h) 2 Gyr + Burst - Balmer Lines

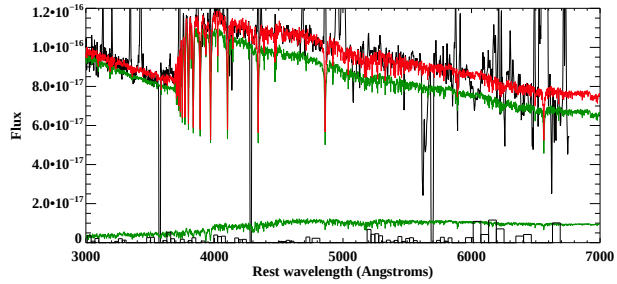

(i) 2 Gyr + Cont - Main Fit

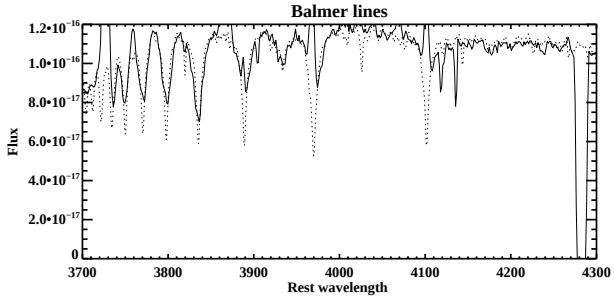

(j) 2 Gyr + Cont - Balmer Lines

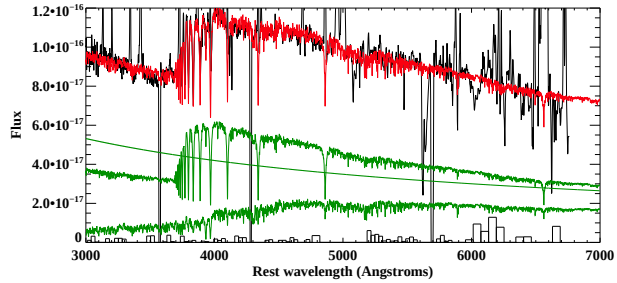

(k) 2 Gyr + Burst + PL - Main Fit

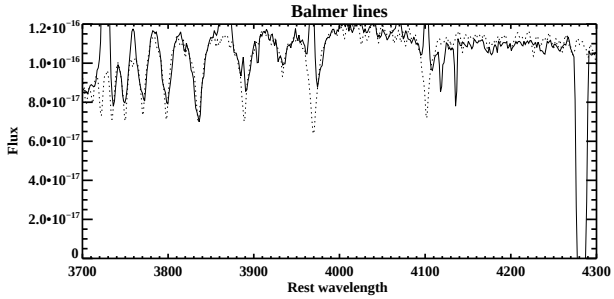

(l) 2 Gyr + Burst + PL - Balmer Lines

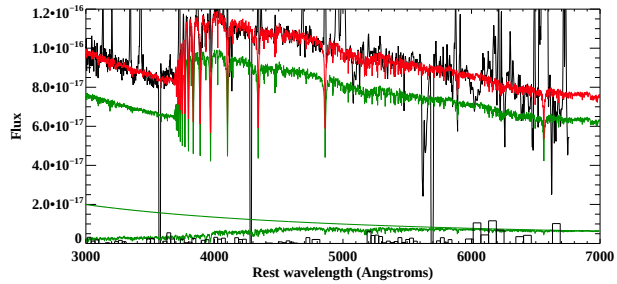

(m) 2 Gyr + Cont + PL - Main Fit

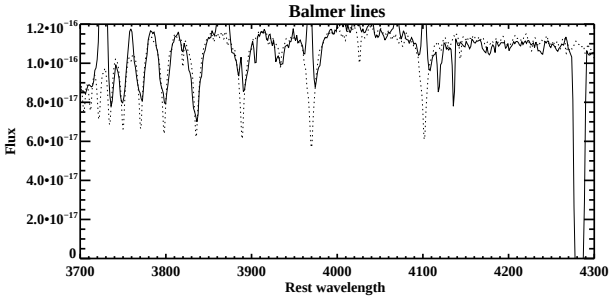

(n) 2 Gyr + Cont + PL - Balmer Lines

Figure A.19: The best fitting CONFIT models for each combination of components that provided an acceptable fit for the aperture extracted from J0904-00

A.14.1 Examples of CONFIT fits for J0923+01

The plots shown in Figure A.20 show examples of acceptable CONFIT fits for the different assumed combinations. The OSP ages and whether a power-law compoent was included are shown in the sub-caption for each figure. The YSP ages and reddenings for each of the sub figures are A.20(a) & A.20(b) $t_{YSP} = 0.05$ Gyr and $E(B-V) = 0.6$, A.20(c) & A.20(d) $t_{YSP} = 0.1$ Gyr and $E(B-V) = 0.4$, A.20(e) & A.20(f) $t_{YSP} = 0.09$ Gyr and $E(B-V) = 0.4$.

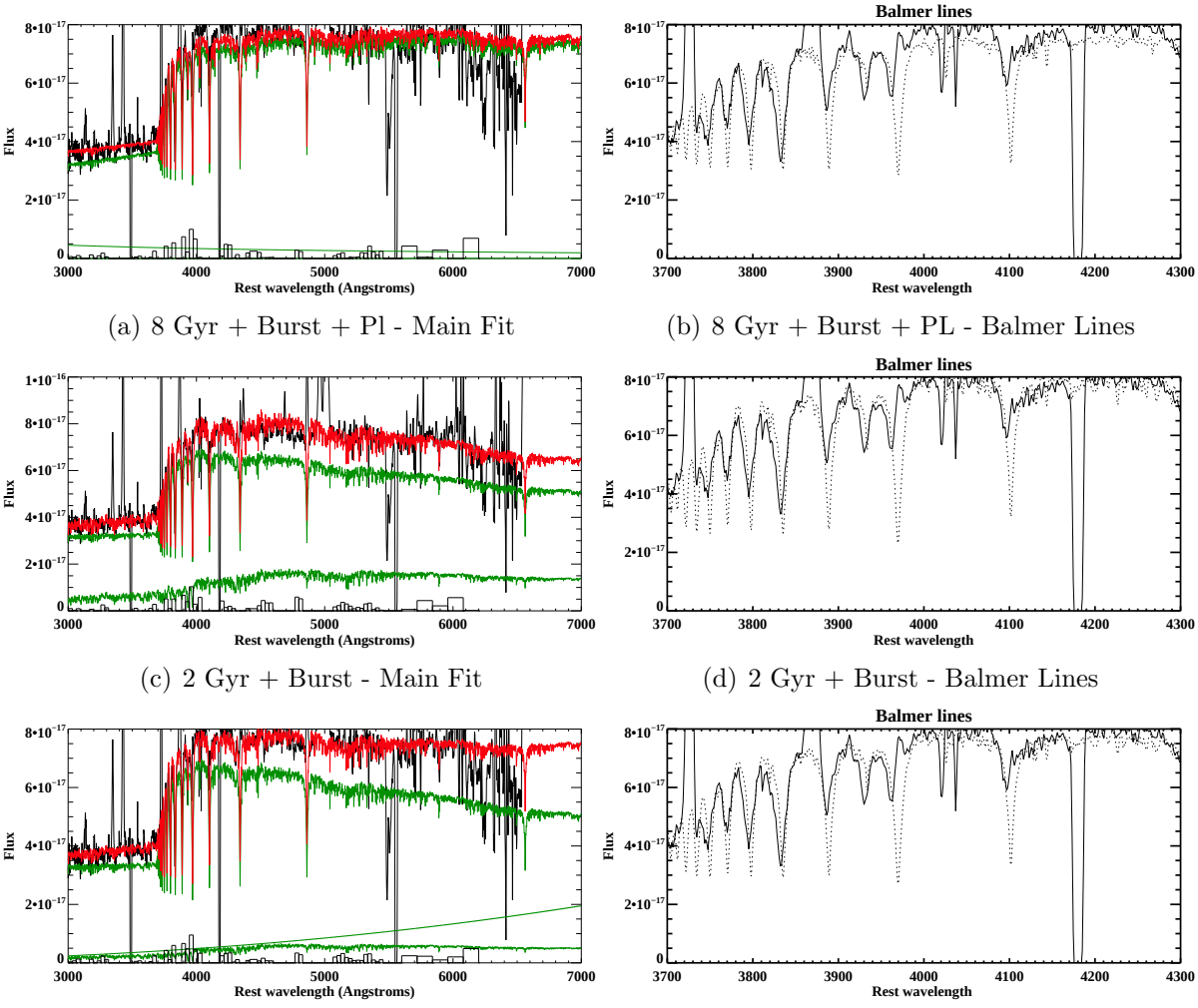

(a) 8 Gyr + Burst + Pl - Main Fit

(b) 8 Gyr + Burst + PL - Balmer Lines

(c) 2 Gyr + Burst - Main Fit

(d) 2 Gyr + Burst - Balmer Lines

(e) 2 Gyr + Burst + PL - Main Fit

(f) 2 Gyr + Burst + PL - Balmer Lines

Figure A.20: The best fitting CONFIT models for each combination of components that provided an acceptable fit for the aperture extracted from J0923+01

A.14.2 Examples of CONFIT fits for J0924+01

The plots shown in Figure A.21 show examples of acceptable CONFIT fits for the different assumed combinations. The OSP ages and whether a power-law compoent was included are shown in the sub-caption for each figure. The YSP ages and reddenings for each of the sub figures are A.21(a) & A.21(b) $t_{YSP} = 0.06$ Gyr and $E(B-V) = 0.9$, A.21(c) & A.21(d) $t_{YSP} = 0.007$ Gyr and $E(B-V) = 1.1$, A.21(e) & A.21(f) $t_{YSP} = 0.2$ Gyr and $E(B-V) = 0.9$, A.21(g) & A.21(h) $t_{YSP} = 0.009$ Gyr and $E(B-V) = 0.9$, A.21(i) & A.21(j) $t_{YSP} = 0.02$ Gyr and $E(B-V) = 1.0$, A.21(k) & A.21(l) $t_{YSP} = 0.007$ Gyr and $E(B-V) = 0.8$, A.21(m) & A.21(n) $t_{YSP} = 0.04$ Gyr and $E(B-V) = 1.1$.

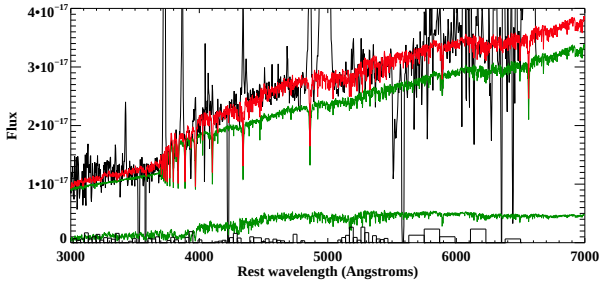

(a) 8 Gyr + Cont - Main Fit

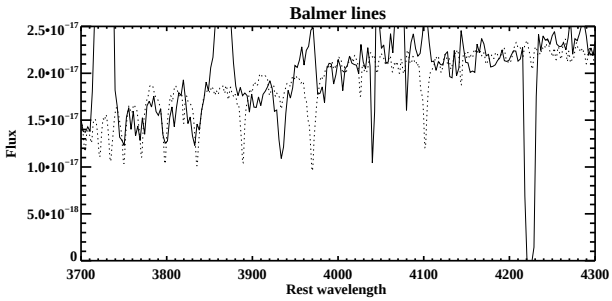

(b) 8 Gyr + Cont - Balmer Lines

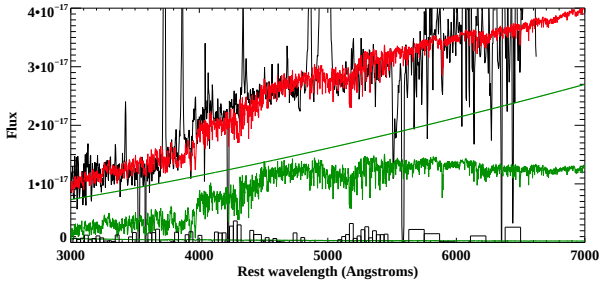

(c) 8 Gyr + Burst + Pl - Main Fit

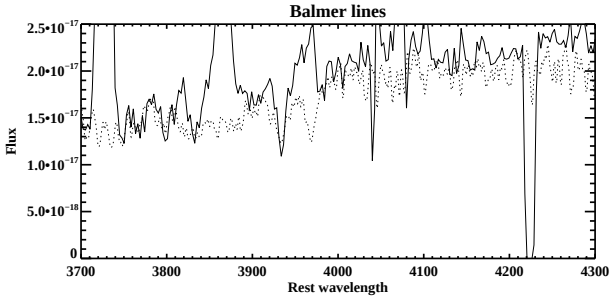

(d) 8 Gyr + Burst + PL - Balmer Lines

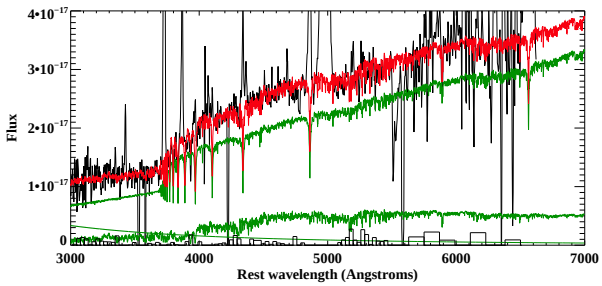

(e) 8 Gyr + Cont + PL - Main Fit

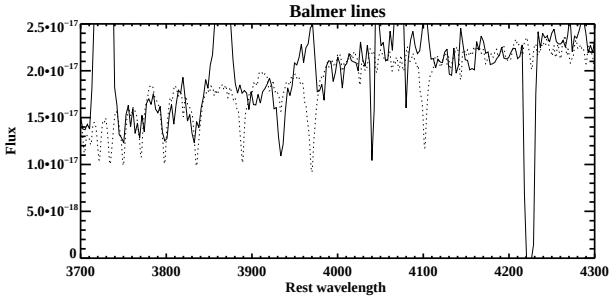

(f) 8 Gyr + Cont + PL - Balmer Lines

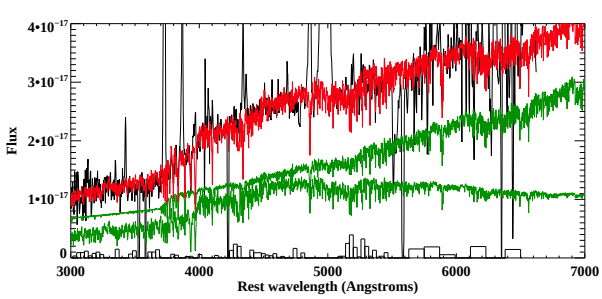

(g) 2 Gyr + Burst - Main Fit

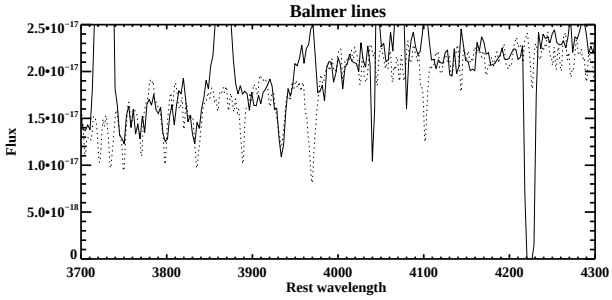

(h) 2 Gyr + Burst - Balmer Lines

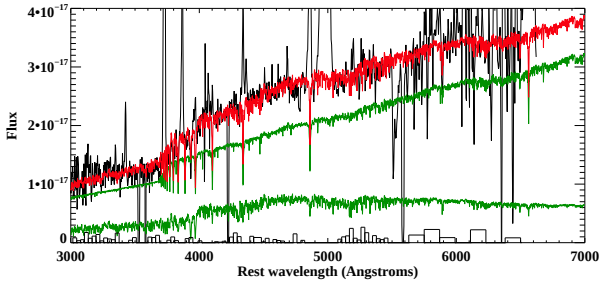

(i) 2 Gyr + Cont - Main Fit

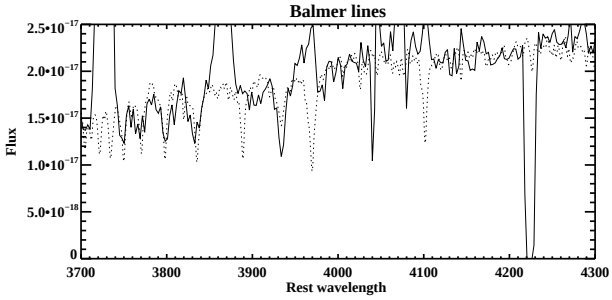

(j) 2 Gyr + Cont - Balmer Lines

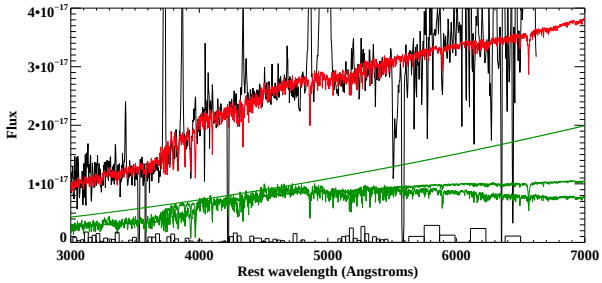

(k) 2 Gyr + Burst + PL - Main Fit

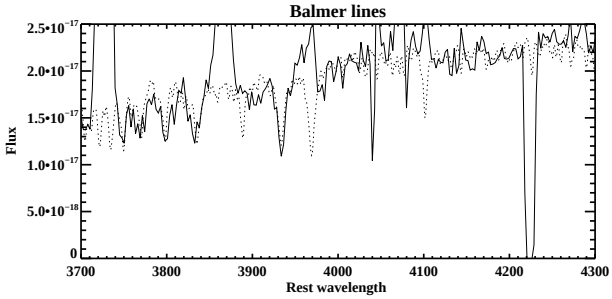

(l) 2 Gyr + Burst + PL - Balmer Lines

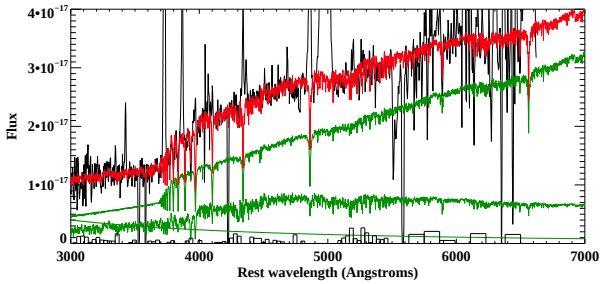

(m) 2 Gyr + Cont + PL - Main Fit

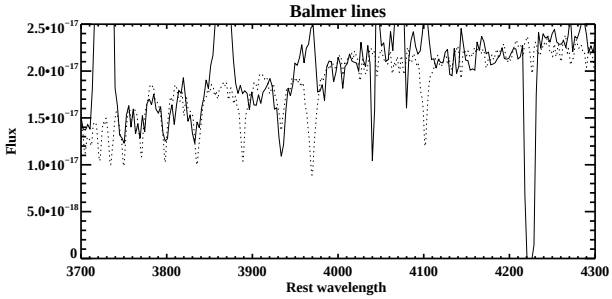

(n) 2 Gyr + Cont + PL

Figure A.21: The best fitting CONFIT models for each combination of components that provided an acceptable fit for the aperture extracted from J0924+01

A.15 Examples of CONFIT fits for J0948+00

The plots shown in Figure A.22 show examples of acceptable CONFIT fits for the different assumed combinations. The OSP ages and whether a power-law compoent was included are shown in the sub-caption for each figure. The YSP ages and reddenings for each of the sub figures are A.22(a) & A.22(b) $t_{YSP} = 0.2$ Gyr and $E(B-V) = 0.1$, A.22(c) & A.22(d) $t_{YSP} = 0.2$ Gyr and $E(B-V) = 0.3$, A.22(e) & A.22(f) $t_{YSP} = 0.3$ Gyr and $E(B-V) = 0.2$.

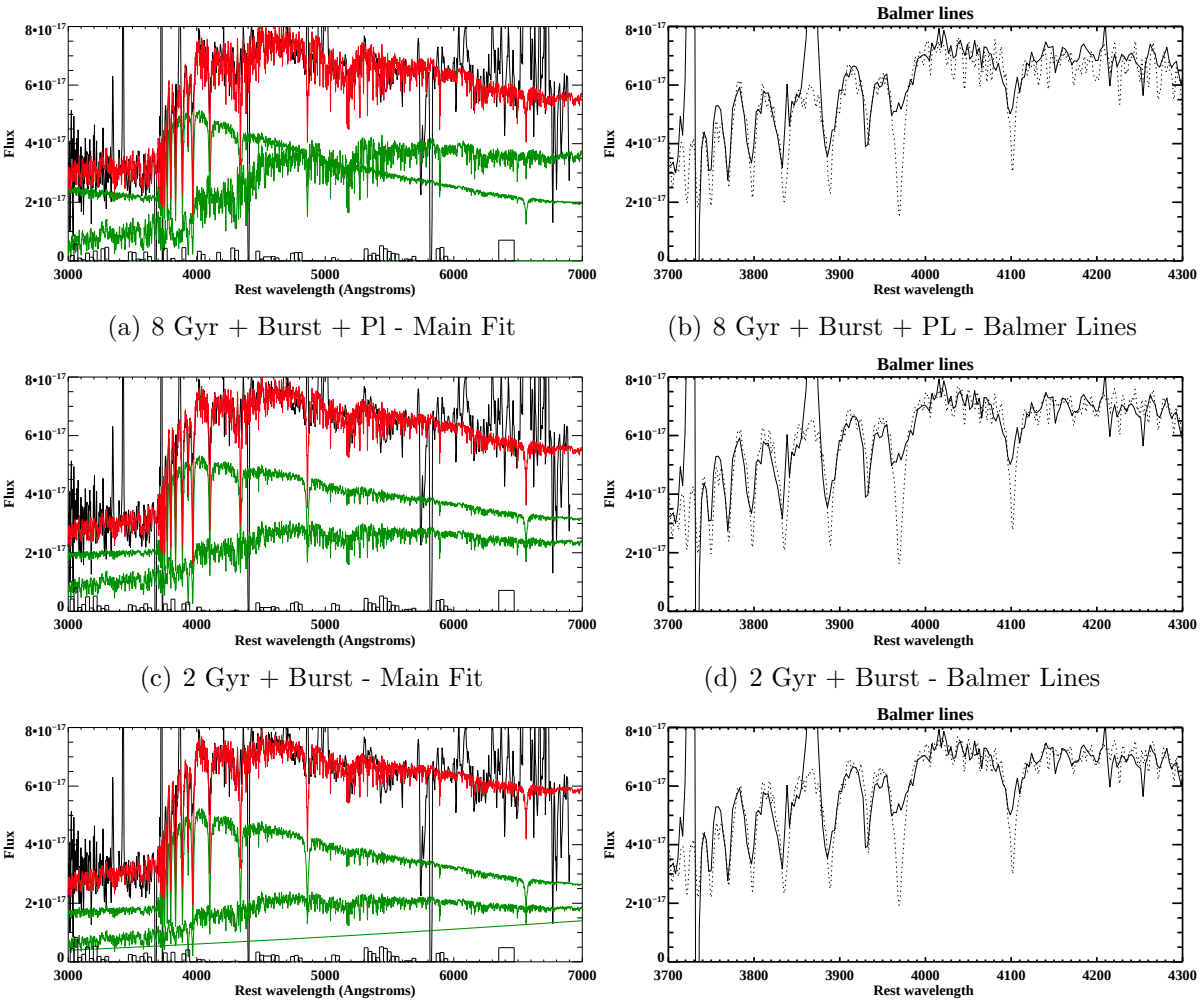

(a) 8 Gyr + Burst + Pl - Main Fit

(b) 8 Gyr + Burst + PL - Balmer Lines

(c) 2 Gyr + Burst - Main Fit

(d) 2 Gyr + Burst - Balmer Lines

(e) 2 Gyr + Burst + PL - Main Fit

(f) 2 Gyr + Burst + PL - Balmer Lines

Figure A.22: The best fitting CONFIT models for each combination of components that provided an acceptable fit for the aperture extracted from J0948+00

A.16 Examples of CONFIT fits for J2358-00

The plots shown in Figure A.23 show examples of acceptable CONFIT fits for the different assumed combinations. The OSP ages and whether a power-law compoent was included are shown in the sub-caption for each figure. The YSP ages and reddenings for each of the sub figures are A.23(a) & A.23(b) $t_{YSP} = 0.1$ Gyr and $E(B-V) = 0.6$, A.23(c) & A.23(d) $t_{YSP} = 0.04$ Gyr and $E(B-V) = 0.6$, A.23(e) & A.23(f) $t_{YSP} = 0.1$ Gyr and $E(B-V) = 0.6$.

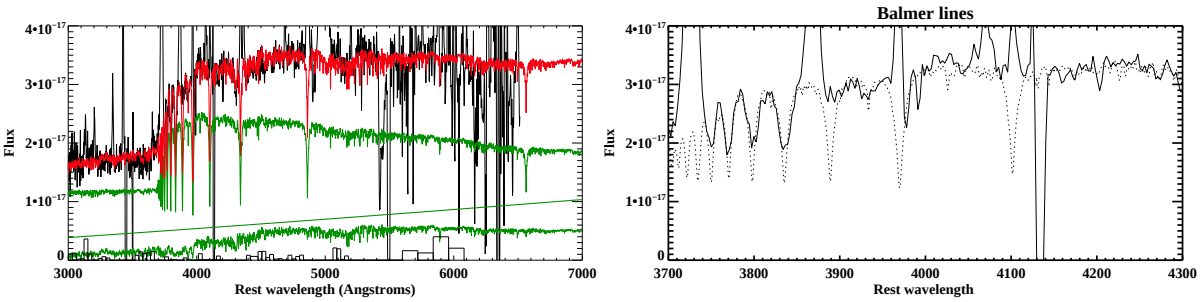

(a) 8 Gyr + Burst + Pl - Main Fit

(b) 8 Gyr + Burst + PL - Balmer Lines

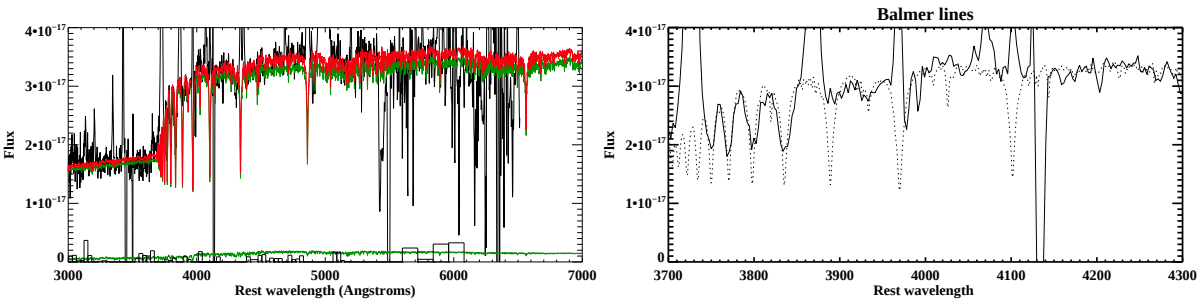

(c) 2 Gyr + Burst - Main Fit

(d) 2 Gyr + Burst - Balmer Lines

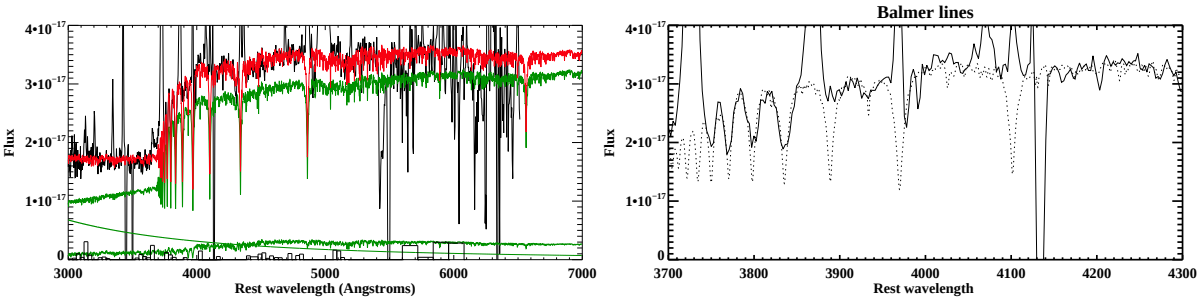

(e) 2 Gyr + Burst + PL - Main Fit

(f) 2 Gyr + Burst + PL - Balmer Lines

Figure A.23: The best fitting CONFIT models for each combination of components that provided an acceptable fit for the aperture extracted from J2358-00